Characterizing Atrial Fibrillation Substrate by Electrogram and Restitution Analysis

Zur Erlangung des akademischen Grades eines

DOKTORS DER INGENIEURWISSENSCHAFTEN (Dr.-Ing.)

von der KIT-Fakultät für

Elektrotechnik und Informationstechnik

des Karlsruher Instituts für Technologie (KIT)

genehmigte

DISSERTATION

von

Mark Nothstein, M.Sc.

geb. in Hof

Tag der mündlichen Prüfung:	02. 12. 2021
Referent:	Prof. Dr. rer. nat. Olaf Dössel
Korreferent 1:	Priv.-Doz. Dr. med. Armin Luik
Korreferent 2:	Dr.-Ing. Axel Loewe

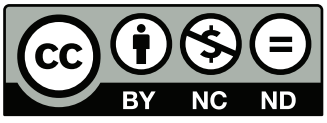

Abstract

Atrial fibrillation (AF) is the most common supraventricular arrhythmia in clinical practice. There is increasing evidence from a mechanistic point of view that pathological atrial substrate (fibrosis) plays a central role in the maintenance and perpetuation of AF. AF is treated by ablation of fibrotic substrate. However, detection of such substrate is an ongoing challenge as demonstrated by poor clinical ablation outcomes. Therefore, the main topic of this work is the characterization of atrial substrate.
Determining signal characteristics at fibrotic substrate sites could make detection and subsequently ablation of such sites easier in future. Additionally, understanding of how these sites uphold AF can increase positive outcome of AF ablation procedures. Lastly, restitution information could be a further tool of substrate characterization that could help with distinction of pathological and non-pathological sites and therefore further improve ablation outcome.
In this thesis two approaches for substrate characterization are presented.
Firstly, substrate was characterized by proposing electrogram characteristics that defined sites maintaining AF, which after ablation terminated AF. This study was performed on 21 patients in whom low-voltage-guided ablation after pulmonary vein isolation terminated clinical persistent AF. Successful termination sites of AF displayed distinct electrogram patterns with short local cycle lengths that included fractionated and low-voltage potentials that were locally highly consistent and covered a majority of the local AF cycle length. Most of these areas also exhibited pathologic delayed atrial late potentials and fractionated electrograms in sinus rhythm.
Secondly, restitution information of local amplitude and local conduction velocity (CV) was acquired and used to infer information on the underlying substrate. Restitution data was gained from 22 AF patients from two clinics by using a S1S2 protocol between pacing intervals of 180 ms to 500 ms. To obtain restitution data from the patient group, an automated algorithm capable of reading, segmenting, and analyzing large amounts of stimulation protocol data had to be developed. This algorithm was developed as part of this work and is called CVAR-Seg. The CVAR-Seg algorithm provided noise-robust signal segmentation up until noise levels far exceeding expected clinical noise levels. CVAR-Seg was released as open source to the community and due to its modular arrangement, enables easy replacement of each of the single process steps by alternative methods according to the user's needs.
Additionally, a novel method called inverse double ellipse method was established to determine local CV within the scope of this study. This inverse double ellipse method estimated CV, fiber orientation and anisotropy factor from any electrode arrangement and reproduced

in-silico CV, fiber orientation and CV anisotropy more accurately and more robust than the current state-of-the-art method. Furthermore, the method proved to be real-time capable and thus a valid consideration to implement in clinical electrophysiology systems. This would enable instantaneous localized measurement of atrial substrate information, gaining a CV map, an anisotropy ratio map, and a fiber map simultaneously during one mapping procedure.
Restitution information of the patient cohort was evaluated using the CVAR-Seg pipeline and the inverse double ellipse method to acquire amplitude and CV restitution curves. Restitution curves were fitted using a mono-exponential function. The fit parameters representing the restitution curves were used to discern differences in restitution properties between pathological and non-pathological substrate. The result was that clinically defined low voltage (LV) zones were characterized by a reduced amplitude asymptote and a steep decay with increased pacing rate, whereas CV curves showed a reduced CV asymptote and a high range of decay values.
Moreover, restitution differences within the atrial body at the posterior and anterior wall were compared, since literature reports revealed inconclusive results. In this work, the posterior atrial wall was found to contain amplitude and CV restitution curves with higher asymptote and more moderate curvature than the anterior atrial wall.
To move beyond the empirically described manually chosen threshold used currently, the parameter space spanned by the fit parameters of the amplitude and CV restitution curves was searched for naturally occurring clusters. While clusters were present, their inadequate separation from each other indicated a continuous progression of the amplitude curves as well as the CV curves with the level of the substrate pathology.
Lastly, an easier and faster method to acquire restitution data was proposed that is based on acquisition of the maximum slope and provides comparable information content to a full restitution curve.

This work presents two novel methods, the CVAR-Seg algorithm and the inverse double ellipse fit that expedite and refine evaluation of S1S2 protocols and estimation of local CV. Furthermore, this work defines characteristics of pathological tissue that help identify sources of arrhythmia. Thus, this work may help to improve the therapy of AF in the future.

Zusammenfassung

Vorhofflimmern ist die häufigste supraventrikuläre Arrhythmie in der klinischen Praxis. Es gibt Hinweise darauf, dass pathologisches Vorhofsubstrat (Fibrose) eine zentrale mechanistische Rolle bei der Aufrechterhaltung von Vorhofflimmern spielt. Die Behandlung von Vorhofflimmern erfolgt durch Ablation des fibrotischen Substrats. Der Nachweis eines solchen Substrats ist jedoch eine ungelöste Herausforderung, was durch die mangelnden positiven klinischen Ablationsergebnisse ersichtlich wird.
Daher ist das Hauptthema dieser Arbeit die Charakterisierung des atrialen Substrats.
Die Bestimmung von Signalmerkmalen an Stellen mit fibrotischem Substrat erleichtert die Erkennung und anschließende Ablation solcher Areale in Zukunft. Darüber hinaus kann das Verständnis der Art und Weise, wie diese Areale das Vorhofflimmern aufrechterhalten, die positiven Ergebnisse von Ablationseingriffen verbessern. Schließlich kann Restitutionsinformation ein weiteres Instrument zur Substratcharakterisierung sein, das bei der Unterscheidung zwischen pathologischen und nicht-pathologischen Arealen helfen und somit das Ablationsergebnis weiter verbessert.
In dieser Arbeit werden zwei Ansätze zur Substratcharakterisierung vorgestellt:
Zunächst wurde eine Charakterisierung des Substrats mit Hilfe des intraatrialen Elektrogramms vorgenommen. Dazu wurde eine Auswahl spezifischer Merkmale des Elektrogramms an Positionen evaluiert, die eine Terminierung von Vorhofflimmern nach Ablation zur Folge hatten. Die Studie beinhaltete 21 Patienten, bei denen eine Ablation nach Pulmonalvenenisolation das klinisch persistierende Vorhofflimmern beendete. Der klinisch vorgeschlagene Grenzwert der Spannungsamplitude von $<0.5\,\mathrm{mV}$ wurde genutzt, um die Positionen der Ablation zu definieren. Die Bereiche, in denen das Vorhofflimmern erfolgreich terminiert wurde, wiesen ausgeprägte Elektrogramm-Muster auf. Diese waren gekennzeichnet durch kurze lokale Zykluslängen, die fraktionierte Potentiale und Niederspannungspotentiale enthielten. Gleichzeitig zeigten sie eine lokale Konsistenz und deckten einen Großteil der lokalen Vorhofflimmer-Zykluslänge ab. Die meisten dieser Bereiche wiesen auch im Sinusrhythmus pathologisch verzögerte atriale Spätpotentiale und fraktionierte Elektrogramme auf.
Im zweiten Teil der Arbeit wurden Restitutionsdaten der lokalen Amplitude und der lokalen Leitungsgeschwindigkeit (CV) erfasst und genutzt, um daraus Informationen über das zugrunde liegende Substrat abzuleiten. Die Daten zur Restitution wurden von 22 Patienten mit Vorhofflimmern aus zwei Kliniken unter Verwendung eines S1S2-Protokolls mit Stimulationsintervallen von 180 ms bis 500 ms gewonnen. Um Restitutionsdaten der Patientengruppe

zu erhalten, musste ein automatisierter Algorithmus entwickelt werden, der in der Lage ist, große Mengen an Stimulationsprotokolldaten zu lesen, zu segmentieren und auszuwerten. Dieser Algorithmus wurde in der vorliegenden Arbeit entwickelt und CVAR-Seg genannt. Der CVAR-Seg Algorithmus bietet eine rauschresistente Signalsegmentierung, die mit extremen Rauschpegeln getestet wurde, die weit über dem erwarteten klinischen Pegel lagen. CVAR-Seg wurde unter einer Open-Source-Lizenz für die Allgemeinheit bereitgestellt. Es ermöglicht aufgrund seines modularen Aufbaus den einfachen Austausch einzelner Verfahrensschritte durch alternative Methoden entsprechend den Bedürfnissen des Anwenders.
Darüber hinaus wurde im Rahmen dieser Studie eine neuartige Methode, die sogenannte inverse Doppelellipsenmethode, zur Bestimmung der lokalen CV etabliert. Diese Methode schätzt die CV, die Faserorientierung und den Anisotropiefaktor bei beliebiger Elektrodenanordnung. In Simulationen reproduzierte die Doppelellipsenmethode die vorherrschende CV, Faserorientierung und Anisotropie genauer und robuster als die aktuell gängigste Methode. Zusätzlich erwies sich diese Methode als echtzeittauglich und könnte daher in klinischen Elektrophysiologiesystemen eingesetzt werden. Die Doppelellipsenmethode würde durch die lokalisierte Vermessung des Vorhofsubstrats ermöglichen während eines Kartierungsverfahrens gleichzeitig eine CV-Karte, eine Anisotropieverhältniskarte und eine Faserkarte zu erstellen. Die Restitutionsinformationen der Patientenkohorte wurden mit der CVAR-Seg-Pipeline und der inversen Doppelellipsenmethode ausgewertet, um Amplituden- und CV-Restitutionskurven zu erhalten. Zur Anpassung der Restitutionskurven wurde eine monoexponentielle Funktion verwendet. Die Parameter der angepassten Funktion, die die Restitutionskurven abbilden, wurden verwendet, um Unterschiede in den Restitutionseigenschaften zwischen pathologischem und nicht-pathologischem Substrat zu erkennen. Das Ergebnis zeigte, dass klinisch definierte pathologische Bereiche durch eine reduzierte Amplitudenasymptote und einen steilen Kurvenabfall bei erhöhter Stimulationsrate gekennzeichnet waren. CV-Kurven zeigten eine reduzierte Asymptote und eine große Variation im Parameter der den Kurvenabfall beschreibt.
Darüber hinaus wurden die Restitutionsunterschiede innerhalb des Vorhofs an der posterioren und anterioren Wand verglichen, da die Literatur keine eindeutigen Ergebnisse lieferte. In dieser Arbeit wurde nachgewiesen, dass die posteriore Vorhofwand Amplituden- und CV-Restitutionskurven mit höherer Asymptote und moderaterer Krümmung verglichen mit der anterioren Vorhofwand aufweist.
Um über den empirisch beschriebenen manuellen Schwellenwert hinauszugehen, wurde der Parameterraum, der von den Anpassungsparametern der Amplituden- und CV-Restitutionskurven aufgespannt wird, nach natürlich vorkommenden Clustern durchsucht. Obgleich Cluster vorhanden waren, deutete ihre unzureichende Trennung auf einen kontinuierlichen, sich mit dem Schweregrad der Substratpathologie verändernden Verlauf der Amplituden- und CV-Kurven hin.
Schließlich wurde eine einfachere und schnellere Methode zur Erfassung von Restitutionsdaten vorgestellt, die einen vergleichbaren Informationsgehalt auf der Grundlage der maximalen Steigung anstelle einer vollständigen Restitutionskurve liefert.

In dieser Arbeit werden zwei neue Methoden vorgestellt, der CVAR-Seg-Algorithmus und die inverse Doppelellipsenmethode, die eine Auswertung von S1S2 Stimulationsprotokollen und die Bestimmung der lokalen Leitungsgeschwindigkeit beschleunigen und verbessern. Darüber hinaus werden in dieser Arbeit Merkmale von pathologischem Gewebe definiert, die zur Identifizierung von Arrhythmiequellen beitragen. Somit trägt diese Arbeit dazu bei, die Therapie von Vorhofflimmern in Zukunft zu verbessern.

Acknowledgments

I would like to thank Prof. Dr. Olaf Dössel for giving me the chance to work in the field of biomedical engineering and supervising my thesis. As someone from a background in solid state physics, this chance allowed me to explore a completely new field, for which I am very grateful.
I also would like to thank Dr.-Ing. Axel Loewe for the time and effort invested in supporting my work with discussions and lots of proofreading.
I want to thank the Deutsche Forschungsgemeinschaft (DFG) for financing my project.
A big thank you goes out to my office mates and friends Laura Unger and Jorge Sánchez. Laura, you introduced me to the clinical side of cardiac electrophysiology and I will remember our time sitting in front of cryptic signal morphologies and guessing at their origins fondly. I want to thank Jorge for sharing all his expertise in cardiac modeling. You always made time for me and helped me out with all modeling things related and beyond that helped addressing reviewer comments, proofreading, and sat through hours of scripting and creating videos for the openCARP project together. Additionally, I want to thank Dr.-Ing. Nicolas Pillia and Dr.-Ing. Michael Kircher for their input, encouragements, and support during my time at the IBT.
I also want to thank the whole IBT team for all their support in scientific or personal matters. Within the IBT team there was never a lack of help and the friendly nature of all of you made the daily work with each other a pleasure. Especially during the time I was injured, at first with my shoulder in a bike accident and a year later when I broke my clavicle after a motorcycle accident, everyone at the IBT was supportive and helped me out.
Much of what is presented in this thesis was conducted in collaboration with the medical experts Priv.-Doz. Dr. med. Armin Luik and Dr. med. Amir Jadidi. A big share of gratitude goes to Priv.-Doz. Dr. med. Armin Luik for introducing me to the clinical aspects surrounding electrophysiology, his help with the clinical hard and software, and his patience. Also, I want to thank him for his perseverance in acquiring patient data during the trying times of the global COVID pandemic, therefore making much of this work possible.
I also would like to thank Annika Haas for her help in manually annotating signals for me on short notice.
I would like to thank Dr. med. Amir Jadidi for all his time investment in our joint publication. He and his colleagues Prof. Dr. med. Thomas Arentz and Dr. med. Björn-Müller Edenborn continuously pushed onward to create a good story line and made our publication possible.
Furthermore, I would like to thank my colleagues in Freiburg Dr.-Ing. Gunnar Seemann and

Eike Wülfers for thoroughly proof reading our manuscripts and giving me valuable feedback along the way.
My thanks also goes out to the students I supervised: Christopher Luz, Hana Dzindo and Johannes Tischer. It was a pleasure working with you and I wish you all the best.
I want to thank Mr. Schroll for his support of the IBT infrastructure. Without his efforts in keeping everything up and running this work would not have been possible.
I want to express my deepest gratitude to my parents Werner Nothstein and Mary Desik. My parents immigrated to Germany to shape a brighter future for themselves and their children. This work is only made possible by their courage and continuous effort in pursuing that goal. They laid down the foundation for me to build upon, for which I am forever grateful.
I thank Arno Nothstein for proofreading as well as my sister Alexandra Nothstein for her continued support along the way, who is now happy to know that this will be the final document she will have to proofread on her free weekends.
Finally, I want to thank my partner Birgit Eisenmann who selflessly supported me throughout all ups and downs and was always there for me.

Contents

Abbreviations

AF atrial fibrillation
AP action potential
APD action potential duration
BCL basic cycle length
CI coupling interval
CS coronary sinus
CV conduction velocity
DBSCAN Density-Based Spatial Clustering of Applications with Noise
E1 primary activated electrode
E2 secondary activated electrode
ECG electrocardiogram
ECM extracellular matrix
EGM electrogram
ERP effective refractory period
IQR interquartile range
IVC inferior vena cava
LA left atrium
LAA left atrial appendage
LAT local activation time
LV low voltage
MinPts minimum number of neighboring points
PV pulmonary vein
PVI pulmonary vein isolation
RA right atrium
SAR sarcoplasmic reticulum
SR sinus rhythm
STD standard deviation

Chapter 1

Introduction

1.1 Motivation

Atrial fibrillation (AF) is the most common, sustained supraventricular cardiac arrhythmia characterized by an irregular heart rhythm and associated with an increased risk of heart failure, stroke, and an increased mortality [1]. Approximately one in five people run the risk of developing AF throughout their lifetime. The risk increases to more than one in three individuals in case of prevalent comorbidities such as hypertension, diabetes mellitus, heart failure, coronary artery disease, chronic kidney disease, obesity, and obstructive sleep apnoea [2]. Projections estimate the number of adults with AF will more than double by the year 2050 [3]. The medical costs of AF were conservatively estimated at 26.0 billion dollars for the USA in 2010 and consequently are also projected to increase [4]. AF poses a financial, medical as well as scientific problem that up to date is still a field of research.
Treatment strategies remain suboptimal in terms of efficiency and outcome, in part because the underlying mechanisms that perpetuate and maintain AF are not fully understood [1]. Fibrosis, among other effects, refers to an excess deposition of collagen inside the cardiac tissue [5, 6] and is suspected to be responsible for the maintenance of arrhythmias [7, 8].
Current invasive AF treatment strategies use multi-electrode catheters to record electrograms and characterize the substrate by the locally measured peak-to-peak amplitude. It has been shown that pathological tissue containing fibrosis correlates with regions of low voltage [9–11]. Beyond pulmonary vein isolation, these low voltage regions are commonly targeted by ablation to terminate AF [12–14].
A second diagnostic parameter available to the clinician is conduction velocity (CV), often represented by a local activation time (LAT) map derived from excitation wave path and CV. While the specific coupling between CV and the underlying pathologies remains unknown, a lower CV has been attributed to pathological tissue [15, 16].
For optimal treatment of AF extensive knowledge of the underlying substrate characteristics such as CV, fiber direction, and amplitude would be beneficial. Therefore, the elicitation of these factors needs to be improved. [17–19].
Following pulmonary vein isolation, the amplitude as well as CV information is used to

derive the location of focal excitations inducing or pathological substrate upholding the arrhythmia. The clinical challenge lies in the correct identification and localization of these areas that upon targeted ablation have the possibility of terminating AF, whilst avoiding unnecessary damage to healthy atrial myocardium [7, 20].
A drawback of the current acquisition method of amplitude and CV is that both are acquired at a single rate of tissue activation, mostly sinus rhythm (SR). However, mapping procedures performed in patients in AF and SR have been shown to yield different voltage amplitude maps [7, 9, 21]. The dependency of parameters on the rate at which the tissue is activated is called restitution. Thus, restitution affects amplitude and CV values and therefore restitution should be considered when evaluating patient data.
Currently, most restitution studies are performed in-silico in individual myocytes or in tissue using a monophasic action potential measurement catheter that averages myocytes action potentials over a small area [22–25]. Only a few studies have been performed at the tissue level in human atria [16, 26]. Thus, there exists no guideline on how to process and evaluate restitution information.
Additionally, the process of gaining precise localized restitution information of CV is not trivial. CV depends on wave direction, underlying atrial fiber orientation, anisotropic conduction of tissue, as well as varying effective refractory periods (ERPs) throughout the tissue and therefore all parameters need to be estimated simultaneously for precise CV reconstruction. Furthermore, for a local estimation of CV, e.g. in the vicinity of the catheter, stimulation artifacts in the recorded signals as well as stimulation specific depolarization wave propagation must be included in the estimation. Precise determination of the localized CV can reveal the arrhythmia pattern and reveal substrate pathologies. By additionally using localized restitution information of CV, a better understanding of rate dependent substrate characteristics could be achieved, especially so, if performed at different locations throughout the atrial cavity.
Consequently, CV restitution information in combination with the amplitude restitution information, could deepen the understanding of substrate characteristics and interplay between amplitude and CV at pathological and non-pathological sites throughout the atria.
Finally, if restitution information precisely characterizes the substrate, restitution curve morphology could be used to determine the pathological burden of the tissue and could be an alternative to the currently established empirical amplitude threshold.
Within the scope of this thesis, firstly, electrogram characteristics of substrate maintaining AF are deduced. Secondly, the way is paved for future in depth evaluations of restitution measurements by establishing an automatic restitution evaluation pipeline. Thirdly, a novel method to precisely evaluate local CV is determined. Finally, amplitude and CV restitution information are leveraged to assess tissue characteristics at different atrial regions and with different pathologies.

1.2 Aims of the Thesis

The main objective of this thesis is to enable characterization of AF substrate using electrograms and restitution information. This is done by addressing the following main objectives:

- Specify clinically relevant electrogram parameters in SR and in AF to distinguish fibrotic substrate upholding atrial fibrillation and give mechanistic insight into targeted ablation.
- Leverage restitution information from clinical measurements to characterize AF substrate:
  - Create an automated pipeline for evaluation of multiple restitution measurements adaptively supporting any of the commercially available electroanatomical mapping systems, while remaining robust under noisy clinical signal conditions.
  - Establish a method for local CV estimation and fiber orientation which is more accurate, faster, and more robust than the current state of the art.
  - Leverage amplitude and CV restitution information to assess differences between clinically defined pathological and non-pathological areas as well as evaluate intra-atrial substrate variation between different measurement positions (posterior and anterior) inside the atrial cavity.
  - Assess possibility of restitution information revealing distinct, separable substrate pathologies by using a clustering algorithm.

1.3 Structure of the Thesis

Part I outlines medical fundamentals, computational cardiac modeling approaches and mathematical fundamentals.

- **Chapter 2** covers the cardiac anatomy and pathophysiology of AF and fibrosis. The electroanatomical mapping procedure is introduced as well as the concept of restitution information.
- **Chapter 3** provides an overview with regards to modeling of cardiac electrophysiology and initiation of excitation propagation and finishes by introducing the current state of the art frameworks.
- **Chapter 4** introduces mathematical ellipse descriptions and the inverse problem approach used for the local CV estimation model and introduces a method for high dimensional data clustering.

Part II presents the study of obtaining clinically relevant electrogram parameters measured in SR and in AF to distinguish fibrotic substrate upholding atrial fibrillation and gives mechanistic insight into targeted ablation.

- **Chapter 5** motivates the topic.
- **Chapter 6** details the simulation setups generated to represent SR and AF and the ablation methods. Additionally, the corresponding patient data evaluation are presented.
- **Chapter 7** contains the computed simulation results for CV, amplitude, cycle length and cycle length coverage as well as the in-silico ablation results, followed by the electrogram characteristics present in clinical data.
- **Chapter 8** relates the mechanistic in-silico results to the clinical data and concludes on a set of distinctive markers specifying fibrotic tissue in SR and AF.

Part III paves the way for evaluation of restitution information by detailing an automated pipeline for evaluation of multiple restitution measurements supporting any of the commercially available electroanatomical mapping systems, while remaining robust under noisy clinical signal conditions

- **Chapter 9** motivates the topic.
- **Chapter 10** details preprocessing of input data, the segmentation of the measured S1S2 protocol and explains the pipeline performance testing procedure using synthetically generated signals with increasing degree of noise generated by a noise model. Lastly, the evaluation of the synthetic as well as the patient data is addressed.
- **Chapter 11** contains the results on how accurately the pipeline reproduced the parameters underlying the synthetically generated signals. Furthermore, the pipeline is tested for different noise levels that far exceed typical clinical noise levels. Finally, the results of the clinical data is presented.
- **Chapter 12** discusses the results of the synthetic evaluation and the clinical data.

Part IV establishes a method for local CV estimation and fiber orientation which is more accurate, faster, and more robust than the current state of the art.

- **Chapter 13** motivates the topic.
- **Chapter 14** introduces the state-of-the-art method and the new inverse double ellipse approach. The in-silico simulation setup of a highly detailed, realistic fibrotic tissue patch is explained. The acquisition of the ground truth values from the simulation is covered as well as the addition of synthetically created noise. Finally acquisition and analysis of patient data is addressed.
- **Chapter 15** shows results of the estimation of CV and fibre orientation with the in-silico model, without and with additional noise as well as the CV and fibre orientation estimation using clinical data.
- **Chapter 16** discusses the results of the synthetic evaluation and the clinical data.

Part V Leverage amplitude and CV restitution information to assess differences in substrate characteristics.

- **Chapter 17** motivates the topic.
- **Chapter 18** describes the patient measurement protocol and evaluation of restitution data.

- **Chapter 19** Shows restitution results at pathological and non-pathological sites, as well as different atrial locations. Additionally, the clustering results to assess the possibility of restitution information revealing distinct, separable substrate pathologies is shown.
- **Chapter 20** discusses the results achieved with restitution information at pathological and non-pathological sites, as well as different atrial locations and answers the question if clustering can uncover different substrate types.

Chapter 21 summarizes all findings of this study and gives a brief outlook.

During the three and a half years of research work at the IBT, I published two journal papers and six conference contributions as first author. As a co-author, three journal papers and two conference contributions were published. Moreover, I supervised three student theses that covered prerequisite studies and yielded insights for the development of the work done in this thesis. See Chapter 21 for a detailed list of all publications.

PART I

FUNDAMENTALS

Chapter 2

Medical Fundamentals

2.1 Anatomy and Physiology

The heart is a cone shaped muscular organ with the primary purpose of supplying oxygenated blood and metabolic end products to all organs. It is located in the center of the thoracic cavity. The heart itself is functionally and anatomically divided into two halves by the septum creating two closed-loop systems (Figure 2.1). Each half consists of an atrium and a ventricle

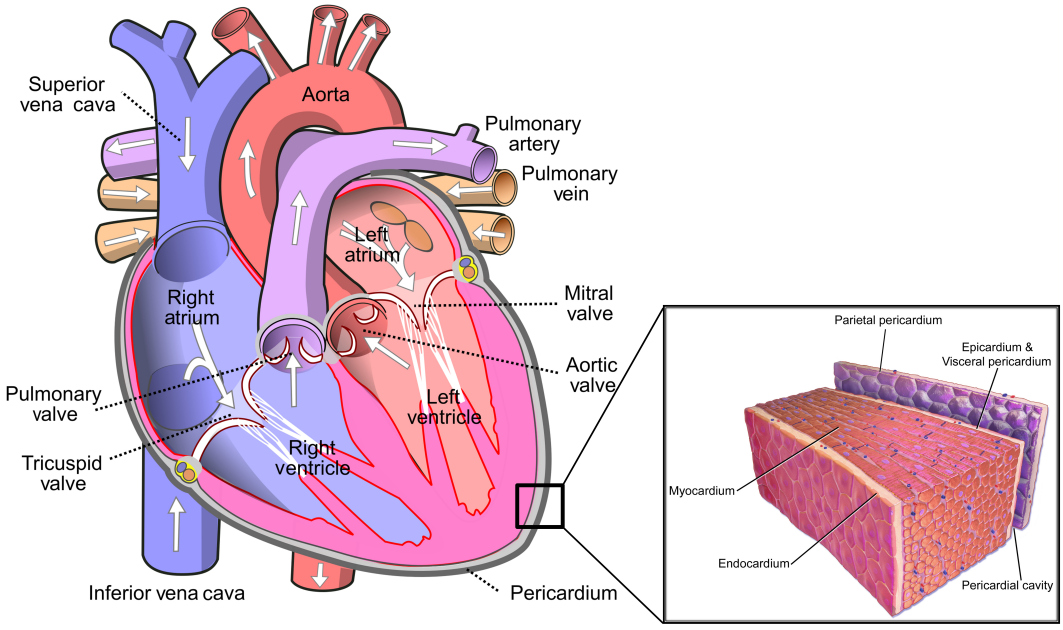

Figure 2.1: Schematic view of the heart cavities. White arrows indicate bloodflow. Adapted from [27] and [28]

that are connected via the tricuspid valve (right) and mitral valve (left). These valves enable unidirectional blood flow from atria to ventricle. The aortic (left) and the pulmonary (right) valve allow for interchanging blood between the left and right loop systems. The pulmonary loop exchanges deoxygenated blood from the organs with oxygen-rich blood from the lungs. The systemic loop pumps the oxygen-rich blood to the organs and returns deoxygenated blood as input to the pulmonary loop.
A single cardiac cycle comprises four steps (Figure 2.1 white arrows): i) Deoxygenated blood flows from the body via the superior vena cava (SVC) and the inferior vena cava (IVC) into the right atrium (RA). The RA contracts, thereby pumping blood into the right ventricle via the tricuspid valve. Once the right ventricle fills with blood the tricuspid valve closes to prevent blood from flowing back into the atrium. ii) The right ventricle contracts and forces blood through the pulmonary valve along the pulmonary artery to the lungs. During this time the RA relaxes into its original state. iii) The left atrium (LA) contracts pushing oxygenated blood from the lungs into the left ventricle via the mitral valve. Once the left ventricle has filled with blood the mitral valve closes. iv) The left ventricle contracts, pumping blood through the aortic valve to the organs throughout the body. Then the aortic valve closes and the left ventricle relaxes. In reality the atrial and ventricular cycle happen simultaneously for the left and the right side. This effectively reduces the heart cycle to two states. The contraction of ventricles is referred to as the systole phase while the relaxation of the ventricles and simultaneous contraction of atria is called the diastole phase.
To ensure a smooth contraction motion, a fibrous sac, called the pericardium encloses the three layers that compose the ventricular and atrial wall (Figure 2.2). The outermost layer is the epicard which ensures a smooth movement within the pericard sac. The myocard is the functional part of the heart wall consisting of several layers of cardiomyocytes that allow for radial as well as apicobasal contraction of the atria. The endocard is the innermost layer consisting of a thin layer of smooth connective tissue over the myocard to ensure non-turbulent blood flow.

2.1.1 Atrial Anatomy

This work focuses on the LA, which can be subdivided into several sections. The mitral valve connects to the ventricle, while the pulmonary veins (PVs) connect to the lungs. In general, there are four PVs, though the number of PVs and branches varies between patients. The four PVs are divided into left and right and upper (superior) and lower (inferior) PV (LS, LI and RS, RI). The main body of the atria consists of the anterior wall, septum, posterior wall, lateral wall, and roof (Figure 2.2) [29]. The hollow bulge on the lateral wall between mitral valve and left PVs is called the left atrial appendage (LAA).
There are multiple connections to the RA, the most significant being a fast conduction pathway connecting the RA with the left atrial roof called the Bachmann bundle (Figure 2.3) [30]. The coronary sinus (CS) is a large vessel that runs along the posterior side of the left atria and connects into the right atrial cavity.

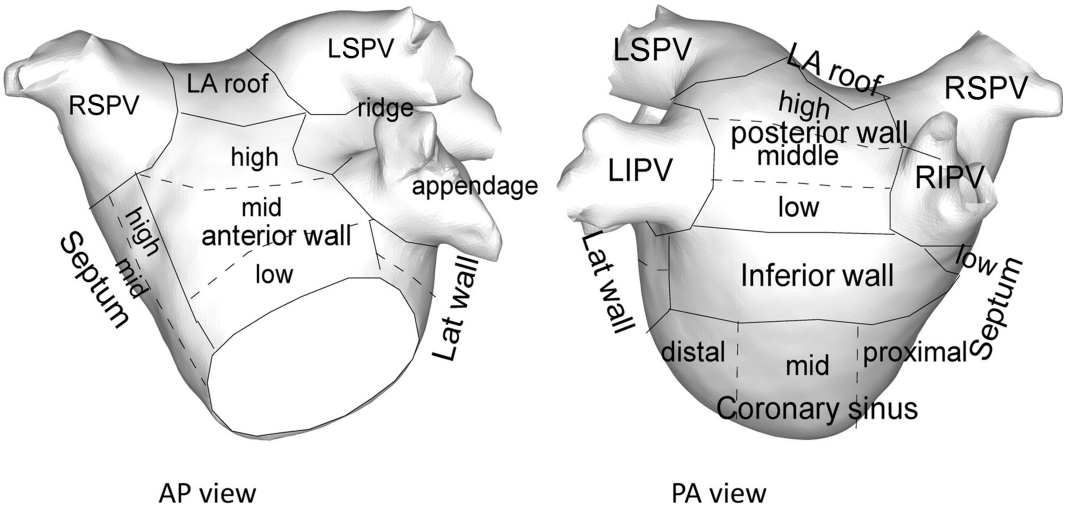

Figure 2.2: Subdivision of the left atria (LA) into defined areas for the anterior to posterior view (AP) and posterior to anterior view (PA). Adapted from [29] with permission.

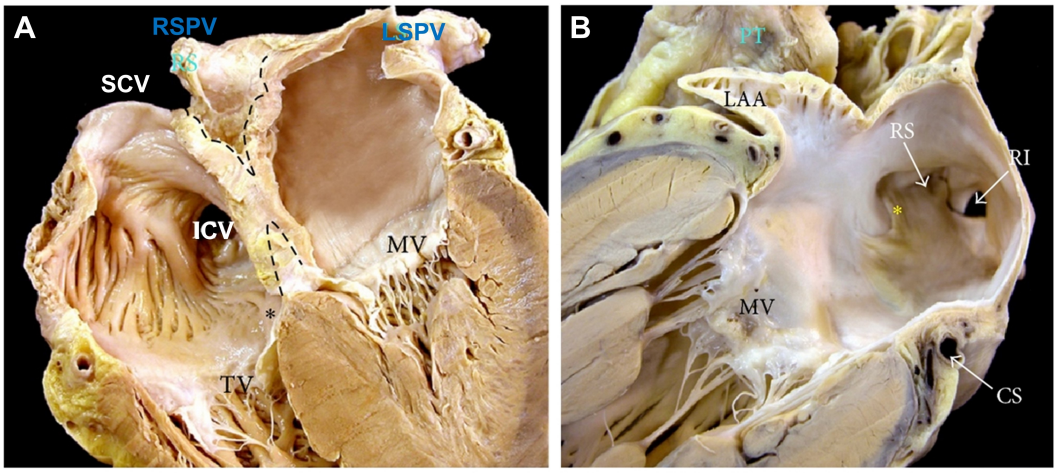

Figure 2.3: A) Four-chamber section through the heart showing the offset arrangement of the mitral valve and tricuspid valve which produces the so-called muscular atrioventricular septum (∗) and the deep infolding of the atrial wall superior and inferior to the floor of the oval fossa (dotted lines). B) Cross-section showing the LAA, mitral valve and CS. Adapted from [30] under the Creative Commons Attribution License.

2.1.2 Myocyte Electrophysiology

A single cardiac myocyte consists of a lipid bilayer forming the cell membrane, thereby dividing the system into an intracellular and an extracellular space. Integrated into the cell membrane are ion channels and exchanger pumps allowing for an exchange between intra- and extracellular space. Different ion types and concentration differences results in an electrochemical gradient which is the driving force behind the passive ionic exchange through

the respective ion channels. Chloride (Cl^-) ion concentration is roughly 40 times larger in the extracellular space compared to the intracellular space. The concentration of sodium (Na^+) is roughly 10 times and Calcium (Ca^{2+}) concentration is roughly 10^4 larger in the extracellular space compared to the intracellular space, while Potassium (K^+) concentration is approximately 40 times larger in the intracellular space. The pumps allow for exchange of ions against the gradient powered by adenosintriphosphate (ATP). The constant exchange of ions creates a transmembrane voltage (V_m) which, under steady-state conditions in human cells, can be calculated using the Goldman-Hodkin-Katz equation and is around 80 mV [31]:

$$V_m = \frac{RT}{F} \ln \left(\frac{P_{Na}[Na]_o + P_K[K]_o + P_{Cl}[Cl]_i}{P_{Na}[Na]_i + P_K[K]_i + P_{Cl}[Cl]_o} \right). \tag{2.1}$$

with R being the gas constant, T being the absolute temperature, F being Faraday's constant, and P_x being the membrane permeabilities for Na^+, K^+, and Cl^-. The subscripts i and o denote the intracellular and extracellular concentrations, respectively.
In case of an external stimulation, which can originate from the self-depolarizing sinus node cells or from an external stimulation source (e.g., an electrode) a change of potential is introduced and V_m decreases. This process of depolarization is illustrated in detail in Figure 2.4. Generally, the opening and closing mechanisms of an ion channels is accompanied

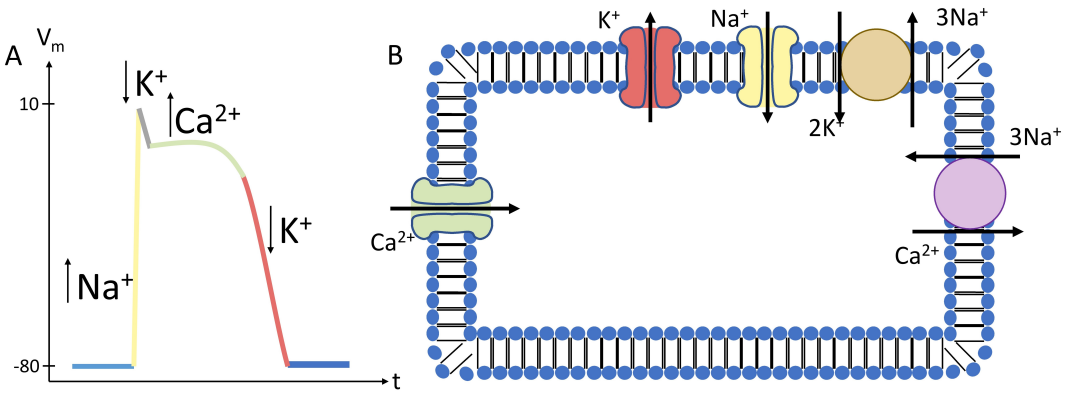

Figure 2.4: Action potential time line (A) and the corresponding cell (B) with sodium, potassium and calcium ion channels (gaps) and exchanger pumps (circles).

by conformation changes [31]. These changes are coupled to the charge movement within the protein and therefore the transition rates depend on membrane potential [31]. Once V_m passes a threshold of approximately -40 mV, voltage sensitive gates that close the sodium ion channels at resting potential open. An inward current I_{Na} (Figure 2.4 A (yellow)) leads to a reduction and an overshoot of transmembrane voltage to approximately 10 mV. Shortly before the maximum upstroke is reached, the sodium gates are inactivated and delayed rectifying potassium channels are activated leading to an influx of potassium and decrease in transmembrane voltage. Subsequently, channels open which permit the influx of Ca^{2+} (Figure 2.4 A (green)). Lastly, the cell is repolarized by an outward current of K^+ until the

resting transmembrane voltage is reached (Figure 2.4 A (red)). Once an action potential is initiated further stimuli will not reactivate the cell. The time before a new action potential can be triggered is called the effective refractory period (ERP), which is mainly determined by the relaxation time of the inactivated sodium gates. The initial ionic distribution is restored by the sodium calcium exchanger (INaCa), the sodium potassium pump (INaK), and the sarcoplasmic endoplasmic reticulum calcium ATPase (SERCA).

2.1.3 Myocyte Orientation

Cardiomyocytes are roughly shaped like a 3D ellipsoid. Myocytes are connected with each other and form tube-like strands called myofibrils, which then create strand-like structures referred to as fibers. Multiple fibers are arranged alongside each other permeating the walls of the atria (Figure 2.5). In the LA the wall has two layers, the subepicardial and the subendocardial layer and it is currently believed that the fibers in both can be rotated up to 120° relative to each other which is referred to as endo-epicard disassociation [32–34].

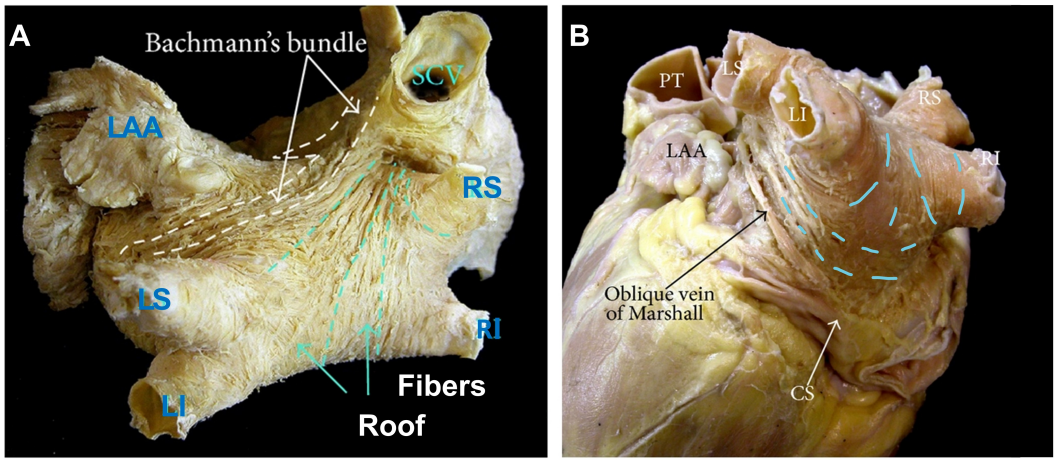

Figure 2.5: A) Superior view showing the Bachmann bundle crossing the anterior interatrial groove and branching toward the LAA. Longitudinal fibers of the septopulmonary bundle (dashed line), which arises from the interatrial groove underneath Bachmann's bundle, fan out to line the PVs and pass longitudinally over the dome and into the posterior wall of the left atrium. B) Posterolateral view of the left atrium and left ventricle to show the myofiber arrangement in the subepicardium of the left lateral ridge, left PVs, and the trajectory of the oblique vein of Marshall. Adapted from [30] under the Creative Commons Attribution License.

2.1.4 Myocyte Connections

A single myocyte is electrically coupled to approximately 9 to 11 neighboring myocytes via gap junctions that allow for both electrical and metabolic coupling [35, 36]. Gap junction

density is higher on the poles leading to a higher electrical propagation speed along the long axis of the cell than perpendicular to it [35]. Most methods of determining the local myocyte orientation (fiber direction) rely on this fact and focus on estimating the direction of highest conduction and corresponding it to the fiber orientation [37].
On the microscopic scale, a single functional gap junction is formed by two neighboring myocytes contributing a half-channel (Connexon) consisting of six connexin proteins (4 membrane spanning domains, 2 extracellular loops) [38]. In the human atrium, the predominant connexins are connexin 43 (Cx43), connexin 40 (Cx40) and to a lesser degree connexin 45 (Cx45). Atrial action potential conduction (altern. depolarization wave) depends on the ratio of Cx40 and Cx43 expression. While there is no correlation between the absolute amount of Cx40 and CX43 and the conduction velocity (CV), right atrial CV in humans is inversely related to the ratio of $\frac{Cx40}{Cx40+Cx43}$ and linearly related to $\frac{Cx43}{Cx40+Cx43}$ [39]. Additionally, the amount and ratio of Cx40 and Cx43 varies between LA an RA, leading to an overall higher CV in the LA [38, 40, 41].

2.1.5 Conduction Velocity

CV describes the speed and direction of a depolarization wave across the myocardium. On the cellular scale CV depends on sodium upstroke velocity [42], cell size [43] and conductivity of gap junctions [38, 40, 41]. Due to the inhomogeneous gap junction distribution CV displays anisotropic propagation, leading to different CV magnitudes along the longitudinal fiber direction ($\parallel$) compared to the transversal ($\perp$) to fiber direction. Mathematically this relation is defined by an anisotropic ratio factor k, relating the transverse magnitude to the longitudinal CV magnitude,

$$k = \frac{CV_{\parallel}}{CV_{\perp}}. \tag{2.2}$$

For a complete description of CV all three values, longitudinal CV, anisotropy ratio and fiber orientation are necessary. All three values encompassing CV stem from inherent physiological substrate properties. Therefore, CV is used to inversely infer information of the substrate and links back to generally pathological regions containing fibrosis [42, 44–46].

2.2 Fibrosis

The term fibrosis is used to describe pathological myocardial remodeling characterized by the excessive deposition of extracellular matrix (ECM) proteins in parenchymal tissues, and typically reflects unrestrained activation of a reparative mechanism [47, 48]. Cardiomyocytes form interconnected strands and occupy approximately 75 % of the myocardial volume. They are surrounded by ECM, which provides a structural scaffold for cardiomyocytes and distributes mechanical forces through the cardiac tissue [47, 49]. The heart has limited regenerative capabilities after injury. Instead, repair processes involve the removal of necrotic cardiomyocytes followed by the formation of fibrotic scar tissue replacing the

necrotic cardiomyocytes to preserve myocardial structural and functional integrity. The process of cellular replacement is mediated by fibroblasts, a cell type occurring within the myocardial interstitium, epicardial and perivascular regions. To repair cell damage, fibroblasts differentiate into myofibroblasts which secrete elevated levels of ECM proteins including collagen type I, collagen type III, collagen type IV, periostin, and fibronectin [47, 49, 50]. The resulting structural changes have been observed ex-vivo in mammalian hearts (Figure 2.6). While the causality is not fully understood, increased fibrosis leads to an

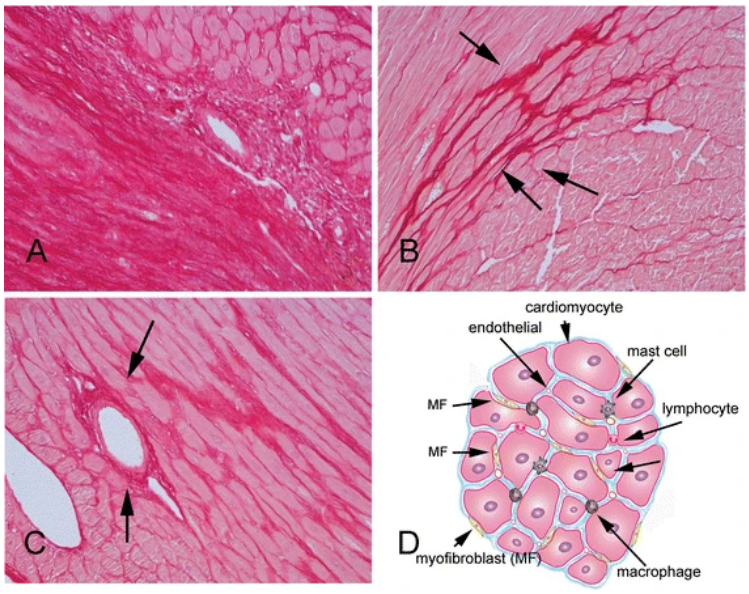

Figure 2.6: Types of cardiac fibrosis (histopathologic images show Sirius-red stained sections of samples from mouse models of fibrosis to identify the collagen network). a Myocardial infarction results in sudden loss of a large number of cardiomyocytes leading to replacement fibrosis. b Interstitial fibrosis is associated with increased deposition of collagen in the cardiac interstitial space in the absence of significant cardiomyocyte loss. c Perivascular fibrosis is characterized by expansion of the vascular adventitial matrix. d The fibrotic heart exhibits expansion of the interstitial space associated with deposition of collagens and other matrix proteins. Myofibroblasts (MF) are the main effector cells in cardiac fibrosis; however, macrophages, lymphocytes, mast cells, vascular endothelial cells, and cardiomyocytes may also participate in the process. Figure and caption adapted from [50] with permission.

adverse myocardial disease outcome. Fibrosis is associated with all major pathophysiologic conditions that cause heart failure, including chronic ischemia, genetic cardiomyopathies, pressure and volume overload and metabolic diseases. Additionally, fibrosis may perturb the propagation of the electrical depolarization wave, and may generate re-entry circuits, thereby contributing to the pathogenesis of arrhythmias [48, 49].

2.3 Atrial Fibrillation

Atrial fibrillation (AF) is a sustained cardiac arrhythmia characterized by an irregular heart rhythm [1]. Approximately one in five people run the risk of developing AF throughout their lifetime. The risk increases to more than one in three individuals in case of prevalent comorbidities such as hypertension, diabetes mellitus, heart failure, coronary artery disease, chronic kidney disease, obesity, and obstructive sleep apnoea [2]. Additional factors increasing risk of AF are advanced age or lifestyle choices such as alcohol and caffeine consumption, smoking, endurance exercise and lack of sleep. These lifestyle choices are simultaneously the most commonly reported triggers for initiation of AF [1, 8]. AF is associated with an increased risk of heart failure, stroke, and an increased mortality [1].
Currently, AF is classified based on the episode duration of the arrhythmia (Table 2.1). The

Table 2.1: Classification of AF as proposed by the 2020 guidelines of the European society of cardiology. Inspired by [1].

AF classification	Definition
First diagnosed	Initial diagnosis irrespective of AF severity.
Paroxysmal	AF termination within 7 days without intervention.
Persistent	AF is sustained for more than 7 days.
Long-standing-persistent	AF prevalent for more than 1 year.
Permanent	AF is accepted by the patient and physician.

AF burden of a patient is currently defined as the overall time spent in AF during a monitoring period, which is clinically realized with intermittent or long-term-ECG monitoring [1]. However it has been indicated that the current temporal classification of AF does not necessarily reflect the severity of the underlying atrial disease [51].

2.3.1 Pathophysiological Mechanisms

The pathophysiology of AF is multifaceted, complex, and not yet fully understood. AF is suspected to result from an interplay of multiple sources and contribution factors. These factors include abnormalities in calcium handling, ion channel dysfunctions, structural remodeling, and autonomic nervous system dysregulation [52]. These pathologies can manifest as ectopic beat incidents originating from focal sources, as reentrant activities termed rotors or cause chaotic depolarization patterns.
Rotors describe a circular movement of the depolarization wave around a geometrically extended core, which can be an anatomical obstacle, a patch of low conductivity or a functionally unexcitable patch of tissue [51].
Focal sources are characterized by a circular spreading of the depolarization wave from

a locally condensed source, which can be a small gap breakthrough or a spontaneously depolarization of tissue. A known source of focal sources are the PV orifices [1, 49, 53–55]. The **Multiple-wavelet hypothesis** states that AF is maintained by a multitude of depolarization waves meandering through the tissue. Depending on the different collision types, e.g., wavefront to waveback or wavefront to wavefront, depolarization waves are generated, terminated or redirected and cause self-sustaining chaotic patterns [56].

2.3.2 Treatment

Treatment follows the "**ABC**" formula. To assess the risk of and avoid ("**A**") stroke there is a risk assessment that yields a vulnerability score named CHA2DS2-VASc. For risk score outcomes >1 anticoagulation therapy with vitamin K antagonist (warfarin) or non-vitamin K antagonist oral anticoagulants (apixaban, dabigatran, edoxaban, and rivaroxaban) has shown reduced stroke occurrence in patients [1, 57].
To better ("**B**") control the symptoms, as a first line of therapy pharmacological rate control is pursued using beta-blockers, calcium transport antagonists (diltiazem and verapamil) or a combination therapy. Anti-arrhythmic drugs (e.g., amiodarone, dronedarone, sotalol) alter ionic currents producing rate-limiting properties, but also show side-effects and therefore are used as a last resort [1]. If medication fails to control the heart rate catheter ablation intervention is performed. The cornerstone approach is pulmonary vein isolation (PVI). Due to limited success in persistent and long-standing persistent AF, additional ablation has been advocated. Linear ablation lines connecting structural obstacles interrupt wave propagation but result in cauterization of extensive tissue areas. Acute ablation of diseased tissue is a method of treatment with the aim of reducing the cauterization area while obtaining AF freedom [7]. The drawback is that areas of diseased tissue are not easy to pinpoint, thereby prolonging the procedure [1].
Finally, cardiovascular ("**C**") risk factors are managed by raising awareness of lifestyle, e.g., weight loss, reducing alcohol and caffeine consumption and indulging in physical activity. Additionally, comorbidities (Chapter 2.3) are treated in an attempt to lower AF susceptibility and recurrence [1].

2.4 Electroanatomical Mapping

To understand electrical excitation propagation and minimize radiation during ablation procedures, electroanatomical mapping systems were developed. The systems visualize the atrial geometry together with the operation catheters, acquire electrophysiological information, visualize propagation pathways, and assess electrogram patterns. Additionally, the system is used as a central communication hub for all hardware components, such as the catheter localization setup (impedance or magnetic field), signal recording stations for electrocardiogram (ECG) and electrogram (EGM), an impulse generator for stimulation and an RF-energy

generator for ablation and various monitors and control units. A full clinical setup is shown in Figure 2.7.

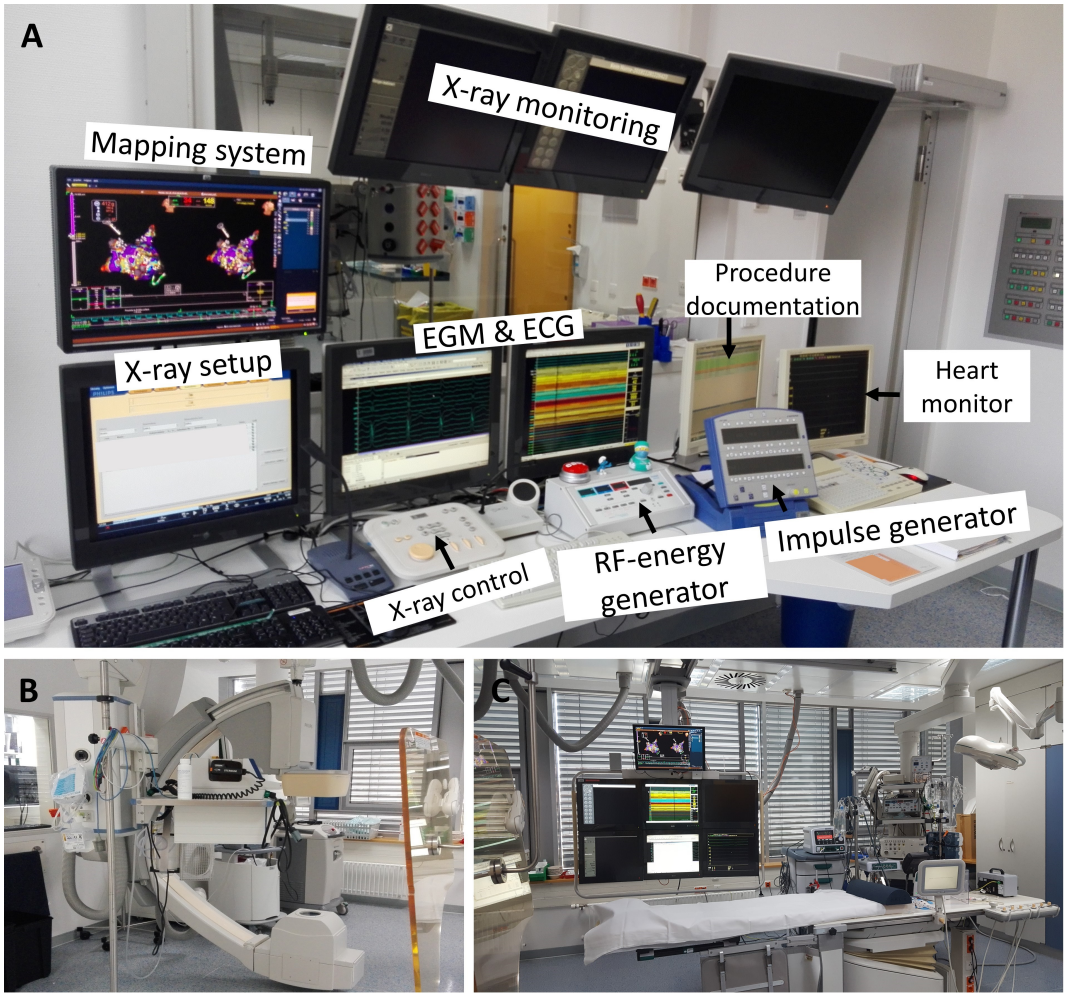

Figure 2.7: Clinical setup for an electroanatomical mapping procedure. A) Control room with utility labels. B) C-arm for visualization of initial insertion of catheters. C) Operating table with monitor panel mirroring control room visuals.

2.4.1 The Electrogram

Cardiac mapping catheters are equipped with electrodes which capture the local electrical potential at their respective position. The potential must be measured with respect to a reference. Signals captured using the Wilson Central Terminal as reference are referred to as unipolar signals. Signal quality of unipolar signals is often strongly compromised by artifacts like power line hum and far fields. In clinical practice high signal quality under adverse measuring conditions is required. Therefore, the clinical standard procedure is a

subsequent subtraction of two neighboring electrode signals along the catheter. Noise present in both electrode signals gets eliminated due to the subtraction revealing the pure signal difference [58]. This remaining signal is called bipolar electrogram. While the bipolar signal is less affected by noise it cannot be related to a single location of each of the initial electrodes. Rather, the bipolar signal is oftentimes assigned to the middle between both measurement electrodes as a substitute location [59]. A disadvantage of bipolar electrograms is their directional dependence. The bipolar signal amplitude and morphology depends on the relative orientation between the measuring electrode axis and the depolarization wave travel direction [58].
While the morphology of signals, e.g. complex fractionated atrial electrograms (CFAESs), has been studied, the signal amplitude and the local activation time (LAT) are considered the standard clinical metrics in determining substrate characteristics from signals.

2.4.2 Mapping

In preparation for a mapping procedure, catheters are threaded through the femoral vein and inferior vena cava (IVC) into the RA, or using a transseptal puncture into the LA (Figure 2.8 left). One catheter is inserted into the CS vein, thus referred to as CS catheter. The CS catheter provides a stable positional reference relative to the atria regardless of patient motion throughout the operation (Figure 2.8 right). A roving mapping catheter is inserted

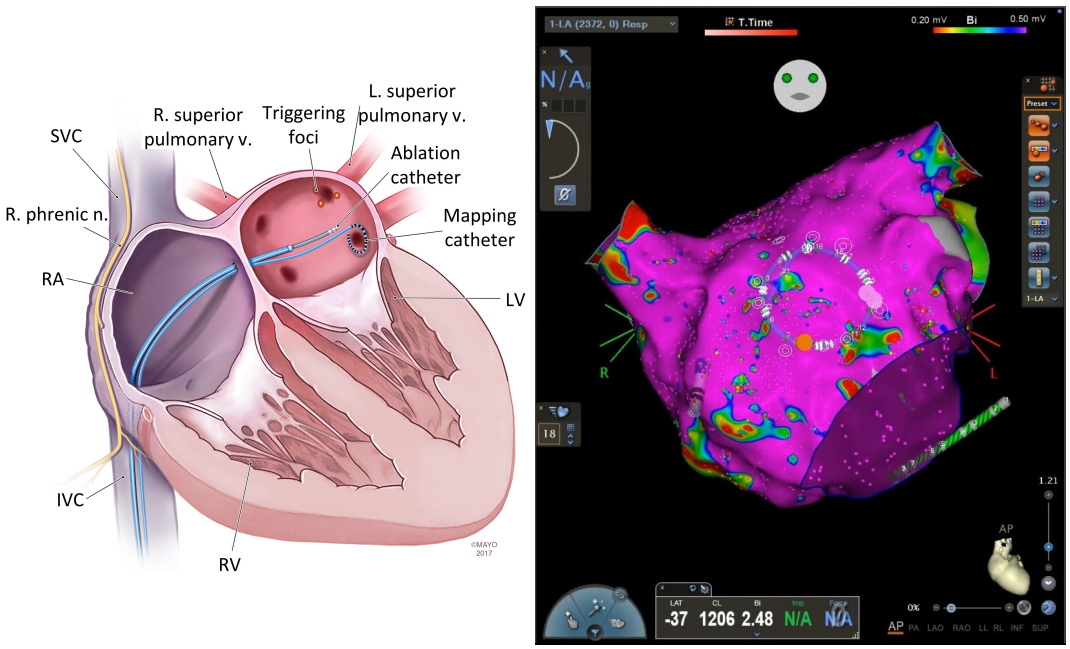

Figure 2.8: Ablation procedure in the LA after transseptal puncture (left). Mapping catheter records electrical potential and calculates voltage map to pinpoint arrythmias (right). Ablation lesions are created using point by point delivery of high frequency energy via the ablation catheter (left). Adapted from [60] with permission.

into the LA. Perpetual subsequent synthetic stimulation from the CS electrodes or natural stimulation from the sinus node creates a reference time point of stimulation. The mapping catheter is steadied on a single location during one stimulation cycle, capturing the changing potential caused by the depolarization wave initiated by the stimulation. Algorithms evaluate signal properties such as amplitude (voltage), fractionation and LAT from the captured signal. As the electrode position is tracked, the evaluation results can be allocated to specific location on the atrial wall. Iteratively, repeating this process while incrementally moving the mapping catheter to a new location along the endocardium of the atrial geometry yields a projection of information onto the geometry. This process is called mapping. Each signal property creates its own map. The voltage map, gained from signal amplitude, reveals zones of low and high voltage separated by a clinical threshold of 0.5 mV for bipolar signals [21, 61, 62]. Low-voltage zones have been associated with pathological tissue and are assumed to promote reentrant activity. The LAT map illustrates depolarization wave travel pathways revealing breakthroughs, propagation blockades and spatially extended (macro-) reentries [63–65].
Mapping catheters are available in a variety of geometric shapes with a collection of different number of electrodes. In this work circular catheters of fixed (20 mm) and variable (15–20 mm) circumference with 10 (Advisor SE, St. Jude Medical,) and 20 (Carto Lasso 2515, Biosense Webster & Optima 20, St. Jude Medical) measurement electrodes were used.

2.4.3 Ablation

Ablation catheters are equipped with a large tip electrode of about 3-4 mm that impresses current from an alternating high frequency source throughout the tissue (Figure 2.8). The passage of current through the tissue leads to resistive heating up to temperatures above 50° causing irrevocable thermal denaturation of underlying cell structures. Tissue scar dimensions are dependent on tip size, contact area and force and ablation duration and power. Thermal conduction causes deeper tissue layers to be affected as well, leading to planar and transmural tissue scar formation [66]. Physicians create multiple overlapping scars, thereby forming long lesions to suppress wave propagation promoting pathological outcomes.

2.5 Restitution

The concept of restitution was characterized by Bass in 1975 and was defined as the transmembrane potential recovery following extrasystoles at various delays in interval between two action potentials (APs) [67]. The majority of research regarding restitution was done on ventricular myocytes and the exact mechanisms underlying restitution are not yet understood. An AP can exhibit two distinctly opposite morphological changes following premature stimulation. i) The AP is characterized by a reduced plateau amplitude, plateau duration and total AP duration compared to the control. ii) The AP is characterized by a higher and prolonged plateau, a steeper repolarization phase and a greater area under the curve compared to the control (supernormal AP) [68]. Several hypotheses concerning this behavior

have been brought forward:
The foreshortened action potential duration (APD) is assumed to be caused by premature initiation of recovering sodium channels, leading to an incomplete activation. The calcium currents that activate in response to the sodium influx depend on the extent of initial membrane depolarization. Reduced calcium currents cannot uphold the plateau phase, leading to a shortening of the plateau and the APD. Additionally, sodium current influx may be hampered by opposing potassium currents of the preceding AP for very short coupling intervals (CIs). Furthermore, dihydropyridine (DHP) receptors function as sensor to open or close the calcium L-type channels and Ryanodine receptors of the sarcoplasmic reticulum (SAR) membrane. The calcium release from the SAR is fast (<5 ms) while the timescale of membrane calcium channel activity is approximately 20 times larger. For a normal AP a small influx of calcium from the extracellular releases a large amount of calcium from the SAR which in turn triggers the calcium L-type channels to close. Therefore, at fast pacing rates the SAR stores are not fully loaded, release less calcium and the calcium L-type channels remain open, leading to a prolongation of the plateau phase. For intermediate pacing rates the SAR is increasingly loaded. Upon premature stimulation calcium is released and leftover calcium from the previous beat contributes to a high calcium concentration in the sarcoplasm, leading to a fast inhibition of the calcium L-type channels. For slow pacing rates the calcium stores are increasingly loaded thereby inhibiting the L-type calcium channels conductivity reestablishing the normal AP behavior [25, 68].
Substrate exposure to increased rates can trigger both cases in succession, creating alternating AP termed alternans [68].
In conclusion the mechanisms behind restitution are twofold. Firstly, incomplete recovery of ionic currents between two subsequent AP and secondly, changes of ion concentrations on either side of the cell membrane resulting from changes in rate or rhythm [68].

2.5.1 S1S2 Protocol

To trigger responses from the atrial tissue under controlled conditions stimulation from catheter electrodes using a stimulation generator is performed. A single stimulation of a stimulation generator has a biphasic pulseform with each part having an exponential amplitude decrease over time (Figure 2.9). The time between stimulation start and polarity switch (Δt_{b1}) can be set to values between 0.1 ms and 2.9 ms for the UHS 3000 (BIOTRONIK SE & Co. KG, Berlin, Germany). The time window (Δt_{b2}) between polarity switch and end of stimulation is fixed to 6 ms. To elicit restitution information a stimulation protocol must be defined that addresses subsequently decreasing stimulation. Each stimulation triggers a pacing-rate dependent response from the substrate.
The dynamic stimulation protocol uses a fixed number of beats in a pacing train with a CI. This pacing train is repeated with successively reduced CI until the atrial signals cannot be captured anymore (Figure 2.10).
For measurements in-vivo continuous decremental pacing runs the risk of inducing AF or inhibiting long-term healthy cardiac function of the patient. For this reason, the S1S2

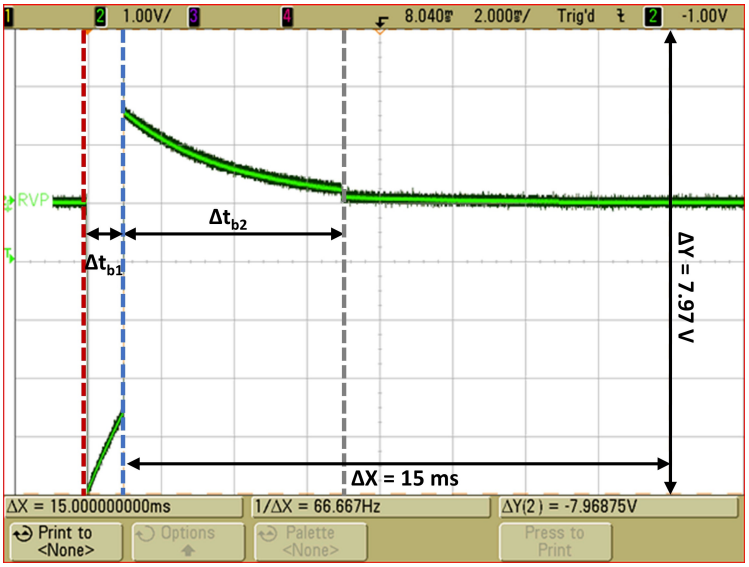

Figure 2.9: Oscilloscope recording of the stimulation pulseform of the BIOTRONIK UHS 3000. Grey rectangles have a scale of 2 ms in x-axis and 1 mV in y-axis. The time window (Δt_{b1}) between pulse start (red dotted line) and polarity switch (blue dotted line) can be manually set and is 1 ms in this example. The time window (Δt_{b2}) between polarity switch and end of stimulation is fixed to 6 ms.

stimulation protocol is the preferred clinical stimulation approach (Figure 2.10). During an S1S2 pacing, each pacing train contains several stimuli with a basic cycle length (BCL), called the S1 stimuli, followed by a single stimulus which is administered after a reduced CI, called the S2 stimulus. This is termed a pacing train and is repeated, with the S1 stimuli retaining their BCL and an incrementally reduced CI between the last S1 stimulus and the S2 stimulus. The pacing protocol ends as soon as the atrial tissue does not capture the stimulus anymore at a certain S2 CI because it falls below the ERP.

2.5.2 Conduction Velocity Restitution

CV restitution is measured on a macroscopic scale and therefore includes not only cellular effects (Chapter 2.5 & 2.1.2) but also reflects cell to cell coupling (Chapter 2.1.4) and structural properties, making the separation of these influences and consequently identification of the origin of CV restitution impossible up to date. In-silico studies on CV restitution have described that an increasingly steep slope of the CV restitution curve to create a dynamical instability which causes the electrical activity to become disorganized [69, 70]. The studies were done in healthy homogeneous tissue and are therefore only remotely applicable to AF patient pathologies. Additionally, the studies make use of the diastolic interval, a cellular property which is not easily measurable in clinical practice.
Clinical studies found that sites of low voltage amplitude, which are assumed to inhibit pathological tissue, also show slow conduction [62]. In a clinical study, reduction of amplitude was correlated with a reduction of CV across four different pacing intervals [16].

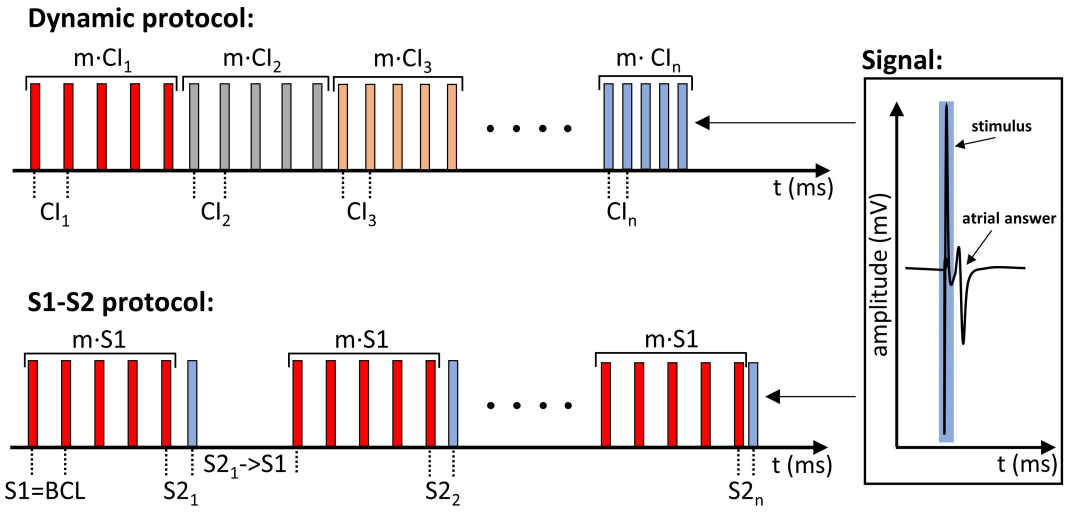

Figure 2.10: Schematic depiction of stimulations (colored bars) during dynamic and S1S2 restitution protocols with an exemplary electrogram. Dynamic stimulation consists of decremented pacing with a constant number (m) of stimuli per CI. The S1S2 pacing protocol consists of a sequence of m (5) equidistantly spaced stimuli (red) and a single S2 stimulus (blue) with a decreased time interval $S2_1$ compared to the basic cycle length (BCL). The whole stimulation protocol consists of multiple repetitions of pacing trains with iteratively decreasing S2 CI. Both protocols elicit an atrial answer that occurs after stimulation.

Therefore it is highly probable that CV restitution can be an indicator for pathological tissue and can help identify reentry sites [16, 59, 69, 70].

2.5.3 Amplitude Restitution

Signal amplitude is created by measuring the electrical potential (Chapter 2.4.1). Under the assumption that each cell of n total amount of cells contributes an ionic current I_n, the potential at a location x_l can mathematically be approximated by a superposition of all cells weighted by the distance between their position x_s location x_l.

$$\Phi = \frac{1}{4\pi\sigma} \sum_n \frac{I_n}{|x_s - x_l|}. \tag{2.3}$$

This formula is known as the infinite homogeneous volume approximation and it shows that all signals depend on the cellular currents. Due to this dependency and the fact that restitution generally inhibits ion channel dynamics, a reduction in amplitude with increasing pacing rate is expected.

Chapter 3

Modeling Fundamentals

This chapter introduces the mathematical formulations of electrophysiological processes. Multiple levels of detail are spanned, from single ion channel conception over cellular interaction to tissue level electrical propagation and forward calculation of intracardiac signals.

3.1 Electrophysiology of the Cell

The mathematical formulation underlying action potential (AP) formation (Chapter 2.1.2) was initially described for a squid axon [71]. The cell is modeled analogous to an electric circuit with the membrane being represented by a capacitor (C_m) and each ion channel type corresponding to a different variable resistor (Figure 3.1) for the respective ionic current I_x where x refers to each type of ion. Following convention, resistors are reciprocally converted

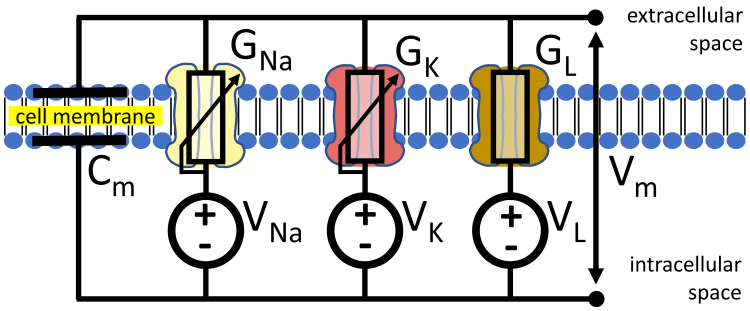

Figure 3.1: Electric circuit of a squid axon following the formulation of Hodgkin and Huxley [71]. Arrow in resistors indicate variable conductance.

to conductivities G_x. The driving force behind the dynamic ionic current is the Nernst-voltage, which is represented by the voltage sources V_x. The electrical circuit setup leads to

the following ordinary differential equation for the transmembrane voltage V_m:

$$\frac{dV_m}{dt} = -\frac{1}{C_m}\left(\sum_x I_x + I_{stim}\right) . \tag{3.1}$$

The additional stimulation current I_x is non zero when an external stimulation is applied. From Ohm's law the current of each channel can be expressed as

$$I_x = G_x \cdot (V_m - V_x) , \tag{3.2}$$

with the conductivity G being dependent on voltage and time. The overall conductivity of a single ion type can be represented as

$$G_x = \tilde{G}_x \cdot p , \tag{3.3}$$

where $\tilde{G}$ is the maximum conductivity that the specific ion type can reach under the assumption that all channels of this type along the cell membrane are open. p is the probability of channels being open and is formulated as an ODE:

$$\frac{dp}{dt} = \alpha(V_m)(1-p) + \beta(V_m)p , \tag{3.4}$$

dependent on transition rates α and β that are determined in voltage clamp experiments for each channel. Since the mathematical formulation in 1952, the model has evolved and has been adapted to represent human cardiac myocyte cells as well [71, 72].

3.2 Simulating Electrical Propagation

Cells are electrically coupled via gap junctions (Chapter 2.1.4). The most realistic model of the coupling between cells up to date is the bidomain model [73]. The bidomain model splits cardiac tissue into two domains reflecting the intracellular and the extracellular space. Both spaces coexist and occupy the same geometrical space. The potentials Φ_i and Φ_e in both domains are coupled to the current source densities via the Poisson equation for stationary electric fields:

$$\begin{aligned} \nabla \cdot (\sigma_i \nabla \Phi_i) &= \beta I_m - I_{istim} , \\ \nabla \cdot (\sigma_e \nabla \Phi_e) &= -\beta I_m - I_{estim} , \end{aligned} \tag{3.5}$$

where β is the surface-to-volume ratio of the myocytes, and I_m is the total transmembrane ionic current density prescribed by the cellular model which links both domains. I_{istim} and I_{estim} are external stimulus currents applied to the intra- or extracellular domain. σ_i and σ_e are respective tensors describing conductivities parallel and transversal to the fiber orientation. Using the definition of the transmembrane voltage $V_m = \Phi_i - \Phi_e$ and disregarding external stimulation allows formulation of the first and second bidomain equation:

$$\nabla \cdot ((\sigma_i + \sigma_e)\nabla \Phi_e) = -\nabla \cdot (\sigma_i \nabla V_m) , \tag{3.6}$$

$$\nabla \cdot (\sigma_i \nabla V_m) + \nabla \cdot (\sigma_i \nabla \Phi_e) = \beta \cdot \left(C_m \cdot \frac{dV_m}{dt} + I_{ion}\right) - I_{istim} . \tag{3.7}$$

Introducing the simplification that the anisotropy ratio k is equal for the intracellular and extracellular conductivity tensors allows substitution of σ_i with $\kappa\sigma_e$, which in turn yields the monodomain equation:

$$\nabla \cdot (\sigma_i \nabla V_m) = (\kappa + 1)\,\beta \cdot \left(C_m \cdot \frac{dV_m}{dt} + I_{ion} \right) - I_{istim} \ . \tag{3.8}$$

In this thesis the simulation frameworks acCELLerate and openCARP were used [74, 75] that are both based on the equations above.

Chapter 4

Mathematical Fundamentals

4.1 Ellipse

The standard ellipse equation centered at x_0 and y_0 in Cartesian coordinates (x, y) is given as:

$$\frac{(x-x_0)^2}{a^2}+\frac{(y-y_0)^2}{b^2}=1\ , \tag{4.1}$$

with a representing the long axis, b the short axis of the ellipse. Removing the initial translation, subsequent rotational transformation and following conversion to polar coordinates yields the radial representation of the ellipse equation

$$r(\phi)=\frac{a\cdot b}{\sqrt{b^2\cdot(c(\phi)c(\theta)+s(\phi)s(\theta))^2+a^2\cdot(s(\phi)c(\theta)-s(\theta)c(\phi))^2}}\ , \tag{4.2}$$

using the abbreviations, $c(x)=\cos(x)$ and $s(x)=\sin(x)$. ϕ becomes the angular portion of the polar coordinate and θ the tilt of the ellipse. Another method to represent an ellipse is an implicit equation referred to as the conic section:

$$\begin{aligned}
&Ax^2+Bxy+Cy^2+Dx+Ey+F=0 \qquad (4.3)\\
&A=a^2\sin^2(\theta)+b^2\cos^2(\theta)\\
&B=2\left(b^2-a^2\right)\sin(\theta)\cos(\theta)\\
&C=a^2\cos^2(\theta)+b^2\sin^2(\theta)\\
&D=-2Ax_0-By_0\\
&E=-Bx_0-2Cy_0\\
&F=Ax_0^2+Bx_0y_0+Cy_0^2-a^2b^2\ .
\end{aligned}$$

The coefficients A-F depend on the long axis of the ellipse a, the short axis b, the tilt of the ellipses θ and the center coordinates x_0 and y_0. This representation can have multiple solutions corresponding to parabolas and hyperbolas. To obtain the ellipse solution for the non-degenerative case, the boundary constraint

$$B^2-4AC<0 \tag{4.4}$$

must apply. Computational solvers generally use the equations 4.3 and 4.2 [76, 77].

4.2 Inverse Problem

Mathematical problems are often composed of three main components: i) the source parameter(s) which produce a change in the outcome, ii) a model which contains the physical theory and links the source parameters to iii) the output parameters which can be measured. The "forward problem" is the calculation of all output parameters under the assumption that all source and model parameters are known and is generally a well posed problem. By definition, well-posed problems have a unique solution that change continuously when the source parameters are changed [78]. If at least one of these conditions does not apply the problem is referred to as ill-posed. The "inverse problem" uses output values to infer the source values which characterize the system and is often ill-posed. Generally, the number of linearly independent measurements is insufficient to reconstruct the higher number of source parameters characterizing the system. Small errors in measurement can have a significant impact on the inverse reconstruction. If a simplified model of the physical process is assumed then using measurements from the real-world complex problem for the inverse reconstruction will yield results deviating from the actual physical process. One method of solving the inverse problem is by regarding them as optimization problems and minimizing errors between measured values and predicted values of the model for a set of parameters $\hat{x}$:

$$\hat{x} = \arg\left(\min_x \| f(x) \|_2^2\right) = \arg\left(\min_x \sum_{i=1}^{n} \left(\left| f_i^{model} - f_i^{measured} \right|\right)^2\right), \tag{4.5}$$

where f_{model} is the forward solution of the model for n measurements and $f_{measured}$ the respective measured solution. The forward model outputs will generally not fit the measured data perfectly yielding a remainder called residual. This type of problem is more easily solved by constraining the parameters to lie within physiological bounds for each source parameter. One method of numerically solving the equations is the trust-region-reflective algorithm. A second order Taylor expansion of the function includes a Hessian matrix which is approximated at an initial starting point x_k. Using the Newton iteration method, a minimum of the current quadratic approximation of the function is found and a single set of source parameters is generated. This method can be repeated for multiple starting points x_k which results in multiple sets of source parameters. By finding the overall minimal residual a best estimation can be obtained.

4.3 Density-Based Spatial Clustering

Density-Based Spatial Clustering of Applications with Noise (DBSCAN) identifies arbitrarily shaped clusters and noise (outliers) in data. Unlike k-means clustering, the DBSCAN algorithm does not require prior knowledge of the number of clusters. Additionally, it is able to cluster parameter distributions that are not spheroidal, which is a disadvantage of clustering methods using Gaussian models. The biggest advantage is that it can detect outliers that do not belong to any cluster [79].

The method assigns points to clusters by checking if the point in question contains a minimum number of neighboring points (MinPts) in the neighborhood, defined by the distance ε (directly density-reachable). Alternatively, the point can lie within the ε neighborhood of another point that satisfies both conditions (density-connected). The algorithm distinguishes between 3 types of points:

- Core point: Point has at least MinPts in its ε neighborhood.
- Border point: Point has fewer MinPts in its ε neighborhood.
- Noise point: Point does not belong to any cluster.

The values of MinPts and ε are determined by the "thinnest" cluster in the database. Using an iterative increasing number of MinPts a sorted k-distance graph reveals a curve which at some distance value shows a sudden change in slope ("knee"). This point can be defined as epsilon, leading to all points with a higher distance value to be defined as outliers. The change in this value introduced by the value of MinPts is very small and as such the smallest feasible number of MinPts should be chosen. Ester et. al. recommend an initial value of 4 [79].

PART II

ELECTROGRAM CHARACTERISTICS OF ARRHYTHMOGENIC SUBSTRATE

Chapter 5

Motivation

Pulmonary vein isolation (PVI) is currently the first line of invasive therapy in patients with atrial fibrillation (AF). Arrhythmia freedom following PVI is high in paroxysmal AF, as pulmonary vein foci represent the main source of arrhythmia in these patients [53]. This contrasts with persistent AF, where arrhythmic sources in the left-atrial body itself, and hence outside of the pulmonary veins, may contribute to the initiation and perpetuation of AF [80]. In this context, fibrotic remodeling of the atrial tissue is hypothesized to contribute to local development of micro-reentries or focal sources sustaining the arrhythmia [14, 80]. As a consequence, arrhythmia freedom with PVI alone can be achieved in only about half of patients suffering from persistent AF [81–83]. The importance of arrhythmogenic sources outside the pulmonary veins for perpetuation of persistent AF is supported by the fact that in 70 % of all patients, local radiofrequency ablation within the left atrium terminates ongoing AF following or even before PVI was performed [21, 84]. The clinical challenge lies in the correct identification of these AF termination sites which is necessary for targeted ablation whilst avoiding unnecessary damage to healthy atrial myocardium.
For the current study, the hypothesis was that AF termination sites share specific electrogram (EGM) characteristics in AF and in sinus rhythm (SR) that would allow identification of these sites in clinical practice for targeted ablation.
A high-resolution computer model including local fibrotic remodeling was used to investigate its impact on local EGM characteristics during AF and SR to mechanistically underpin the clinical observations. Additionally, a spatially extended computer model including a dense fibrotic core with a radially decreasing gaussian fibrotic (borderzone) was created to identify characteristics of rotational sources upholding an arrhythmia.
Lastly, an in-silico ablation was performed to investigate results of different ablation techniques on identified fibrotic areas.

Chapter 6

Methods

6.1 In-silico Fibrotic Tissue Patch Models

This work made use of three in-silico tissue patch models containing fibrotic tissue (Figure 6.1). The first in-silico setup (Figure 6.1 A) was used to replicate sinus rhythm (SR)

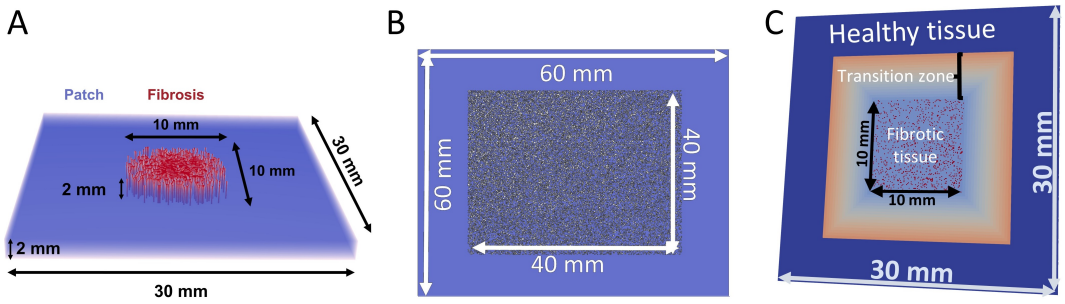

Figure 6.1: Layout and dimensions of in-silico tissue patch setups containing a centered fibrotic area. A is used to replicate sinus rhythm (SR) using plane wave propagation and atrial fibrillation (AF) using a rotational wave propagation. B shows an extended patch to observe depolarization wave behavior inside an extensive fibrotic area. C shows a tissue patch supporting recurrent focal excitation which is used for study of ablation.

conditions using a single uniformly propagating wave across the tissue patch as well as replicate atrial fibrillation (AF) conditions using a rotational wave anchoring to and propagating around the fibrotic core.

Figure 6.1 B shows the setup to observe the behavior of a depolarization wave inside an extended fibrotic area in regards to long-term rotational maintenance, long-term rotational stability, and initiation of focal exits with multiple depolarization wavelets.

Figure 6.1 C was used to study ablation of focal excitations. This required insertion of a depolarization wave into a fibrotic area analogous to Figure 6.1 C, with the modification that the fibrotic area could create consistent recurring focal excitation at an exit area.

6.1.1 SR and AF Model

A virtual tissue patch measuring 30 mm × 30 mm × 2 mm with a spatial resolution of 0.1 mm (0.1 mm × 0.1 mm × 0.1 mm) was set up with isotropic conductivity (Figure 6.1 A). Membrane kinetics were represented by the Courtemanche et al. model adapted to mimic persistent AF conditions [72]. Using the same geometrical mesh, two setups with different conductivities were generated. The conductivity of the non-fibrotic region was adapted to yield a plane wave conduction velocity (CV) of 0.8 m/s for the plane wave case and 0.22 m/s for the rotational activity case. Both setups were adjusted to generate a peak-to-peak voltage of 1 mV. Regional fibrosis was incorporated into the model within an area of 10 mm × 10 mm × 2 mm at the center of the patch and was modeled by setting the conductivity for fibrotic elements to zero. To represent severe fibrosis patterns observed in clinical data such as MRI and electroanatomical mappings [11, 85, 86], a Gaussian distribution of transmural 200 µm × 200 µm non-conductive elements within the fibrotic area affecting 40 % of elements was considered. The fibrotic volume percentage and distribution provided the opportunity to simultaneously observe electrogram (EGM) characteristics stemming from a non-traversable dense fibrotic core, and a fibrotic border zone that is traversable by the depolarization wave. The size of non-conductive elements was extrapolated from histological studies on collagen septa in aging human atria [87]. Excitation propagation was simulated using the cardiac electrophysiology solver acCELLerate [74]. Extracellular potentials were sampled with 1 kHz. The plane wave mimicking SR was generated by applying a depolarization boundary condition on a single row of cells along the y-axis border. The stable rotational source was generated by cross field stimulus protocol in the bottom left quadrant of the patch. This setup was additionally used to test ablation strategies on rotational sources.

6.1.2 Model for Extended Rotational Activity

To observe the behavior of a depolarization wave inside an extended fibrotic area a setup with an extensive fibrotic area was created (Figure 6.1 B). In order to achieve unobstructed depolarization wave propagation while simultaneously retaining comparability to fibrotic arrangement patterns observed in clinical data, a medium fibrosis burden (Stage III [85]) was chosen. The fibrotic density and distribution were implemented by creating a 60 mm × 60 mm × 2 mm tissue patch with a 40 mm × 40 mm × 2 mm area consisting of equally distributed fibrosis with a 20 % fibrotic volume percentage. Tissue conductivity of the non-fibrotic region was adapted to yield a plane wave CV of 0.4 m/s. Fibrotic element modeling and initiation of excitation by crossfield stimulus was analogue to Chapter 6.1.1.

6.1.3 Model for Focal Activity

To create a focal activity and observe the impact of different ablation methods on the excitation spread throughout the atrial substrate a final simulation setup (Figure 6.1 C) was created.
The simulation addressed pinpointed ablation using a single- or two-point ablation lesions for recurrent atrial activity. To create a simulation setup with recurrent atrial activity a 30 mm × 30 mm × 0.1 mm tissue patch with a 10 mm × 10 mm × 0.1 mm area consisting of equally distributed fibrosis with a 10 % fibrotic volume percentage was set up. The fibrotic density corresponded to a light fibrotic burden (Stage I [85]) and was chosen to allow for a multitude of propagation paths, thereby increasing the difficulty of successful arrhythmia termination.
Tissue conductivity of the non-fibrotic region (outermost layer) was adapted to yield 0.8 m/s. To ensure a smooth transition of the excitation spread and prevent excitation travel along steep clashes of conductivity regions a gradient consisting of 18 regions of decreasing conductivity was implemented (0.8 m/s to 0.25 m/s in steps of 0.05 m/s, followed by 0.18, 0.13, 0.1, 0.08, 0.065, 0.05 m/s). The final gradient step yielded a plane wave CV of 0.05 m/s in the fibrotic area.
The second simulation addressed ablation of a rotational activity using ablation of extensive areas and ablations of extensive areas combined with lines of block. To create a rotational activity a cross field stimulus protocol was used.
Ablation points were modeled as circular non-conductive regions with radius 2 mm as suggested by experimental studies [66, 88].

6.2 Patient Data Evaluation

Patient data acquisition and evaluation was performed by the medical expert team of the Universitäts Herzzentrum Freiburg-Bad Krozingen.

All 21 patients presented in clinical persistent AF and underwent left-atrial mapping using the CARTO-V3 system (Biosense Webster). The EGMs were filtered using the standard 0.05–250 Hz low-/high pass filter. Low voltage areas were delineated based on a bipolar voltage <0.5 mV during AF. High mapping density using 2–3 acquisitions per site integrated voltage variations that occur in AF. Based on clinical and in-silico observations of fibrotic areas, AF termination sites were evaluated using the following features: prolonged activity during AF, fractionation of signal morphology combined with delayed activity in SR, reduced cycle length and increased cycle length coverage [89, 90]. This led to the following EGM criteria defining target sites for ablation:

1. EGM patterns recorded within low-voltage areas and their 1 cm-wide border zone showing a sequential activation on the circumferential mapping catheter that exceeded

8 electrodes (>210°) and covered $\geq$70 % of the local AF cycle length were considered as sites with spatio-temporal dispersion. Local AF cycle length defines the time interval between the two starting points of a repetitive signal sequence across the electrodes of the circumferential catheter. These sites were targeted if spatio-temporal dispersion was observed in more than 3 of 10 consecutive AF beats.

2. Electrical activity covering $\geq$70 % of the AF cycle length at a site, e.g. prolonged fractionated activity on 1–2 adjacent bipoles.
3. Rapid local activity was diagnosed when local AF cycle length was $\geq$15 % shorter than the concomitant AF cycle length in the coronary sinus. Local AF cycle length was averaged over ten consecutive AF beats on a given bipolar electrode and AF cycle length was concomitantly measured in the coronary sinus.

Patient data evaluation was performed using IBM SPSS Statistics 20 (IBM Corporation, Armonk, NY) and Graphpad Prism 7.0 (Graphad Software, San Diego, CA, USA). Data were checked for normal distribution by visual assessment of histograms and q–q plots. Normally distributed data are presented as mean $\pm$ SD and intergroup differences calculated with t-test or ANOVA with Bonferroni-post hoc correction, as appropriate. Non-normally distributed variables are given as median and interquartile range, with differences calculated using Mann-Whitney-U test or Dunn's multiple comparison test. For all analyses, a p-value of ≤ 0.05 was considered significant. Additional details of the clinical measurement method and evaluation can be found in [7].

Chapter 7

Results

7.1 CV and Amplitude

The in-silico replication of sinus rhythm (SR) consisted of a single uniformly propagating wave front across the tissue patch (Figure 7.1). The wave front was concavely warped when

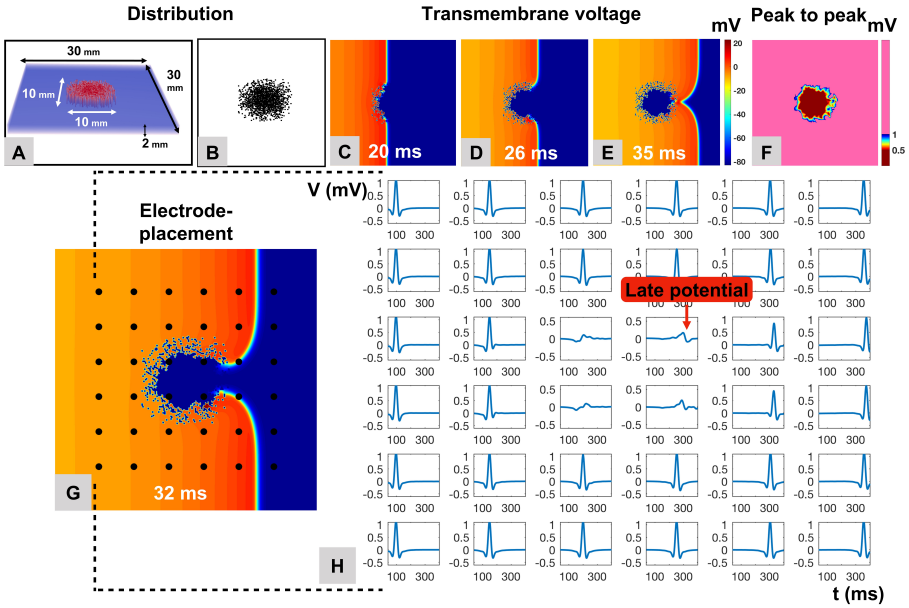

Figure 7.1: Development of fractionated delayed electrogram (EGM) components in simulated SR. A single uniformly propagating wave front to emulate SR was used in a 3D model (A) with centrally incorporated fibrotic elements (B) simulating atrial fibrosis. Upon striking the simulated fibrotic area, the wave front warps concavely due to the change of the local source-sink relation and reduced conduction velocity (CV) (C–G). Local electrogram (EGM)s recorded within the fibrotic area demonstrate low bipolar voltage (F) and late potentials (H). Figure and caption adapted from [7] under the Creative Commons CC BY Attribution 4.0 International License.

hitting the fibrotic area due to the change of the local source-sink relation and reduced

conduction velocity (CV) caused by different fibrotic element densities. The plane wave could not propagate throughout densest fibrotic conglomeration near the fibrotic core but rather propagated throughout the less dense distributed fibrotic tissue at the border zones. The bipolar voltage map of the tissue patch showed an area with low voltage (<0.5 mV using clinical definition) which spatially correlates with the fibrotic elements introduced into the simulation patch (Figure 7.1 F). From an array of virtually placed bipolar electrodes (Figure 7.1 G) the local electrogram (EGM) shows a reduction of amplitude near the fibrotic zone of up to 82 %. Additionally, the maximum deflection, a surrogate measure for the depolarization front, of the signal is shifted towards later time points creating so called 'late' or 'delayed' potentials.

7.2 Cycle Length and Cycle Length Coverage

In the atrial fibrillation (AF) model, the wave front invaded the fibrotic area and anchored to it, leading to development of a stable rotational source displaying rotational electrical activity around the fibrotic area (Figure 7.2 C–E). Simulated EGMs recorded from within

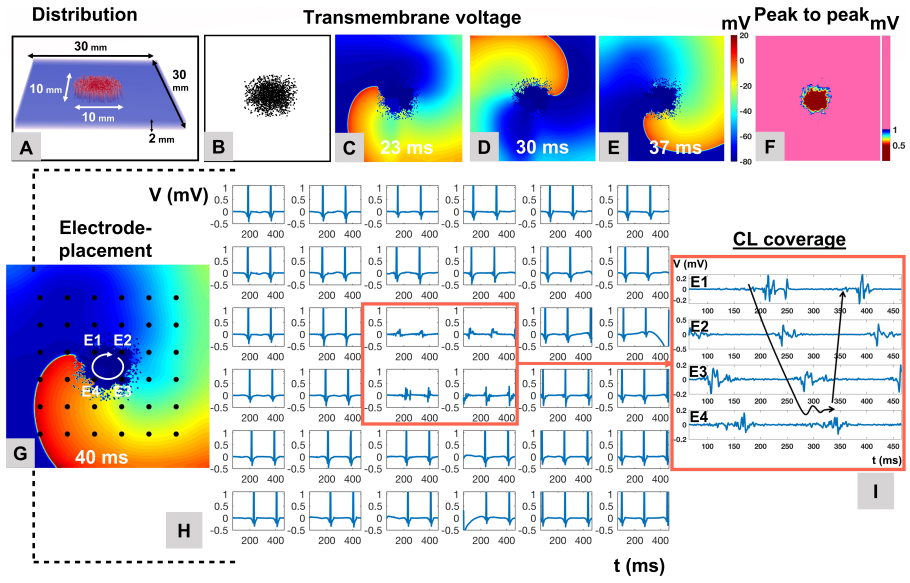

Figure 7.2: Stabilization of Localized Reentrant Activity with EGM Fragmentation in AF. A 3D model incorporating a regional fibrosis constituted of 40 % non-conductive elements in a Gaussian distribution served to simulate the impact of fibrosis on maintenance of rotational activity in an AF model (A, B). Transmembrane voltage maps show anchoring and stabilization of a reentrant rotational source around the fibrotic area (C–E). The fibrotic area displays low peak-to-peak bipolar voltage in AF (F). A 6 × 6 electrode arrangement with inter-electrode distances of 2 mm was overlaid (G). Local EGMs recorded over the rotational source and within the fibrotic area display low voltage and prolonged fractionated activity with a coverage of >70 % of the AF cycle length at the center of the rotational source (H, I). Figure and caption adapted from [7] under the Creative Commons CC BY Attribution 4.0 International License.

this area showed low bipolar voltage (Figure 7.2 F) with prolonged duration that covered >70 % of the simulated AF cycle length with spatio-temporal dispersion pattern on virtual electrodes E1-4 (Figure 7.2 G–I).
The model for the extended rotational activity (Chapter 6.1.2) with a fibrotic area of 40 mm × 40 mm × 2 mm (Figure 7.3 A) similarly lead to anchoring of the wave front to the affected area. In addition, the wave front split into multiple wavelets within the fibrotic area which exited the area at different sites propagating in different directions (Figure 7.3 B–J). Moreover, a localized reentry with variable focal exit sites from the border zone of the fibrotic area was observed (Figure 7.3 K–N).

7.3 Electrogram Specific Ablation

Four different ablation strategies were applied in-silico to assess their ability to terminate an arrhythmia: i) single-point ablation, ii) two-point ablation, iii) ablation of complete fibrotic area and iv) ablation of area and an additional line to the next propagation obstacle.
The initiated rotational activity experienced a conduction block inside the healthy tissue (Figure 7.4 A1-2), but continued propagation inside the slow conducting fibrotic area reemerging at the bottom left corner of the fibrotic area after the effective refractory period (ERP) of the healthy tissue had expired (Figure 7.4 A3-8). The reemerging depolarization wave created a spontaneous fast circular depolarization wave spread near the fibrotic border zone exit point. Ablation of this focal activity using a **single ablation point** did not stop the arrhythmia, since the pathway taken by the depolarization wave could not be covered completely, leading to a shift in focal excitation exit location (Figure 7.4 B1-3).
Ablation using **two points** on the expected pathway of propagation terminated the focal excitation and concurrently the arrhythmia.
Since a few well-placed ablation lesions sufficed to terminate the atrial activity for the case of a focal excitation, ablation of additional tissue (area and area with additional line) would yield equal results. Instead, the case of a rotational activity is demonstrated.
The rotational activity anchored to the fibrotic core and traveled through the fibrotic border zone (Figure 7.4 D1-4). Using a single ablation point or two ablation points in the fibrotic area would merely change the circumferential propagation wave trajectory by extending the obstructed area within the fibrotic region.
Ablation of the complete **fibrotic area** did not terminate the arrhythmia but rather creates a consistent rotation pattern (atrial flutter) (Figure 7.4 E1-3). EGM features would be less fractionated since less source-sink mismatches occur, less pathways are available and a more consistent depolarization group velocity is achieved. This is comparable to the difference between EGMs in unobstructed healthy tissue (Figure 7.2 H) and EGMs in the vicinity of fibrotic tissue (Figure 7.2 I).
Ablation of the complete **fibrotic area with an additional line** to a geometric obstacle (e.g., pulmonary vein, mitral valve) terminated the arrhythmia (Figure 7.4 F1-3).

7.4 Electrogram Characteristics of Clinical Data

Patient data discussed in this section was measured and evaluated by the medical expert team of the Universitäts Herzzentrum Freiburg-Bad Krozingen and are used here to substantiate insights gained from the in-silico models.
In 21 patients 105 evenly spread randomly selected non-targeted sites within the left atria were compared to AF termination sites. The AF termination sites demonstrated lower local bipolar voltage (0.83±0.76 mV vs. 0.49±0.39 mV, p<0.0001, Figure 7.5 A). A trend toward longer absolute EGM-duration at successful termination sites was not significant (139±35 ms vs. 118 ±37 ms, p=0.09, Figure 7.5 B), although EGM fractionation was present. Nonetheless, EGMs at AF termination sites covered a significantly greater part of the local AF cycle length in comparison to control sites (cycle length coverage: 79±16 % at termination sites vs. 59±22 % at control sites, p=0.0022, Figure 7.5 C) and showed higher consistency of prolonged activity over 10 consecutive AF beats (0.8 [0.6/1.0] vs. 0.3 [0.2/0.8], p<0.01; Figure 7.5 D, respectively).
EGM voltage and EGM duration were compared between AF termination and non-termination sites. EGM voltage at AF termination sites was 0.49 ±0.39 mV while non-termination sites yielded 0.48±0.35 mV (p=1.0; Figure 7.5 A). EGM duration AF termination sites was 139±35 ms while non-termination sites yielded 129±42 ms (p=0.33; Figure 7.5 B). Thus, EGM voltage and EGM duration showed a comparable range of values. A significant difference was found between cycle length coverage and the consistency of prolonged activity at AF termination sites and non-termination sites. Cycle length coverage at AF termination sites yielded 79±16 % and was therefore significantly higher than at non-termination sites that yielded 63±23 % (p=0.02, Figure 7.5 C). The consistency of prolonged activity at AF termination sites yielded a median of 0.8 (whiskers: [0.6/1.0]) and was therefore significantly higher than non-termination sites with a median of 0.4 (whiskers: [0.2/0.8]) (p=0.01; Figure 7.5 D).
Shorter AF cycle lengths were found at successful AF termination sites compared to targeted sites without termination (173±49 ms vs. 210±44 ms, p=0.002). Additionally, AF cycle lengths were shorter compared to non-targeted control sites (173±49 ms vs. 198±34 ms, p=0.047; Figure 7.5 E). The cycle length was significantly shorter than the concomitant cycle length in the coronary sinus at AF termination sites (by -39±43 ms) compared to unsuccessful targeted sites (by -3±35 ms) and non-targeted control sites (by -12±31 ms) ($p < 0.05$; Figure 7.5 F).
A cycle length more than 15 % shorter compared to the concomitant AF cycle length in the coronary sinus defined rapid focal activity and was found at 7 of 21 AF termination sites.
All AF termination sites were reassessed in SR following termination. A 1 cm-wide border zone around the ablation site was evaluated and in 15 of 21 (71 %) patients, the border zone demonstrated low voltage-EGMs (<0.5 mV) with delayed components that showed fractionation as well. These delayed components correspond to the simulations that showed 'local late potentials'. The voltage of these delayed fractionated components (0.26±0.13 mV) was sig-

nificantly lower than the maximum bipolar voltage of all AF termination sites (0.52±0.3 mV, p=0.0009). Lastly, the EGM duration at these sites measured 79±24 ms.

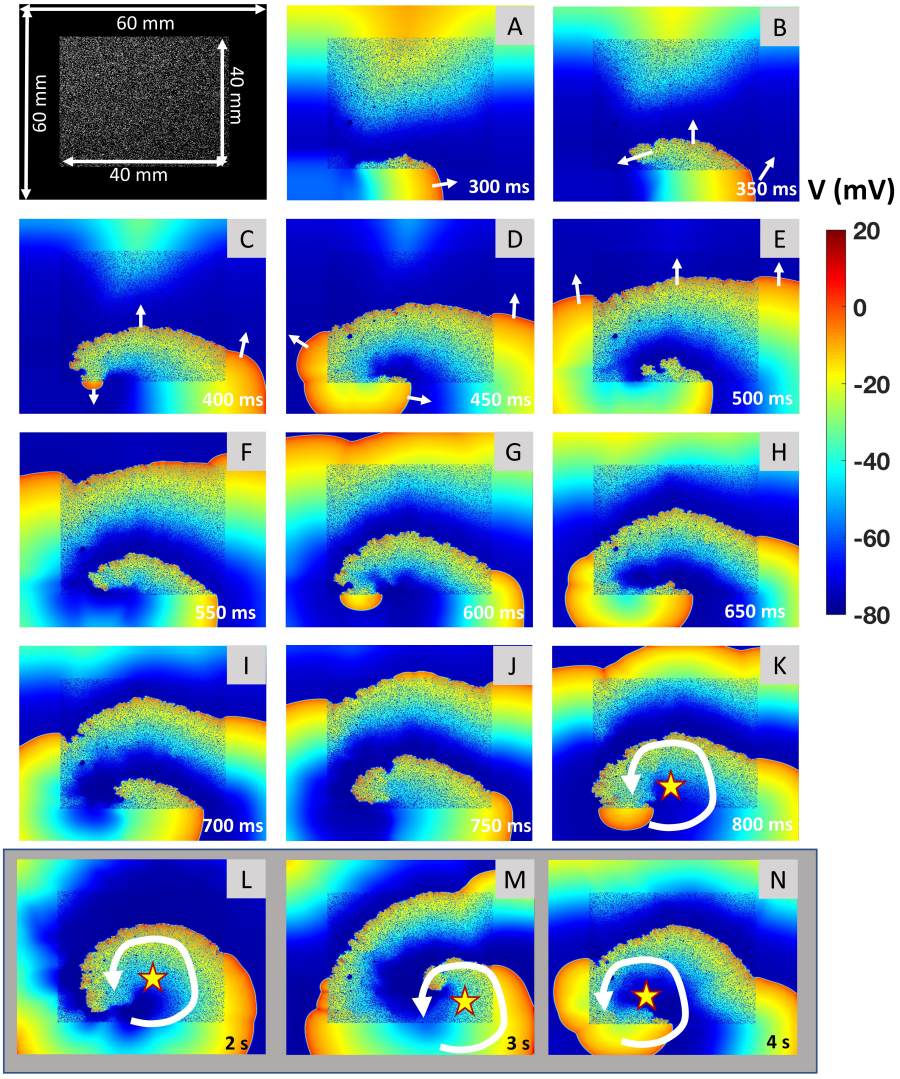

Figure 7.3: Multiple wavelet formation with large simulated fibrosis in AF. Transmembrane voltage of a fibrotic tissue simulation of a meandering re-entry circuit. The top left picture shows the patch dimensions; white speckles indicate fibrotic tissue modeled as non-conductive elements. Elements (A–K) are equidistantly distributed in time (Δt = 50 ms). After crossfield stimulation, the depolarization wave propagates outside of fibrotic tissue (A). The depolarization wave then enters the fibrotic tissue and continues propagation outside the fibrotic region (B). The depolarization wave exits the fibrotic region in (C). This pattern occurs repeatedly (D–K). The reentrant activity is marked with a circular arrow; the yellow star marks the center of rotation (K). Larger time intervals (Δt =1 s) showing the long-term meandering propagation of the rotor and its center throughout the fibrotic tissue is shown in (L, M). Figure and caption adapted from [7] under the Creative Commons CC BY Attribution 4.0 International License.

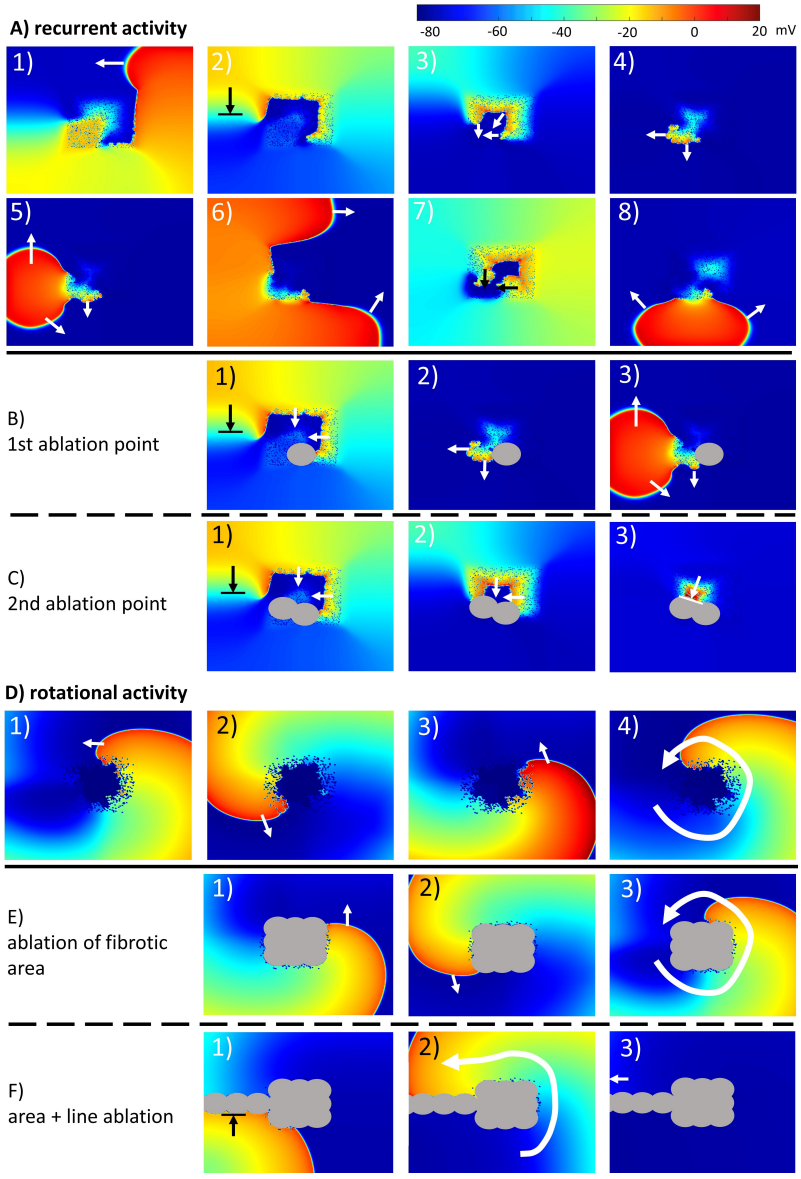

Figure 7.4: Ablation strategies for AF. Conduction block of rotational activity in healthy tissue (A1-2) but continued slowed propagation through fibrotic tissue (A2-3). Focal excitation on bottom left corner leads to two separate wavefronts (A5-7). This phenomenon repeats with different focal excitation point for each cycle (A8). Different ablation techniques were tested for the ability to terminate the arrhythmia: i) single-point ablation (B1-3), ii) two-point ablation, iii) ablation of complete fibrotic area and iv) ablation of area and an additional line to the next propagation obstacle.

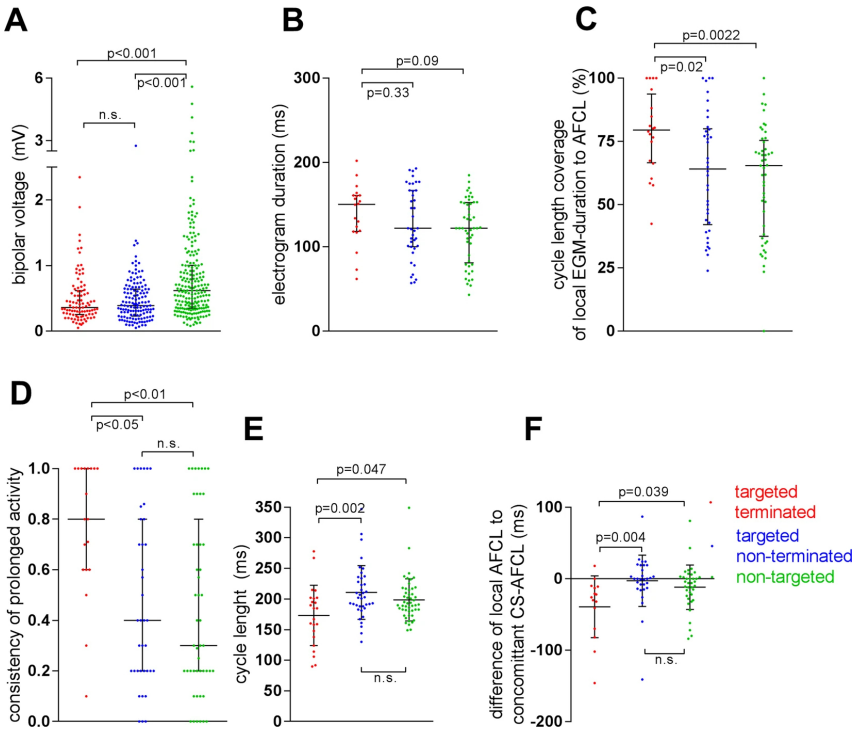

Figure 7.5: Evaluation of selected EGM characteristics defining AF termination sites (A-F) at sites targeted for ablation (ablation successful in termination of AF in red; sites at which ablation did not terminate AF in blue) compared to sites that were not target off ablation (green). Cycle length coverage (C) is given as percentage of local AF cycle length. The consistency of prolonged EGMs (D) is given as percentage of ten consecutive AF-beats at a given site with prolonged EGMs. Adapted from [7] under the Creative Commons CC BY Attribution 4.0 International License.

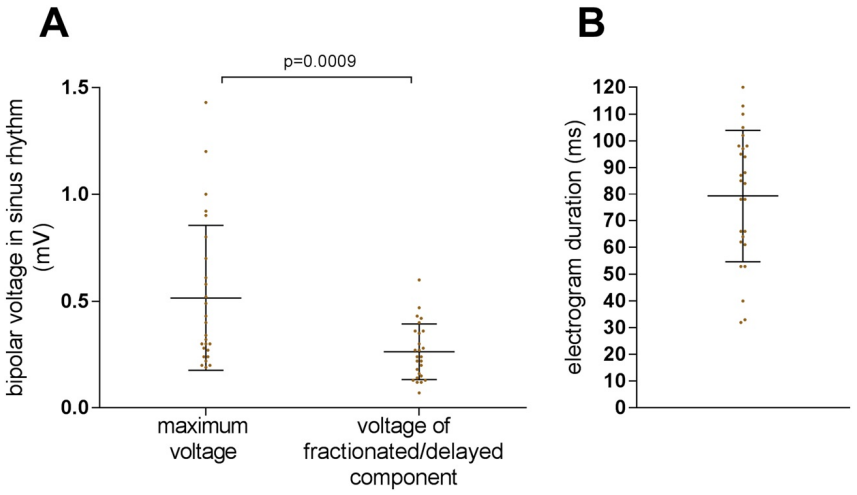

Figure 7.6: Electrogram characteristics in SR at successful termination sites. EGMs recorded in the within 1 cm of successful AF termination sites were reevaluated following SR restoration for maximum bipolar voltage (A) and duration of the total electrogram. Adapted from [7] under the Creative Commons CC BY Attribution 4.0 International License.

Chapter 8

Discussion

The findings obtained from the in-silico models were supported by clinical measurements. Three main outcomes help to identify arrhythmic sources of atrial fibrillation (AF) outside the pulmonary veins and further support the role of local fibrotic remodeling in maintaining persistent AF:

1. AF termination sites are spatially linked tightly to low-voltage areas. 90 % of AF termination sites were found in areas with a bipolar voltage $<$0.5 mV in AF. The remaining 10 % of AF termination sites were located in the immediate border zone around low-voltage areas.
2. The local electrogram (EGM) at AF termination sites show several characteristics. These are low local bipolar voltage, short local AF cycle length , high cycle length coverage, and high consistency of these EGM characteristics over multiple AF beats.
3. In sinus rhythm (SR) border zones of AF termination sites also show fractionation and delayed EGM components, indicating that ablation of these sites removes pathways using the underlying arrhythmogenic slow conduction substrate.

Atrial sites that maintain AF show consistent in-vivo and in-silico EGM properties: Fibrotic remodeling is known to play a role in the occurrence and maintenance of persistent AF. Dependent on amount and density of fibrotic substrate singular sites can uphold AF [91]. It has been demonstrated that ablation of these arrhythmogenic sites terminates AF [92, 93]. The results demonstrate that sites of AF termination are generally located either within or in the immediate border zone of pathological sites with decreased bipolar voltage $<$0.5 mV in AF. The simulation predicted the reduction of the electrical wave front amplitude by more than 80 % upon entering the simulated fibrotic area resulting in simulated bipolar EGM voltages $<$0.5 mV, which is in line with another in-silico study [94]. The reduction of amplitude was confirmed by patient evaluations, which showed that targeted EGMs with successful termination exhibited bipolar voltages of 0.49$\pm$0.39 mV in AF. Clinical trials showed that ablation of low-voltage areas, along with PVI decreases arrhythmia recurrence in persistent AF, which supports the findings of this study [21, 95, 96]. The in-silico ablation setups underpin the process mechanistically, by illustrating anchoring of the depolarization wave

to areas of fibrosis that are observable as low-voltage areas and ablation of the pathological pathways leads to termination of AF (Figure 7.4 & 7.3). Both the clinical and in-silico studies are consistent with clinical studies in which sites in the left atrium driving AF identified by non-invasive panoramic mapping were compared with MRI data visualizing fibrotic areas. Sites driving AF were found to be located in or at the borders of fibrotic areas [89, 97].
While all successful AF termination sites displayed low-voltage EGMs, this feature was not exclusive and also found in targeted sites that failed to terminate AF. Isolated low bipolar amplitude may thus be considered a sensitive, yet not highly specific criterion for sites that perpetuate AF. This could be due to measurement inaccuracies, bipolar electrode orientation or have an as yet unknown origin and should be further investigated.

EGM duration, cycle length coverage and consistency:
EGM duration difference was not significant between AF termination sites and other sites (Figure 7.5 B), even though fractionation was observed in low voltage AF termination sites. In contrast, cycle length coverage was remarkably high at AF termination sites (Figure 7.5 C) and displayed high consistency of prolonged activity (median: 80 %) (Figure 7.5 D). These findings suggest an underlying localized reentry- or repetitive focal activity with anisotropic and/or inhomogeneous conduction to the surrounding myocardium at the prevalent activation rates. Heterogeneous conduction in simulated fibrotic areas was able to support localized reentries in the presented in-silico model (Figure 7.2). The simulated EGM patterns recorded from within these localized reentries demonstrated locally consistent and repetitive prolonged and fractionated EGMs, similar to clinical observations. Observation of these EGMs characteristics at potential target site may therefore be due to narrow slow conduction isthmuses (Figure 7.4 A-C) in the reentrant path, which also would explain the success of local ablation.

Local cycle length and rapid focal drivers:
The in-silico experiments illustrated that the rotational source around a fibrotic area will adapt its wavelength according to the established conduction velocity (CV) and adapted effective refractory period (ERP) and will create EGMs with a cycle length significantly smaller than the length of a depolarization cycle across the whole patch (Figure 7.3 C-F). Similar observations were made in clinical data. AF termination sites harbored EGMs with significantly shorter mean local cycle lengths (173$\pm$49 ms) than unsuccessful ablation sites (210$\pm$44 ms) or control sites (198$\pm$34 ms) (Figure 7.5 E). In contrast to unsuccessful ablation or control sites, successful AF termination sites additionally displayed shorter local cycle lengths than the concomitant AF cycle length within the coronary sinus (by -39$\pm$43 ms) (Figure 7.5 F). This study defined rapid focal activity as a local AF cycle length shorter than 15 % than the concomitant cycle length in the coronary sinus at the respective AF termination site. One third of patients met this criteria. Local AF cycle length can thus be considered a decisive criterion to identify arrhythmogenic sources of AF. This was underpinned mechanistically in the in-silico rotational simulation (Figure 7.2) and is also indicated in literature [90, 93]. Therefore, cycle length should be considered for the development of novel mapping algorithms.

SR EGM properties:
The SR EGM was characterized by low-voltage, fractionation, and delayed components when measured in the border zones and surroundings of AF termination sites in most (71 %) cases (Figure 7.6 A, B), which is in line with a preceding in-silico study on the impact of fibrosis on signal morphology [94]. For the in-silico model a single uniformly propagating activation wave front was used to simulate SR. The model revealed a high resemblance of EGMs recorded from within the simulated fibrotic area to the clinical EGMs acquired from the AF termination sites. This advocates that EGM characteristics observed in fibrotic areas are not only due to the rapid fibrillatory activity and thus are not of a functional nature, but rather specific to the underlying substrate and demonstrate slow and locally delayed conduction within the fibrotic areas.

8.1 Limitations

Endocardial contact mapping is sequential and therefore ill-suited to represent the continuous chaotic activation of persistent AF. Additionally, shifts between measuring position and atrial geometry can occur [21, 84, 98]. Basket-catheters can increase the simultaneously mapped area, but are disadvantaged by uneven electrode distribution with few electrodes having sufficient tissue contact.
Current computer models of AF on the other hand, are based on human action potential kinetics that were adapted to cardiomyocytes from patients with AF [72]. While the model, in contrast to previously employed models, uses a spatial resolution comparable to the physiological scales in human atrial fibrosis, it does not incorporate all the molecular and cellular changes that develop in an aging human heart exposed to AF.
Though simulations indicate that the ablated sites terminate AF due to cancellation of the arrythmogenic pathways, these points could be secondary termination sites that terminate AF only in combination with previously set ablation points or are AF maintaining sites but not the source itself. Differentiation of these points was not part of this study and by using a statistical approach the influence of these occurrences should be minimized.
Finally, the exact voltage threshold to be considered pathological in AF or SR remains unknown. In literature studies emphasize bipolar cut off-values as low as <0.24 mV in AF, and roughly correspond these values to <0.5 mV in SR [21, 99]. One clinical approach advises a threshold of <0.5 mV in AF and <1.0 mV in SR [21], is based on empirical observation that fractionated and prolonged EGMs in AF and delayed activity with 'atrial late potentials' in SR are frequently found within these voltage ranges [84, 99], under the assumption that mapping includes recordings from all existing bipole spacings of the 20-polar Lasso catheter.

8.2 Conclusion

Successful termination sites of AF display distinct EGM patterns with short local cycle lengths harboring fractionated and low-voltage potentials that are locally highly consistent and cover a majority of the local AF cycle length. Most of these areas also display pathologic delayed atrial late potentials and fractionated EGMs in SR.

PART III

A FULLY AUTOMATED PIPELINE FOR S1S2 PROTOCOLS: CVAR-SEG

Chapter 9

Motivation

Atrial fibrillation (AF) is the most common supraventricular cardiac arrhythmia, with a fourfold increase in prevalence over the last 50 years [101]. Treatment strategies remain suboptimal in terms of efficiency and outcome [1]. Fibrosis, among other effects, refers to an excess deposition of collagen inside the cardiac tissue [5, 6] and is suspected to be responsible for maintaining arrhythmias, e.g., due to anchoring of reentrant depolarization waves [7, 8]. Current invasive AF treatment strategies use multi-electrode catheters to record electrograms and characterize the substrate by the peak-to-peak amplitude (often simply distinguishing between 'high' and 'low' voltage) and local activation time (LAT). This information helps to guide the ablation procedure. It has been shown that fibrotic tissue correlates with regions of low voltage [9–11]. Beyond pulmonary vein isolation, these low voltage regions are commonly targeted by ablation [12–14]. A drawback of the low voltage guided approach is that it ignores the rate-dependent nature, i.e., restitution information, of both amplitude and conduction velocity (CV). Restitution is the property that as the diastolic interval of a proceeding beat varies the action potential duration (APD) and CV of the current beat also vary. In general, a decrease of diastolic interval is followed up with a decrease in APD and CV. On a cellular level this is caused by an incomplete recovery of the membrane voltage to the resting potential, which in turn reduces sodium channel availability, thereby reducing sodium influx and upstroke velocity of the following beat. Due to its potential as a predictor for AF and AF recurrence [54, 102], restitution is an active field of research. Furthermore, fibrotic regions are present in paroxysmal as well as persistent AF patients [103] hinting at a more complex interconnection. Subtypes of AF might be uncovered by using restitution information.

Both the CV and amplitude restitution curves have the potential to reflect and uncover the underlying mechanisms related to the initiation and perpetuation of atrial and ventricular arrhythmias [104, 105]. Compared to a healthy control group, the APD restitution curves in AF patients are shifted towards lower values and exhibit a less steep slope for basic cycle lengths (BCL) under 400 ms [106]. Furthermore, [105] reported that an increase in fibrosis

resulted in a shift of the CV restitution curve towards lower CV values. Therefore, the slope and asymptote of the restitution curve are connected to substrate characteristics and could be used for diagnostical purposes, or can be used to monitor drug intervention to adjust the slope beyond a threshold [25]. For restitution studies in clinical practice, rate-varying S1S2 stimulation protocols are predominantly used [54]. They minimize the risk of inducing AF that continuous high frequency pacing carries. S1S2 protocols allow measuring the immediate electrophysiological response to a change in pacing coupling interval [107]. The S1S2 protocol consists of several pacing trains. Each pacing train contains several stimuli with a BCL, called the S1 stimuli, followed by a single stimulus administered after a reduced coupling interval, called the S2 stimulus. This pacing train is repeated, with the S1 stimuli retaining their BCL and a sequentially decreasing coupling interval between the last S1 stimulus and the S2 stimulus. The pacing protocol ends as soon as the atrial tissue does not depolarize at a certain S2 coupling interval anymore because the S2 stimulus falls inside the effective refractory period (ERP). Multiple challenges arise for an automatic signal processing pipeline. Different clinical hardware setups lead to a morphological variability of signals. Additionally, all variable input parameters (filter and stimulation setup) that the physician can control have to be considered. Lastly, in clinical practice, different protocol settings are used, and ad-hoc deviations from the initial study protocol can be required.
In an EP study, signals may be fractionated due to fibrosis, measurement artifacts, or noise influences, making detection of LAT of active signal segments challenging. Two common methods are the non-linear energy operator (NLEO) [108] and the wavelet transform [109], however there exist multiple alternative ways of determining the LAT [37, 108, 110]. These approaches lack the ability to detect atrial activities lower in amplitude and maximum slope than a nearby stimulation artifact, necessitating an additional step of stimulus removal to make them viable if a stimulation artifact partly overlaps with the atrial activity of interest.
These considerations led to three requirements for our S1S2 segmentation pipeline: i) the pipeline must not rely on a-priori knowledge of the procedural parameters; ii) an automated pipeline is needed, which segments and annotates time windows of activities and stimulations; iii) a clean removal of the stimulus artifact is necessary to uncover the underlying atrial activity for local measurements with stimuli originating in proximity to mapping electrodes. The independence of procedural parameters allows for verification of measurement data and saves time by eliminating potentially bad outlier measurements at an early research stage.
To the best of our knowledge, there is no established best practice for an atrial activity segmentation pipeline of S1S2 measurements to date. Such a pipeline must meet high quality standards regarding accuracy, robustness, and reproducibility. To address this issue, we propose the CVAR-Seg pipeline for the automatic segmentation of intracardiac S1S2 protocol measurements to gain temporal (LATs) and spatial (distances) parameters from patient data as a basis for deducing restitution curves of both amplitude and CV. The pipeline was designed modular, to allow users to exchange the existing modules with alternatives for atrial detection, LAT assignment or CV calculation components. By releasing the software as open source, the pipeline can be freely used and adapted.
The pipeline was tested on synthetic signals with a known ground truth. Noise estimated

from a clinical EP case was added to the synthetic signal to test the pipeline robustness for increasing noise levels. Finally, we applied the method in a clinical proof of concept with one patient data acquired with the widely-used CARTO system.

Chapter 10

Methods

In this section, an overview of CVAR-Seg (Figure 10.1) and the basic ideas behind each step are presented. For more detailed information, the interested reader is referred to the supplementary material. The pipeline uses electrogram (EGM), electrocardiogram (ECG), and geometry data from clinical S1S2 stimulation routines. From these, the pipeline segments activities and computes amplitude and CV restitution curves.

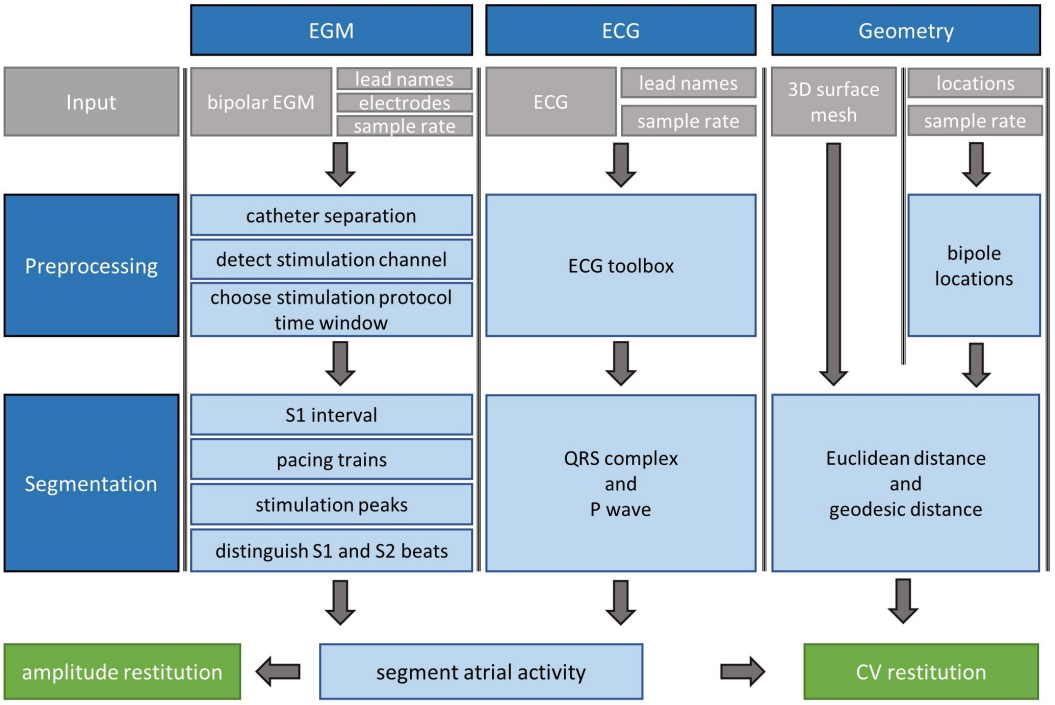

Figure 10.1: Segmentation pipeline for clinical S1S2 protocol measurements consisting of EGM, ECG, and geometry data. Grey boxes are pipeline input. The pipeline yields segmented atrial activities. In additional steps, CV and amplitude restitution can be calculated. Figure and caption adapted from [100] under the Creative Commons CC BY Attribution 4.0 International License.

10.1 Preprocessing of Input Data

Electrograms (EGM)

In the first processing step of the segmentation pipeline, different catheters used throughout the experiment are detected, thereby enabling the distinction between stimulating and non-stimulating catheters. Both unipolar and bipolar signal evaluation is supported. Since the bipolar signals are less noisy this is used for all segmentation steps and the final segmentation windows are then evaluated on the unipolar traces. Therefore, from the input the bipolar signals are extracted and used for all further steps. From electrical field theory, we know that the stimulation artifact has the highest amplitude in the stimulating channel, and with increasing spatial distance to the stimulation source, the amplitude decreases. Therefore, neighboring channels should have the second highest amplitudes. This relation is used to detect the stimulating catheter. The channel with the highest signal amplitude and the channel with the second highest amplitude during stimulation are found and checked if they are spatially neighboring channels. This step adds robustness against high amplitude noise artifacts in non-stimulating channels. The following manual selection of the EGMs evaluation window is turned off for the fully automated processing where the whole input segment is evaluated.

Electrocardiogram (ECG)

In the case of the optional use of a corresponding ECG trace, the signal is first up-sampled by linear interpolation to the sampling rate of the EGM signal. ECG segmentation is based on the open source ECGdeli toolbox [111], yielding a fiducial point table comprising 13 crucial time points characterizing the ECG trace. Of those, this pipeline uses the start, peak, and end of the QRS-complex.

10.2 S1S2 Protocol Segmentation

Stimulation detection and S1 cycle length estimation

To distinguish stimulation components from physiological signal components, a high pass filter with a cutoff frequency of 450 Hz is applied to exclude most components of biological origin and their low order harmonics [112], retaining stimulation-related peaks in the clinically filtered signal traces. To detect stimulation segments in the so filtered signals, the wavelet method using the bior1.5 mother wavelet following [109] is applied. Each channel trace is analyzed, and the temporal start, peak, and end of all active signal segments are annotated. To create exact time points of start and end of active signal segments, a threshold

is applied to the resulting wavelet-filtered signal. The threshold was defined as the standard deviation of the amplitudes across all samples in the segment multiplied by a factor k that is determined iteratively: starting from a low initial k value of 0.01 to include as many active segments as possible (Figure 10.2A, yellow segments), the wavelet segmentation is performed. A histogram of the temporal distances Δt between all peaks is evaluated, and the three most common values are identified (Figure 10.2B) based on the idea that the S1 cycle length will occur most often in an S1S2 protocol. The second and third highest peaks in the histogram should be integer multiples of the S1 cycle length within a tolerance of 10 samples. This holds true for cases with increased extra beats (Figure 10.2C). If the integer relationship is confirmed, k, the detected segments, and the S1 cycle length are determined. If the second and third highest peaks are not integer-multiples, k is successively increased by a Δk of 0.01 until a consistent S1 cycle length is identified. Should this condition not be met after a maximum number of iterations a warning is issued. This concludes the estimation of the S1 cycle length by using the S1 time interval detection.

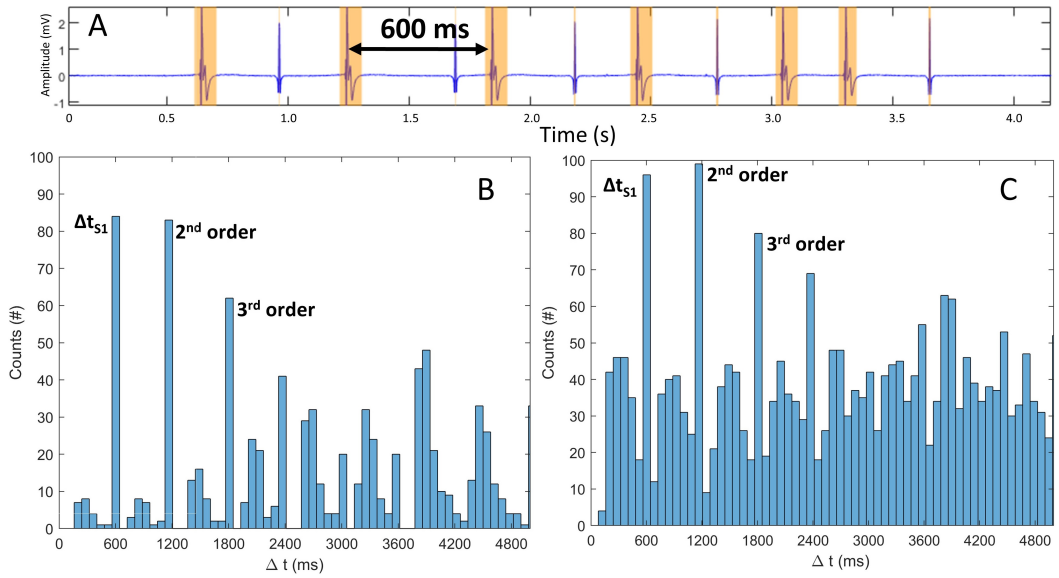

Figure 10.2: A: Active segment detection (yellow intervals) of a stimulation block segment of a synthetic 80-second-long S1S2 protocol with 20 randomly distributed extra beats - A shows 5 extra beats. S1 peaks have a cycle length of 600 ms. B: Histogram of all time intervals between active segments. x-axis cut at 5000 ms. Time interval corresponding to S1 cycle length and the harmonics present the highest contribution. C: Fourfold increase of extra beats does not change the three main contributors. Figure and caption adapted from [100] under the Creative Commons CC BY Attribution 4.0 International License.

Number of Pacing Blocks and Stimuli Estimation

Based on the approach of the previous section, the S1 cycle length is known. However, the time interval between S1S2 pacing trains (i.e. the interval between a S2 stimulus and the following S1 stimulus, Δt_{S2S1}) and the number of S1 stimuli contained within each S1S2 pacing train remain unknown. Therefore, the time differences Δt between peaks are classified with a k-means clustering algorithm (Lloyd, 1982) using two clusters. This yields one cluster containing the S1 cycle lengths (Δt_{S1}) and S2 coupling intervals (Δt_{S2}), respectively, and the second cluster containing the markedly longer S2 to S1 (Δt_{S2S1}) intervals between pacing trains. With this information, different pacing trains can be separated. The mode (most frequent value) of the number of identified successive S1 cycles present is used to identify the number of S1 stimuli within a pacing train. To identify the S2 coupling interval, a time window of interest after the last S1 stimulus is defined with the length of S1 because the S2 interval is normally shorter than S1. The rationale for the statistical k-means approach was that extra beats could impair signal segmentation performed on single segments of the measurement. Also, no knowledge of the time window between pacing trains and the S2 time windows was needed. The only assumption used was that the time between trains is longer than the S1 cycle length.

Detection of Stimulus Time Segments

The previous segmentation step detects the time segments of pacing trains. Segmentation of stimulation time segments based solely on time intervals between peaks would be prone to errors in peak detection and noise since an extra beat would disrupt the time interval between neighboring stimuli. For noise-robust stimulus time detection, five conditions (C1-C5) were formulated:

- C1: Stimulations are detected in multiple channels of the catheter at the same time.
- C2: Stimulations detected by NLEO after high-pass filtering agrees with the detected stimulation time segments by wavelet filtering as detailed previously.
- C3: In the first principal component computed across all channels, peaks overlap with the detected stimulation time segments and surpass an amplitude threshold of 90 % of the maximum first principal component amplitude. This is motivated by the difference of far field effect on the stimulation signal in the spatially varying channels and the fact that the stimulation artifact in the stimulation channel will follow the morphology given by the stimulus generator, which differs in morphology from the far field in the other channels.
- C4: The time interval between neighboring stimuli does not deviate from the S1 cycle length by more than 10 samples.

C5: The first principal component of all derivatives of all channel signals overlaps with the detected stimulation time segments and surpasses 90 % of the first principal component signal.

The threshold to determine trustworthy stimulation time segments was set such that a stimulation had to be detected in at least half of all channels (C1, C2) and had to pass the derivative (C4) and the amplitude (C3, C5) conditions. Applying that threshold separates the detected time segments into trusted and discarded stimulus time segments. The remaining trusted stimulation time segments are then classified as either S1 or S2 beats using counters or cross-correlation methods.

Atrial Activity Segmentation

After all stimulus time segments were assigned either an S1 or S2 tag in the previous step, the atrial activities have to be segmented. Two main problems arise: i) the stimulation peak is more prominent in amplitude and slope than the atrial activity; ii) for some combinations of CV and electrode distance, the atrial signal overlaps with the stimulation peak, thereby making it indiscernible for most activity detection algorithms. Thus, a matched filtering method was implemented designed to find specific signal morphology embedded in noise. This methodology maximizes the signal-to-noise ratio (SNR) using a template of a known signal, which is correlated with the measured noisy signal. Short signal segments and morphological impulses can lead to filter artifacts and oscillations, motivating an adapted approach. We detail the key aspect of template choice and our 3-step matched-filter implementation sub pipeline (Figure 10.3) in the following. To decide on a stimulation signal template, all detected stimulation segments are checked for an overlap with the previously detected QRS complexes to exclude those with ventricular far field overlap from step 2. In the second step, a stimulation signal template is chosen for each channel as the first available S2 stimulation signal starting from (and including) the shortest S2 coupling interval. In most cases, the S1S2 protocol continues until the ERP is reached. Thus, the time interval after the S2 stimulus with the shortest coupling interval either contains no atrial answer signal or, if stopped prematurely, the atrial answer has the highest time interval to the S2 stimulation artifact making it the best candidate for a “clean” stimulation template. In the third step, the amplitude of the signal template is scaled to individually match each stimulus of the channel signal. The template signal segment is cross-correlated with the channel signal and subsequently subtracted from the channel signal at the time point of highest correlation value. Finally, the time between start and stimulation peak in the initially detected stimulation time window is linearly interpolated to avoid large derivatives between samples, which would distort the following atrial activity detection. The NLEO method [113] is used to detect the atrial activity. Applying the previously defined threshold k to these signals yields time points of start, peak, and end of the atrial activity time window. The time segments in which the NLEO signal of the atrial activity does not exceed the threshold are defined as having no

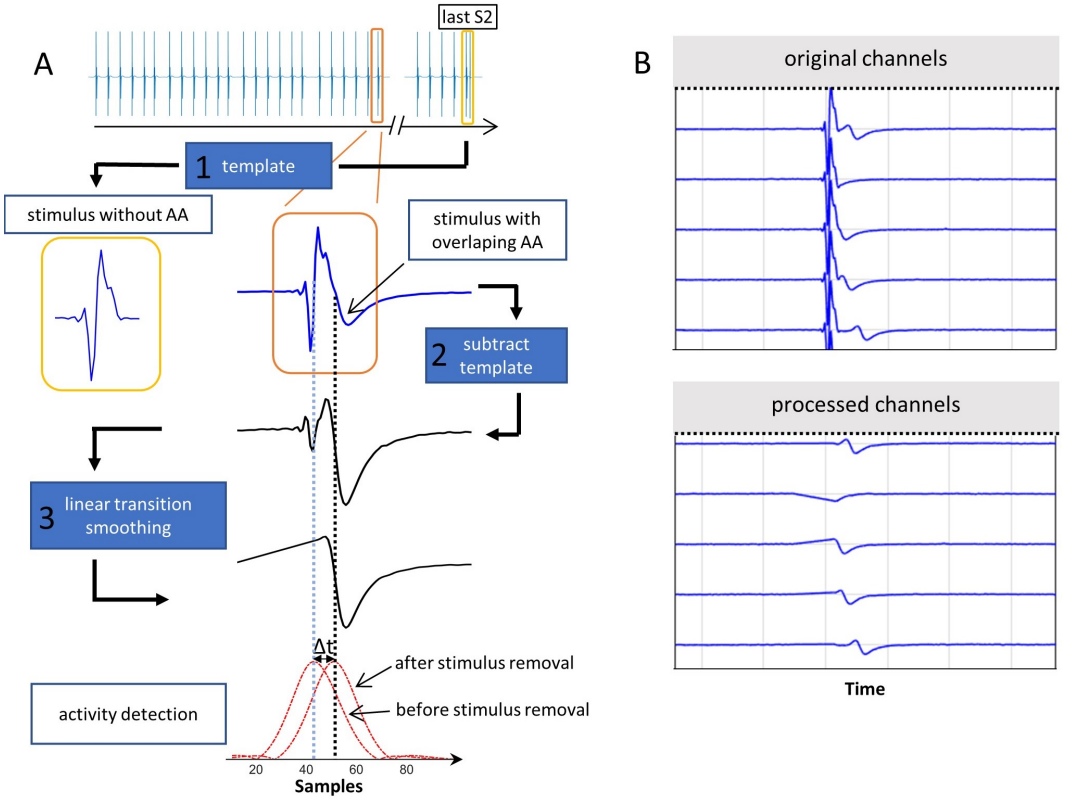

Figure 10.3: A: Elimination of stimulation artifact. Exemplary stimulation signal covering an atrial activity from an S1S2 pacing protocol (orange). Template (1, yellow) chosen from the last part of the S1S2 protocol. After template subtraction (2) and linear signal smoothing (3), the maximum of the NLEO activity detection signal (red), shifts by Δt from the stimulation (vertical blue dotted line) to the now uncovered atrial activity (black dotted line). B: A synthetic signal segment containing stimulations followed by atrial activities. In some cases, the atrial activity is covered by the stimulation (original channels). After the matched filtering method is applied, all atrial activities become visible (processed channels). Figure and caption adapted from [100] under the Creative Commons CC BY Attribution 4.0 International License.

detected activity. This can be the case for measurements with loss of capture during the measurement.

ERP Estimation

The last segmentation step is the detection of the ERP. After ventricular far field exclusion, the ERP is determined by checking when the atrial activity to an S2 stimulus dropped below an empirically determined threshold of 20 % of the mean amplitude of all atrial activities compared to the mean of the respective S1 stimuli in the same pacing train. The mean of the S1 stimuli inside a pacing train is considered since, in clinical practice, slight catheter shifts due to respiration and muscle contraction can lead to amplitude changes in the signal. The ERP is detected for the stimulating as well as the non-stimulating catheter.

Processing of Location Data

The location of each electrode per time sample is extracted from the clinical EP system. Since the pipeline uses bipolar signals, the mean location of the two electrodes is taken as a surrogate for bipole location. Inter-bipole distances between catheters are calculated using the geodesic distance by searching the shortest path on the mesh and subsequent Bézier spline interpolation [114]. For the electrode distances within a single catheter, the Euclidean distance is chosen, since often the surface mesh is too coarse to compute mesh-based distances, and additionally, the projection onto the mesh results in non-negligible errors.

Amplitude and LATs

Amplitudes are determined within the previously detected active segments and are calculated by subtracting the minimum from the maximum amplitude of the signal (peak-to-peak voltage).
The LATs of the atrial activities are known, and the distance between stimulation (r_s) and measuring electrode (r_m) is known. If an atrial geometry with sufficient LATs is given CV, anisotropy and fiber direction can be estimated [19]. To calculate CV from an electrode, existing method such as the ellipse fit [115], the cosine fit [26] or the CV fit for multipolar catheters [18] can be applied. These methods create a single restitution curve for the substrate at the specific measurement location by combining all LATs with the catheter geometry. However, most approaches are dependent on certain measurement setups or specific catheter orientation to the wavefront, which might not always be given for all S1S2 protocols. Thus, we use the general velocity equation from classical mechanics to showcase the CVAR-pipeline:

$$p(t) = \frac{\|\vec{r_s} - \vec{r_m}\|}{LAT}. \tag{10.1}$$

This is not the true CV of the depolarization wave but rather the scalar projection of the CV vector onto the path between stimulation and measuring electrode. We refer to this as propagation speed (p). Since the pipeline provides all spatial and temporal values, it is well suited to provide input to any other CV estimation method as well.

10.3 Pipeline Performance Testing

Synthetic S1S2 Protocol Setup

Stimulus signals were modeled as exponentially decaying biphasic pulses (Figure 10.4A) following the formulation of [116]. The amplitude of the stimulation artifact was set to 4.7 mV as observed in our patient measurement. The total stimulation signal length was set

to 8 ms, with the first part of the biphasic signal being 2 ms in accordance with the clinical stimulation setup. Atrial activities were modeled following [117] based on a moving dipole in an infinite homogeneous conductor. The atrial activity synthetic signal morphology was scaled to have an amplitude of 2 mV and duration of 35 ms (Figure 10.4A). Using these

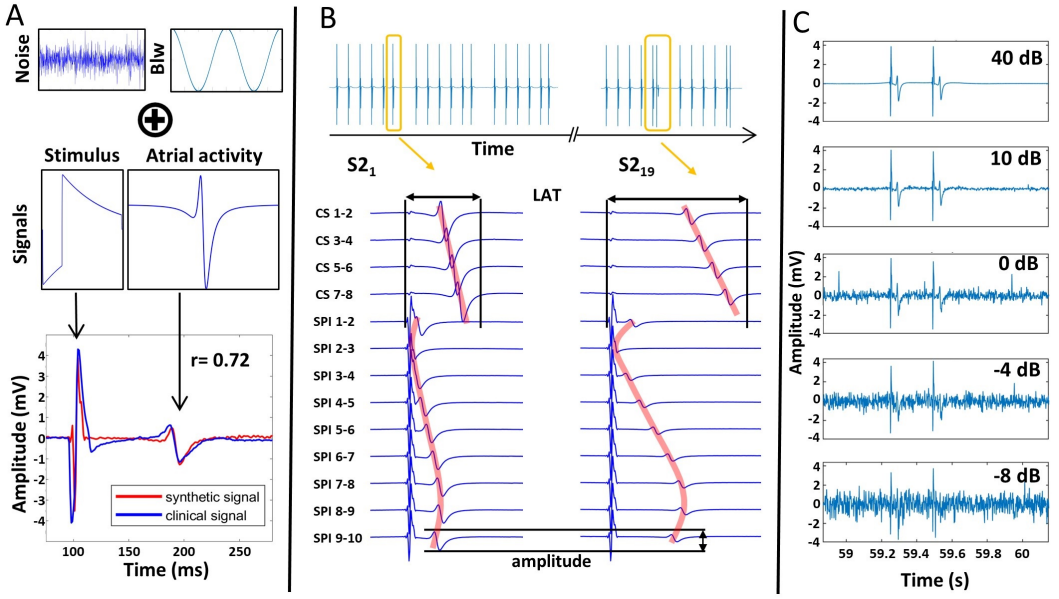

Figure 10.4: Clinical noise and baseline wander (Blw) are combined with synthetic stimulus and atrial activity signals to create a synthetic signal close to clinical signals with the Pearson correlation coefficient r of 0.72. B: Complete synthetic S1S2 protocol setup with multiple pacing trains (yellow), catheters, and catheter channels, anisotropic wave propagation (red) as well as amplitude & LAT changes due to restitution. C: Effect of noise scaling on the signals. Figure and caption adapted from [100] under the Creative Commons CC BY Attribution 4.0 International License.

activity templates, a complete S1S2 protocol was created with an S1 BCL of 600 ms and a Δt_{S2S1} of 1.2 s. The S2 coupling interval was decreased from 500 ms to 350 ms in steps of 50 ms and from 340 ms to 180 ms in steps of 10 ms, yielding 21 pacing trains. The ERP was assumed to be 200 ms. Therefore, the last two pacing trains generated no atrial activity.
The S1S2 protocol was set up to mimic a clinical dataset for a circular catheter with a radius of 10 mm and 10 equidistant electrodes on a plane creating 9 neighboring bipolar signal channels. 4 bipolar coronary sinus (CS) catheter channels were set up with 35, 40, 45, and 50 mm distance to the stimulating channel. The stimulation was set up at channel 1 corresponding to the bipolar electrode pair 1-2. The LATs of the atrial activities in the channels were assigned, assuming elliptic excitation conduction with an anisotropy factor of 1.5. To mimic restitution behavior, an exponential decay of amplitude and CV was defined for the atrial activities of S2 stimuli, starting from 2 mV for amplitude and 650 mm/s for CV (Figure 10.4B red line). The exponential decay of amplitude and of LATs for a circular

catheter was defined as

$$y_{restitute} = -a \cdot e^{-b \cdot (t_{s2} - t_{ERP})} + c. \tag{10.2}$$

where a was 2 mV for amplitude and 1000 mm/s for CV, b was 0.05 mV for amplitude and 0.1 1/ms for CV, t_{s2} were the S2 intervals, t_{ERP} was the S2 coupling interval where the ERP was reached and c was 2 mV for amplitude and 650 mm/s for CV.
Different LATs across channels resulted in different levels of overlap with the stimulation signal. The overlap was determined by subtracting the LAT of the atrial activity template from the temporal end of the stimulation template in the global signal protocol. Channel 2 had an overlap of 51 %, channel 1 46 %, channel 3 48 %, and channel 4 10 % between atrial activity and stimulation. All other channels had no overlap (Figure 10.4B).

Synthetic Noise Generation

To represent noise, segments containing no atrial activity from clinical recordings were extracted. From these, a signal with equivalent frequency components was reconstructed using the discrete inverse Fourier transfer function. Additional baseline wander was implemented following [118], by adding frequency components f_n ranging from 0.001 to 5 Hz with uniform random distributed phases and amplitude of twice the magnitude of the atrial activity (Figure 10.4A). To test the limits of the pipeline, noise was added successively to the synthetic signal. This was implemented by amplification of the established noise time domain signal with a noise level factor n. This factor scaled the signal to the desired SNR power ratio according to

$$n = 10^{\left(\frac{P_{signal}}{P_{noise}} - SNR\right) \cdot \frac{1}{20}}. \tag{10.3}$$

P is the power of the signal for the signal and the noise, respectively (Figure 10.4C).

10.4 Evaluation

A single stimulation protocol with 9 channels combined with 19 S2 stimuli with decreasing coupling interval (the ERP is reached for lower S2 coupling intervals) led to 171 signals. Exclusion of the stimulation channel yields 152 signals and thus the same number of detectable LAT values. The measure of error was the deviation of the respective pipeline results (number and value of LAT, amplitude) from the ground truth.
To evaluate the performance of the pipeline under noise-free conditions, the restitution curves of amplitude and propagation speed were compared against the ground truth used to create the synthetic signals. We report conduction speed since we computed the scalar projection of the CV vector onto the path between stimulation and measuring electrode.
To evaluate the overall change of accuracy for decreasing SNR levels, the median of all 152 values was used. Additionally, the 25th (Q1) and 75th (Q3) quantiles of deviation from the ground truth were computed across all channels and all S2 stimuli. We plot the interquartile range here since no outliers exist for the clinical SNR range after exclusion of channel 2

which was used to test the absolute limits of the pipeline in regards to overlap between stimulation artifact and atrial activity (Chapter 10.2). Since the median does not account for missed LAT detections, the number of atrial activities which were not detected but were present in the synthetic signal was evaluated as well.

10.5 Clinical Data

The proposed pipeline was additionally tested on one clinical dataset recorded in the EP department of Städtisches Klinikum Karlsruhe. The patient (59 years) presented with paroxysmal AF. The S1S2 stimulation was carried out with a 20-pole circular catheter on the posterior atrial wall. The signals were stored in the Bard recording system (Boston Scientific, Marlborough, Massachusetts, USA). The atrial geometry was recorded with the CARTO EP mapping system (Biosense Webster, Irvine, California, USA). Data were anonymized and exported for further investigation. The study was part of a standard ablation procedure and approved by the ethics committee. The patient gave informed written consent.
LATs from the clinical signals acquired from the S1S2 protocol were manually annotated by two independent electrophysiology experts for evaluation of the tool. Furthermore, morphological, and physiological qualitative accordance with literature data was assessed for both amplitude and propagation speed restitution curves in lack of ground truth data.

Chapter 11

Results

11.1 Synthetic Recreation of Clinical Electrogram

To test the pipeline with a known ground truth, synthetic signals resembling clinical recordings were created as described above. Similarity of clinical and synthetic signal was assessed by evaluating the Pearson correlation on a signal excerpt of one channel for each noise realization and was found to have a maximum at 40 dB (r = 0.72). Decreasing SNR (Figure 10.4 C) below 40 dB decreases similarity with the clinical signals down to 0.17 for -10 dB. At 0 dB, mean noise amplitude reaches a third of the atrial activity amplitude, which is seldomly seen in clinical bipolar measurements. For even lower SNR values, noise peak amplitude is equal to or surpasses atrial activity amplitude.

11.2 Reproduction of CV and Amplitude from Synthetic S1S2 Protocol

The temporal histogram approach consistently estimated the S1 BCL of the synthetic signals with an error below a single sample duration (1 ms). The same holds true for the statistical k-means clustering method used to detect the number of pacing trains and pacing stimuli contained in the single pacing trains. These two segmentation steps build the foundation for all future segmentation steps and proved to be robust for all noise conditions. The ground truth atrial amplitudes were compared to the amplitude curves reconstructed by the pipeline and showed a maximum deviation of 0.05 mV (Figure 11.1 A). The estimated propagation speed values (Figure 11.1 B) resulting from the pipeline revealed channel 5 to have the largest error with a mean deviation of 7.81 mm/s (1.3 %), originating from an LAT error of approximately 0.34 ms across all data points. Channel 3 shows a single deviation of 35.2 mm/s (5.7 %) at a coupling interval of 230 ms, resulting from an LAT error of 0.7 ms. The LATs of the channels were set up to create different levels of overlap of the atrial signal and the stimulation peak (Figure 10.4 B). The pipeline was unable to detect the atrial signals

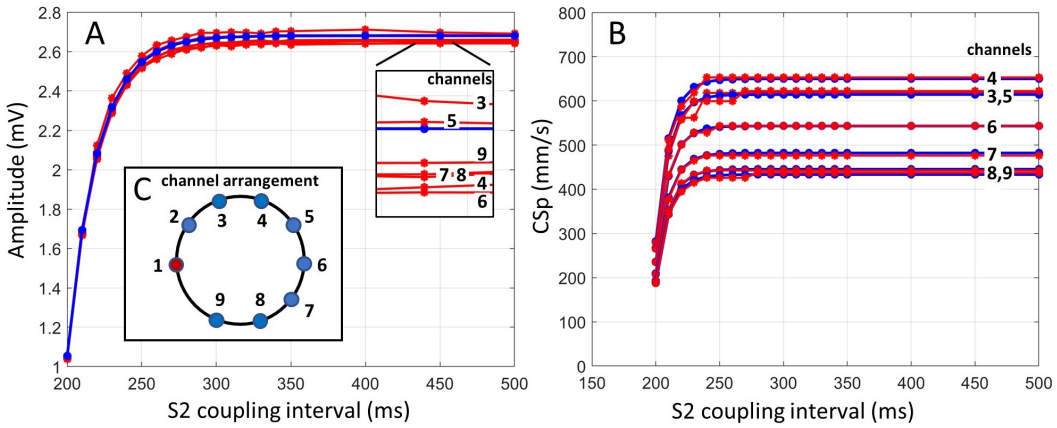

Figure 11.1: A: Ground truth amplitude of atrial activity for all channels (blue) and pipeline outcome amplitudes (red). B: Ground truth propagation speed (blue) and pipeline outcome propagation speed (red). Both panels represent a near noise-free case (SNR 40 dB). C: Schematic sketch of bipolar channel arrangement mimicking a clinical case resulting from 10 electrodes. Figure and caption adapted from [100] under the Creative Commons CC BY Attribution 4.0 International License.

where the atrial activity overlapped more than 50 % with the stimulation artifact, which was the case for channel 2. All other atrial answers were detected. However, channel 1 was excluded since it was defined as the stimulating channel. Channels 3 and 5 had the same propagation speed restitution curve due to the circular geometry and the LAT model and only differed in noise to test the consistency of the algorithm in later noise evaluations.

11.3 Pipeline Performance Beyond Clinical Noise Levels

The reconstructed amplitude for synthetic signals with decreasing SNR (Figure 11.2 A) showed a stable mean amplitude error of 0.06 mV down to 10 dB. Below 10 dB, there was a marked increase in the interquartile range, and the median value dropped. At 0 dB, the median error exceeded 0.2 mV. The amplitude error relative to the true value exceeds 10 % at 1 dB and 20 % at -1.5 dB (Figure 11.2 C). The median LAT was stable with errors below a single sample down to -1 dB (Figure 11.2 B). The median value began to oscillate within the 1 sample error margin for values below -1 dB. For values lower than -3 dB, interquartile distance drastically increases, and the median oscillates by values larger than one sample. Figure 6D shows the number of atrial activities in the synthetic signal which were not detected. Above 9 dB, the number of failed detections was below three resulting in relative errors close to 0 %. For lower SNR levels, the number of failed detections increased up to a value of 142, resulting in relative errors close to 90 %. These values exceed the range of clinically valid measurements and are used to test the limits of the pipeline.

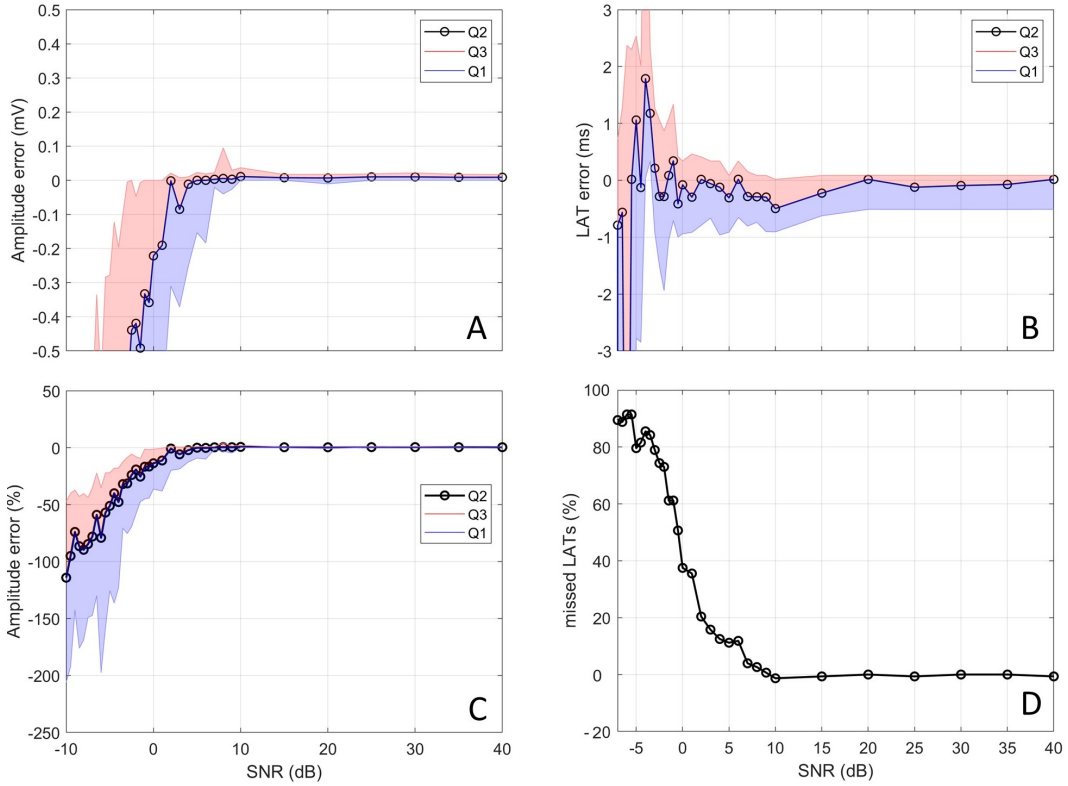

Figure 11.2: Influence of noise. A: Median (Q2) amplitude error and interquartile distance (Q1, Q3). B: Median LAT error and interquartile distance. C: Relative amplitude error with respect to true amplitude. D: Percentage of missed LAT detections. For A and B the y-axis was capped for visualization purposes. Figure and caption adapted from [100] under the Creative Commons CC BY Attribution 4.0 International License.

11.4 Results for Clinical Signals

The LAT error was created by subtracting LATs resulting from the pipeline from the manual expert annotations. LAT errors of the stimulation signal remained in the range of -4 ms to 1.5 ms (Figure 11.3 A). CS LAT error had a larger variance in median value between channels while the median LAT error in the circular catheter remained approximately -1 ms for all channels except PV 3-4 (1.9 ms). Atrial activity error (Figure 11.3 B) median values remained in the range between -1.5 ms and 3 ms for all channels (Figure 11.3 B). Interquartile ranges were below 3.5 ms for all channels except CS 1-2, PV 1-2 and PV 7-8, in which the interquartile range was approximately 7.5 ms. Asterisks at the upper boundary of Figure 11.3 B denote the number of extreme outliers beyond the y-axis limits for each channel. In total, 23 (7 %) out of 321 LAT errors were considered extreme outliers. Excerpt signals of the extreme deviations show the expert annotation (black) and pipeline results (brown). Figure 11.4 A shows an exemplary output of the pipeline when applied to a clinical measurement with stimulation from the circular catheter (PV) electrodes 13-14. The reconstructed propagation

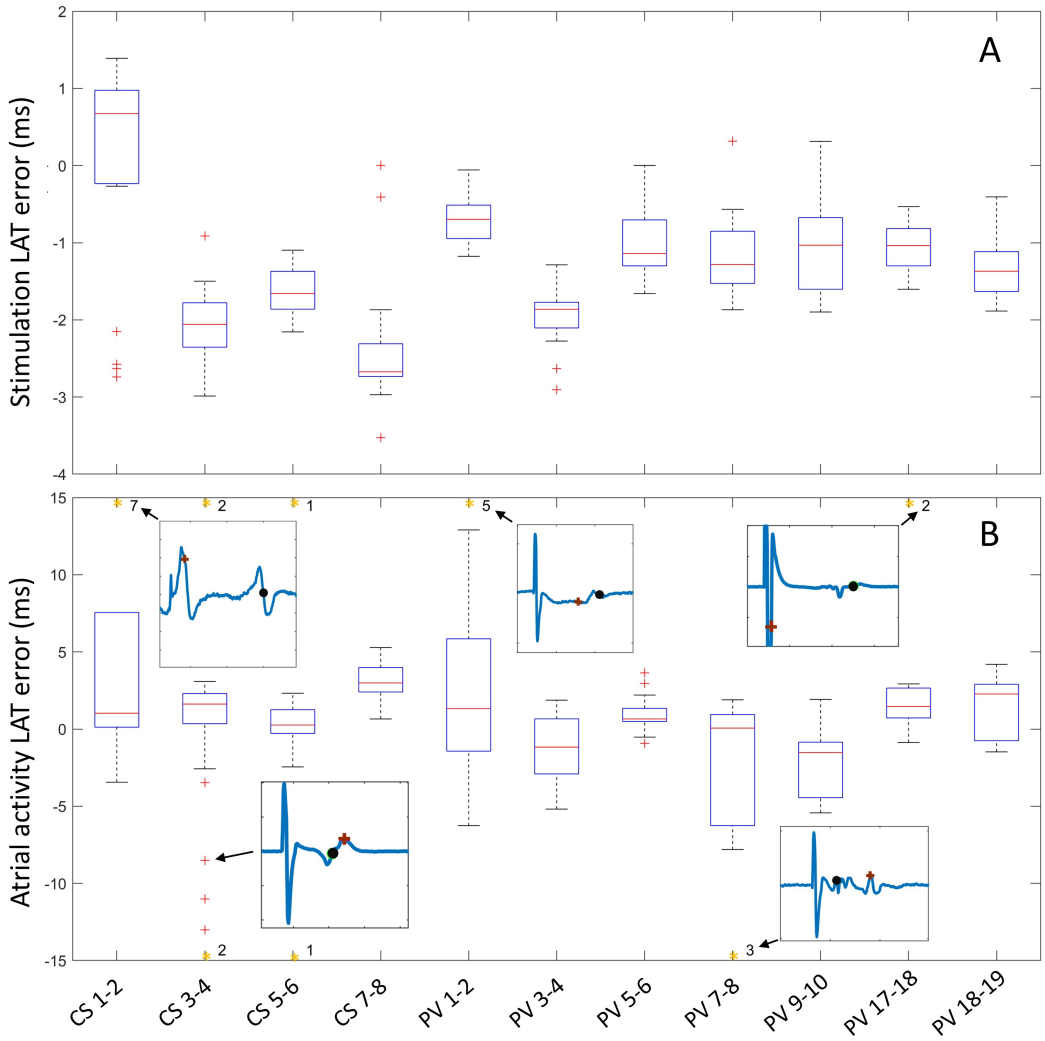

Figure 11.3: LAT error of stimulation signal (A) and atrial activity (B) calculated by subtraction of pipeline LAT from expert annotation. The number of outliers beyond the y-axis limit (orange asterisk) is shown, along with an exemplary signal showing the differences between the expert annotation (black) and the pipeline annotation (brown). Figure and caption adapted from [100] under the Creative Commons CC BY Attribution 4.0 International License.

speed restitution curves in the spatially distant CS catheter (Figure 11.4 A top) showed a smooth morphology. The propagation speed asymptote ranged from 407 to 510 mm/s. In the circular catheter (Figure 11.4 A bottom), the channels neighboring the stimulation channel (11-12, 15-16) are removed by default by the pipeline. For all other channels, the stimulus directly transitioned into the atrial activity (Figure 11.4 A right). The atrial activity, however, remained distinguishable from the stimulation. The automated removal of the stimulation signal delivered plausible results for clinical measurements inside the stimulating catheter, as shown by the morphology of the restitution curves. A jump can be seen in PV 7-9 (green curve) at 300 ms. This is due to prolonged atrial activity (green box), where

at one instance, the peak nearer to the removed stimulation (gray bar) is detected at the next point the further peak is detected, creating a jump in propagation speed. The clinical voltage map (Figure 11.4 B left) with the highlighted catheter position indicated that the measurement took place in a region of normal voltage. Most amplitude restitution curves have an asymptote of approximately 1 mV, thus above the prevalent clinical threshold for low voltage of 0.5 mV. The curve PV 7-8 has an asymptote around 0.5 mV. PV 1-2 is the only curve seemingly without restitution morphology. Since the absolute amplitude of the whole channel measurement was consistently lower than all other channels, the morphology is most likely a result from insufficient atrial wall contact due to rigid catheter design. The amplitude measured by the circular catheter follows a restitution pattern with the largest decay between 350 and 330 ms S2 coupling interval (Figure 11.4 B right). This is in accordance with the drop of propagation speed at 350 ms S2 (Figure 11.4 A). The amplitudes for shorter S2 intervals varied strongly for 2 of the 6 channels.

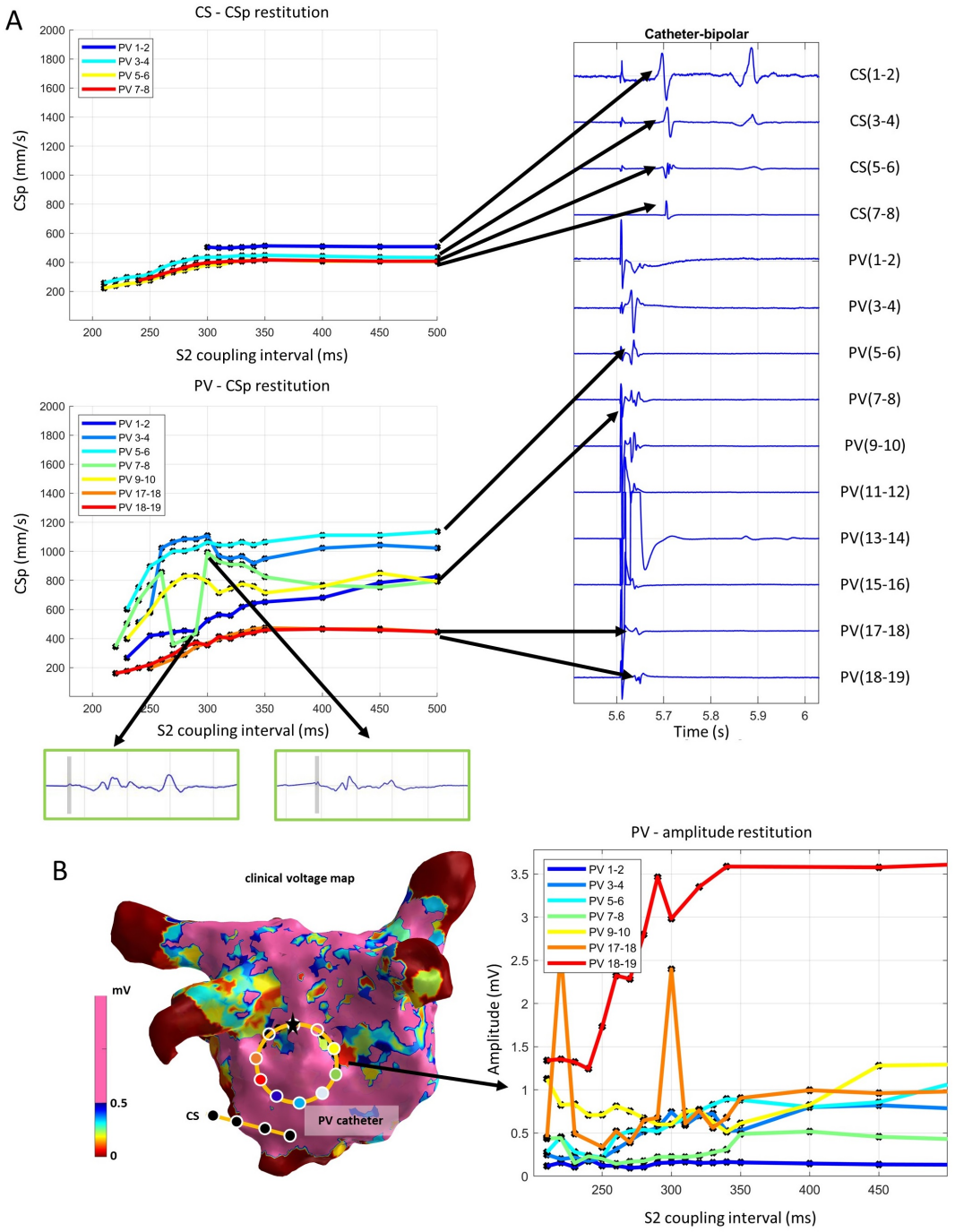

Figure 11.4: A: Exemplary output of the pipeline applied on a clinical measurement with stimulation from the circular catheter electrodes 13-14. Propagation speed restitution curves of each channel of the CS and the circular (PV) catheter (left) and the first corresponding S2 signal segment (right). Green boxes show excerpts of atrial activity signal after removal of the stimulation artifact (time segment marked in grey). B: Voltage map (left) with circular catheter (PV) with white circles showing bipolar channel positions. Reconstructed amplitudes of circular catheter (stimulation from electrodes 13-14) with black dots representing data points (right). Lines are linearly interpolated in between. Line colors correspond to the color of the dot of the channel position on the voltage map. Figure and caption adapted from [100] under the Creative Commons CC BY Attribution 4.0 International License.

Chapter 12

Discussion

12.1 Pipeline Methods and Synthetic Evaluation

This study presents and evaluates a fully automated signal segmentation pipeline for the S1S2 protocol. The pipeline has 3 guiding requirements: i) No a-priori knowledge of the measurement should be used, and all evaluations should be derived purely from the input. ii) All steps should be fully automated and yield precise results while remaining robust under noise conditions. iii) It should handle the evaluation of the atrial activity in proximity to the stimulation artifact. The main result of this work is the openly available CVAR-Seg pipeline [100], which can accurately segment an S1S2 protocol and create amplitude and propagation speed curves under a wide range of noise conditions. The pipeline fills the gap of automatically evaluating restitution protocol information independently from mapping system, stimulus generator, catheters, and stimulation parameter setups. To the best of our knowledge, there is no other complete pipeline for evaluation of the S1S2 protocol or closely related stimulation protocols.

An LAT detection pipeline was proposed by [119] where a clean reference channel is used for rough pre segmentation of activity, then ventricular far field is blanked, the signal is rectified, and the center of mass is calculated. We use the same fundamental idea by first identifying the stimulation peaks and using them as reference points to create time windows in which to assess the atrial activities. For our pipeline, regular far field blanking is not possible. Due to the changed pacing intervals, atrial activities can overlap partially with the ventricular far field segments and excessive blanking might erase large parts of the atrial activity in some pacing trains. The approach proposed by [119] focuses solely on signal traces without stimulation artifacts and, in part, relies on unipolar signals which are not always available. Therefore, alternative methods were sought.

[37] reviewed the most common methods for automated LAT annotation: morphological approaches, NLEO, time-delay cross-correlation, wavelet decomposition, deconvolution, template methods, and gradient methods. We used the two best performing signal segmentation algorithms, namely the wavelet and the NLEO method, as proposed by [109]. The wavelet method relies on a mother wavelet which in turn necessitates some estimation of the

signal. This can only be done for the stimulation signals. Using the bior1.5 as proposed by [109], we only assume a steep flank in the stimulation signal, which is always present in any stimulation and therefore does not violate our requirement of not using a-priori information. For atrial activities, no assumptions were made. Therefore, we used the wavelet to detect the stimulations and the NLEO method for the atrial activity. To determine non-detected activities, we used an NLEO threshold proposed by [109]. The choice of threshold is a tradeoff between detecting more peaks with potentially increasing errors versus detecting less but more trustworthy peaks. We see a potential for improvement here by using an adaptive NLEO threshold based on estimation of the SNR of the signal as proposed by [119].
[120] proposed to detect signal components in different complex fractionated atrial electrograms (CFAE) classes based on the wavelet transform. This could be used to extend this pipeline to incorporate an evaluation of fibrillatory events and annotate atrial activities. An alternative approach could be to use the recently published openEP project [121], which enables EP data parsing and analysis.
Other works use manual [110] or semi-automatic pipelines [122, 123] to evaluate restitution curve morphology. The latter might be more proficient for an evaluation on the atrial surface mesh. The CVAR-Seg pipeline rather focuses on evaluating singular electrodes, and the evaluation would have to be projected on the 3D atria in a subsequent step.
CVAR-Seg works in a fully automated manner, can be used on large patient cohorts, and demonstrated applicability on clinical recordings. This was shown by evaluating 37 different SNR noise scenarios (55,278 synthetic signals) and an exemplary clinical case without manual interaction. While SNR of clinical signals can, in general, be estimated by comparing filtered versions of the signal, reliable estimates are hampered by different filter settings, clinical setups, and measurement quality. Our arbitrarily picked clinical measurement corresponded to a synthetic case of 40 dB and is assumed to be a good representation of a mean clinical noise level. The range was expanded by looking for the noisiest possible signals in literature. Visual comparison with literature [7, 124, 125] and available clinical measurements suggest a clinical noise level between 40 dB and 10 dB which was included in the synthetic setup (Figure 10.4 C).
Extra beats were accounted for in the detection of the pacing trains and during the evaluation of the single stimulus and following atrial activity time segments. In most cases the stimulation will create the depolarization wave and the tissue will not be activated by extra beats due to the ERP. Should an extra beat occur in the time window of evaluation it cannot be morphologically distinguished from a stimulation induced depolarization wave and must therefore be excluded during postprocessing. We suggest excluding points above threefold standard deviation of the curve. The proposed pipeline gives accurate results for amplitude, LAT, and consequently propagation speed (Figure 11.1) down to SNR values of 0 dB. If some misdetection of atrial activities is acceptable, the signal quality can even deteriorate to -4 dB (Figure 11.2). LAT evaluation errors remain mostly below a single sample and amplitude errors in the range of 0.06 mV. Down to 1 dB, the relative amplitude error is below 10 %, which is deemed acceptable since other processing steps influence the amplitude more profoundly, e.g., density of sampling points, voltage map interpolation, and

method of amplitude calculation in each EP system.
For SNR beyond the clinical range of 10 dB, the errors in amplitude and LAT increase markedly while, at the same time, the number of non-detected LATs rises. The LAT errors translate to larger errors in propagation speed. However, the median LAT value remains nearly constant for all SNR. This means we still obtain mostly correct values and several extreme outliers stemming from large noise peaks in proximity to the atrial activity in some channels. Signal processing solutions would most likely also impact atrial activity morphology. Another way these outliers could be mitigated is by using one of the fitting approaches incorporating all measured values [26, 115]. The general underestimation of amplitude for SNR below 10 dB is due to high noise amplitudes causing the pipeline to mistake noise peaks for atrial activity. As noise grows larger in amplitude, the error trends towards more negative values due to the algorithm increasingly overestimating the amplitude. The increase in spread is then due to different noise realizations in the different channels. For extreme SNR cases below -4 dB, we observe noise amplitudes of equal magnitude as the atrial activities with occasionally noise peaks higher than atrial activity amplitude. Evaluation of such measurements necessitating adjustments of the default filter settings of the pipeline.

12.2 Outlook for Clinical Data

Comparison of expert annotation LATs against the pipeline produced LATs revealed good accordance for the stimulation signal. Most LATs from the circular catheter channel median values were merely deviating by -1 ms from the expert annotation. The larger shift in median (-2 ms) present in the CS catheter channels. The large variability can be explained by the fact that during stimulation in the spatially distant circular catheter the stimulation presents as far field in the CS catheter channels with minimal amplitude and slope due to the bipolar arrangement, and signal noise around the stimulation artifact incurred small deviances in the non-linear energy operator peak.
The median atrial activity error with an error of 0 ms is a promising result. Interquartile ranges of most channels resulted in minimal, but acceptable shifts in LAT since all LATs remained within the atrial activity. The different annotation styles (maximum and minimum peaks or maximum slope) between experts explained the larger interquartile ranges of CS 1-2, PV 1-2, and PV 7-8. The extreme outliers reveal that deviations occurred due to several reasons:

i) Different annotation between pipeline and manual evaluation.
ii) Ventricular far field overlap with the stimulation in the CS catheter. For time windows that contain a stimulation, no far field removal was performed since, in many cases, the bipolar signal would reduce the ventricular far field enough for evaluation, and exclusion of all stimuli overlapping with ventricular far field could result in deletion of too many time segments.
iii) Incomplete removal of stimulation artefact leading to premature LATs.

iv) Extended atrial activities. These cases accounted for 7 % of all annotations, leading to the conclusion that the pipeline yields adequate results.

Outliers produced by extreme cases can be filtered out in a postprocessing step since they will be deviating from the restitution morphology of all other points.
The segmented restitution curves from the paroxysmal AF patient showed the following properties: All catheter channels show different asymptotes of propagation speed curves, which is expected due to fiber orientation-induced CV anisotropy. Using the minimum and the maximum propagation speed curves as a first estimate, the resulting anisotropy ratio of 3.4 is in accordance with experimental reports ranging up to anisotropy levels of 5 and above [19, 126, 127]. With a mean asymptote of 692 mm/s, our propagation speed lies within the reported ranges values for experimental data ranging from 100 mm/s [126] to 1800 mm/s [19] and is close to the value of 600 mm/s reported in [124]. Global CV for AF patients has been reported in a range of (511 ± 110) mm/s [40] in line with our asymptote measurement of 439 mm/s between the circular catheter on the inferior posterior wall and the CS catheter. Recent works extend CV estimation by including LAT measurement uncertainty [128, 129] which could potentially be incorporated into CVAR-Seg in the future. [130] extend the concept of scalar CV by estimating atrial fiber direction along the endocardial surface. Using CVAR-Seg, this method could be applied to restitution data to see if preferential conduction directions stay consistent when derived from CVs acquired at different pacing rates.
Local amplitude restitution ranges from approximately 1 mV to below the clinically used low-voltage threshold of 0.5 mV [21] for each spatially stable measurement. Thus, the amplitude decrease stems from restitution behavior of the tissue, not catheter roving. This also demonstrates that the single threshold used for voltage guided ablation might not be optimal for all patients since they present with different and highly variable heart rates due to AF [131].
The clinical voltage map shows that our measurement was done in a region with normal voltage associated with healthy tissue. We observed a clear exponential morphology for both amplitude and propagation speed, which is in line with the exponential restitution curve morphology of healthy tissue reported in literature [24, 26].

12.3 Limitations

In the scope of this work, not all signal morphology varieties that can arise clinically due to different hardware (e.g., electrode dimensions, catheter spacing) and software (filtering values, filtering algorithms) setups could be covered in silico. Therefore, we considered the most important cases including restitution of amplitude and propagation speed, overlap of atrial activity with stimulation, and clinical noise variation. Since a guiding principle was to not use any a-priori information, the pipeline is not limited to the shown synthetic signals and does not exclude signals that deviate from our setup.
For pacing train detection, the k-means algorithm requires markedly longer intervals between

pacing trains than the S1 cycle length. For values lower than 1.2 times the S1 cycle length the k means clustering can yield unreliable results. A value of twice the S1 cycle length yielded correct clusters for the clean signal setup as well as a setup with noise and extra beats. For suppression of the stimulation signal, our matched filtering approach gives accurate results provided the depolarization slope of the atrial signal is not more than 50 % covered by the stimulation. This creates a temporal lower boundary on detectable atrial activities, which is in large parts due to the linear smoothing of the first part of the stimulation time segment. This smoothing step is necessary to erase stimulation parts that cannot be erased by the subtraction of the template and becomes increasingly important when dealing with noisy signals and cannot be removed. In the future, other methods could improve detection of the atrial activities and dispense with the smoothing step, thereby lowering the temporal detection threshold further. One such approach could be the Changepoint method [132], which might achieve better detection results for fractionated signals. Additionally, other signal segmentation methods using statistical or machine learning approaches could prove beneficial for a better atrial activity segmentation and further improve robustness and lower the number of misdetected LATs for high noise cases.

12.4 Conclusion

In this work, we provide the noise-robust signal segmentation pipeline CVAR-Seg for the widely used S1S2 stimulation protocol. It enables automatic computation of amplitude and propagation speed restitution curves from clinical data. The pipeline is built for S1S2 stimulation protocol measurements. However, the methodology could easily be transferred and adapted to any other stimulation protocols used in EP studies since the main problem of proximity between stimulus signal and atrial activity remains the same. At the same time the pipeline components are modular and can be easily replaced by alternative methods according to the user's needs. This tool allows for a fast and precise evaluation of large datasets and eliminates the need to analyze each dataset manually. The proposed CVAR-Seg pipeline could serve as a basis for a standardized way of evaluation fostering reproducibility and comparability of future restitution studies.

PART IV

ESTIMATION OF CV, ANISOTROPY RATIO AND FIBER ORIENTATION

Chapter 13

Motivation

Atrial fibrillation (AF) mechanisms are caused and affected by structural, electrophysiological, and anatomical conditions [19]. On the tissue level pathologies stemming from these three sources are reflected as changes in depolarization wave speed, e.g., conduction velocity (CV), and propagation path. While the specific coupling between CV and the underlying pathologies remains unknown, a lower CV has been attributed to pathological tissue [15, 16]. For an optimal treatment of AF extensive knowledge of underlying substrate characteristics such as CV, fiber direction and anisotropy would be beneficial, since excitation wave spread and speed (local activation time (LAT) and CV maps) are the main diagnostic tools available for clinicians and are therefore target of continuous improvement [17]. The maps are used to derive the source and propagation path of the arrhythmia and individually tailor the ablation procedure to maximize outcome chance of AF freedom [20].

The complex interplay of CV, fiber direction and anisotropy necessitates evaluating all parameters simultaneously, making their quantification an ongoing challenge in general and especially so in-vitro [16, 37, 59, 115, 124, 130].

There exist several methods to detect a singular CV value such as the cosine fit [59] or the adapted cosine fit [18]. Both methods yield the wavefront propagation direction, which is not necessarily the fiber orientation and therefore does not incorporate anisotropy. Additionally the cosine fit method has the drawback of being dependent on catheter geometry. Other approaches include the anisotropy factor by fitting radial basis functions or polynomial planes to the space-time coordinates of the LAT map on the atrial geometry [133–135] or use iterative local fitting of ellipses to regions of interest [19, 130]. The most advanced approach additionally accounts for the atrial topology and errors in measurement using Gaussian process manifold interpolation [128]. A resulting CV map can be processed into a fiber atlas detailing the anatomically prescribed preferential propagation direction [130]. These methods often necessitate a complete atrial 3D geometry with multiple LAT maps containing a sufficient amount of acquisitioned data points. The time intensive sequential acquisition of multiple LAT maps is undesirable, prolonging the medical procedure. Furthermore, a complex and time-intensive post-processing pipeline is necessary for the approach.

All approaches above make use of LATs recorded using one or several distant excitation sources, such as the coronary sinus (CS) catheter or sinuatrial node in the right atrium,

making them global CV estimation methods.
Up to date the only method conceptualized to derive CV, the anisotropy ratio, and the fiber angle simultaneously for local measurements is the Blauer method, relying on multiple consecutive excitations from different electrodes within a circular catheter and a subsequent elliptic fit over directional CV vectors [115]. The disadvantage is that the method is dependent on catheter shape and requires multiple measurements with a fixed catheter location as well as assuming the electrodes to be point sources ignoring the extensive initial area created by extracellular stimulation [136]. Measurements with a permanently fixed catheter prove difficult in a clinical setting since hemodynamics near the pulmonary veins and contractions of the atria can create enough force to displace the catheter throughout consecutive measurements.
In order to address these issues, in this work, an inverse double ellipse estimation method to obtain CV, anisotropy ratio and fiber orientation in real-time from any catheter shape is proposed. The method includes the initially activated area under the stimulation electrode after extracellular stimulation and can be used for single as well as multiple stimulation measurements. Additionally, it is a local measurement technique and does not rely on obtaining a complete LAT map. The method enables estimation of parameters using sparse datasets and perturbed LAT measurements. In future this method opens up a new acquisition possibility, where the locally stimulating catheter can be roved around the atrial wall while instantaneously creating local CV, anisotropy, and fiber orientation maps in real-time. This can increase patient pathology insight, save time by reducing the need for multiple stimulations and not requiring a whole LAT map to be created. Finally, the patient values gained with this method could be used to create personalized models (digital twin) of patients to test treatment possibilities preemptively and help increase the understanding of mechanisms perpetuating and upholding AF.
The following chapters discuss the mathematical background of the method and the development of a realistic high-resolution clinical in-silico model. To evaluate the estimation errors of this method, both in-silico derived LAT measurements and synthetically perturbed LAT measurements were compared with Blauer's method from the literature. Both methods are then evaluated on clinical data and compared to each other.

Chapter 14

Methods

In the following the Blauer method, which is the state-of-the-art method is explained followed by the inverse double ellipse method, which is the new method proposed in this work. The methods follow a three-part naming scheme. Firstly, the abbreviation of the model in question, where **B** stands for the Blauer ellipse and '**PX**' stands for the double ellipse method with **X** free parameters. This is followed by the number of measurements '**MY**' where **Y** is the number of measurements. The number of electrodes opposite of the stimulation site **Z** inputted to the model is abbreviated as '**OZ**', leading to descriptors such as B-M3-O2 or P4-M3-O8.

14.1 State of the Art: Ellipse Fit

The Blauer ellipse fit requires multiple subsequent stimulations from different sides of a circular catheter [115]. CV is calculated along the direct path of stimulation to measurement location resulting in multiple CV vectors that are then centered at a mutual starting point (Figure 14.1). After normalization, an ellipse is fitted to the vectors and the long axis, short axis and tilt of the ellipse yields longitudinal and transversal CV along with the fiber orientation respectively [115].
The Blauer Method was intended to be performed with consecutive stimulation from all electrodes of the catheter (e.g., B-M10-08). In clinical practice this is a drawback due to time constraints. The working hypothesis of this study was that with 3 measurements from approximately 120° spaced stimulation sites a similar result can be achieved while reducing measurement time, therefore in the following we redefine the standard Blauer model to be B-M3-O8.
This Blauer method can be improved by using the two electrodes opposite (with the most distance) the stimulation electrodes (B-M3-O2), since electrodes near the stimulation area will be prone to stimulation artifacts. Additionally, in the electrodes with maximal distance to the stimulation site the error introduced by the initial area via the stimulation is minimized by the proportionally smaller impact of the initial area compared to the whole distance.
In the original proposed version, the Blauer method is solved as an unconstrained least square

problem. Imposing physiological constraints can further improve the obtained results. To allow a fair comparison of the methods, the same physiological limits were applied to both the Blauer ellipse and inverse double ellipse parameters in the implementation used for this work (Chapter 14.2).

14.2 Inverse Double Ellipse Approach

To analyze all LATs across a set of catheter electrodes irrespective of electrode arrangement a quantitative analytical double ellipses fit method was developed. The method includes the initial stimulation pattern observed around electrodes after extracellular biphasic stimulation (Figure 2.9) in in-silico experiments (Figure 15.1) [136].
Between the onset of the stimulation and the switching of the biphasic stimulation pulse (phase 1), an initial area is formed and an elliptical outward propagation from primary activated electrode (E1) begins. After the switch (phase 2) a second initial area forms at secondary activated electrode (E2) with a time delay dt_i (the subscript i denotes the electrode) compared to E1. Both initial area's formations were approximated as ellipses that were determined by the substrate characteristics and were, therefore, coupled via the underlying fiber orientation, conduction velocity (CV) and anisotropy ratio k. To describe a single ellipse, the radial representation was chosen (Chapter 4.1). After the stimulation forms the initially activated area, CV was assumed to be constant between initial area and measurement

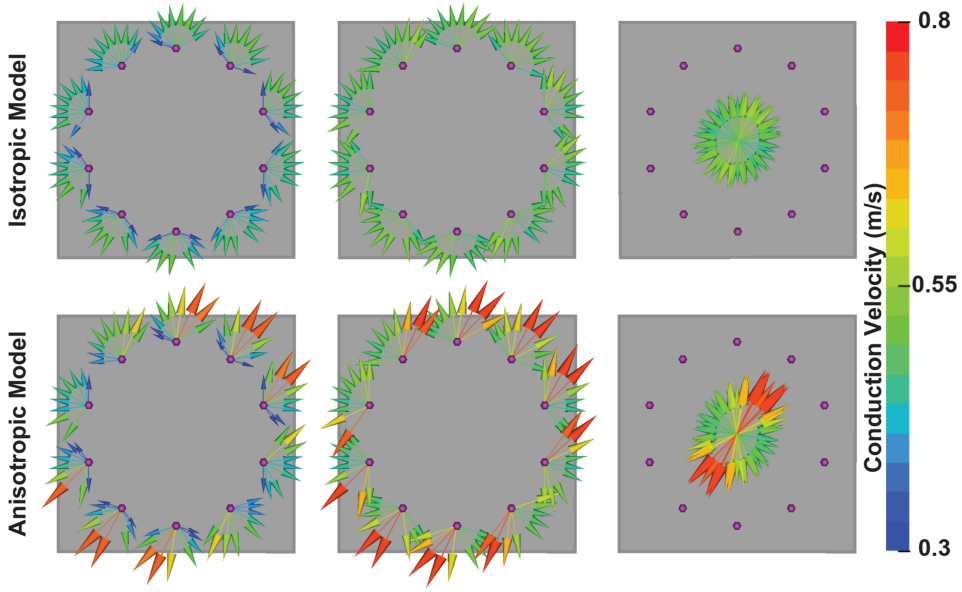

Figure 14.1: Characterization of local conduction properties with a loop catheter. Left Column – Vectors (colored arrows) at recording electrodes (purple spheres) point away from pacing site. Length and color correspond to conduction velocity (CV). Center Column – CV vectors normalized to fixed distance from pacing site. Right Column – Compact representation of regional conduction. Figure and caption adapted from [115] under the Creative Commons CC BY Attribution 4.0 International License.

electrode. The ellipse axis parameters were substituted using a linear propagation model that accounts for temporal ellipse growth according to Table 14.1. a_{0i} and b_{0i} are the long

Table 14.1: Different substitutions of the ellipses long (a) and short axis (b) result in models with various degrees of freedom. The model name is chosen as PX, where X corresponds to the number of parameters to be estimated. The two electrodes (rows) involved during extracellular stimulation each produce an elliptically propagating depolarization wave under the respective electrode, denoted by the subscript e1 and e2. The P4 model assumes both initial areas to be equivalent and dispenses with the distinction between electrodes.

ellipse axis	P7 model	P6 & P5 model	P4 model
a_{e1} (long axis)	$a_{01} + a_{CV} \cdot (t + dt_1)$	$a_{01} + a_{CV} \cdot (t + dt_1)$	$a_0 + a_{CV} \cdot (t + dt_1)$
b_{e1} (short axis)	$b_{01} + \frac{a_{CV}}{k} \cdot (t + dt_1)$	$b_{01} + \frac{a_{CV}}{k} \cdot (t + dt_1)$	$\frac{a_0}{k} + \frac{a_{CV}}{k} \cdot (t + dt_1)$
a_{e2} (long axis)	$a_{02} + a_{CV} \cdot (t + dt_2)$	$\frac{a_{01}}{m} + a_{CV} \cdot (t + dt_2)$	$a_0 + a_{CV} \cdot (t + dt_2)$
b_{e2} (short axis)	$b_{02} + \frac{a_{CV}}{k} \cdot (t + dt_2)$	$\frac{b_{01}}{m} + \frac{a_{CV}}{k} \cdot (t + dt_2)$	$\frac{a_0}{k} + \frac{a_{CV}}{k} \cdot (t + dt_2)$

and short axis of the ellipse at an electrode i, describing the initially activated area under the electrode. a_{CV} describes the longitudinal CV. The division of a_{CV} by the anisotropy factor k yields transversal CV.

Executing the substitution for both ellipses coupled both ellipses with the longitudinal CV, fiber direction and anisotropy factor while leaving the initial area parameters to be estimated individually. This defined the most generalized double ellipse representation with 7 free parameters (P7). Using a commercially available 10 electrode catheter, two electrodes are used for stimulation leaving 8 remaining electrodes for measuring local activation time (LAT). Due to anatomical impediments and dynamic motion of the atria not all catheter electrodes necessarily possess and retain tissue contact throughout the measurement. Additionally, a sharp decrease in atrial activity may occur for electrodes in proximity to sites of structural remodeling [52, 137]. Both factors lead to a decline or absence of atrial activity and subsequently the number of LATs.

To adapt the model to function with sparse LAT datasets, different couplings of the initial axis of the two ellipse parameters were introduced while keeping the three parameters CV, anisotropy ratio and fiber direction coupled for both ellipses throughout all further models. The initial area follows the electrical field generated between the two stimulating electrodes. For the second ellipse the induced extracellular voltage is decreased compared to the first electrode and the hyperpolarized substrate must be repolarized, leading to a smaller initial area at the second electrode location. A 6-parameter model was derived (P6), which beside incorporating the three basic parameters CV, anisotropy ratio, and fiber orientation, determined the long and short axis of the initial area and then coupled the ellipses of the second stimulation with a factor m to the ellipses of the first stimulation.

In pursuit of further simplification, a P5 model was derived where m was set as a constant

factor of 2.12 derived from 625 simulations (Chapter 14.5) considering varying fiber orientation, anisotropy, CV, and stimulation strength.
The P4 model was derived as the model with the minimum number of necessary parameters to allow solving of sparse datasets without introducing factors originating from additional external measurements. The P4 model was attained by imposing the simplification that the activation of the initial area adheres to the anisotropy principles, which allows substitution of b_0 (Chapter 14.1). Additionally, for this model it is assumed that the factor m coupling the initial areas of both electrodes is close to 1, meaning the initial area underneath both electrodes was approximated as equal. This approximation allowed for the use of a single set of initial area ellipse parameters a_0 and b_0 for both electrode ellipses, creating a reduced model with 4 free parameters.
From a theoretical point of view the P7 and P6 model are the most promising models with regards to their close depiction of the underlying physiological process. However, initial studies showed that the P7 and the P6 model had too many free uncoupled parameters making the solution highly dependent on the starting value chosen for the solver under the assumption of 8 perturbed measurement values. Since this work is focused on a robust and accurate method to gain all substrate parameters under clinical conditions the P7 and P6 model were not further pursued but will be included in the discussion (Chapter 16).
All model equations derived here were solved using MATLAB [138] by minimizing the fit residuals (sum of squared deviations) between forward model and measured LAT at each measurement point. The general equation (Chapter 4.2) formulation has to be adapted for the combined fitting process of two ellipses. The ellipse angles (fiber orientation) for both ellipses were equal to ensure parallel orientation. Using this mathematical constraint, the ellipses were solved using the following minimization:

$$\min_x \parallel f(x) \parallel_2^2 = \min_x \left(\sum_{i=1}^{n} \min \left[\left(\left| f_i^{model} - f_i^{measured} \right| \right)_{e1}, \left(\left| f_i^{model} - f_i^{measured} \right| \right)_{e2} \right] \right). \tag{14.1}$$

f is the functional of the forward model as well as the data of the measured values i for each electrode e_1 and e_2. Additionally, physiological constraints where required of all variables. The longitudinal CV was fitted in a range of 100 mm/s to 2000 mm/s, encompassing ranges found in literature (300 mm/s - 1800 mm/s) ([19]), (450 mm/s - 1250 mm/s) [139]. The anisotropy ratio was set between a factor of 1 and 10 enabling a greater solution range than suggested literature ranges from 1 to 3 [19]. Due to its directional independence fiber orientation was constrained between 0° and 180°. All initial long and short axis parameters a_{0i} and b_{0i} had a lower bound of 1 mm, expecting the initial area to be at least as large as the stimulating electrode with an edge length of 1 mm, which is currently one of the smallest electrodes available. The upper bound on a_{0i} and b_{0i} was set to 6 mm, resulting from a preliminary study incorporating 625 (Chapter 14.5) stimulation simulations considering varying fiber orientation, anisotropy, CV, and stimulation strength.
The number of free parameters as denoted by the naming scheme is based on single stimulation measurements. For multiple measurements the three parameters CV, anisotropy factor and fiber direction remain universally equal across all measurements, the initial area, however,

varies between each measurement depending on substrate characteristics and hardware setup such as fiber orientation and stimulation strength. Therefore, the number of free parameters per measurement (M) increases based on the initial area a_0 and b_0 as shown in Table 14.2.

Table 14.2: Adaptation of the double ellipse models for multiple measurement (M) data input. Function to calculate the number of free parameters dependent on absolute number of measurements ($\mathsf{f}_\omega(\mathsf{M})$) and number of free parameters (P). Example calculated with 3 measurements $\mathsf{f}_\omega(3)$

Model	$\mathsf{f}_\omega(\mathsf{M})$	$\mathsf{f}_\omega(3)$
P4	$3+(1\cdot\mathsf{M})$	6
P5	$3+(2\cdot\mathsf{M})$	9
P6	$3+(3\cdot\mathsf{M})$	12
P7	$3+(4\cdot\mathsf{M})$	15

14.3 In-silico Model of a Realistic Fibrotic Tissue Patch

The synthetic clinical replica consists of three main parts: tissue (T), bath (B) and catheter consisting of electrodes (E) and insulator (I) (Figure 14.2). The components are combined to a simulation domain (Ω) according to

$$\Omega = T_0 \subset T_i \subset F \subset E_i \subset I \subset B. \tag{14.2}$$

The tissue region had dimensions of $30\times30\times3\,\mathrm{mm}^3$ and is separated into a tissue region outside T_0 (dark blue) and inside T_i (light blue) and a network of collagen deposits F (white). In direct contact with the tissue lies the catheter with a diameter of 20 mm and an inner tube diameter (also electrode diameter) of 1 mm. The electrodes of 1 mm depth are spaced using an edge to edge spacing of 5-5-5 mm replicating a NavX Advisor SE 10 pole catheter. Tissue and catheter are enclosed by a bath with 0.3 cm distance to the tissue edges and 0.5 cm distance to the top of the catheter. The unstructured tetrahedral mesh of tissue and catheter has a mean edge length of 0.16 mm and the mean edge length of the bath is 0.4 mm. Cardiac myocytes are represented by the Courtemanche model [72] in T_i and T_o. Conductivities between myocytes were tuned to yield desired CV values based on a 1D bidomain strand simulation. Conductivity of insulator nodes were set to $\sigma_I = 10\times10^{-12}\,\mathrm{S/m}$ and electrode nodes to $\sigma_{E_i} = 10\times10^{12}\,\mathrm{S/m}$. In the control setup the conductivities of T_i, T_o and F were equalized to create homogeneous tissue. Simulations were set up and solved using openCARP [75] by prescribing extracellular biphasic pulse stimulation to the electrode nodes. A single patch was independently stimulated from 3 different electrode pairs (1-2, 5-6, 8-9). All parameter variations of the model are listed in Table 14.3.

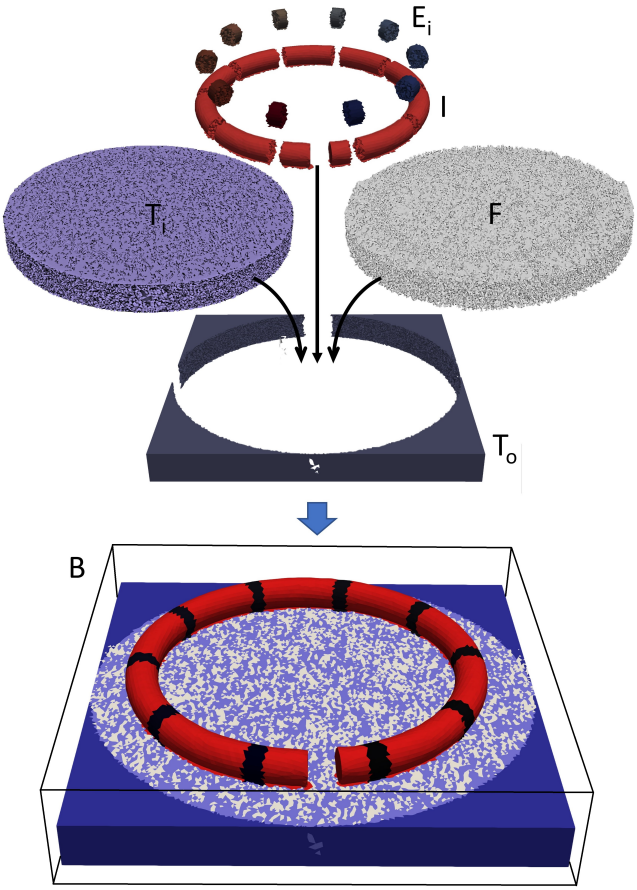

Figure 14.2: Simulation setup consisting of the healthy surrounding tissue T_o, collagen deposit (F), cellular medium in contact with collagen (T_i) and the circular catheter consisting of insulator (I) connecting 10 electrodes E_i.

Table 14.3: Variation of tissue parameters and their ranges within the standard simulation setup.

name	symbol	unit	start:step:end values
CV longitudinal	CV_l	$\mathrm{mm/s}$	300 : 300 : 900
CV anisotropy	k		1.5 : 1 : 2.5
fiber orientation	θ	°	0 : 15 : 90

14.4 Determining Reference Values from Simulation Data

Assuming that there is a single wavefront with planar propagation, the CV of a depolarization wave in cardiac tissue can be modeled using a simple tissue strand. CV is determined iteratively in the strand model, and the resulting conductivity values are applied to the more complex simulation setups. In general, the CV values and consequently the anisotropy factor in complex setups deviate from the strand simulation due to the occurrence of multiple wavefronts leading to source-sink interactions and the non-planar propagation of the waves. To quantify the CVs present in the respective simulations, the openCARP tool glGradient was used to identify the magnitude of the 3D CV vector of each mesh node. A probability density function of all CVs acquired from all nodes was created and the two highest peaks marked the closest estimation of the mean longitudinal (higher) and mean transversal (lower) CV. Figure 14.3 depicts two separate simulations, with an initially desired anisotropy of 1.5 (blue) and 2.5 (red) (Table 14.3). Running this evaluation revealed the resulting intrinsic anisotropy ratio values of 1.3 and 1.9. CV is affected as well, as seen with the longitudinal CV of the low anisotropy case (blue) with 333 mm/s instead of 300 mm/s and the high anisotropy case (red) retaining 822 mm/s instead of 900 mm/s (Figure 14.3). Performing the evaluation for all simulation cases exhibits two distinct peaks of CV, yielding a mean deviation of 5 mm/s for the desired 300 mm/s case, −42 mm/s for the desired 600 mm/s case and −91 mm/s for the 900 mm/s case. In the following, the values were corrected with the mean values, however the naming will remain 300, 600 and 900 since there is no single true value, but a range of values belonging to the ground truth of 300, 600 and 900 mm/s. For the anisotropy this evaluation was performed across all simulations as well, yielding a

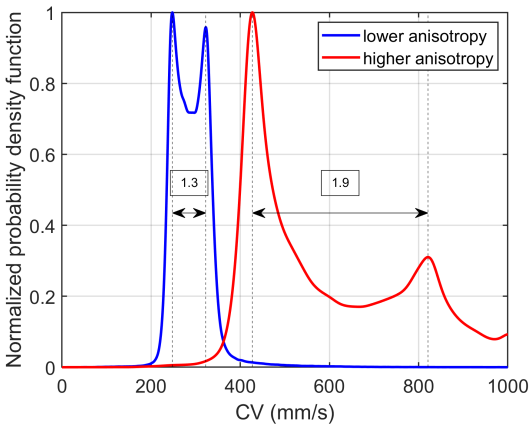

Figure 14.3: Normalized probability density function of CV uncovering ground truth CV and anisotropy values from simulation data using a gradient based estimation method. An exemplary lower anisotropy simulation case (blue) yielded an anisotropy of 1.3 compared to the theoretically expected value of 1.5. A high anisotropy simulation (red) produced 1.9 instead of the theoretically expected 2.5.

median value of 1.3 for the desired 1.5 and 1.8 for the desired 2.5 value. Since the anisotropy ratios differ heavily from their respective ground truths, the naming will be changed to the mean value throughout the chapter. The implications of these differences will be discussed in chapter 16.

14.5 Determining Initial Area From Simulation Data

The initial area ground truth was determined by extending the existing tissue area (Chapter 14.3) to $50\times50\times3\,\mathrm{mm}^3$ with the catheter remaining in its original location at the bottom left corner (Figure 14.4). The spatial extension coupled with a stimulation prescribed from

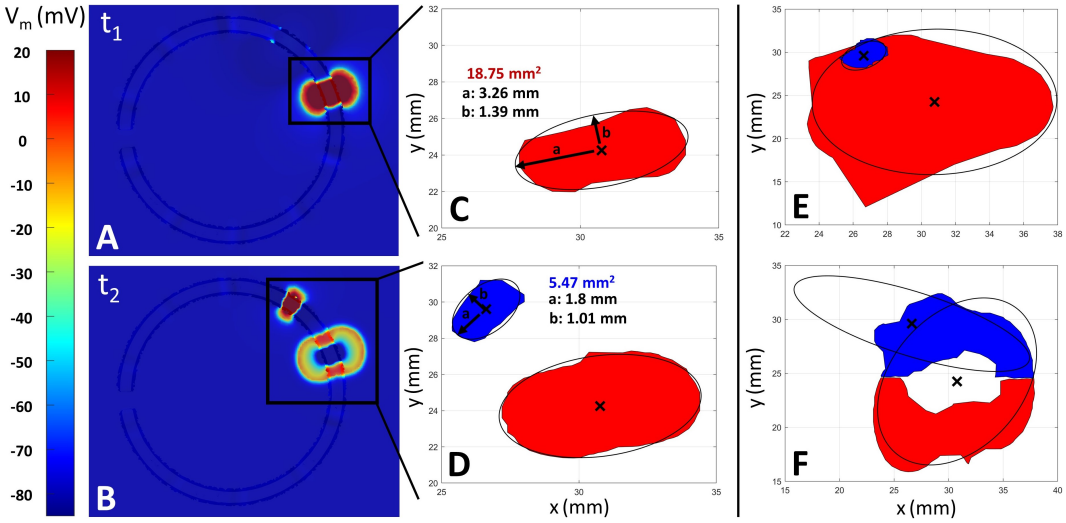

Figure 14.4: Initial area estimation via ellipse fitting. A & B show transmembrane voltage after extracellular stimulation at time points t_1 =2 ms and t_2=4.2 ms. C shows initial activated area (red) extracted from the simulation at time t_1 using a threshold on the transmembrane voltage and subsequent fitting of an ellipse. D shows initial area (blue) of first electrode as well as the continued growth of the first initial area under electrode 1 (red) at time point t_2. The in-silico setup used a CV of $450\,\mathrm{mm/s}$, an anisotropy ratio of 1 and fiber orientation of $0°$ respective to the x-axis. A & B were cropped along the positive x and y axis for visualization purposes but were set up with tissue dimensions of $50\times50\times3\,\mathrm{mm}^3$. E & F show examples where separation of the two forming areas is impossible due to their overlap, resulting in arbitrary fitting results.

electrode pair 6-7 (Figure 14.4 black box, top right), allowed a full capture of activated region for all stimulation cases. 625 simulations covered fiber directions 0° to 90°, anisotropy ratios 1 to 3, longitudinal CVs 200 mm/s to 1200 mm/s in 5 equidistant steps respectively and stimulation strengths 3, 5, 7, 9 and 12 V corresponding to a commercially available clinical stimulus generator UHS 3000 (BIOTRONIK SE & Co. KG, Berlin, Germany).
The initial area of the first electrode is formed by the first phase of the biphasic pulse with

a duration of t_1=2 ms (Chapter 2.10). This simultaneously defines the time point of initial area evaluation under the first electrode after the start of the stimulation (Figure 14.4 B). It is assumed that the area under the curve of both stimulation phases must be equivalent to ensure that the same activation strength was transferred by each electrodes to the tissue. For this purpose, the area under the curve of the first phase (illustrated in Figure 2.9 Δt_{b1}) and the corresponding area under the curve of the second phase were calculated. The time at which the calculated area of the second phase ended was $t2$=4.2 ms. Thus, $t2$ described the time of equivalent tissue activation and was used as the time point describing the formation of the initial area under the second electrode.
The LATs of each mesh node were extracted by applying a threshold of -25 mV to the transmembrane potential at the time points t_1 and t_2. At the first time point, a single initial area is present. The second time point contains all active nodes near the first electrode as well as the initial area forming underneath at the second electrode. An expectation maximization (EM) algorithm was used to allocate nodes to the two electrode centers (Figure 14.4 C-F (black crosses)) and gain separated initial areas [140, 141]. An ellipse was fitted to the boundary points of each classified initial area separately, yielding our ground truth initial area ellipses long and short axis for both time points (Figure 14.4 C-F).
For some cases the initial areas overlapped (Figure 14.4 E & F). This occurs for high stimulation strengths, fiber orientation parallel to the inter electrode axis or interplay of all the above mentioned factors. For the simulation setup (Chapter 14.3) a set of parameters was chosen to avoid such cases.

14.6 Adding Synthetic Error

Clinical measurements are prone to systemic errors due to patient movement, dynamic motion of the atria, hemodynamic pressure, anatomical impediments as well as statistical errors occurring during signal analysis. Additive inclusion of these errors to the in-silico LAT values leads to a more realistic depiction of acquired LATs, approaching clinical measurement resemblance. Therefore, a normal distributed error between a magnitude of 1 ms and 4 ms was assumed based on the clinical expert annotation of atrial active segments (Chapter 11.3). The values were multiplied with a uniformly distributed random sign ($\pm$) and added to the "clean" in-silico LATs.

14.7 Electrode Activation Order

The order of electrode activation depends on the connection of the catheter to the stimulus generator, and the prescribed pulseform (positive or negative amplitude first, followed by the respective counterpart). For most cases this information is accessible by checking the hardware and software setup in the clinic. However, in cases where no hardware information can be acquired, for example during anonymized studies, an easy method to detect the correct

activation order is provided here as well. The double ellipse method was run twice, once with electrodes 1 and 2 in natural order and once in reversed order. Using, for example, the P4 method, this can be achieved by interchange dt_1 and dt_2 between the two runs. The correct electrode activation order can be determined by choosing the order that yields the smallest residual error.
The timing of dt_1 is set up by the clinician in the stimulus generator and can be protocolized. Alternatively, given a sufficient sampling rate the biphasic switch timing can be estimated from the electrogram (EGM) traces containing stimulation artifacts.

14.8 Clinical Data Acquisition & Analysis

Three patient cases were recorded in the clinic at two intra atrial measurement sites (posterior & anterior) per patient. Data were anonymized and exported for further investigation. The study was part of a standard ablation procedure and approved by the ethics committee. The patients gave informed written consent. The anterior atrial wall is generally more prone to heterogeneous remodeling than the posterior wall [46, 55]. This dissimilarity should be reflected in longitudinal CV [15, 16].
Clinically a restitution measurement was conducted, since singular CV measurements would be prone to error and could not be classified as correct or incorrect. In contrast, the morphology of a restitution curve is known to be an exponential decrease [16, 54, 70] giving an intra-patient trend to reproduce. Additionally, the measurement would allow observation of changes respective to preceding S2 intervals and the catheter location. The measured restitution data was preprocessed using the CVAR-Seg tool (Chapter 9) yielding LATs and catheter position data.
For clinical data catheter positions are given for each electrode. LATs can be unipolar but are more commonly acquired as bipolar recordings. To adjust the positions to match the bipolar recordings the center between each of the electrode pairs was calculated respectively and used as a surrogate position for the case of bipolar LATs.
Clinical catheters are oriented in 3D space inside the atrial cavity. The LATs are acquired along the atrial wall approximately in plane with the catheter electrodes that are oriented approximately parallel to the atrial wall.
Therefore, a 2D dimensional ellipse fit is the optimal approach. In order to convert the 3D electrode positions to accommodate a 2D fitting process, an initial plane is fitted through all electrodes, followed by a translation of the catheter center to the coordinate center (Figure 14.5 A, B). A subsequent rotation orients the previously fitted catheter plane onto the xy plane (Figure 14.5 C). A projection of the electrodes along the plane normal sets all catheter electrodes onto the xy plane finalizing the dimension reduction and enabled the 2D ellipse fitting process (Figure 14.5 D). After the fitting step, CV, anisotropy ratio and fiber orientation are estimated. To relate these values back onto the original catheter position on the atrial geometry the projection process is reversed.

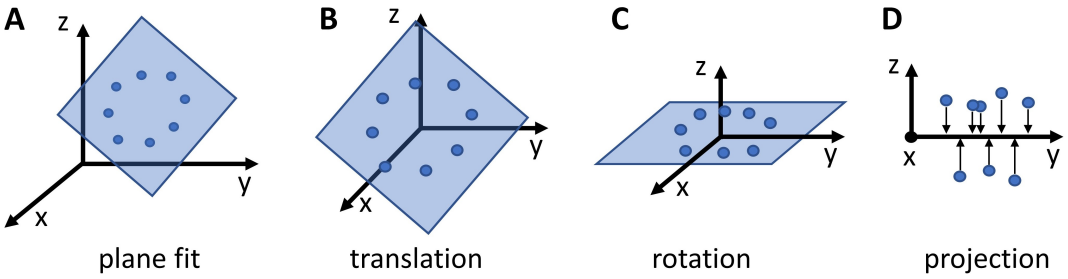

Figure 14.5: Schematic dimension reduction workflow of catheter location data. A) Plane fit (blue) through 3D location of catheter electrodes (blue points). B) Translation of catheter center to coordinate center. C) Rotation of catheter plane to xy plane. D) Projection of electrodes along plane normal onto xy plane eliminating z-axis, resulting in a 2D representation of location data.

CV values were plotted over the S2 interval and points larger than 2.5 times the standard deviation of the all curve values were excluded as outliers stemming from bad measurements. The points were then fitted with a mono-exponential curve to reveal their relative positions and trend.

Chapter 15

Results

15.1 Simulated Data

To showcase that the model follows the physiological spatio-temporal expansion of the depolarization wave, the transmembrane voltage of the simulation was overlaid with the two ellipses using the P4-M3-O8 model as an example (Figure 15.1). The depolarization wave is

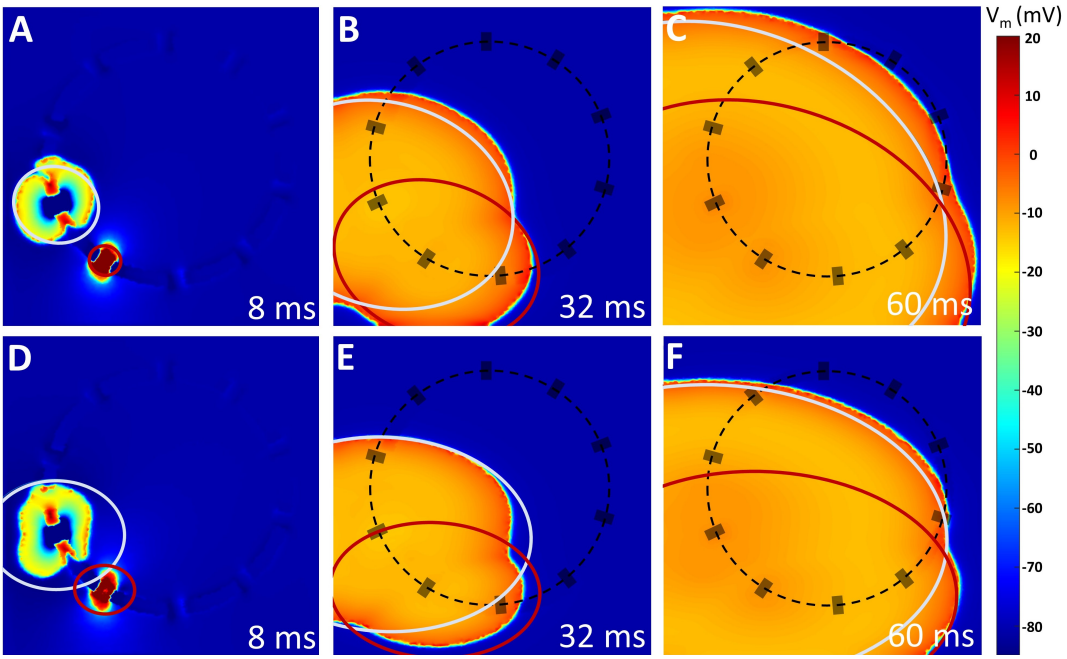

Figure 15.1: Simulation showing the transmembrane voltage of the depolarization wave spread caused by a biphasic pulse applied to 2 electrodes. The tiles show the transmembrane voltage at different time steps. A, B and C originate from a simulation with a conduction velocity (CV) of $300\,\mathrm{mm/s}$, anisotropy ratio of 1.3 and fiber angle of $0°$. For D, E and F the anisotropy ratio differed (1.9). The ellipses show the result of the double ellipse method for the first (light blue) and second (red) electrode. The catheter (black ring) and electrodes are indicated.

visualized via the transmembrane voltage resulting from the simulation after extracellular stimulation. The ellipse is spatially aligned with the depolarization wavefront and with increasing time the depolarization wavefront distance to ellipsis edge decreases, resulting in an optimal fit near the location of the electrodes.
In the following paragraph, errors in conduction velocity (CV), anisotropy ratio and fiber angle a_0 and b_0 resulting from the fitting of the models to the in-silico local activation times (LATs) are presented. Additionally, the results are shown when adding errors to all LAT measurements (perturbed LATs).

Longitudinal CV

With regards to the longitudinal CV 300 mm/s, 600 mm/s, and 900 mm/s respectively, the standard Blauer model (B-M3-O8) displayed a median error of 101 mm/s, 128 mm/s, 179 mm/s, and an interquartile range (IQR) of 104 mm/s, 78 mm/s, 97 mm/s. The adapted Blauer model (B-M3-O2), showed a significant decrease in IQR of 81 %, 69 %, 29 % for CVs of 300, 600 and 900 mm/s respectively (measured between whiskers) compared to the standard Blauer (B-M3-O8) method.
The double ellipse models P4 and P5 exhibited median values lower than ±22 mm/s

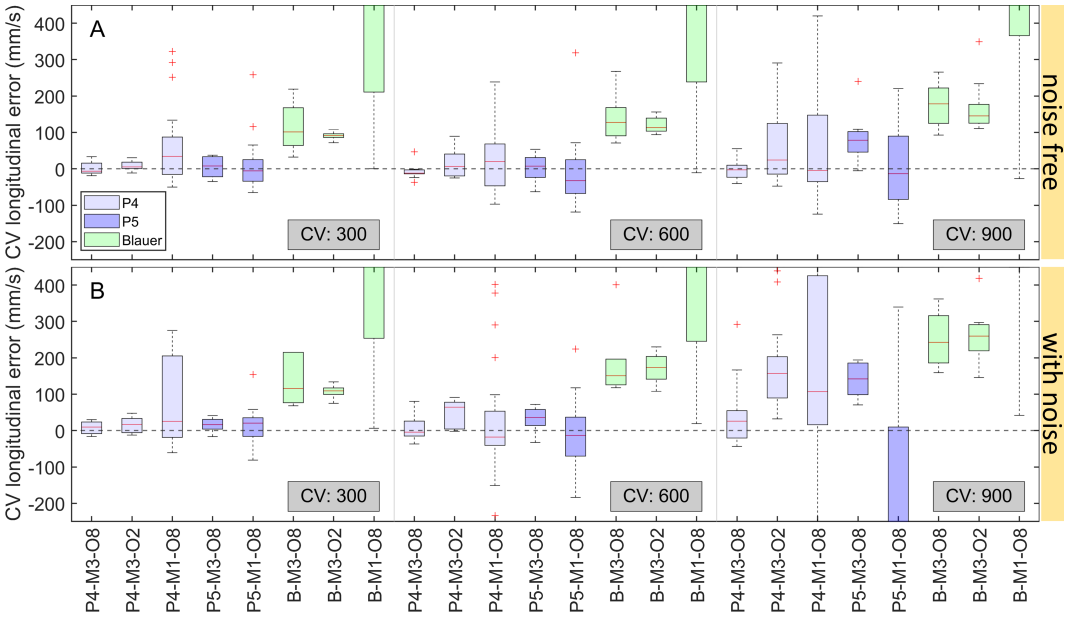

Figure 15.2: Resulting error of longitudinal CV for three ground truth CVs (gray boxes) using different double ellipse models (blue) and different Blauer model adaptations (green). Evaluation for LATs from simulation (top) and LATs with a random uniformly distributed error added to the measurement data.

across all CVs except for P4-M1-08 at 300 mm/s deviating by 34 mm/s, and P5-M3-08 at 900 mm/s deviating by 79 mm/s. The whisker range of all double ellipse models increased with rising ground truth CV. The use of multiple measurements made the fitting methods more accurate towards the ground truth than single measurement evaluations.

The Blauer method, which was not conceptualized for single measurement purposes, when using a single measurement(B-M1-O8) produced median and IQR outside the 500 mm/s y-axis bounds whereas the double ellipse methods give valid results for these cases as well. An overall trend to higher IQRs for higher CVs can be seen
Using perturbed LATs by including LAT error, increased IQR across all models (Figure 15.2 B). The single measurement cases (P4-M1-08, P5-M1-O8) were most affected with the IQR increasing by a factor of 2.2 and 2.4 for P4-M1-O8 at CVs 300 mm/s and 900 mm/s. The P5-M1-O8 IQR increase at a CV of 900 mm/s extended beyond the lower plotting boundaries. For CV 600 mm/s the largest IQR change was present in B-M3-O2 and P4-M3-O8 which increased by a factor of 1.7 and 3.8 respectively. Both models had a low IQR for the in-silico LATs (B-M3-O2: 10 mm/s, 36 mm/s, 52 mm/s; P4-M3-O8: 27.3 mm/s, 11 mm/s, 33 mm/s) across the whole CV range. Even though the relative increase is large, P4-M3-O8 retained the lowest absolute value of 41 mm/s IQR for the perturbed case at a CV of 600 mm/s.
Calculating the mean shift for all model medians across all CVs, excluding the single measurement cases, produced a mean absolute shift value of 11 mm/s for 300 mm/s, 32 mm/s for 600 mm/s and 80 mm/s for 900 mm/s. Therefore, the LAT induced median shift errors were magnitudes smaller than the estimated values in the multiple measurement cases. Similarly, the IQR only changed marginally. Calculating the absolute mean shift for all model IQRs across all CVs, excluding the single measurement cases, produced a mean absolute value of 8 mm/s for 300 mm/s, 11 mm/s for 600 mm/s and 20 mm/s for 900 mm/s. Therefore, the LAT induced IQR errors for multiple measurement cases were magnitudes smaller than the estimated values as well. Whiskers and extreme outliers (red cross) increased by 11 counts, corresponding to an increase of outliers from initially 2 % for the in-silico LATs to 4 % of all estimated cases for perturbed LATs. However, calculating the median of all whiskers for all multi measurement cases revealed that the extreme outliers are smaller than 13 % of the desired ground truth value. A detailed summary of all values is given in (Appendix A.1)

Summary:
The P4-M3-O8 model estimates the longitudinal CV best in terms of accuracy and robustness. The P5-M3-O8 is only slightly behind in terms of accuracy but shows increasing estimation errors for perturbed LATs, and therefore, is not as robust as P4-M3-O8.

Fiber angle
The adapted Blauer model (B-M3-O2) had an absolute median/mean (denoted by <median>/<mean> in the following) offset of all boxplot medians throughout all fiber angles of 10°/10° and the least IQR of all models 1°/1°) (Figure 15.3 A). The standard Blauer method (B-M3-O8) had a larger IQR with an absolute median IQR over all angles of 12°/12° and an absolute mean/median median offset throughout all fiber angles of 5°/6° to the ground truth value.
The single measurement Blauer (B-M1-O8) method fails to accurately detect the fiber angle with errors larger than $\pm 40°$ at 30° fiber angle.

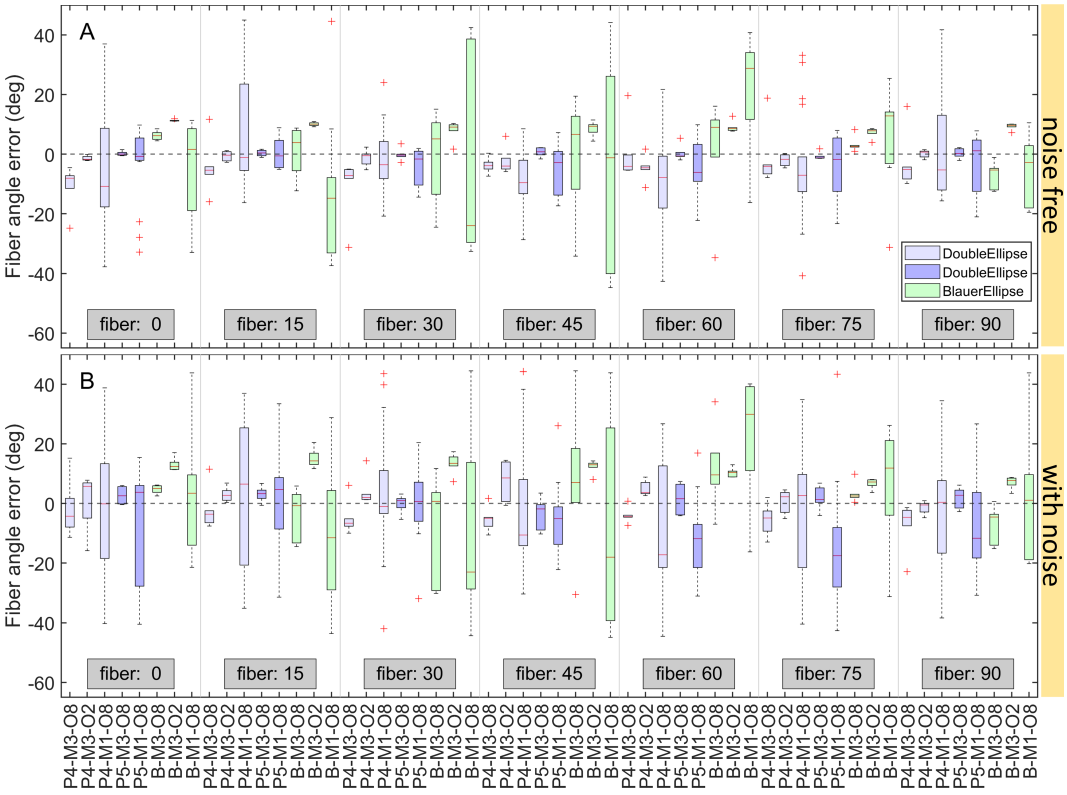

Figure 15.3: Resulting error of fiber direction angles for three ground truth angles (gray boxes) using different double ellipse models (blue) and different Blauer model adaptations (green). Evaluation for LATs from simulation (top) and LATs with a random uniformly distributed error added to the measurement data.

In the comparison of the multi measurement cases, the median of the P5-M3-O8 model is closest to the ground truth with an absolute median/mean median of 0°/1° while the models P4-M3-O2 (2°/2°) and P4-M3-O8 (5°/5°) are slightly higher. The IQR of P5-M3-O8 is slightly lower 1°/2° than for P4-M3-O8 (3°/4°) and P4-M3-O2 (3°/3°).
Comparing the single measurement cases (P5-M1-O8, P4-M1-O8), the P4-M1-O8 model revealed an absolute mean/median median deviation of 7°/6° for all fiber angles. The absolute mean/median IQR was 17°/19°. The P5-M1-O8 showed an absolute mean/median median deviation of 12.9°/10.2°.
With inclusion of LAT errors, the IQR and whiskers increase (Figure 15.3 B). Absolute IQR means over all angles of P4-M3-O8 and B-M3-O8 increased by a factor of 1.4 and 1.2, while the absolute mean median was 4.8° and 4.3°. The adapted Blauer model (B-M3-O2) showed the lowest absolute mean IQR across all fiber angles (2.4°) for the perturbed LATs. In contrast The P4-M3-O8 and P5-M3-O8 models had an absolute mean IQRs of 4.5° and 5.9° across all fiber angles. The single measurement models were the most sensitive to perturbed LATs. P4-M1-O8 displayed a mean absolute IQR of 29° and an absolute mean median of 6°. P5-M1-O8 produced a mean absolute IQR of 19° and an absolute mean median of 8°.

Summary:
The most robust model was the B-M3-O2 model with the least IQR change after introduction of perturbation, but had low accuracy. The next best models in terms of robustness were the multiple measurement P4-M3-O8 and P5-M3-O8. The most accurate model was the P5-M3-O8 followed by the P4-M3-O8 model.

Anisotropy
The adapted Blauer method (B-M3-O2) captured the anisotropy ratio well, highlighted by the median deviating by 0.02 from the ground truth for the case of 1.3 as well as 1.8. IQR increased for B-M3-O2 from 0.07 to 0.3 from 1.3 and 1.8 (Figure 15.4 A). Compared to

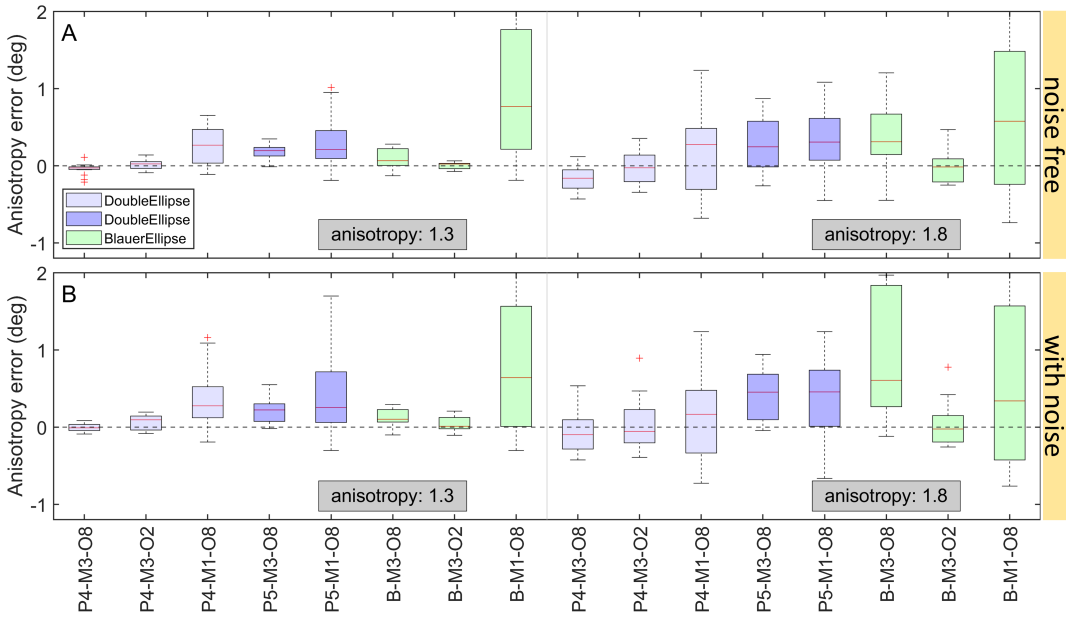

Figure 15.4: Resulting error of anisotropy ratio for two ground truth anisotropy ratios using different double ellipse models (blue) and different Blauer model adaptations (green). Evaluation for LATs from simulation (top) and LATs with a random uniformly distributed error added to the measurement data.

B-M3-O2 the standard Blauer approach (B-M3-O8) showed an increase in median (0.06 and 0.31) and IQR (0.22 and 0.52). The single measurement Blauer method (B-M1-O8) was unable to estimate the anisotropy ratio and will be excluded from further evaluation.
P5-M3-O8 presented with median values of 0.19 and 0.24 and IQR of 0.11 and 0.59 for anisotropy ratios of 1.3 and 1.8. The P4-M3-O8 model presented with medians of -0.03 and -0.16 and IQRs of 0.03 and 0.24 for the ground truth anisotropies of 1.3 and 1.8. The P4-M3-O2 model performed equally well with median values of 0.02 and -0.03 and IQR of 0.09 and 0.34. Between the single measurement cases, P4-M1-O8 showed the best results with a median offset of 0.27 for both anisotropy ground truths and IQRs of 0.44 and 0.79 while P5-M1-O8 medians (0.21 and 0.31) and IQRs (0.36 and 0.54) were increased.
With inclusion of LAT errors, the interquartile range increased. The adapted Blauer method

(B-M3-O2) captured the anisotropy ratio well, highlighted by the median deviating by 0.01 from the ground truth of 1.3, and 0.02 for the case of 1.8. IQR increased for B-M3-O2 from 0.2 to 0.3 from 1.3 and 1.8 (Figure 15.4 B). Compared to B-M3-O2 the standard Blauer approach (B-M3-O8) showed an increase in median (0.1 and 0.6) and IQR (0.2 and 1.6). P5-M3-O8 presented with median values of 0.2 and 0.5 and an IQR of 0.2 and 0.6. The P4-M3-O8 model presented with medians of 0 and -0.1 and IQRs of 0.1 and 0.4 for the ground truth anisotropies of 1.3 and 1.8. The P4-M3-O2 model performed equally well with median values of 0.1 and 0.1 and IQR of 0.2 and 0.4.

Summary:
Both the adapted Blauer (B-M3-O2) as well as the P4-M3-O8 and P4-M3-O2 model show approximately equal accuracy and robustness when evaluating the anisotropy ratio.

Initial area long axis
The Blauer method does not support acquisition of initial area, therefore only the double ellipse models are reported (Figure 15.5). The P4-M3-O8 model captured the initial electrode

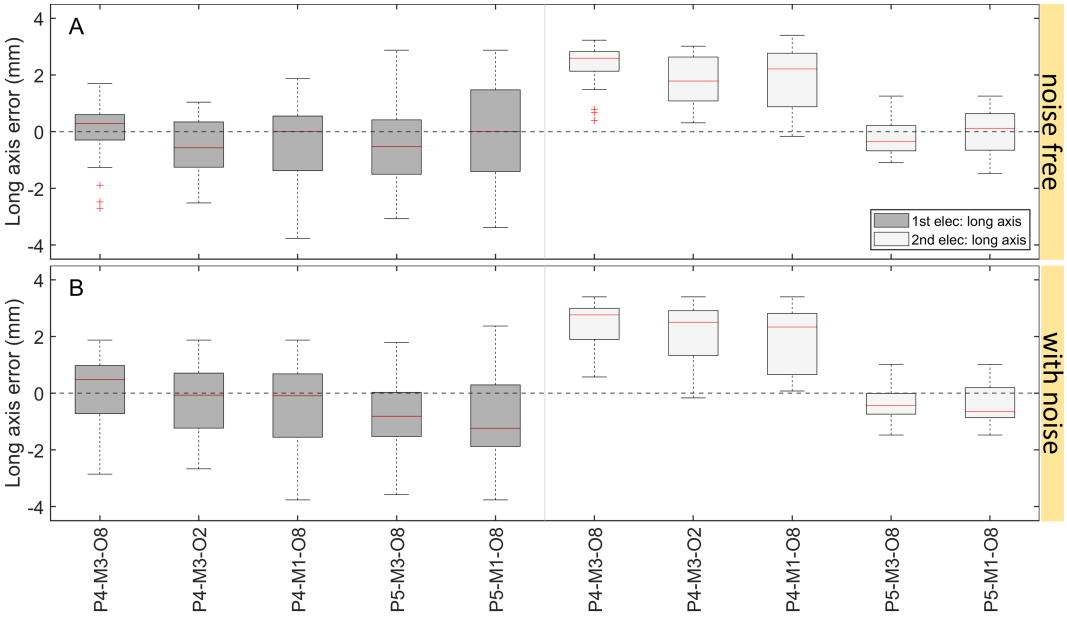

Figure 15.5: Resulting error of initial ellipse long axis for the first (dark grey) and second (light grey) electrode using different double ellipse models. Evaluation for LATs from simulation (top) and LATs with a random uniformly distributed error added to the measurement data.

area long axis of the first electrode most accurate and robust, with a median error of 0.29 mm and IQR of 0.9 mm. P5-M1-O8 showed a median of 0 mm but an IQR of 2.88 mm. The single measurement cases P4-M1-O8 exhibited a median of 0 mm and an IQR of 1.92 mm and was on par with the other P4 multi measurement cases. P5-M3-O8 presented with a median of -0.53 mm and an IQR of 1.92 mm. The second electrode was best estimated by

the P5-M3-O8 and P5-M1-O8 model with medians of -0.34 mm and 0.12 mm and IQRs of 0.89 mm and 1.29 mm respectively. P4-M3-O8 had the highest median offset (2.59 mm), followed by P4-M1-O8 (2.21 mm) and P4-M3-O2 (1.78 mm). P4-M1-O8 showed the highest IQR (1.89 mm) followed by P4-M3-O2 (1.55 mm) and P4-M3-O8 (0.69 mm).
Inclusion of LATs perturbation increased IQR (Figure 15.5 B). For the first electrode, P5-M3-O8 and P5-M1-O8 reduced in IQR by (19 % & 25 %) and displayed large shifts to -0.81 mm and -1.24 mm. All P4 models exhibited a mean combined increase in IQR of 26 %. For the second electrode IQRs of the P5 models dropped by a combined mean of 22 % while IQR of the P4 models increased by a combined mean of 17 %.

Summary:
The P5-M3-O8 model captured the initial area long axis most accurate and showed the highest robustness, immediately followed by P5-M3-O2. The most accurate and robust estimation out of the P4 models was given by P4-M3-O8.

Initial area short axis
The median initial area long axis for the first electrode is captured well for all P4 models within an absolute error range of <0.54 mm (Figure 15.6 A). P4 models evaluate the initial

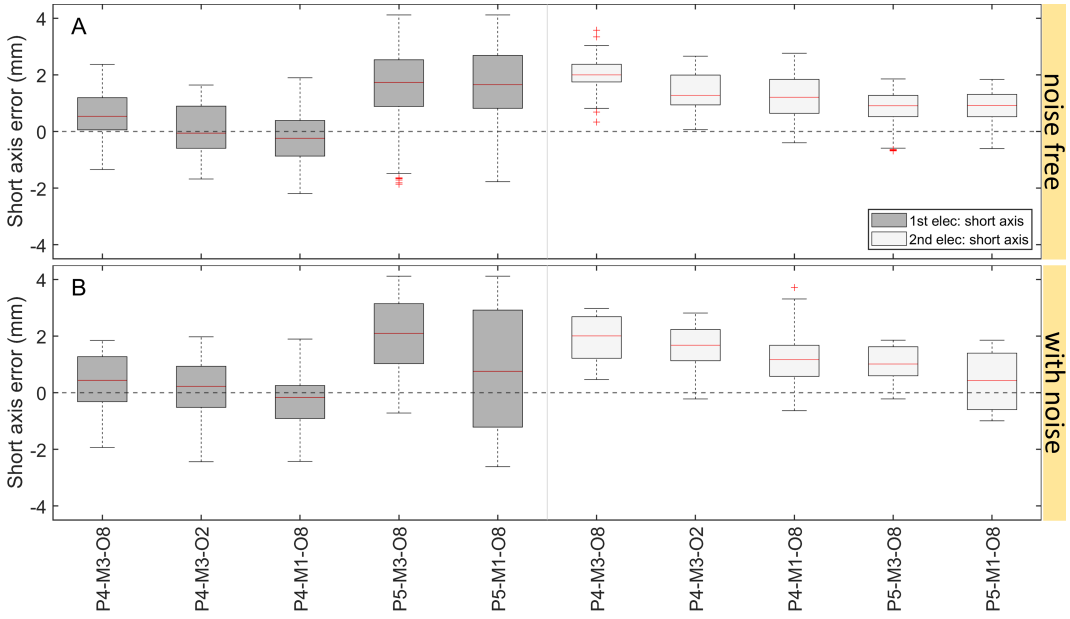

Figure 15.6: Resulting error of initial ellipse short axis for the first (dark grey) and second (light grey) electrode using different double ellipse models. Evaluation for LATs from simulation (top) and LATs with a random uniformly distributed error added to the measurement data.

electrode area long axis of the first electrode well, with medians of 0.54 mm, -0.06 mm, -0.24 mm and IQRs 1.14 mm, 1.49 mm, 1.26 mm (in order of occurrence). Th P5 models present with medians 1.73 mm, 1.65 mm, and IQRs of 1.64 mm and 1.87 mm. The sec-

ond electrode long axis evaluation revealed medians 2 mm, 1.27 mm, 1.21 mm, 0.91 mm, 0.92 mm and IQRs of 0.62 mm, 1.05 mm, 1.2 mm, 0.75 mm, 0.79 mm.
Inclusion of LAT perturbation increased IQR (Figure 15.6 B). For the first electrode, P5-M3-O8 and P5-M1-O8 increased in IQR by (22 % & 54 %) and had a large shift in median to 2.1 mm and 0.76 mm. P4-M3-O8 increased in IQR by 29 % compared to the unperturbed case. The models P4-M3-O2 and P4-M1-O8 exhibited a mean combined decrease in IQR of 0.05 %. For the second electrode IQRs increased (in order of occurrence) by 58 %, 0.05 %, −0.09 %, 27 % and 60 %.

Summary:
The P4 models captured the initial area short axis of the first electrode most accurate and showed the highest robustness. The initial area short axis of the second electrode is slightly overestimated by all models. For the P4 models this is expected, since they do not differentiate between initial areas. The P5 models which fit both initial areas explicitly show values closer to the ground truth.

15.2 Detecting Activation Order

To detect the correct activation sequence for the electrodes, both combinations of sequences (Chapter 14.8) were used for the model input and were fitted to the LATs with and without additional errors (Figure 15.7). In case of errorless LATs, the resulting median squared norm

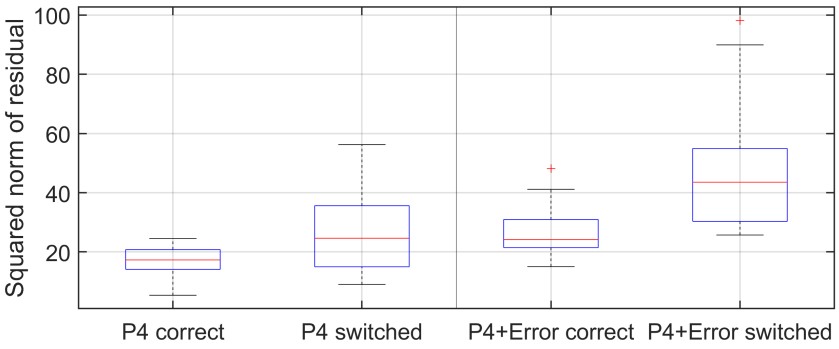

Figure 15.7: Squared residual norm for the correct order of electrode activation and the switched/opposite case using the P4 model. Boxplots contain 42 measurements with stimulation from three different sites. Additionally, all cases were evaluated with an additional random uniformly distributed error between 1 and 2 ms on each LAT measurement.

of the residual differed between the correct activation order (17.3 arb.u.) and the incorrect (switched) order (24.6 arb.u.). The IQR of P4 and P4-switched differed in their respective Q1 (14.1 arb.u. & 15 arb.u.) but otherwise overlapped by 33 %. Q3 significantly differed

with values of 20.8 arb.u. for the correct and of 35.6 arb.u. for the switched order.
The median values for the LATs including errors yielded an increase in median difference (24.2 arb.u. and 43.6 arb.u.). Additionally, the IQR showed almost no more overlap (0.6 arb.u.), with a Q3 value of the correct order case of 30.9 arb.u. and a Q1 value of the switched case of 30.3 arb.u..

15.3 Clinical Patient Data

The inverse double ellipse method was able to generate CV restitution curves that exponentially decrease with decreasing S2 coupling interval (Figure 15.8 A–F).

Patient 1: The longitudinal CV curves appear in ascending order P4, P5 and Blauer method for both measurement locations. The first measurement location (Figure 15.8 A) presents with CVs of 718 mm/s, 764 mm/s, and 897 mm/s at an S2 interval of 500 ms. At the same S2 interval the second measurement location (Figure 15.8 B) shows CVs of 389 mm/s, 519 mm/s, and 622 mm/s.
The effective refractory period (ERP) was reached as of 250 ms for all curves at measurement location 1 (Figure 15.8 A). At measurement location 2 (Figure 15.8 B), the Blauer method reached a premature ERP as of 270 ms compared to the P4 and P5 model (240 ms).
The voltage map showed an extensive non-low voltage area for measurement location 1 (Figure 15.8 a) while measurement location 2 (Figure 15.8 b) showed low voltage islands within and near the catheter electrodes.

Patient 2: Curve order at the first measurement location (Figure 15.8 C) follows the ascending order P4, P5 and Blauer method for S2 intervals up to 350 ms, at which point the P4 and P5 model curves overlap. For an S2 interval of 500 ms the P5 model (1420 mm/s) remains below the Blauer method (1496 mm/s) while the P4 method reaches a CV of 1628 mm/s.
The second measurement location (Figure 15.8 D) shows the ascending order P4, P5 and Blauer method with CVs of 877 mm/s, 1061 mm/s, and 1144 mm/s at an S2 interval of 500 ms. The Blauer method falls below the P4 and P5 model in CV for S2 intervals below 350 ms and shows a premature ERP as of 330 ms compared to the P4 and P5 models (310 ms).
The voltage map showed largely non-low voltage areas with small low voltage island near two catheter electrodes for measurement location 1 (Figure 15.8 c) while measurement location 2 (Figure 15.8 d) showed extensive low voltage areas within and near the catheter electrodes.

Patient 3: Curve order at the first measurement location (Figure 15.8 E) follows the ascending order P4, P5 and Blauer method (1467 mm/s, 1534 mm/s, 1774 mm/s) at an S2 interval of 500 ms. Between 260 ms and 350 ms the P4 curve lies above the P5 curve. The second measurement location (Figure 15.8 F) shows the ascending order P4, P5 and Blauer

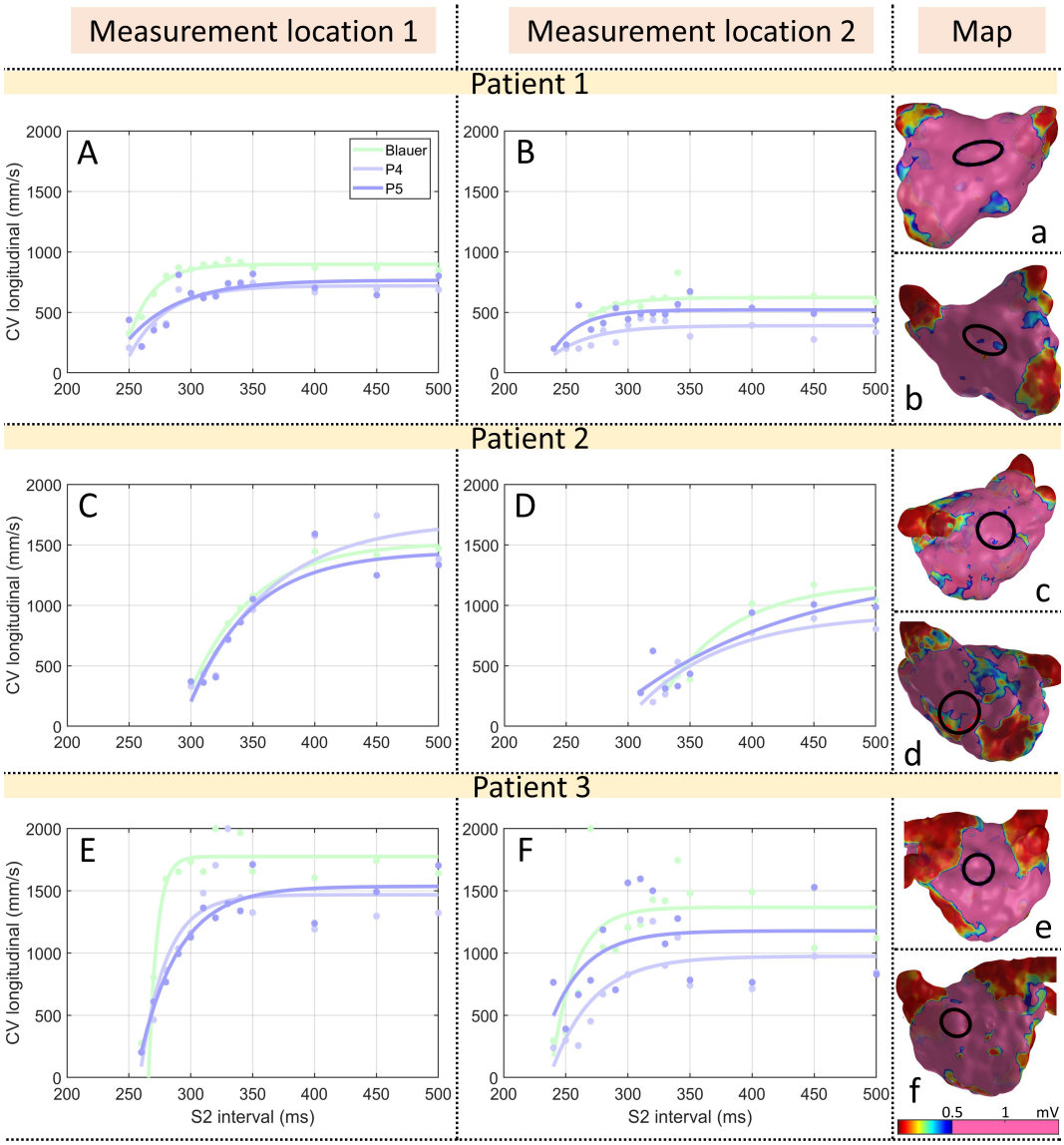

Figure 15.8: Restitution of longitudinal CV for the Blauer (green) and double ellipse methods (light and dark blue) gained from three patient measurements of LATs from the two atrial wall measurement locations (A-F). Exponential curve fits (lines) were applied for visualization of restitution behavior. The voltage map with the catheter position (black circle) denotes the measurement location and is given with the corresponding lowercase alphabetic descriptor (a-f).

method with CVs of 973 mm/s, 1177 mm/s, and 1366 mm/s at an S2 interval of 500 ms. All curves reach the same ERP as of 260 ms for measurement location 1 and as of 240 ms for measurement location 2.

The voltage map showed an extensive non-low voltage area for measurement location 1 (Figure 15.8 e) while measurement location 2 (Figure 15.8 f) showed low voltage islands peripheral to the catheter electrodes.

Chapter 16

Discussion

This chapter discusses how well the inverse double ellipse method (Chapter 14.2) succeeded in obtaining the conduction velocity (CV), anisotropy ratio and fiber orientation of the underlying substrate. Out of the four inverse double ellipse methods presented here (P4, P5, P6, P7) the most promising models P4 and P5 were compared to the Blauer method from literature. First, the P4, P5 and Blauer model were evaluated regarding their parameter estimation accuracy and robustness. Secondly, the applicability of these models on clinical data of three patients is compared. Lastly, the most promising options for extending the model are discussed and a conclusion is given.

16.1 Accuracy and Robustness

In the following the in-silico data is discussed, since the in-silico data offers a ground truth that the model values can be quantitatively compared to in regards to accuracy and robustness. Accuracy of the model was assessed by median deviation from in-silico ground truth value. Additionally, lower interquartile range (IQR) describe higher accuracy. Robustness was assessed equivalently with use of perturbed local activation times (LATs).

Improving the state of the art

Up to date the only method able to derive CV, the anisotropy ratio, and the fiber angle simultaneously for local measurements is the Blauer method [115]. The method was proposed for a circular catheter and is achieved by consecutive stimulation from all electrodes. Consequently, the Blauer method was never intended to be used with a single stimulation measurement. Additionally, none of the methods in literature include an initially activated area that occurs when using extracellular local stimulation. This omission might be neglectable for global CV estimation methods [16, 37, 59, 124, 130], but for methods using local stimulation in proximity to measurement electrodes such as the Blauer method, it creates an overestimation of CV (Example for ground truth of 900 mm/s: Blauer:19.8 % overestimation). It stands to reason, that this is due to the omission of the initial area (Example for ground truth of 900 mm/s: P4 method including initial area: 0.3 % overes-

timation). The proposed double ellipse method additionally removes the dependency on a specific catheter shape and remedies the inability to evaluate single measurements for local stimulation. It was able to generate valid results for single measurements with median values close to ground truth (P4 method: 0.5 % error vs Blauer method: 122.3 % error at a ground truth of 900 mm/s) was robust under measurement noise (P4 IQR without noise: 33.1 mm/s vs P4 IQR with noise: 75.2 mm/s vs Blauer IQR without noise: 97 mm/s vs Blauer IQR with noise: 129.9 mm/s) and increased in estimation accuracy with a rising amount of measurement data (P4 method: -2.75 mm/s median error vs Blauer method: 178.5 mm/s median error using 3 measurements). If the analysis is constrained to using the Blauer method, this study found that results can be improved by restricting the measurement electrodes to using only the 2 electrodes (B-MX-O2) opposite the stimulation location. This is due to the fact that the proximity to the stimulation site distorts the norm of CV vectors due to the initial region and the highly non-planar wavefront. Omission of these error inducing electrodes can lead to a better estimation with a median closer to ground truth and smaller interquartile range (At a ground truth of 900 mm/s: Median: 145.4 mm/s vs 178.5 mm/s, IQR: 51.7 mm/s vs 97 mm/s).

Excellent results were obtained despite use of catheter with sparse electrode amount
The results (e.g., P4-M3-O8 model median: CV at 300 mm/s: 2.1 % error, fiber orientation at 90°: 5.1° error, anisotropy at 1.3: 2.3 % error) generated in this study were achieved by replicating a realistic clinical setup in-silico using a commercially available catheter. The 10 pole catheter was chosen since it is the most commonly available catheter across all mapping systems and currently the mapping catheter with the least number of electrodes. Thereby, the models were evaluated on the most scarce amount of input data available by clinical means, making it the most challenging estimation case. The choice of catheter ensured that the method will perform equally or better for the case of more electrodes as given by a 20 pole or HD Grid catheter (16 electrodes). Additionally, the method accuracy will increase in the future, provided the current trend of increasing electrode amount while decreasing electrode size per catheter continues. Should measured data increase, the P6 and P7 models might become a viable option in the future as well, since they are held back by sparsity of input data, leading to premature estimation termination due to local minima. This makes the double ellipse method more advantageous than the Blauer method since it yields increasingly better results with increasing measurement as well as electrode number. By contrast this study shows that the Blauer method increases in accuracy when removing electrode measurements and using only opposite electrodes.

Choice of method
The in-silico results showed that the P4 model was the overall best choice to estimate CV, anisotropy ratio and fiber orientation with respect to a combined maximization of robustness and accuracy while keeping the number of estimation parameters and consequently the amount of necessary measurement data minimal. It was mostly better or equal to other models with respect to interquartile range and median for the unperturbed LATs as well as

the error induced LAT cases. The only exception was estimation of the initial area of the second electrode which was slightly better for the P5 model.
The choice of method comes down to application. While for the CV the P4-M3-O8 model has the most accurate results, for the fiber orientation in most cases the P5-M3-O8 model outperforms the other cases in pure accuracy. Each methods accuracy regarding either CV, anisotropy ratio or initial area estimation can be checked in chapter 15.1. However, to achieve the highest combined accuracy and robustness and to take advantage of all measurements acquired by physicians in the clinics, from the in-silico results the P4-M3-O8 method is recommended.

16.2 Evaluating Model Application Using CV of Clinical Data

Model yields restitution information from clinical data
All restitution measurement points are estimated independently, meaning the model does not have information of the previous measurements but still results in an exponentially decreasing restitution curve (Figure 15.8). This proves that the model does not merely adjust the initial area to compensate for changing CVs but rather changes in CV are respected and the model adapts to the dynamic changes.

CV ranges conform with literature
Literature data on the range of clinically acquired CV showed a mean value from 624 mm/s to 1265 mm/s, acquired from 412 left and right atrial measurements [139]. Other sources, detail similar ranges of 750 mm/s to 1080 mm/s [59], 860 mm/s to 1250 mm/s [18] and 200 mm/s to 600 mm/s with outliers up to 1400 mm/s [124] which extends the range further. The extended lower range is further solidified by a study on 73 patients paced from two directions that yielded a mean lower range of CV of 244 ± 130 mm/s for patients in atrial fibrillation (AF) [44]. The CV ranges of our restitution curves exceed 1400 mm/s (Figure 15.8 C, E), since they are local measurements. A study on global and local CV evaluated 22 patients and showed that while global CV was 950 mm/s the local CV ranged from 270 mm/s to 2200 mm/s [45]. An evaluation of 2 clinical recordings using iterative estimation of local CV yielded a range from 300 mm/s to 1800 mm/s [19]. These value ranges corresponded well with the range of our restitution curve estimations of 200 mm/s to 1774 mm/s. The CV results of patient 2 (Figure 15.8 C, D) are well reflected in a previous restitution study on 18 patients, which showed a mean CV of 1590 mm/s at a basic cycle length of 600 ms in non-low voltage zones and 980 mm/s at low voltage zones [46].

ERP values conform with literature
While the process is complex, effective refractory period (ERP) is one of the few tissue specific parameters that can be determined in clinical measurements. At the same time the ERP is a locally changing substrate characteristic. Data acquisition over a larger area or

at multiple widespread locations will yield varying ERP results. This, in turn, influences the model result when using all the acquired measurements in combination. A previous restitution study on 18 patients reported a mean ERP around 260 ms while the ERPs in this study ranged from 240 ms to 300 ms [46]. A study on 5 patient cases showed that ERPs were close to or slightly below an ERP of 300 ms with a single ERP being 200 ms [110], which reflects the range for our measurements (Figure 15.8 A-F) well.The multitude of ERPs for different measurements should also be considered when a collective evaluation of multiple measurements, as is the case in this work, is pursued. Should the measurements from different sides vary regarding ERPs, then at some point an initially prepared multi-measurement can reduce down to a single measurement due to lack of capture. This phenomenon can be seen in Figure 15.8 A, D where the Blauer method terminates earlier than the double ellipse methods highlighting the fact, that the double ellipse models now allow for single measurement solving.

Clinical data reproduces in-silico results

Clinical data results showed that for valid LAT measurements the P4 model show the lowest CV followed by the P5 model. The Blauer method produced the highest CV, thereby reproducing and confirming the in-silico CV curve sequence (Figure 15.8 & Figure 15.2).
Assuming the clinical data to be closer to the in-silico perturbed data (Figure 15.2 B), allowed exemplary comparison of the respective curve differences of patient 1 (Figure 15.8 A, B) to their in-silico counterpart. Since in clinical data the parameter of fiber orientation, catheter alignment, initial area are unknown, no direct comparison between in-silico value and clinical value is possible. Therefore, the clinical data must fall in the range of the in-silico boxplot that encompass a wide range of parameters. Ideally the clinical data will fall into the Q1 to Q3 range between two models being compared, e.g., P4 Q1 and P5 Q3. For in-silico longitudinal CV of 600 mm/s the difference between P4-M3-O8 Q1 and P5-M3-O8 Q3 was 73 mm/s while the difference between P5-M3-O8 and the Blauer method was 198 mm/s and the overall range between P4-M3-O8 and Blauer method was 212 mm/s. For Figure 15.8 A, the P4-P5 difference of 46 mm/s was inside the in-silico value range. The P5-Blauer method difference (133 mm/s) was within the in-silico value range, and therefore the overall P4-Blauer difference (179 mm/s) was within the in-silico range as well. For Figure 15.8 B, the difference between P4 and P5 (130 mm/s) is higher, while the difference between P5 and the Blauer method (109 mm/s) was lower than the in-silico results. However, the overall CV range between P4 and Blauer (233 mm/s) came close to the in-silico data (212 mm/s; Δ 21 mm/s).
Therefore, not only was the curve order identical between in-silico and clinical data, but also the difference between curves resulting from the different methods was recreated well. Since clinical data follow the same characteristics as the in-silico data and the in-silico data reproduced the ground truth well, this confirms the applicability of the inverse double ellipse method to clinical data.

16.3 Outlook on Future Model Expansions

In this study we remained with a single simulation setup with a single catheter. While this setup was chosen on purpose to represent the hardest case for reconstruction, no other catheters with more electrodes are explicitly shown. This limitation is justifiable since general mathematical fitting theory states that with more accurate points statistically the fitting of the model will improve.
A second point is that we provide a single distance between the two stimulating electrodes. The change in distance coupled with different initial stimulation properties such as changed stimulation pulseform or amplitude might impact the formation of the initial area under the respective electrodes as well as impact spatio-temporal propagation of the depolarization wave front. This in turn could lead to a propagation wave front pattern which does not follow the shape of a double ellipses anymore. This can be easily avoided by using a higher stimulation amplitude neutralizing the distance effect. And the general trend for higher electrode densities results in less distance between electrodes, alleviating this problem. Simulating all currently commercially available catheters as well as electrode distances, stimulation setups and pulse forms is beyond the scope of this study since this study is meant to introduce the general method.
A related point is that only a single error was introduced to the LATs being a surrogate for a variety of measurement errors during collection and evaluation of data. Naturally this does not encompass all possible errors occurring during measurement and evaluation. A specific division in occurring errors and their impact on the fitting process could be studied in more detail. The same reasoning holds true for the fact that no fibrosis was incorporated into the model due to the amount of distributions and models of fibrosis to test and evaluate.
Furthermore, no in-silico CVs above $900\,\mathrm{mm/s}$ were evaluated even though there are reports of higher values. The reasoning being that, firstly, the offset created by the estimation of the in-silico value is error prone and creates larger IQRs for increasing CVs making it difficult to separate model estimation from ground estimation errors. Secondly, highly conductive tissue is generally regarded as healthy tissue and therefore not as relevant to be estimated with such high accuracy as is the case for tissue near low-voltage areas. These areas show slow conduction and are important for the process of finding and terminating the arrhythmia of the patient.
Finally, only a single coupling between the two ellipses was incorporated. These proposed couplings already produce estimated CVs, anisotropy ratios and fiber angles very close to the ground truth even under perturbed measurement conditions. We believe that further investigation could yield other couplings of the two ellipses that might improve upon the model versions proposed here to an even higher degree.

16.4 Conclusion

CV is a parameter containing diagnostic value. Localized CV measurements have the prospect of yielding localized substrate information, thereby increasing the information accuracy more than global CV methods and subsequently helping the clinician plan the ablation therapy. The goal was to improve upon the existing Blauer method in accuracy, robustness and make the model independent of catheter type.
With the inverse double ellipse models of this study, we were able to show that CV, fiber orientation and anisotropy factor are reproduced better than using the Blauer method. Additionally, the usefulness of the inverse double ellipse models is likely to increase in the future with the trend of increasing number of catheter electrodes. Along with the increased number of measurements the advanced models P6 and P7 could detail substrate characteristics even further.
The method is real-time capable and a valid consideration to implement in clinical electrophysiology systems. This would enable instantaneous localized measurement of atrial substrate, gaining a CV map, an anisotropy ratio map, and a fiber map simultaneously during a mapping procedure. The information gathered could subsequently be used to diagnose the path and source of the arrhythmia and facilitate creation of a digital twin to investigate optimal ablation procedures.

PART V

PATIENT SPECIFIC RESTITUTION STUDY

Chapter 17

Motivation

It is notoriously difficult to classify the burden of atrial fibrillation (AF) and produce a sustained long term positive interventional outcome [1, 51]. Relevant parameters for analysis and interpretation of AF are voltage amplitude, local activation time (LAT), conduction velocity (CV), and effective refractory period (ERP) [142, 143]. In clinical practice the amplitude is used to detect zones of low voltage that have been shown to correlate with fibrotic tissue for targeted ablation [7, 9–11, 15, 21]. The interplay between CV and ERP in general, and especially near fibrotic tissue zones, is known to be detrimental for creation and upholding of AF [137, 144].

The clinical mapping procedure is currently performed for patients during AF or sinus rhythm (SR) yielding different voltage amplitude maps [7, 9, 21]. The rate at which the tissue is activated by pacing or ongoing depolarization changes the outcome of evaluated parameters such as amplitude or CV and thus, is an import factor to take into consideration when evaluating patient data and treating patients with AF. Among other markers, sites designated for ablation are identified by a threshold on voltage maps [10, 21]. Should different types of tissue react differently to rate changes using a single threshold might yield misleading results for the distinction of ablation sites. In order to alleviate this problem rate information should be part of the evaluation of pathological tissue. To increase accuracy of designated ablation sites, CV restitution information should be included in the decision process as well. Both the CV as well as amplitude decrease near pathological tissue has been demonstrated at singular basic stimulation rates [16, 21, 46, 142]. The implication of rate in the context of CV and amplitude is not yet described in detail. Honarbakhsh et al. estimated that an amplitude decrease is accompanied by a CV decrease which changes at higher rates [46]. However, this study used only four pacing rates and did not detail the course or quantify the drop of CV at higher pacing rates. Regarding the amplitude, the author is not aware of any study detailing course or value range of amplitude restitution.

Additionally, to the distinction between pathological and non-pathological tissue, the distribution of pathological areas throughout the atria is not clear. Driven by in-vivo voltage measurements Honarbakhsh et al. showed that the posterior wall was less prone to pathological tissue than the anterior wall, while Marcus et al. found the posterior to be more prone to low voltage zones and Miyamoto et al. found no significant difference between the two sites

[46, 61, 62].
To better understand the restitution behavior in pathological areas as well as at different locations in the atrial cavity this work followed three main objectives:

Firstly, this work aimed to describe pathological areas using amplitude and CV restitution curves to discern differences between pathological and non pathological substrate by using the clinical definition of pathological and non-pathological tissue as a first approach.
Secondly, this work aimed to discern restitution differences within the atrial body at two different locations, the posterior and anterior atrial wall.
Lastly, to move beyond the empirically described manual threshold used currently, this work aimed to discern clusters within the restitution data of amplitude and CV that link back to specific substrate types.

Chapter 18

Methods

18.1 Measurement Protocol

To gain restitution information a measurement protocol was established using two measurement locations, posterior and anterior, per patient (Figure 18.1). If low voltage was present in these areas, the catheter was centered on the low voltage area if possible or electrodes were set adjacent to the low voltage area. Per measurement site, three stimulation electrode

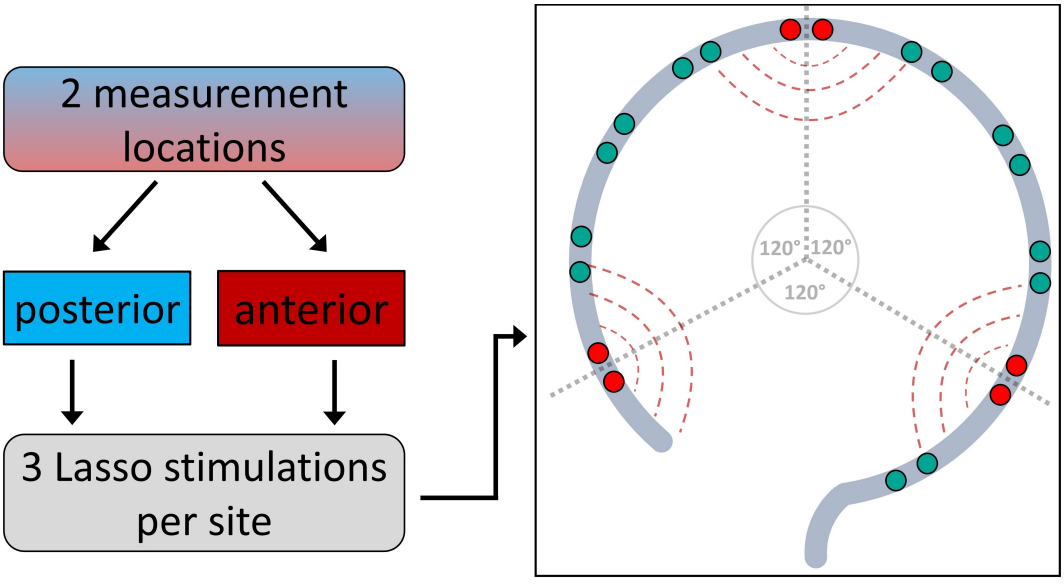

Figure 18.1: Measurement protocol for the restitution study. Measurement takes place using a lasso catheter at two separate positions on the posterior and anterior atrial wall. After catheter placement the S1S2 stimulation protocol is run subsequently from three measurement sites. Angular distance between three measurement sites should be maximized to capture directional tissue dependencies.

pairs along the catheter were selected by maximizing the angle between the stimulation sites, thereby ensuring capture of directional tissue dependencies. From each stimulation site an

S1S2 stimulation protocol was performed.
The S1S2 basic cycle length was fixed at 600 ms and the S2 intervals were set to steps 50 ms between 500 ms to 350 ms and 10 ms from 350 ms to 180 ms. Additionally, technical details such as stimulation time and strength and time shifts between clinical hardware were noted. The complete measurement protocol is given in the Appendix B.1.
The clinical partner of this project were Priv.-Doz. Dr. med. Armin Luik and Prof. Dr. med. Claus Schmitt from the Städtisches Klinikum Karlsruhe as well as Dr. med. Amir Jadidi from the Universitäts Herzzentrum Freiburg-Bad Krozingen. Data were anonymized and exported for further investigation. The study was part of a standard ablation procedure and approved by the ethics committee. The patients gave informed written consent.

18.2 Patient Evaluation

22 Patients were evaluated in this work. After obtaining a voltage map, circular catheters of fixed (20 mm) and variable (15-20 mm) circumference with 10 (Advisor SE, St. Jude Medical,) and 20 (Carto Lasso 2515, Biosense Webster & Optima 20, St. Jude Medical) measurement electrodes were used to perform the stimulation protocol and measure the atrial response. The datasets from the electrophysiology systems CARTO (Biosense Webster, Diamond Bar, CA, USA), NavX (St. Jude Medical, Saint Paul, MN, USA) and Rhythmia (Boston Scientific, Natick, MA, USA) were collected from clinical experts which were made available in anonymized form for evaluation.

The criteria for evaluation were:

- Electrogram segments of all S1S2 measurements are present.
- Amplitude of atrial answer exceeds baseline signal.
- An atrial answer exists in at least 3 channels.
- Catheter electrode positions are available.
- Geometric 3D mesh of atria is available.
- Order of stimulation procedure is available.
- Measurement was performed with a basic cycle length of 600 ms.

The acquired voltage maps including the measurement locations of all patients is available in Appendix D. For patients recorded with the CARTO system which only allows for 2.5 seconds of signal capture, additional export of electrogram data from the LabSystem PRO (Boston Scientific, former BARD, USA) system was necessary. Therefore, procedural documentation was vital to assimilate both data sets.

Local activation times (LATs), locations and amplitudes were obtained from the CVAR-Seg pipeline (Chapter 9) for each bipolar catheter channel. Restitution curves for amplitude were created by plotting the resulting amplitudes from the pipeline over the respective S2 intervals. Restitution curves for conduction velocity (CV) were created by using the inverse

double ellipse P4 model (Chapter 14.2). The P4 model characterized the tissue with regards to longitudinal and transversal CV and fiber direction. The result of the P4 fit of all patients is detailed in Appendix E. The longitudinal CV value for each S2 pacing interval was used to represent the tissue CV. Therefore, only a single CV curve is yielded for each of the two measurement locations.
Evaluation of restitution curves was done by fitting the mono-exponential curve

$$y = -a \cdot e^{-b \cdot (x-d)} + c, \tag{18.1}$$

where $a =$ scale factor, $b =$ decay, $c =$ asymptote, $d =$ estimated ERP to the restitution data. Points deviating from the mean by more than 2.5 times the standard deviation (STD) were defined as outliers and excluded from the fitting process. The exponential curve captured the trend but reduced impact of outliers due to measurement inaccuracies induced by hardware, software, and intra-operative patient dynamics.

18.3 Clustering

Clustering was performed using the Density-Based Spatial Clustering of Applications with Noise (DBSCAN) (chapter 4.3 algorithm implemented in MATLAB [138]). The method used two user supplied clustering parameters to discern clusters (chapter 4.3). The minimum number of neighboring points (MinPts) parameter, was checked and set to 4 as proposed by [79]. The ε-neighborhood parameter was determined using the k-nearest neighbor curve. Since automatic detection of the "knee" of the curve can be difficult, manual segmentation was used to determine an initial ε guess. Additionally, a $\Delta\varepsilon$ was defined so that $\varepsilon + \Delta\varepsilon$ encompassed the "knee" of the curve. The DBSCAN algorithm was iteratively rerun using values between $\varepsilon \pm \Delta\varepsilon$ and the silhouette coefficient was calculated. Choosing the ε which was near the initial choice but additionally maximized the silhouette coefficient in the $\Delta\varepsilon$ region around the initial choice ensured the best possible separation of clusters while reducing manual bias.
Resulting clusters from the DBSCAN algorithm were visualized using boxplots across all clusters as well as all data parameters.

Chapter 19

Results

19.1 Patient Evaluation

An overview of the clinical characteristics of the patient cohort was assembled in Table 19.1. The cohort represented an unequal amount of male and female sex (14/8). Every possible

Table 19.1: Clinical characteristics of the patient cohort. Values are given as n (%) or mean with standard deviation (STD).

	Total (n=22)
parox./pers. AF (#)	13/9
Sex m/f (#)	14/8
Age (y)	68±9
CHA_2D_2VASc	2.4±1.3
LVEF (%)	60.6±6.9
LAdiam long. (mm)	39.8±10.8
LAdiam plan. (mm)	23.6±8.7
IVSD (mm)	10.3±2.4
LVIDD (mm)	51.0±6.1

CHA_2D_2VASc score (1-5) was represented at least once within the cohort and the cohort revealed a wide range comorbidities (2.4±1.3). Ejection fraction was 60.6±6.9 %. Additionally anatomical dimensions of the left atrium (LA) were measured and are given in Table 19.1. A more detailed view of the patient-specific data is available in Appendix C.

The evaluation of conduction velocity (CV) and amplitude restitution in patients is explained with an example in Figure 19.1. The voltage map showed that the posterior atrial wall mostly displayed an amplitude above 0.5 mV, which by definition corresponds to healthy tissue. In addition, there were individually distributed small islands with voltages slightly below 0.5 mV (diseased tissue). The voltage map revealed that the anterior wall showed

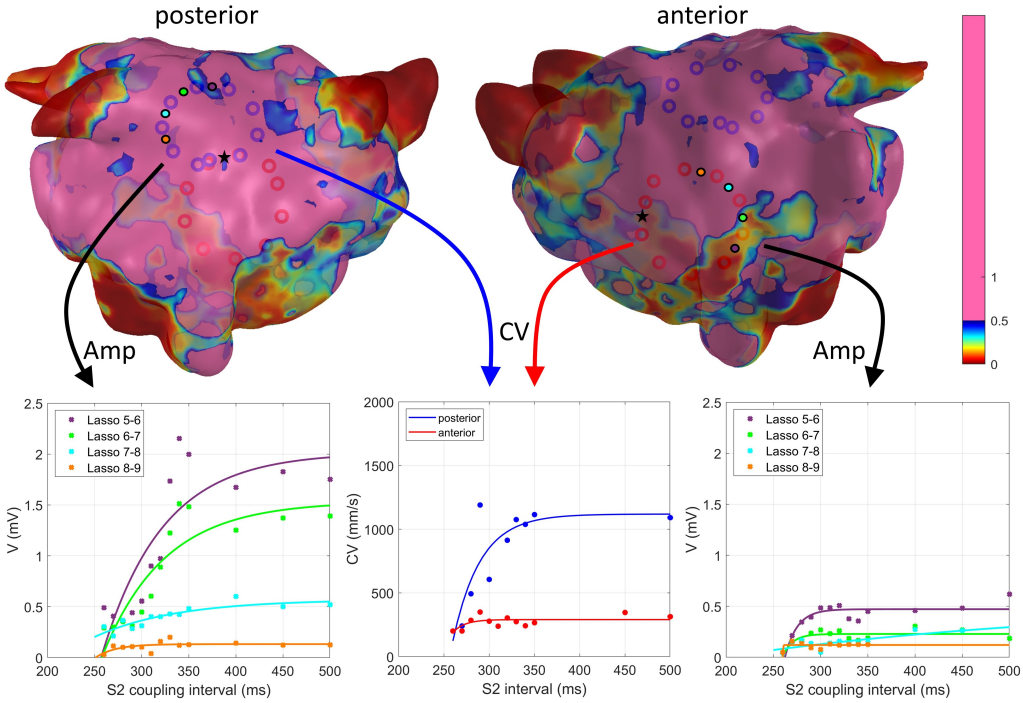

Figure 19.1: Amplitude and CV restitution information gathered from lasso catheter measurements. Voltage map with a threshold of $0.5\,\mathrm{mV}$ overlaid with catheter electrode positions on the posterior (blue circles) and anterior (red circles) atrial wall. Bipolar channel locations (black circles) are indicated between electrode locations and the circle center is color coded to match the respective amplitude restitution curves (bottom left & right). Channels without capture were omitted. Stimulation site is indicated with a black star. Multiple local activation time (LAT) measurements yielded one CV restitution curve (bottom middle) per measurement site.

extensive areas with voltages below $0.5\,\mathrm{mV}$.
From both measurement sites four channels provided amplitude signals. The results of the mono exponential fits are listed in Table 19.2. The posterior amplitude curves displayed large dispersion regarding their asymptote compared to the anterior region (Table 19.2 c columns). The CV restitution curve parameters a-c differed markedly between measurement locations. The parameters a-c will be used in the following to characterize the restitution curves and thereby the substrate characteristics.

19.2 Comparison of Posterior and Anterior Measurements

In the following the comparison between posterior and anterior atrial wall characteristics with regards to the parameters effective refractory period (ERP), amplitude and CV is presented.

Table 19.2: Exponential curve ($y = -a \cdot e^{-b\cdot(x-d)} + c$) fitting results for amplitude and CV curves.

	posterior				anterior			
amplitude	a (mV)	b (ms^{-1})	c (mV)	d (ms)	a (mV)	b (ms^{-1})	c (mV)	d (ms)
Lasso 5-6	5.66	0.016	2.02	190.24	2.23	0.077	0.47	241.99
Lasso 6-7	3.68	0.015	1.53	199.76	1.13	0.096	0.23	243.10
Lasso 7-8	1.08	0.012	0.57	157.26	0.67	0.003	0.54	115.23
Lasso 8-9	0.58	0.047	0.13	219.26	0.29	4.519	0.12	259.68
	posterior				anterior			
CV	a (mm/s)	b (ms^{-1})	c (mm/s)	d (ms)	a (mm/s)	b (ms^{-1})	c (mm/s)	d (ms)
long. CV	4939.92	0.033	1118.53	211.29	711.62	0.077	290.17	234.65

19.2.1 ERP Results

A total of 130 ERP measurements were divided according to their respective measurement location on the posterior and anterior wall of the atrial cavity (Figure 19.2). Both posterior and anterior ERP evaluation determined a median value of 280 ms, a Q1 of 250 ms and a Q3 of 300 ms. The posterior lower whisker was 210 ms while the anterior lower whisker measured 180 ms. The posterior upper whisker value of 360 ms was higher than the anterior whisker of 350 ms. The mean ERP was 277 ms and standard deviation (STD) was 38 ms.

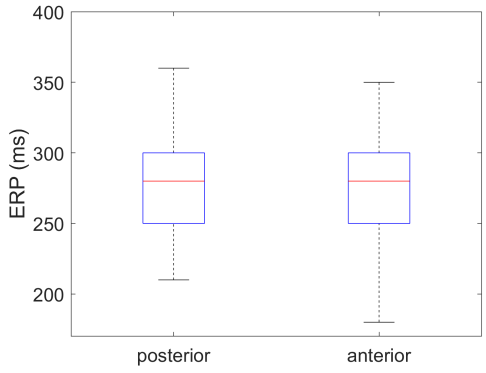

Figure 19.2: Effective refractory period (ERP) taken from clinical protocol entries of all evaluated patients respective to the measurement locations anterior and posterior atrial wall.

19.2.2 Amplitude

The results of the exponential fit parameters between the posterior and anterior location showed a slight difference in scale factor with median values of 3.63 mV and 2.07 mV, Q1 values of 1.49 mV and 0.76 mV and Q3 values of 10.22 mV and 6.73 mV. The posterior upper whisker value of 22.47 mV deviated strongly from the anterior upper whisker value of 15.66 mV (Figure 19.3).
The largest difference between posterior and anterior measurements was given by Q3 of the

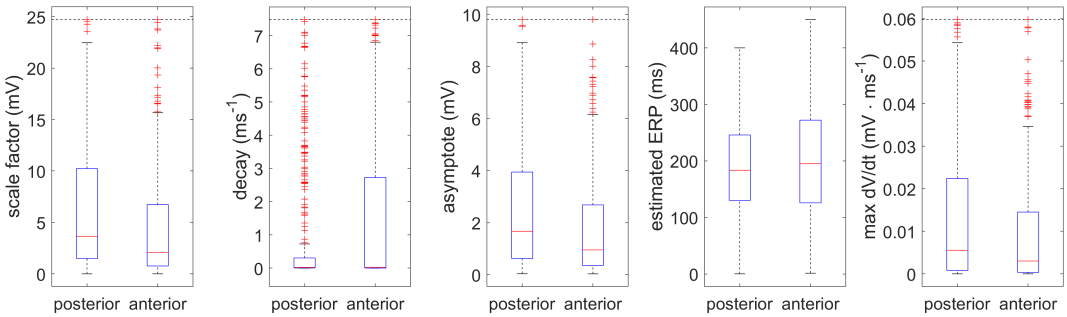

Figure 19.3: Amplitude fit results for patient cohort using an exponential function $y = -a \cdot e^{-b \cdot (x-d)} + c$, where a = scale factor, b = decay, c = asymptote, d = estimated ERP. Additionally, the maximum slope of the fit curve dV/dt is given. Extreme outliers (+) were cut above the grey horizontal dashed line for visualization purposes.

decay parameter. Posterior Q3 was 0.31 ms^{-1} while anterior Q3 was 2.73 ms^{-1}. Also, the upper whisker value of posterior (0.73 ms^{-1}) was lower than the anterior value (6.81 ms^{-1}). Posterior Q1 and median (0 ms^{-1}, 0.023 ms^{-1}) did not differ from anterior Q1 and median value (0 ms^{-1}, 0.025 ms^{-1}).
The asymptote values for Q1, median and Q3 differed slightly between posterior (0.62 mV, 1.66 mV, 3.94 mV) and anterior (0.35 mV, 0.95 mV, 2.68 mV).
The estimated ERP values of Q1, median and Q3 showed slight differences between posterior (130 ms, 183.32 ms, 245.73 ms) and anterior (125.69 ms, 195.01 ms, 271.99 ms) measurement location.
The maximum slope inside the pacing interval range to ERP showed the posterior region to have slightly larger slope values for Q1, median and Q3 (0 mV ms^{-1}, 0.006 mV ms^{-1}, 0.02 mV ms^{-1}) compared to the anterior measurement location (0 mV ms^{-1}, 0.003 mV ms^{-1}, 0.01 mV ms^{-1}).

19.2.3 CV

The results of the exponential fit parameters between the posterior and anterior location showed a slight difference in scale factor with median values of 2798.5 mm/s and

1982.98 mm/s, Q1 values of 1634.83 mm/s and 1245.34 mm/s and Q3 values of 4323.71 mm/s and 3333.57 mm/s. The posterior upper whisker value (6660.48 mm/s) deviated strongly from the anterior upper whisker value (5129.14 mm/s) (Figure 19.4).
Posterior anterior comparison of the decay parameter yielded no difference in Q1 (0.001 ms^{-1}

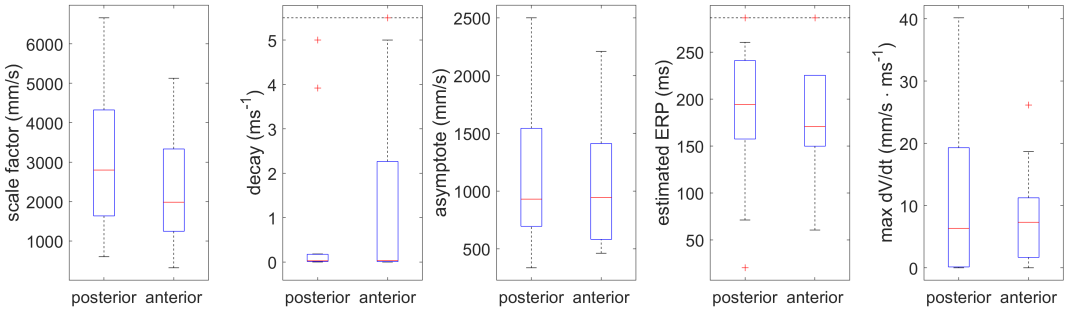

Figure 19.4: CV exponential fit ($y = -a \cdot e^{-b \cdot (x-d)} + c$) results for patient cohort, where a = scale factor, b = decay, c = asymptote, d = estimated ERP. Extreme outliers (+) were cut above the grey horizontal dashed line for visualization purposes.

vs 0 ms^{-1}) and only a slight difference in median (0.027 ms^{-1} vs 0.033 ms^{-1}). Q3 varied between posterior (0.18 ms^{-1}) and anterior (2.27 ms^{-1}).
Posterior anterior comparison of the asymptote parameter yielded a slight difference in Q1 (694.89 mm/s vs 582.03 mm/s), in median (929.95 mm/s vs 942.53 mm/s) and in Q3 between posterior (1542.7 mm/s) and anterior (1411.14 mm/s).
Posterior anterior comparison of the estimated ERP parameter yielded no differences in Q1 (157.37 ms vs 149.75 ms). Larger differences were present in the median values (194.15 ms vs 170.64 ms) and Q3 values between posterior (240.89 ms) and anterior (225.27 ms).
Posterior anterior comparison of the maximum slope (dCV/dt) parameter yielded differences in Q1 0.14 mm/s·ms^{-1} vs 1.68 mm/s·ms^{-1}) and in median (6.33 mm/s·ms^{-1} vs 7.32 mm/s·ms^{-1}). Q3 varied between posterior (19.29 mm/s·ms^{-1}) and anterior (11.24 mm/s·ms^{-1}).
The upper whiskers differed by 14 mm/s·ms^{-1} (40.15 mm/s·ms^{-1} vs 26.15 mm/s·ms^{-1})

19.3 Comparison of LV and Non-LV Measurements

In the following the results for the exponential fit parameters are presented according to their occurrence in low voltage (LV) and non-LV areas. LV and in non-LV areas were defined by comparing the exponential curve amplitude value at an S2 interval of 500 ms against a threshold of 0.5 mV.

19.3.1 Amplitude

Amplitude restitution results of exponential fit parameters were sorted into LV and non-LV areas (Figure 19.5). Comparison between LV and non-LV areas with regards to the scale

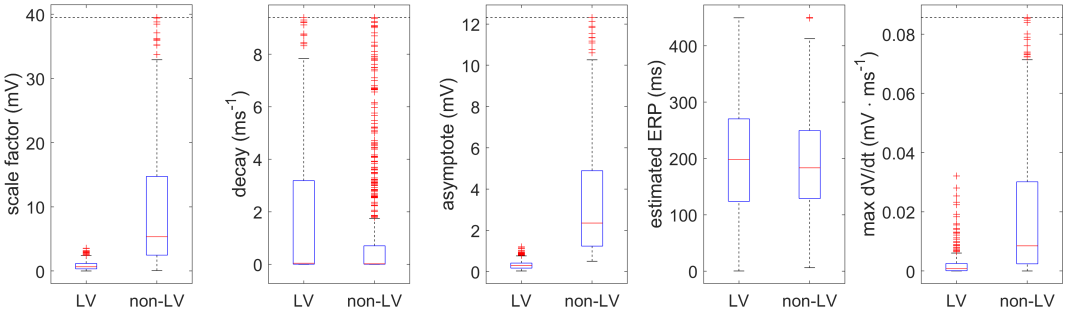

Figure 19.5: Amplitude fit results for patient cohort using an exponential function $y = -a \cdot e^{-b \cdot (x-d)} + c$, where a = scale factor, b = decay, c = asymptote, d = estimated ERP. Additionally, the maximum slope of the fit curve dV/dt is given. Extreme outliers (+) were cut above the grey horizontal dashed line for visualization purposes.

factor parameter yielded differences in Q1 (0.33 mV vs 2.47 mV). Differences were achieved in median (0.66 mV vs 5.34 mV) and Q3 between LV (1.17 mV) and non-LV (14.73 mV). Upper whisker values differed strongly (2.41 mV vs 32.92 mV).
Comparison between LV and non-LV areas with regards to the decay parameter yielded no differences in Q1 (0 ms^{-1} vs 0 ms^{-1}), slight differences in median (0.041 ms^{-1} vs 0.019 ms^{-1}). Q3 differed between LV (3.19 ms^{-1}) and non-LV (0.71 ms^{-1}). Upper whisker values differed strongly (7.83 ms^{-1} vs 1.75 ms^{-1}).
Comparison between LV and non-LV areas with regards to the asymptote parameter yielded differences in Q1 (0.17 mV vs 1.24 mV) and in median (0.294 mV vs 2.353 mV). Q3 differed between LV (0.41 mV) and non-LV (4.89 mV). Upper whisker values differed strongly (0.76 mV vs 10.26 mV).
Comparison between LV and non-LV areas with regards to the estimated ERP parameter yielded negligible differences in Q1 (123.78 ms vs 128.69 ms) and in median (197.9 ms vs 183.2 ms) as well as in Q3 between LV (270.03 ms) and non-LV (249.36 ms) areas.
Comparison between LV and non-LV areas with regards to the maximum slope parameter yielded differences in Q1 (0 mV ms^{-1} vs 0.002 mV ms^{-1}) and in median (0.001 mV ms^{-1} vs 0.009 mV ms^{-1}). Q3 differed between LV (0.003 mV ms^{-1}) and non-LV (0.03 mV ms^{-1}). Upper whisker values differed strongly (0.006 mV ms^{-1} vs 0.07 mV ms^{-1}).

19.3.2 CV

CV restitution results of exponential fit parameters were sorted into LV and non-LV areas (Figure 19.6). Comparison between LV and non-LV areas with regards to the scale factor parame-

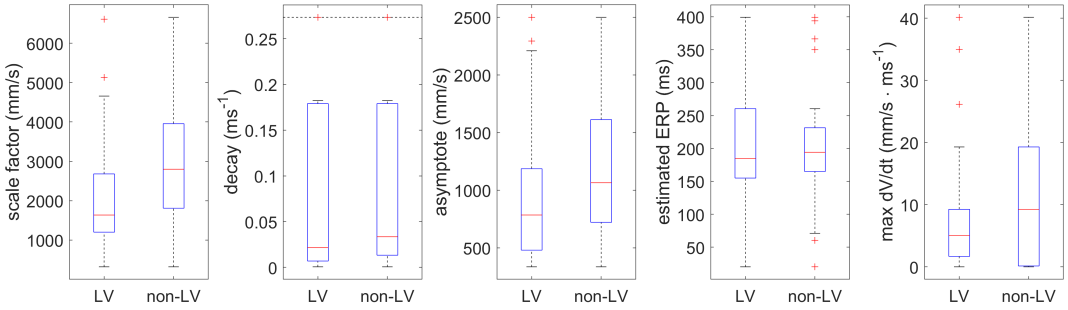

Figure 19.6: CV fit results for patient cohort using an exponential function $y = -a \cdot e^{-b \cdot (x-d)} + c$, where a = scale factor, b = decay, c = asymptote, d = estimated ERP. Additionally, the maximum slope of the fit curve dV/dt is given. Extreme outliers (+) were cut above the grey horizontal dashed line for visualization purposes.

ter yielded differences in Q1 (1199.67 mm/s vs 1808.38 mm/s). Differences were achieved in median (1634.83 mm/s vs 2798.5 mm/s) and Q3 between LV (2679.27 mm/s) and non-LV (3956.02 mm/s). Upper whisker values differed (4657.82 mm/s vs 6660.5 mm/s).
Comparison between LV and non-LV areas with regards to the decay parameter yielded slight differences in Q1 (0.007 ms^{-1} vs 0.013 ms^{-1}) and in median (0.022 ms^{-1} vs 0.033 ms^{-1}). Q3 was equal between LV (0.18 ms^{-1}) and non-LV (0.18 ms^{-1}).
Comparison between LV and non-LV areas with regards to the asymptote parameter yielded differences in Q1 (480.25 mm/s vs 721.23 mm/s) and in median (784.85 mm/s vs 1064.95 mm/s). Q3 differed between LV (1186.25 mm/s) and non-LV (1612.31 mm/s). Upper whisker values differed slightly (2209.15 mm/s vs 2499.3 mm/s).
Comparison between LV and non-LV areas with regards to the estimated ERP parameter yielded negligible differences in Q1 (155 ms vs 165 ms) and in median (184.79 ms vs 194.15 ms) as well as in Q3 between LV (260.38 ms) and non-LV (231.41 ms) areas.
Comparison between LV and non-LV areas with regards to the maximum slope parameter yielded differences in Q1 (1.68 mm/s·ms^{-1} vs 0.14 mm/s·ms^{-1}) and in median (5.04 mm/s·ms^{-1} vs 9.25 mm/s·ms^{-1}). Q3 differed between LV (9.26 mm/s·ms^{-1}) and non-LV (19.29 mm/s·ms^{-1}). Upper whisker values differed strongly (19.29 mm/s·ms^{-1} vs 40.15 mm/s·ms^{-1}).

19.4 Clustering

In the following the results of the clustering process using parameters gained from restitution curves are presented.

19.4.1 Amplitude

Amplitude clustering resulted in a single main cluster (C1) and an outlier cluster (C-1) when using the four parameters of the mono-exponential restitution fit as an input (Figure 19.7). Relevant values gained by using the four restitution curve parameters are listed in Table 19.3.

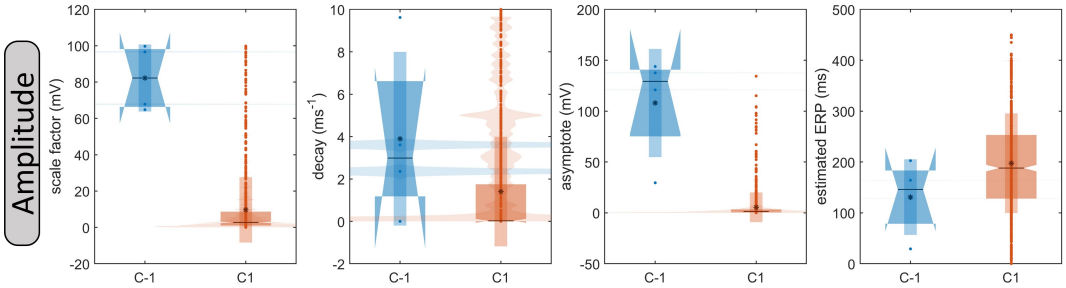

Figure 19.7: Amplitude clustering results. Using the four parameters from the mono-exponential fit. The input set resulted in a single main cluster (C1 red) and an outlier cluster (C-1 blue). Clusters show mean (black dot) and STD (thin vertical box) as well as median (black horizontal line) and interquartile range (IQR) (thick vertical box) with notch. Point density distribution is plotted for each boxplot along the vertical axis. For C-1 the notch is larger than the box size and folds back in on itself, highlighting the large uncertainty of the presented median value due to the small sample size.

The high STD of the outlier cluster showed that points from all value ranges were marked as outliers, thereby not forming a cluster in itself. The decay parameter showed low values near $0\,\mathrm{mV/ms}$ which results in nearly linear fits through the measurement points. Therefore, restitution curve morphology could range from anywhere between a straight line to an exponential curve.

Table 19.3: Values of the amplitude clustering (C-1, C1) using the four parameters (rows) of the mono-exponential fit as input. Reported values include Q1, median and Q3 as well as the mean and STD. Units for scale factor and asymptote are mV, for decay ms^{-1} and ms for the estimated ERP.

			Q1	Median	Q3	Mean	STD
Amplitude	scale factor (mV)	C-1	66.3164	82.2212	98.1588	82.2376	18.4691
		C1	1.0146	2.7410	8.6595	9.6582	17.9910
	decay (ms^{-1})	C-1	1.1792	2.9847	6.6151	3.8971	4.0975
		C1	0.0042	0.0240	1.7478	1.4066	2.5871
	asymptote (mV)	C-1	75.2086	129.2257	140.7349	107.9717	53.1653
		C1	0.4707	1.3552	3.3606	5.4786	14.6138
	estim. ERP (ms)	C-1	78.5580	146.0274	183.3655	130.9618	74.3935
		C1	128.0758	188.0540	253.0941	197.5565	97.9960

19.4.2 CV

CV clustering yields two main clusters (C1, C2) and an outlier cluster (C-1) when using the four parameters of the mono-exponential restitution fit as an input (Figure 19.8). All values

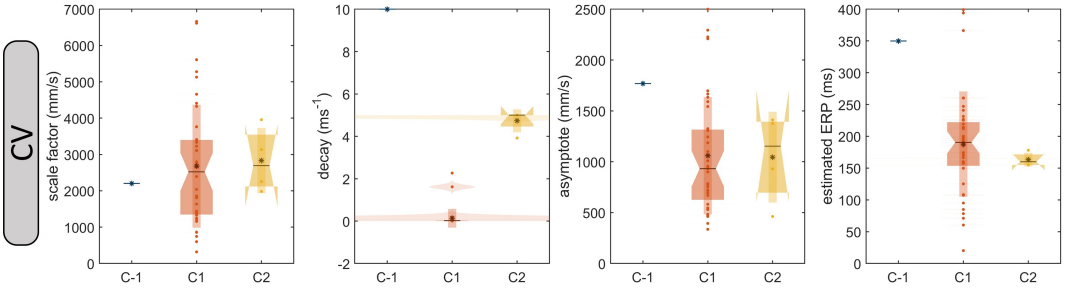

Figure 19.8: CV clustering results. The input parameter sets of all four CV exponential fit parameters resulted in two main clusters (C1 red and C2 yellow) and an outlier cluster (C-1 blue). Clusters showed mean (black dot) and STD (thin vertical box) as well as median (black horizontal line) and interquartile range (IQR) (thick vertical box) with notch. For C2 the notch was larger than the box size and folds back in on itself, highlighting the large uncertainty of the presented median value due to the small sample size.

of the boxplot using the four restitution curve parameters are listed in Table 19.4. The decay

Table 19.4: Values of the CV clustering (C-1, C1, C2) using the four parameters (rows) of the mono-exponential fit as input. Reported values include values Q1, median and Q3 as well as the mean and STD. Units for scale factor and asymptote are $\mathrm{mm/s}$, for decay ms^{-1} and ms for the estimated ERP.

			Q1	Median	Q3	Mean	STD
CV	scale factor (mm/s)	C-1	2203.9294	2203.9294	2203.9294	2203.9294	0.0000
		C1	1346.3986	2521.8910	3399.5245	2676.8754	1692.8679
		C2	2118.2314	2693.8270	3545.0995	2831.6655	896.3358
	decay (ms^{-1})	C-1	10.0000	10.0000	10.0000	10.0000	0.0000
		C1	0.0094	0.0197	0.0327	0.1323	0.4407
		C2	4.4597	5.0000	5.0000	4.7299	0.5403
	asymptote (mm/s)	C-1	1768.4686	1768.4686	1768.4686	1768.4686	0.0000
		C1	625.6426	931.7328	1315.8526	1058.8613	576.0089
		C2	696.0139	1152.9947	1393.5901	1044.8020	445.9734
	estim. ERP (ms)	C-1	349.9143	349.9143	349.9143	349.9143	0.0000
		C1	153.5608	190.4322	222.2756	187.7319	82.7654
		C2	155.0000	160.0000	171.5555	163.2777	10.9549

of the restitution curves showed the biggest difference with clearly separated interquartile range (IQR) between clusters. Clusters C2 and C3 contained 38 and 4 points. The asymptote parameter remained ambiguous depending on the choice of mean or median and is therefore not regarded as a distinctive parameter. The scale factor showed no big differences between clusters. The estimated ERP parameter for C2 was lower in mean, median and IQR.

19.4.3 Amp and CV

Clustering the combined input of amplitude and CV yielded two main clusters (C1, C2) and an outlier cluster (C-1) (Figure 19.9). Relevant values gained by using the four restitution curve parameters of amplitude combined with the four restitution parameters of CV are listed in Table 19.4. Patient BK02 created a single cluster and suppressed creation of further clusters (see Appendix F) and was therefore removed from evaluation. Clustering of the combined input of amplitude and CV restitution parameters of the mono-exponential fit revealed marked differences in amplitude scale factor and amplitude asymptote. Differences could be seen in the median of estimated ERP of both amplitude and CV, however the IQRs of both clusters slightly overlapped in these cases. The decay factor difference between both clusters was less consequential since medians were similar and IQR completely overlapped.

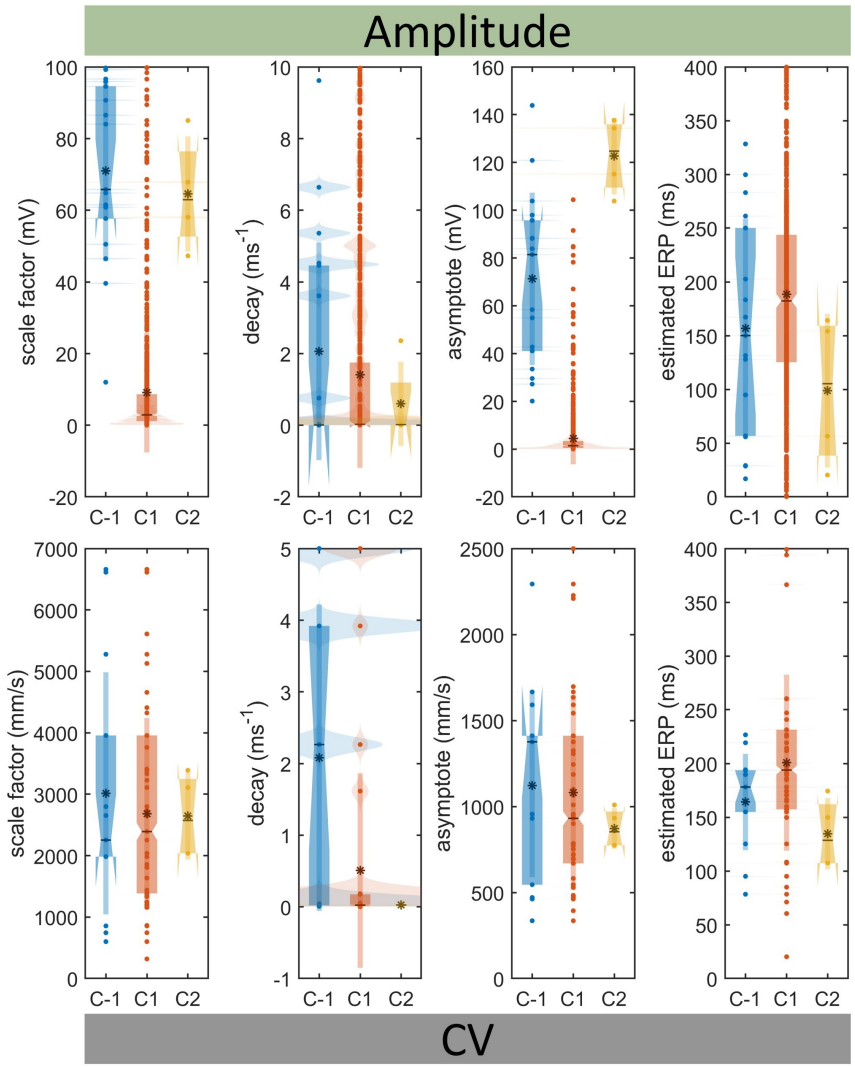

Figure 19.9: CV combined with amplitude clustering results. All exponential fit parameters of CV and amplitude restitution curves were used as an input parameter set and resulted in two main clusters (C1 red and C2 yellow) and an outlier cluster (C-1 blue). Clusters show mean (black dot) and standard deviation (thin vertical box) as well as median (black horizontal line) and IQR (thick vertical box) with notch. For C2 the notch is larger than the box size and folds back in on itself, highlighting the large uncertainty of the presented median value due to the small sample size.

Table 19.5: Values of the clustering using the four parameters (rows) of the mono-exponential fit of CV and amplitude as well. Reported values include values Q1, median and Q3 as well as the mean and STD. Units for amplitude scale factor and amplitude asymptote are mV, for CV scale factor and CV asymptote $\mathrm{mm/s}$ and in both cases the unit for decay is ms^{-1} and the estimated ERP unit is ms.

			Q1	Median	Q3	Mean	STD
Amplitude	scale factor (mV)	C-1	57.6947	65.7838	94.5585	70.9651	25.2201
		C1	1.1227	2.8815	8.6397	9.1173	16.7000
		C2	52.6501	62.9305	76.4312	64.5406	16.0347
	decay (ms^{-1})	C-1	0.0015	0.0075	4.4563	2.0592	3.0329
		C1	0.0039	0.0228	1.7478	1.4092	2.5988
		C2	0.0072	0.0151	1.1888	0.5980	1.1731
	asymptote (mV)	C-1	41.1009	81.4142	95.7245	71.2648	36.0748
		C1	0.4887	1.4284	3.3476	4.4714	10.8310
		C2	109.4806	124.7353	135.9735	122.7270	16.0301
	estim. ERP (ms)	C-1	56.7287	150.0281	250.0679	156.8748	101.9072
		C1	125.2717	182.3192	243.7988	188.5303	91.0584
		C2	38.3583	105.2937	159.1471	98.7527	71.3928
CV	scale factor ($\mathrm{mm/s}$)	C-1	1982.9841	2253.4787	3956.0237	3014.4224	1970.5483
		C1	1385.1442	2391.5962	3956.0237	2682.4507	1557.0804
		C2	2037.5718	2573.0937	3248.6460	2643.1089	708.5003
	decay (ms^{-1})	C-1	0.0193	2.2649	3.9194	2.0812	2.1371
		C1	0.0096	0.0235	0.1748	0.5056	1.3568
		C2	0.0212	0.0255	0.0292	0.0252	0.0047
	asymptote ($\mathrm{mm/s}$)	C-1	545.3403	1376.0434	1411.1369	1122.2438	533.1299
		C1	669.2537	931.0406	1411.1369	1081.5581	568.0024
		C2	773.6498	853.0374	970.7278	872.1888	118.0027
	estim. ERP (ms)	C-1	155.0000	178.1110	193.6709	164.2097	44.7988
		C1	157.3678	193.9092	231.4104	200.7542	81.8552
		C2	107.3190	128.5364	162.0646	134.6918	33.1672

Chapter 20

Discussion

20.1 Dissimilar Restitution Parameters for Posterior and Anterior Wall

It is well known, that there exist differences in fiber orientation between the posterior and anterior walls, as well as differences in anatomical structures and pathways such as the Bachmann bundle [30]. These differences suggest that there might be differences in substrate characteristics and susceptibility to pathology between both locations.
In literature contrasting observations were reported. For example, two in-vivo voltage measurements of Honarbakhsh et al. showed that the posterior wall was less susceptible to pathological tissue than the anterior wall. On the other hand, Marcus et al. found the posterior wall to incorporate more low voltage (LV) zones, and Miyamoto et al. found no difference between the two sites [16, 46, 61, 62]. In these studies, the threshold values 0.5 mV, 0.75 mV and 1.0 mV were used, respectively, to separate LV and non-LV zones. Additionally, different pacing rates were used, which is known to cause changes in amplitude as seen when comparing sinus rhythm (SR) and atrial fibrillation (AF) maps. These two factors make a comparison of studies challenging. This indicates that, evaluating patients at a single pacing rate and using a specific threshold value might not yield an optimal starting point for comparison of patient data.
Therefore, unlike in previous literature, in this work, restitution information was used to gain detailed information on tissue pathology and to include rate information and avoid the usage of a threshold.

Amplitude reveals differences between posterior and anterior wall:
In this work, restitution curves containing information on tissue rate dependency were obtained from both the posterior and anterior atrial walls to provide information on the tissue pathology. The curves were fitted using a mono-exponential curve with four parameters. Comparison of the fitting parameters for the posterior and anterior atrial wall showed that the posterior restitution curves displayed a slightly higher scale factor (Median: 3.63 mV vs

2.07 mV) and asymptote (Median: 1.66 mV vs 0.95 mV) but a lower decay value (Median: 0.023 ms^{-1} vs 0.025 ms^{-1}; Q3: 0.31 ms^{-1} vs 2.73 ms^{-1}). This means posterior restitution curves were generally higher in amplitude, had moderate curvature with increasing pacing rate, and displayed a larger interquartile range (IQR) for scale factor and asymptote compared to the anterior location. The larger IQR resulted in a greater spread of values and thus a more dispersed arrangement of the restitution curves compared to the anterior location (Figure 19.1).
This study is the first to evaluate amplitude restitution curves for prespecified locations in the atria. Most restitution studies address action potential duration (APD) and alternans on a single cell level in-silico or in-vitro using monophasic action potentials [22, 67, 145]. Besides single rate (SR) experiments highlighting cohort differences between posterior and anterior measurement locations, the author is unaware of any literature covering this topic up to date.

ERP was similar between posterior and anterior wall:
The effective refractory period (ERP) measured by the physicians (Figure 19.2) showed an equal median (280 ms) for both sites. Moreover, ERP values were within the expected ERP range (212 ms to 320 ms without antiarrhythmic drugs and 380 ms with antiarrhythmic drugs) for patients with AF found in literature [110, 146, 147]. The equality between both positions was confirmed reasonably well by the estimated ERP value obtained from the mono-exponential fit (183.32 ms vs 195.01 ms). The difference in absolute value between the ERP (Figure 19.2) and estimated ERP (Figure 19.3) values results from the fact that the estimated ERP described the intersection of the exponential fit with the x-axis. The estimated ERP is generally lower than the physiological ERP due to the mono-exponential function approximating the physiological restitution mechanism. Thus, a tradeoff was made between reflecting the trend and using as few parameters as possible to enable fitting of sparse measurements (no capture due to early ERP).
Jaïs et al determined a mean ERP of 253$\pm$21 ms [148]. To obtain this, they used multiple pacing sites to record the left atrium (LA) ERP at 2 to 4 different locations along the lateral wall or appendage, superior, posterior, and/or inferoseptal regions. In the presented study, a mean ERP of 277$\pm$38 ms was determined, which was higher than the ERP of Jaïs et al. Considering that Miyamoto et al. showed that the septal regions were highly pathological, it is likely that the mixture of measurement locations, especially the septal regions, used in the case of the study by Jaïs et al. resulted in a reduced overall ERP (253$\pm$21 ms) compared to our value (277$\pm$38 ms) [62, 148]. One assumption could be that the patient cohort in this study had a generally more healthy substrate and therefore no clear difference between posterior and anterior wall could be detected. However the voltagemaps (Appendix D.2) indicated a wide variety of underlying pathologies, refuting this point. This leads to the conclusion that the process of remodeling could change tissue properties of amplitude and conduction velocity (CV) while leaving the ERP unchanged. To expand on this a further study measuring the ERP at different locations inside the atria should be performed.

CV shows differences between posterior and anterior wall:
As already observed for amplitudes, CV restitution parameters also differed between posterior and anterior measurement locations. Posterior restitution curves had a higher scale factor (Median: 2798.5 mm/s vs 1982.98 mm/s) and an overall slightly higher maximal asymptote (Q3: 1542.7 mm/s vs 1411.14 mm/s), but an overall lower minimum decay value (Q3: 0.18 ms^{-1} vs 2.27 ms^{-1}) than the anterior measurements. Additionally, the estimated ERP was larger for posterior measurements (Median: 157.37 ms vs 149.75 ms). The values measured in this work indicate that the CV restitution curves at the posterior wall were generally of equal or slightly higher amplitude, but displayed a moderate curvature with increasing pacing rate compared with the curves of the anterior measurements.
Kurata et al. reported CV values of 790 mm/s at anterior and 990 mm/s at posterior measurement sites [142]. Data presented here follow the literature trend, however, the difference between measurement sites was not as prominent in the present results because the sample size of Kurata et al. being 13 times larger than the cohort used in this work (279 vs 22 patients).
The cohort used in this work had higher voltage and CV along the posterior wall compared to the anterior wall. However, the wide range of IQR in the measurements indicates that a broad range of values are possible for both regions. Given the high dependency on electrode positioning, number of sample points, and patient cohort size, a larger data set with a high density acquisition of restitution information is needed to confirm that amplitude and CV show significant differences between posterior and anterior atrial walls, whereas there is no difference for the ERP.

20.2 Restitution Parameters Distinguish Pathological Tissue Areas

Using the clinical threshold of 0.5 mV at a pacing rate of 500 ms for LV classification, all amplitude restitution curve parameters were divided into LV and non-LV areas. The scale factor (Median: 0.66 mV vs 5.34 mV) as well as the asymptote clearly distinguishes LV from non-LV areas (Median: 0.29 mV vs 2.35 mV). The decay parameter in LV areas had a larger IQR and was overall higher in LV areas than in non-LV areas (Q3: 3.19 ms^{-1} vs 0.71 ms^{-1}). Therefore, amplitude restitution curves near LV areas were, by definition, lower in asymptote and had a much sharper curvature ("cliff") compared to non-LV areas.
Similarly, CV restitution curves for LV areas showed a reduced scale factor (Median: 1634 mm/s vs 2798 mm/s) and asymptote (Median: 784.85 mm/s vs 1064.95 mm/s) compared to non-LV areas. The decay factor was slightly lower for LV zones (Median: 0.022 ms^{-1} vs 0.033 ms^{-1}), but was equal in IQR compared to non-LV areas. Consequently, CV restitution curves near LV areas were lower in asymptote and showed a moderate curvature.
Multiple studies exist that associate singular CV values with LV zones [16, 62, 124]. One clinical study using 50 patients by Miyamoto et al. refined this observation by correlation of CV across three defined LV intervals (LV<0.5 mV: 0.8 mm/s; LV0.5-0.75 mV: 1.2 mm/s;

LV0.75-1.0 mV: 1.5 mm/s), showing that a decrease in voltage is accompanied by a decrease in CV [62]. A further study by Honarbarkesh et al. additionally measured CV at four different pacing intervals and found that with decreasing voltage the curve flattens, e.g., decreases in decay. While the study presented here agreed with the general findings that with decreasing amplitude, CV decreases as well, the statement that the curve flattens was not as clear. In this study a slight tendency towards curve flattening was found, however, due to the equal IQR between LV and non-LV areas all curvatures were represented, leading to the conclusion that there could be a continuous transition between clinically defined LV and non-LV areas. A further study with higher resolution for high pacing rates is needed to characterize the rate of decline more profoundly between both locations, as currently this study indicates that a distinction of LV areas using the decay parameter alone may lead to wrong conclusions.

20.3 Enabling Easier Restitution Acquisition

From the data presented in this study, it can be concluded that the restitution properties were able to describe substrate characteristics. To obtain these values, it is necessary to collect a sufficient number of data points at a single location to allow for a subsequent fitting process. Measurement of a restitution curve at a single location is time-intensive and difficult due to hemodynamics and patient movement. This work showed that the maximum slope (dV/dt) is well suited to distinguish between pathological and non-pathological tissue (amplitude: $0.001\,\mathrm{mV\,ms^{-1}}$ vs $0.009\,\mathrm{mV\,ms^{-1}}$; CV: $5.04\,\mathrm{mm/s{\cdot}ms^{-1}}$ vs $9.25\,\mathrm{mm/s{\cdot}ms^{-1}}$) (Figure 19.5 and Figure 19.6). Thus, the maximum slope provided an equivalent indicative value compared to a complete restitution curve. The second indicative value from the restitution curve measurements was the asymptote.
In the following a more time-efficient method to gain insight into the restitution properties of the substrate is proposed which could be investigated in future. Firstly, the S1S2 protocol should be used at low pacing intervals of 180 ms (high rate) (as indicated by ERP measurements, Figure 19.2) and should be increased in small increments towards higher pacing intervals (lower rates). The first stimulation will most likely not yield any capture since the pacing interval will likely be smaller than the ERP of the tissue. The ERP will be determined by the onset of tissue activity after the gradually increased pacing intervals. Overall, only two consecutive atrial activities have to be acquired. These points represent the steepest part of the restitution curve and are thus used to calculate the maximum slope. Finally, a single S1S2 pulse will be given at a high pacing interval, e.g. 800 ms, to determine a surrogate value for the asymptote value. This method will allow more data to be collected while shortening the duration of the measurement process.

20.4 Clustering of Restitution Information

In literature, both LV areas and areas of slow CV are associated with pathological tissue [7, 9–11, 15, 21, 42, 44–46]. The presented work extends these reports by corresponding rate dependent information to these areas and demonstrates that there exist differences between amplitude and CV restitution curves at clinically defined LV and non-LV areas. Consequently, this work shows that the amplitude and CV restitution curves characterize the atrial substrate. In the scope of this work, amplitude, and CV restitution information from a cohort of patients were used to search for evidence of the formation of underlying substrate classes by using a clustering algorithm. This was done in three steps: First, only the four amplitude restitution parameters were used as input for the clustering algorithm, secondly, only CV parameters were used, and finally, all restitution parameters of amplitude and CV were combined and used.

Clustering amplitude parameters:
Using the four amplitude restitution parameters exclusively resulted in the formation of a single cluster, indicating that amplitude is a continuously changing parameter throughout the atrial tissue (Figure 19.7). This result is plausible since there are multiple remodeling pathways leading to altered ionic currents which is a continuous process [50, 149]. Therefore, the accumulation of multiple myocytes (tissue) should remain continuous. Ng et al. showed that the remodeling progression underlying AF is a continuous development process between paroxysmal to persistent AF [56]. Regarding the measurement procedure, the signal captured by a single electrode is the mean of the surrounding myocytes, which causes the signal to change continuously depending on the underlying tissue [150, 151]. In addition, the inclination of the catheter with respect to the surface affects the amplitude measurement [151]. Finally, movements of the catheter due to hemodynamics and contractions of the atria continuously change the distance of the electrode to the tissue. Therefore, in future it could be considered to evaluate amplitude restitution ex-vivo in a controlled environment. This would allow a preliminary analysis of the substrate for locations of fibrosis. Subsequent recording of highly sampled restitution curves could be performed without major patient induced measurement influences. This could be repeated for different pathological sites with different severity of pathology to obtain the change of restitution curve morphology depending on substrate pathology.

Clustering CV parameters:
Using the four CV restitution parameters for clustering resulted in two clusters (Figure 19.8). The two clusters differed mainly with respect to their decay parameter (Mean: $0.13\,\mathrm{ms}^{-1}$ vs $4.73\,\mathrm{ms}^{-1}$) and showed ambiguous results in the asymptote with equal mean ($1059\,\mathrm{mm/s}$ vs $1044\,\mathrm{mm/s}$) but higher median ($932\,\mathrm{mm/s}$ vs $1153\,\mathrm{mm/s}$). Thus, the clustering distinguished two types of CV curves independent of amplitude. The first cluster defined a restitution curve similar to chapter 20.2 with a moderate curvature, while the second cluster

described a restitution curve that was approximately linear through all pacing measurement points and displayed an instant drop ("cliff") at the ERP value.
These two types of restitution curves described tissue that is reactive to varying pacing rates and tissue that was rigid with regard to different pacing rate. The cluster with reactive tissue components contained a larger number of points (38 vs 4) and covered a larger range of values throughout all parameters compared to the rigid cluster. Compared to the amplitude clustering fewer data was available for the CV clustering since three measurements using all electrode signals were used to evaluate CV at a single location (e.g. for a 10 pole catheter: Amplitude: 10·3=30 values; CV: 1 value). Therefore, it is unclear whether the separation of clusters was due to lack of data in the transition zone between the two types of restitution curves described, or whether this was a valuable distinctive feature describing substrate characteristics. For the future an increased amount of measurements could be aimed at. However, additionally the catheter size should be reduced to enable a more pinpointed evaluation of substrate. This would allow a spatially more pinpointed measurement of previously identified fibrotic areas (e.g., using late gadolinium enhancement techniques) to gain restitution curve morphology depending on substrate pathology.

Clustering amplitude and CV parameters:
Using all amplitude as well as CV restitution parameters for clustering yielded two clusters (Figure 19.9). The first constitutes a broad range across all parameters overlapping with the second cluster at all parameters. The largest differentiation between the clusters was found in the asymptote parameter of the amplitude values (C1-Q3:3.35 mV vs C2-Q1:109.5 mV). However, the maximum value contained in the first cluster overlapped with the lowest value of the second cluster, suggesting that the division created here was due to insufficient sample size and that, in general, a continuous transition of curve parameters in both amplitude and CV is the more likely scenario for the pathological evolution of atrial substrate. This is also reflected in the phrase "AF begets AF", which describes that starting from an initially mild structural remodeling of the underlying tissue a continuously increasing detrimental remodeling leads to increasing tissue pathologies that perpetuate AF [48, 152].
The clustering of restitution parameters, as well as the range of restitution curves obtained in this work, suggests that the existing empirical approach of using thresholds to characterize tissue does not fully capture tissue characteristics. Rather, a rethinking of the empirical approach is suggested. The underlying biology of remodeling and wave propagation is continuous in nature and so is tissue characterization. This relates well to the study by Ng et al. on the transition between paroxysmal and persistent AF patients, which states that "...a range of fibrillation electrophenotypes exists along a continuous spectrum, and the predominant mechanism in an individual case is determined by the nature and extent of remodeling of the underlying substrate" [56].

20.5 Conclusion

Characterization of atrial substrate as well as knowledge of the various regional substrate characteristics are of important diagnostic and scientific value.
The goal of this study was threefold. Firstly, this work aimed to describe pathological areas using amplitude and CV restitution curves to discern differences between pathological and non-pathological substrate by using the clinical definition of pathological and non-pathological tissue as a first approach. This work has demonstrated that substrate can be characterized using restitution curves. Clinically defined LV zones are characterized by a reduced amplitude asymptote and a high decay parameter, whereas CV curves show a reduced CV asymptote and a high range of decay values. Therefore, in contrast to literature, this work found low CV curvature could be considered a sensitive, yet not highly specific criterion for defining LV areas.
Secondly, this work aimed to discern restitution differences within the atrial body at two different locations, the posterior and anterior atrial wall since literature reports of differences between posterior and anterior walls in amplitude and CV are inconclusive. In this work, the posterior atrial wall was found to contain amplitude and CV restitution curves with higher asymptote and more moderate curvature than the anterior atrial wall.
Lastly, to move beyond the empirically described manual threshold currently used, this study attempted to find naturally occurring clusters of substrate characteristics using restitution data from patients with AF. While clusters were present, their inadequate separation from each other indicated a continuous progression of the amplitude curves as well as the CV curves.
Overall, pathological, and non-pathological substrate show different restitution behavior. Therefore, restitution information can be used to distinguish different degrees of tissue pathology. This work suggests a continuous progression of restitution parameters, so the question of whether restitution information can be used to overcome the empirical threshold remains open and requires further investigation. To enable this, in this work, we proposed an easier and faster method for acquisition of restitution data which provides the same information content, which might enable acquisition of more data enabling larger study cohorts in future.

Chapter 21

Conclusion and Outlook

The main topic of this work was characterization of atrial substrate. Improving characterization of atrial substrate can increase knowledge of the substrate and its underlying mechanisms and subsequently can help clinicians determine correct sites to target for ablation and improve overall positive outcome of atrial fibrillation (AF) therapy. This work showed that successful termination sites of AF display distinct electrogram patterns with short local cycle lengths harboring fractionated and low-voltage potentials that are locally highly consistent and cover a majority of the local AF cycle length. Most of these areas also display pathologic delayed atrial late potentials and fractionated electrograms in sinus rhythm.

Additionally, this work demonstrated that substrate can further be characterized using restitution curves. Clinically defined low voltage (LV) zones are characterized by a reduced amplitude restitution asymptote and a high decay parameter, and conduction velocity (CV) curves show a reduced CV asymptote and a high range of decay values compared to non-LV zones. Overall, pathological, and non-pathological substrate show different restitution behavior. Therefore, restitution information can be used to broadly distinguish differing degrees of tissue pathology.

A natural clustering of tissue pathologies could not be found since clustering indicated a continuous progression of the amplitude curves as well as the CV curves. Therefore, the distinction between closely related disease states is most likely not as straightforward.

This leads to the following overall conclusion that pathological substrate can be determined and treated using either the proposed electrogram characteristics as a guideline or by acquiring restitution information of the local substrate.

The latter approach is still hampered by the time-intensive acquisition and complex evaluation of pacing protocol data. To alleviate this the noise-robust signal segmentation pipeline CVAR-Seg for the widely used S1S2 stimulation protocol was created and released as open source to the community. The pipeline components are modular and can be easily replaced by alternative methods according to the user's needs enabling automated, fast, and precise evaluation of restitution data of amplitude as well as CV data.

Regarding the acquisition of CV data, in this work local CV data was used to better characterize local substrate. In this context a novel method was proposed. The method is real-time capable and a valid consideration to implement in clinical electrophysiology systems. This

would enable instantaneous localized measurement of atrial substrate, gaining a CV map, an anisotropy ratio map, and a fiber map simultaneously during a mapping procedure. The information gathered could subsequently be used to diagnose the path and source of the arrhythmia and facilitate creation of a digital twin to investigate optimal ablation procedures.

Appendix A

Double Ellipse Results

Table A.1: Boxplot values of longitudinal CV estimation for in-silico LATs including first quartile (Q1), third quartile (Q3), interquartile range (IQR) and lower & upper whiskers (1.5 & 3.5 · IQR). The column of outliers is an amount and therefore without unit. All other values have the unit $\mathrm{mm/s}$.

Model_CV	Q3	Q1	3.5· IQR	1.5· IQR	IQR	median	# of outliers
P4-M3-O8_300	15.67	-11.66	33.32	-18.86	27.32	-6.49	0
P4-M3-O2_300	18.38	0.55	30.34	-11.4	17.83	5.26	0
P4-M1-O8_300	87.27	-15.23	133.76	-50.08	102.5	34.27	3
P5-M3-O8_300	33.35	-21.74	37.46	-34.89	55.09	7.85	0
P5-M1-O8_300	25.25	-34.05	65.44	-65.21	59.29	-5.66	2
B-M3-O8_300	167.73	64.27	218.91	32.26	103.46	101.36	0
B-M3-O2_300	96.28	86.11	107.45	71.72	10.16	91.31	0
B-M1-O8_300	1694.35	210.9	1694.35	0.27	1483.45	1694.35	0
P4-M3-O8_600	-2.9	-13.71	-0.95	-23.99	10.8	-11.77	2
P4-M3-O2_600	40.65	-19.49	89.46	-25.07	60.14	6.75	0
P4-M1-O8_600	68.3	-46.78	238.62	-97.01	115.08	20.04	0
P5-M3-O8_600	30.92	-23.62	53.66	-62.87	54.54	7.46	0
P5-M1-O8_600	24.98	-67.68	71.58	-118.67	92.67	-32.5	1
B-M3-O8_600	168.34	90.71	267.79	70.99	77.64	127.57	0
B-M3-O2_600	139.35	103.51	156.17	93.9	35.85	113.17	0
B-M1-O8_600	1405.95	238.69	1405.95	-10.83	1167.27	1405.95	0
P4-M3-O8_900	9.99	-23.1	55.31	-40.4	33.09	-2.75	0
P4-M3-O2_900	124.85	-14.4	290.76	-47.48	139.25	24.21	0
P4-M1-O8_900	147.52	-35.17	419.94	-124.37	182.69	-4.62	0
P5-M3-O8_900	102.22	45.92	108.7	-5.23	56.31	78.56	1
P5-M1-O8_900	89.88	-83.96	220.82	-150.58	173.84	-13.33	0
B-M3-O8_900	222.03	125.01	265.69	92.75	97.02	178.46	0
B-M3-O2_900	177.07	125.37	233.7	110.69	51.7	145.39	1
B-M1-O8_900	1103.05	365.73	1103.05	-26.84	737.32	1100.46	0

Table A.2: Boxplot values of fiber estimation for in-silico LATs including first quartile (Q1), third quartile (Q3), interquartile range (IQR) and lower & upper whiskers (1.5 & 3.5 · IQR). The column of outliers is an amount and therefore without unit. All other values have the unit °.

Model_FiberDegree	Q3	Q1	3.5· IQR	1.5· IQR	IQR	median	# of outliers
P4-M3-O8_0	-7.23	-11.49	-4.54	-11.49	4.26	-8.05	1
P4-M3-O2_0	-0.78	-1.96	-0.09	-2.18	1.19	-1.75	0
P4-M1-O8_0	8.67	-17.68	36.94	-37.77	26.35	-10.78	0
P5-M3-O8_0	0.59	-0.37	1.53	-0.53	0.97	0.02	0
P5-M1-O8_0	5.41	-2.07	9.76	-2.51	7.48	-0.75	3
B-M3-O8_0	7.22	4.94	8.49	4.46	2.28	6.18	0
B-M3-O2_0	11.3	11.11	11.3	11.05	0.19	11.15	1
B-M1-O8_0	8.54	-18.92	11.33	-32.96	27.45	1.62	0
P4-M3-O8_15	-4.24	-6.75	-4.24	-6.75	2.51	-5.37	2
P4-M3-O2_15	0.81	-2.26	1.17	-2.74	3.07	-0.34	0
P4-M1-O8_15	23.49	-5.47	44.96	-16.28	28.96	-1.07	0
P5-M3-O8_15	1.27	-0.55	1.65	-1.09	1.82	0.4	0
P5-M1-O8_15	4.62	-4.53	8.84	-5.08	9.15	-0.59	0
B-M3-O8_15	7.93	-5.55	8.74	-12.29	13.48	3.86	0
B-M3-O2_15	10.51	9.61	10.91	9.18	0.9	10.07	0
B-M1-O8_15	-7.86	-33.11	8.44	-37.38	25.25	-14.76	1
P4-M3-O8_30	-5.15	-8.15	-5.01	-8.15	3	-7.15	1
P4-M3-O2_30	0.04	-3.29	2.36	-5.23	3.33	-0.53	0
P4-M1-O8_30	4.24	-8.19	13.15	-20.77	12.43	-3.56	1
P5-M3-O8_30	0	-0.84	0	-0.84	0.83	-0.32	2
P5-M1-O8_30	0.99	-10.36	1.95	-14.4	11.35	-1.64	0
B-M3-O8_30	10.52	-13.45	15.08	-24.49	23.96	5.11	0
B-M3-O2_30	9.85	7.86	10.27	7.86	1.98	9.07	1
B-M1-O8_30	38.6	-29.61	42.42	-32.6	68.2	-23.97	0
P4-M3-O8_45	-2.69	-4.98	0.31	-7.37	2.3	-3.88	0
P4-M3-O2_45	-1.35	-4.98	-1.35	-5.85	3.63	-4	1
P4-M1-O8_45	-2.03	-13.24	8.5	-28.67	11.21	-9.57	0
P5-M3-O8_45	2.11	-0.24	2.18	-1.61	2.34	0.78	0
P5-M1-O8_45	0.92	-13.72	7.21	-17.33	14.64	-2.85	0
B-M3-O8_45	12.7	-11.75	19.43	-34.19	24.45	6.63	0
B-M3-O2_45	9.88	7.36	11.46	4.38	2.53	9.36	0
B-M1-O8_45	26.11	-40.06	44.12	-44.76	66.17	-1.23	0
P4-M3-O8_60	-0.28	-5.31	-0.28	-5.39	5.03	-4.07	1
P4-M3-O2_60	-3.94	-5.19	-3.94	-5.19	1.24	-4.59	2
P4-M1-O8_60	-0.67	-18.07	21.72	-42.64	17.4	-7.82	0
P5-M3-O8_60	0.59	-0.75	0.59	-1.93	1.34	-0.63	1
P5-M1-O8_60	3.27	-9.1	9.85	-22.22	12.37	-6.09	0
B-M3-O8_60	11.46	-0.98	16.07	-0.98	12.43	9.01	1
B-M3-O2_60	8.88	7.97	8.88	7.74	0.91	8.58	1
B-M1-O8_60	34.06	11.65	40.74	-16.23	22.41	28.77	0
P4-M3-O8_75	-3.61	-6.61	-3.61	-7.85	3	-4.11	1
P4-M3-O2_75	-0.24	-3.85	0.22	-4.62	3.61	-1.71	0
P4-M1-O8_75	-0.92	-12.56	-0.92	-26.82	11.64	-7.06	5
P5-M3-O8_75	-0.69	-1.34	-0.69	-1.41	0.65	-1.26	1
P5-M1-O8_75	5.42	-12.49	7.97	-23.28	17.91	-1.76	0
B-M3-O8_75	2.94	2.37	2.94	2.37	0.56	2.59	2
B-M3-O2_75	8.23	6.91	8.55	6.91	1.32	7.81	1
B-M1-O8_75	14.13	-3.12	25.38	-4.49	17.25	12.82	1
P4-M3-O8_90	-4.31	-8.32	-4.31	-9.83	4.02	-5.12	1
P4-M3-O2_90	1.01	-0.94	1.5	-1.9	1.95	0.7	0
P4-M1-O8_90	13.05	-12.02	41.69	-15.67	25.07	-5.3	0
P5-M3-O8_90	1.8	-0.66	2.16	-2.11	2.47	0.23	0
P5-M1-O8_90	4.72	-12.46	7.8	-21.03	17.18	1.12	0
B-M3-O8_90	-4.75	-12	-1.12	-12.47	7.25	-5.32	0
B-M3-O2_90	10	9.14	10.08	9.14	0.86	9.66	1
B-M1-O8_90	2.86	-18.04	10.51	-19.48	20.9	-2.8	1

Table A.3: Boxplot values of anisotropy factor (k) estimation for in-silico LATs including first quartile (Q1), third quartile (Q3), interquartile range (IQR) and lower & upper whiskers (1.5 & 3.5 · IQR). k is a ratio and therefore all values here are without unit.

Model_k	Q3	Q1	3.5· IQR	1.5· IQR	IQR	median	# of outliers
P4-M3-O8_1.3	-0.02	-0.05	0.01	-0.05	0.03	-0.03	4
P4-M3-O2_1.3	0.05	-0.04	0.14	-0.09	0.09	0.02	0
P4-M1-O8_1.3	0.47	0.03	0.65	-0.11	0.44	0.27	0
P5-M3-O8_1.3	0.24	0.13	0.35	-0.01	0.11	0.19	0
P5-M1-O8_1.3	0.45	0.09	0.95	-0.19	0.36	0.21	1
B-M3-O8_1.3	0.22	0	0.28	-0.13	0.22	0.06	0
B-M3-O2_1.3	0.03	-0.04	0.06	-0.08	0.07	0.02	0
B-M1-O8_1.3	1.76	0.21	3.59	-0.19	1.55	0.77	0
P4-M3-O8_1.8	-0.05	-0.29	0.12	-0.43	0.24	-0.16	0
P4-M3-O2_1.8	0.14	-0.21	0.35	-0.35	0.34	-0.03	0
P4-M1-O8_1.8	0.48	-0.31	1.24	-0.68	0.79	0.27	0
P5-M3-O8_1.8	0.58	-0.02	0.87	-0.26	0.59	0.24	0
P5-M1-O8_1.8	0.61	0.07	1.08	-0.45	0.54	0.31	0
B-M3-O8_1.8	0.67	0.14	1.2	-0.45	0.52	0.31	0
B-M3-O2_1.8	0.09	-0.21	0.47	-0.25	0.3	-0.02	0
B-M1-O8_1.8	1.48	-0.24	3.96	-0.74	1.72	0.58	6

Table A.4: Boxplot values of initial ellipse long axis (a0) of first (e1) and second (e2) electrode for in-silico LATs including first quartile (Q1), third quartile (Q3), interquartile range (IQR) and lower & upper whiskers (1.5 & 3.5 · IQR). The column of outliers is an amount and therefore without unit. All other values have the unit mm.

Model_electrode	Q3	Q1	3.5· IQR	1.5· IQR	IQR	median	# of outliers
P4-M3-O8_a0e1	0.6	-0.3	1.7	-1.26	0.9	0.29	3
P4-M3-O2_a0e1	0.34	-1.25	1.04	-2.51	1.6	-0.57	0
P4-M1-O8_a0e1	0.55	-1.37	1.87	-3.76	1.92	0	0
P5-M3-O8_a0e1	0.42	-1.5	2.87	-3.07	1.92	-0.53	0
P5-M1-O8_a0e1	1.47	-1.4	2.87	-3.38	2.88	0	0
P4-M3-O8_a0e2	2.83	2.13	3.22	1.48	0.69	2.59	3
P4-M3-O2_a0e2	2.63	1.08	3.01	0.31	1.55	1.78	0
P4-M1-O8_a0e2	2.76	0.88	3.4	-0.17	1.89	2.21	0
P5-M3-O8_a0e2	0.21	-0.68	1.25	-1.09	0.89	-0.34	0
P5-M1-O8_a0e2	0.63	-0.65	1.25	-1.48	1.29	0.12	0

Table A.5: Boxplot values of initial ellipse short axis (b0) of first (e1) and second (e2) electrode for in-silico LATs including first quartile (Q1), third quartile (Q3), interquartile range (IQR) and lower & upper whiskers (1.5 & 3.5 · IQR). The column of outliers is an amount and therefore without unit. All other values have the unit mm.

Model_electrode	Q3	Q1	3.5· IQR	1.5· IQR	IQR	median	# of outliers
P4-M3-O8_b0e1	1.19	0.06	2.37	-1.34	1.14	0.54	0
P4-M3-O2_b0e1	0.89	-0.59	1.64	-1.68	1.49	-0.06	0
P4-M1-O8_b0e1	0.39	-0.87	1.89	-2.19	1.26	-0.24	0
P5-M3-O8_b0e1	2.53	0.89	4.11	-1.48	1.64	1.73	7
P5-M1-O8_b0e1	2.68	0.82	4.11	-1.77	1.87	1.65	0
P4-M3-O8_b0e2	2.37	1.75	3.03	0.82	0.62	2	4
P4-M3-O2_b0e2	1.99	0.94	2.66	0.06	1.05	1.27	0
P4-M1-O8_b0e2	1.84	0.64	2.76	-0.4	1.2	1.21	0
P5-M3-O8_b0e2	1.27	0.52	1.85	-0.59	0.75	0.91	7
P5-M1-O8_b0e2	1.31	0.52	1.84	-0.6	0.79	0.92	1

Table A.6: Boxplot values of longitudinal CV estimation for perturbed LATs including first quartile (Q1), third quartile (Q3), interquartile range (IQR) and lower & upper whiskers (1.5 & 3.5 · IQR). The column of outliers is an amount and therefore without unit. All other values have the unit $\mathrm{mm/s}$.

Model_CV	Q3	Q1	3.5· IQR	1.5· IQR	IQR	median	# of outliers
P4-M3-O8_300	23.58	-8.38	29.98	-16.27	31.96	9.72	0
P4-M3-O2_300	33.31	-5.71	47.73	-12.36	39.02	16.78	0
P4-M1-O8_300	205.17	-18.69	275.38	-60.8	223.86	25.39	0
P5-M3-O8_300	30.73	4.02	41.15	-16.49	26.71	16.34	0
P5-M1-O8_300	35.24	-15.97	58.23	-81.15	51.22	20.57	1
B-M3-O8_300	215.01	76.52	215.01	68.13	138.49	115.64	3
B-M3-O2_300	117.21	99.38	133.8	74.93	17.84	109.13	0
B-M1-O8_300	1694.35	253.67	1694.35	6.33	1440.67	1694.35	0
P4-M3-O8_600	26.07	-14.98	80.3	-36.83	41.06	-4.29	0
P4-M3-O2_600	77.92	4.26	91.27	-1.98	73.66	64.29	0
P4-M1-O8_600	53.34	-40.59	98.54	-151.09	93.93	-17.81	6
P5-M3-O8_600	57.94	13.88	71.72	-32.67	44.06	35.92	0
P5-M1-O8_600	36.88	-70.13	117.58	-183.67	107.01	-13.31	3
B-M3-O8_600	196.5	125.71	196.5	117.73	70.78	150.74	3
B-M3-O2_600	203.61	141.39	230.01	107.66	62.22	173.42	0
B-M1-O8_600	1405.95	245.49	1405.95	19.17	1160.47	1405.95	0
P4-M3-O8_900	54.71	-20.44	166.57	-43.44	75.15	25.85	1
P4-M3-O2_900	203.01	89.63	263.24	32.13	113.39	156.88	2
P4-M1-O8_900	425.52	16.02	806.53	-401.88	409.5	107.11	0
P5-M3-O8_900	185.7	98.69	194.07	70.52	87.02	142.07	0
P5-M1-O8_900	9.76	-696.95	339.62	-696.95	706.71	-696.95	0
B-M3-O8_900	315.77	185.9	361.8	159.16	129.87	242.55	0
B-M3-O2_900	291.14	219.2	296.95	145.87	71.94	259.71	2
B-M1-O8_900	1103.05	449.38	1103.05	41.83	653.67	964.72	0

Table A.7: Boxplot values of fiber estimation for perturbed LATs including first quartile (Q1), third quartile (Q3), interquartile range (IQR) and lower & upper whiskers (1.5 & 3.5 · IQR). The column of outliers is an amount and therefore without unit. All other values have the unit °.

Model_FiberDegree	Q3	Q1	3.5· IQR	1.5· IQR	IQR	median	# of outliers
P4-M3-O8_0	1.73	-7.92	15.2	-11.35	9.64	-4.27	0
P4-M3-O2_0	6.9	-4.9	7.8	-15.82	11.8	5.76	0
P4-M1-O8_0	13.31	-18.41	38.74	-40.28	31.72	-0.14	0
P5-M3-O8_0	5.65	-0.16	6	-0.38	5.81	2.57	0
P5-M1-O8_0	6.03	-27.71	15.39	-40.48	33.75	3.75	0
B-M3-O8_0	5.92	3.73	6.17	2.53	2.19	5.04	0
B-M3-O2_0	13.83	11.4	17.03	11.32	2.42	12.39	0
B-M1-O8_0	9.58	-13.99	43.77	-21.41	23.57	3.44	0
P4-M3-O8_15	-2.45	-6.45	-2.45	-7.56	4	-3.59	1
P4-M3-O2_15	4.31	1.07	6.83	0.33	3.24	2.73	0
P4-M1-O8_15	25.34	-20.66	36.93	-35.12	46	6.5	0
P5-M3-O8_15	4.47	1.7	6.71	-0.63	2.76	3.29	0
P5-M1-O8_15	8.68	-8.57	33.43	-31.41	17.25	4.7	0
B-M3-O8_15	3.03	-13.23	5.84	-14.44	16.26	-0.75	0
B-M3-O2_15	16.86	13.05	20.43	11.67	3.8	14.26	0
B-M1-O8_15	4.34	-28.97	28.77	-43.61	33.31	-11.5	0
P4-M3-O8_30	-5.15	-7.62	-5.15	-9.96	2.47	-6.62	1
P4-M3-O2_30	3.08	1.32	3.08	1.25	1.76	2.01	1
P4-M1-O8_30	11.03	-3.36	32.19	-21.18	14.39	-1	3
P5-M3-O8_30	1.64	-1.42	3.16	-5.33	3.07	0.96	0
P5-M1-O8_30	7.13	-5.97	20.39	-10.16	13.1	0.67	1
B-M3-O8_30	3.66	-29.21	11.71	-30.16	32.88	0.72	0
B-M3-O2_30	15.59	12.58	17.34	12.58	3.01	13.47	1
B-M1-O8_30	13.77	-28.67	44.45	-44.35	42.45	-22.99	0
P4-M3-O8_45	-4.67	-7.64	-4.67	-10.56	2.97	-4.97	1
P4-M3-O2_45	13.9	0.65	14.47	-0.64	13.25	8.55	0
P4-M1-O8_45	8.02	-14.14	38.27	-30.34	22.17	-10.58	1
P5-M3-O8_45	-0.4	-8.91	3.47	-10.23	8.51	-1.84	0
P5-M1-O8_45	-1.14	-13.71	7.07	-22.17	12.57	-5.08	1
B-M3-O8_45	18.44	0.32	44.47	0.32	18.12	7.03	1
B-M3-O2_45	13.52	12.12	14.26	12.12	1.4	12.96	1
B-M1-O8_45	25.32	-39.28	43.8	-44.88	64.6	-18.01	0
P4-M3-O8_60	-3.93	-4.6	-3.93	-4.6	0.67	-4.41	2
P4-M3-O2_60	7.03	3.29	8.85	2.63	3.74	3.63	0
P4-M1-O8_60	12.6	-21.47	26.71	-44.53	34.06	-17.21	0
P5-M3-O8_60	6.44	-3.84	7.42	-4.11	10.28	1.59	0
P5-M1-O8_60	-7.01	-21.49	5.62	-31.04	14.47	-11.8	1
B-M3-O8_60	16.91	6.47	16.91	-6.95	10.44	9.57	1
B-M3-O2_60	10.83	8.89	12.98	8.88	1.94	10.35	0
B-M1-O8_60	39.15	11	40.07	-16.23	28.16	29.89	0
P4-M3-O8_75	-2.53	-9.28	2	-12.93	6.76	-4.87	0
P4-M3-O2_75	3.67	-2.99	4.53	-5.08	6.66	2.23	0
P4-M1-O8_75	9.73	-21.48	34.83	-40.43	31.21	2.65	0
P5-M3-O8_75	5.21	0.36	6.82	-4.03	4.85	1.36	0
P5-M1-O8_75	-8.05	-28	7.43	-42.65	19.96	-17.51	1
B-M3-O8_75	3.09	2.02	3.09	2.02	1.07	2.5	2
B-M3-O2_75	7.92	6.02	8.04	3.66	1.91	7.19	0
B-M1-O8_75	21.08	-3.93	26.15	-31.23	25.01	11.86	0
P4-M3-O8_90	-2.29	-7.5	-1.35	-7.5	5.21	-4.65	1
P4-M3-O2_90	-0.07	-2.86	0.91	-4.79	2.8	-0.51	0
P4-M1-O8_90	7.66	-16.65	34.43	-38.38	24.31	0.4	0
P5-M3-O8_90	4.46	-1.52	6.15	-2.71	5.98	2.77	0
P5-M1-O8_90	3.71	-18.27	26.68	-30.78	21.98	-11.66	0
B-M3-O8_90	-3.63	-14	0.64	-15.12	10.37	-4.56	0
B-M3-O2_90	8.5	6.19	8.75	3.38	2.31	7.73	0
B-M1-O8_90	9.67	-18.86	43.77	-20.17	28.53	1.09	0

Table A.8: Boxplot values of anisotropy factor (k) estimation for perturbed LATs including first quartile (Q1), third quartile (Q3), interquartile range (IQR) and lower & upper whiskers (1.5 & 3.5 · IQR).

Model_k	Q3	Q1	3.5· IQR	1.5· IQR	IQR	median	# of outliers
P4-M3-O8_1.3	0.03	-0.04	0.08	-0.09	0.08	-0.01	0
P4-M3-O2_1.3	0.14	-0.04	0.19	-0.08	0.18	0.09	0
P4-M1-O8_1.3	0.52	0.12	1.09	-0.19	0.4	0.28	1
P5-M3-O8_1.3	0.3	0.07	0.55	-0.02	0.23	0.22	0
P5-M1-O8_1.3	0.72	0.06	1.7	-0.3	0.66	0.25	0
B-M3-O8_1.3	0.23	0.07	0.29	-0.1	0.16	0.1	0
B-M3-O2_1.3	0.12	-0.02	0.21	-0.11	0.15	0.01	0
B-M1-O8_1.3	1.56	0.01	3.35	-0.3	1.56	0.64	0
P4-M3-O8_1.8	0.09	-0.28	0.53	-0.43	0.38	-0.1	0
P4-M3-O2_1.8	0.23	-0.2	0.47	-0.39	0.43	-0.06	1
P4-M1-O8_1.8	0.48	-0.34	1.24	-0.73	0.81	0.17	0
P5-M3-O8_1.8	0.68	0.09	0.94	-0.04	0.59	0.45	0
P5-M1-O8_1.8	0.74	0.01	1.24	-0.66	0.73	0.46	0
B-M3-O8_1.8	1.83	0.26	1.97	-0.12	1.57	0.61	4
B-M3-O2_1.8	0.15	-0.19	0.42	-0.26	0.34	-0.02	1
B-M1-O8_1.8	1.57	-0.43	4.55	-0.76	1.99	0.34	3

Table A.9: Boxplot values of initial ellipse long axis (a0) of first (e1) and second (e2) electrode for perturbed LATs including first quartile (Q1), third quartile (Q3), interquartile range (IQR) and lower & upper whiskers (1.5 & 3.5 · IQR). The column of outliers is an amount and therefore without unit. All other values have the unit mm.

Model_electrode	Q3	Q1	3.5· IQR	1.5· IQR	IQR	median	# of outliers
P4-M3-O8_a0e1	0.98	-0.72	1.87	-2.85	1.69	0.48	0
P4-M3-O2_a0e1	0.71	-1.23	1.87	-2.67	1.94	-0.07	0
P4-M1-O8_a0e1	0.68	-1.55	1.87	-3.76	2.23	-0.09	0
P5-M3-O8_a0e1	0.03	-1.52	1.79	-3.58	1.55	-0.81	0
P5-M1-O8_a0e1	0.29	-1.88	2.37	-3.76	2.17	-1.24	0
P4-M3-O8_a0e2	2.99	1.9	3.4	0.57	1.1	2.76	0
P4-M3-O2_a0e2	2.91	1.33	3.4	-0.17	1.58	2.5	0
P4-M1-O8_a0e2	2.81	0.66	3.4	0.08	2.15	2.33	0
P5-M3-O8_a0e2	-0.01	-0.74	1.02	-1.48	0.73	-0.44	0
P5-M1-O8_a0e2	0.2	-0.86	1.01	-1.48	1.06	-0.65	0

Table A.10: Boxplot values of initial ellipse short axis (b0) of first (e1) and second (e2) electrode for perturbed LATs including first quartile (Q1), third quartile (Q3), interquartile range (IQR) and lower & upper whiskers (1.5 & 3.5 · IQR). The column of outliers is an amount and therefore without unit. All other values have the unit mm.

Model_electrode	Q3	Q1	3.5· IQR	1.5· IQR	IQR	median	# of outliers
P4-M3-O8_b0e1	1.27	-0.32	1.85	-1.93	1.59	0.44	0
P4-M3-O2_b0e1	0.93	-0.52	1.97	-2.44	1.45	0.23	0
P4-M1-O8_b0e1	0.25	-0.91	1.89	-2.43	1.16	-0.17	0
P5-M3-O8_b0e1	3.14	1.02	4.11	-0.72	2.12	2.1	0
P5-M1-O8_b0e1	2.92	-1.21	4.11	-2.61	4.13	0.76	0
P4-M3-O8_b0e2	2.68	1.22	2.98	0.46	1.47	2	0
P4-M3-O2_b0e2	2.23	1.13	2.81	-0.22	1.1	1.68	0
P4-M1-O8_b0e2	1.67	0.58	3.31	-0.63	1.1	1.17	1
P5-M3-O8_b0e2	1.62	0.6	1.85	-0.22	1.02	1.01	0
P5-M1-O8_b0e2	1.4	-0.6	1.85	-0.99	1.99	0.43	0

Appendix **B**

Patient Protocol

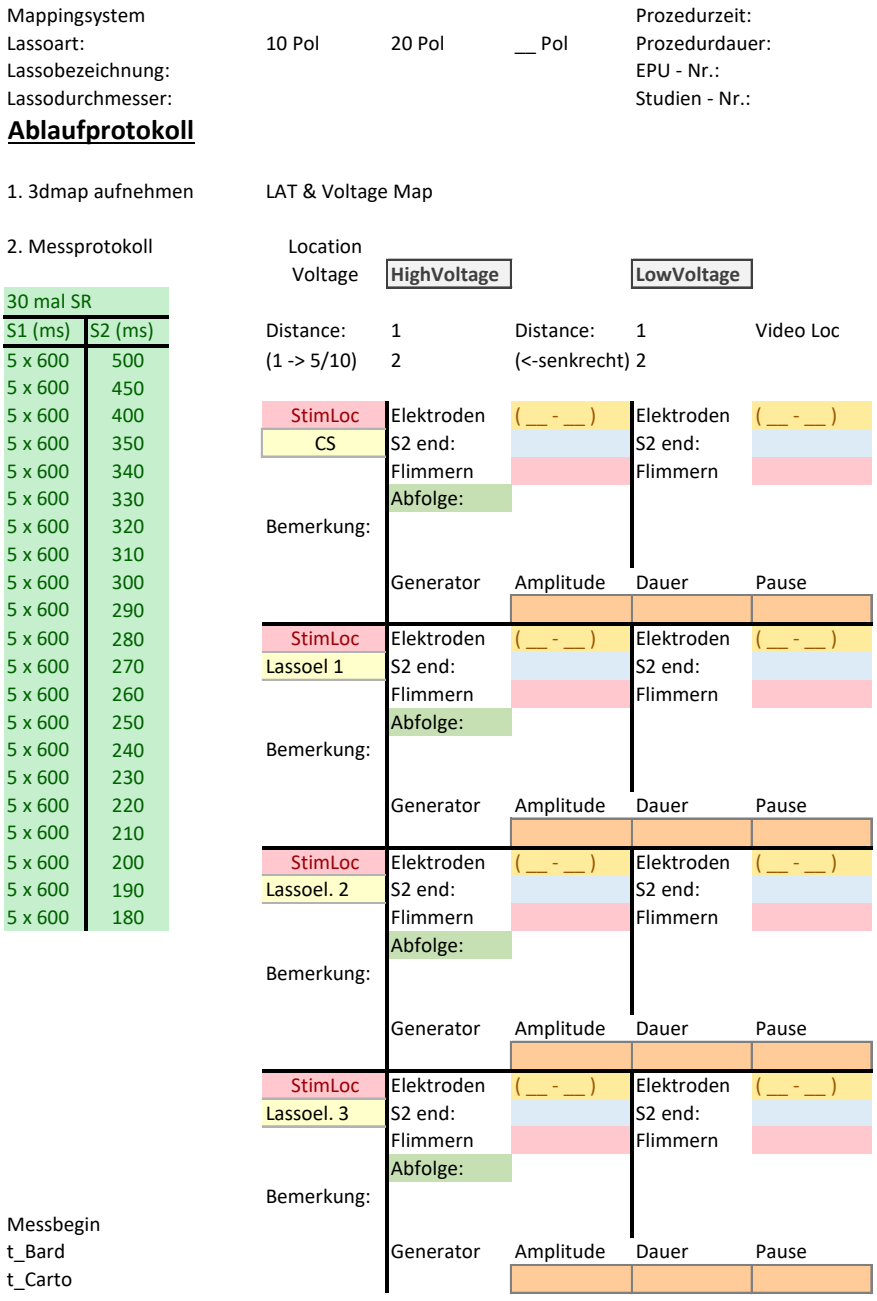

Figure B.1: Procedural Protocol for S1S2 restitution study at posterior and anterior atrial catheter locations. EPU-Number is for the doctors copy of the protocol only. For the digitalized protocol transferred to the IBT a study number (Studien-Nr.) was assigned.

Appendix C

Patient Characteristics

Table C.1: Extended version of patient data includes anatomical dimensions of left atria as well as detailed echocardiogram values.

	General						LAdiam			Echo			
Identifier	AFGroup	Sex	Age	Height	Weight	Score	long	plan	EF	IVSD	LVIDD	LVPWD	LAAVmax
BK_{0002}	pers	w	57	177	101	1	44	–	62	9	55	9	–
BK_{0005}	par	w	75	162	101	4	37	–	–	9	50	9	–
BK_{0006}	par	w	58	174	96	3	43	–	–	8	52	7	–
BK_{0007}	par	w	75	168	79	–	–	–	–	–	–	–	–
KA_{0001}	pers	m	54	192	122	3	0	26	50	11	59	10	35.3
KA_{0002}	pers	m	57	182	105	3	35	23	65	12	52	1369	69
KA_{0004}	par	m	82	168	82	1	42	0	65	8	53	10	64
KA_{0006}	par	m	59	182	91	2	51	35	65	8	58	10	45
KA_{0010}	pers	m	65	181	75	1	37	22	65	8	45	10	62
KA_{0012}	par	w	69	160	70	2	–	–	55	10	48	11	–
KA_{0013}	par	w	77	157	64	–	39	16	65	7	46	10	65.7
KA_{0014}	par	m	64	196	104	1	49	33	50	12	56	13	62
KA_{0015}	pers	m	78	178	84	5	43	26	45	16	54	11	44
KA_{0019}	pers	m	73	168	76	2	–	–	65	12	36	18	34.8
KA_{0021}	par	m	78	180	84	3	44	26	65	10	41	10	56
KA_{0022}	par	m	54	191	117	1	40	18	65	8	52	10	67
KA_{0023}	par	w	70	160	71	–	41	18	65	10	46	9	47.5
KA_{0024}	pers	m	70	188	85	1	43	28	50	12	52	–	–
KA_{0025}	par	m	71	186	89	4	38	24	60	9	61	10	63
KA_{0026}	par	w	70	162	88	3	43	35	65	11	51	11	45
KA_{0032}	pers	m	66	180	97	2	48	24	65	15	46	16	60.7
KA_{0033}	pers	m	81	187	88	4	–	–	65	11	57	14	–

Appendix D

Patient Voltage Maps

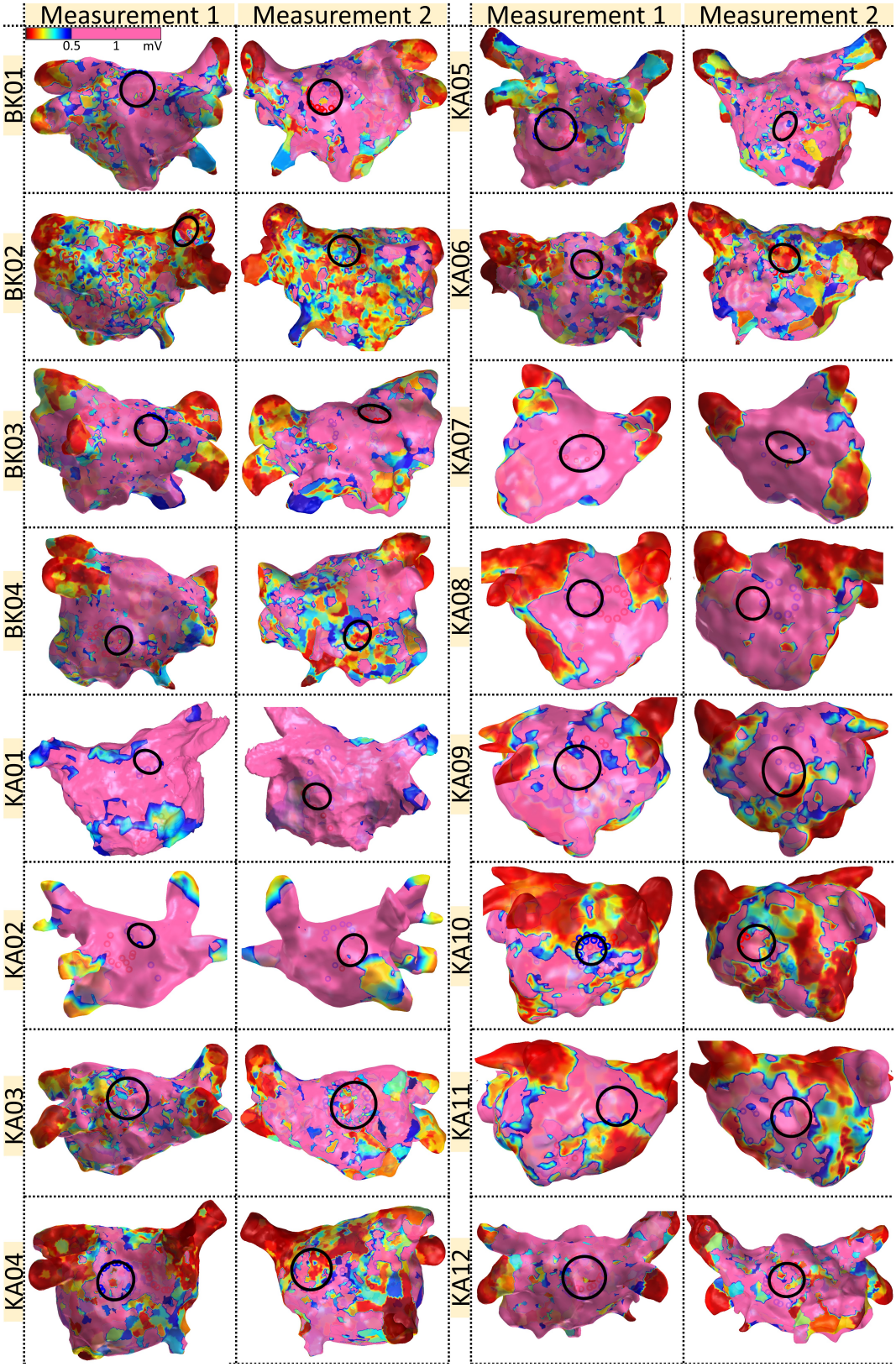

Figure D.1: Patient voltage maps are shown with a $0.5\,\mathrm{mV}$ threshold and both measurement areas are highlighted with a black circle.

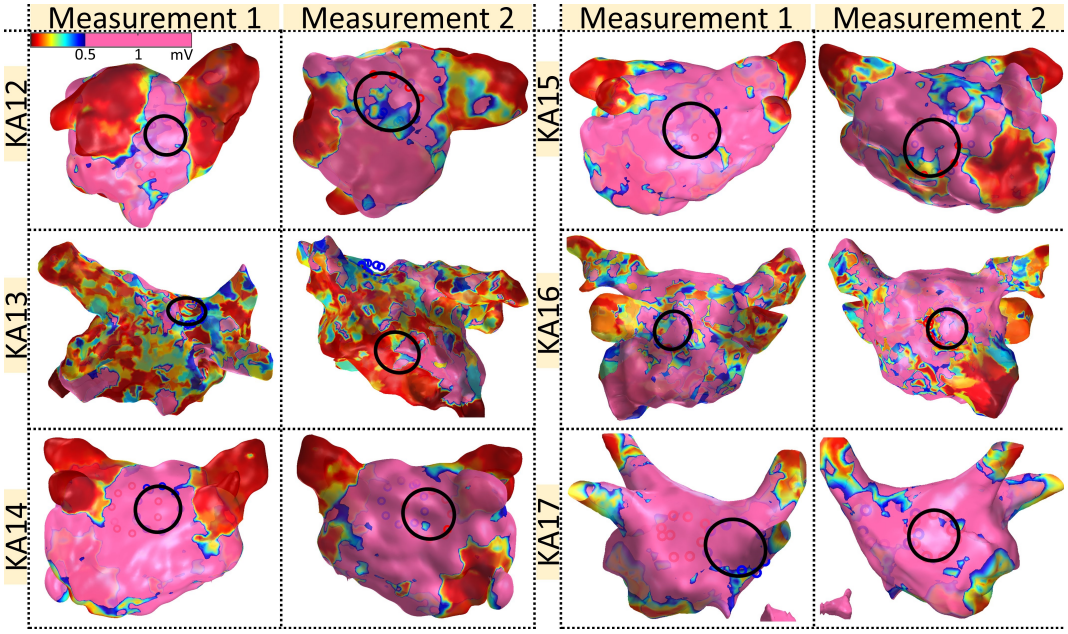

Figure D.2: Patient voltage maps are shown with an $0.5\,\mathrm{mV}$ threshold and both measurement areas are highlighted with a black circle.

Appendix E

Patient CV Curves

Figure E.1,Figure E.2 and Figure E.3 show CV curves of the inverse double ellipse method P4 for different atrial locations.

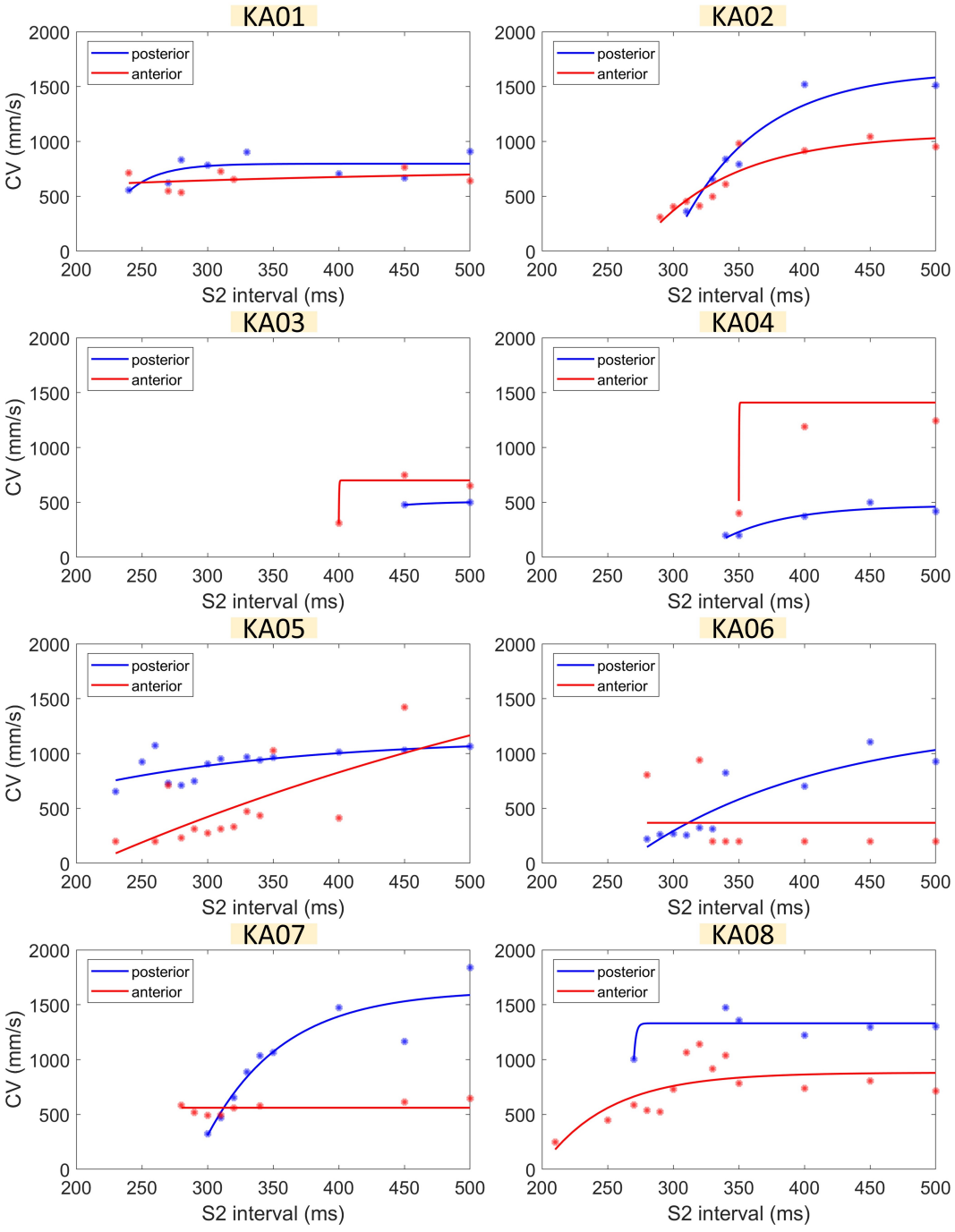

Figure E.1: Patient CV curves evaluated with the inverse double ellipse method P4.

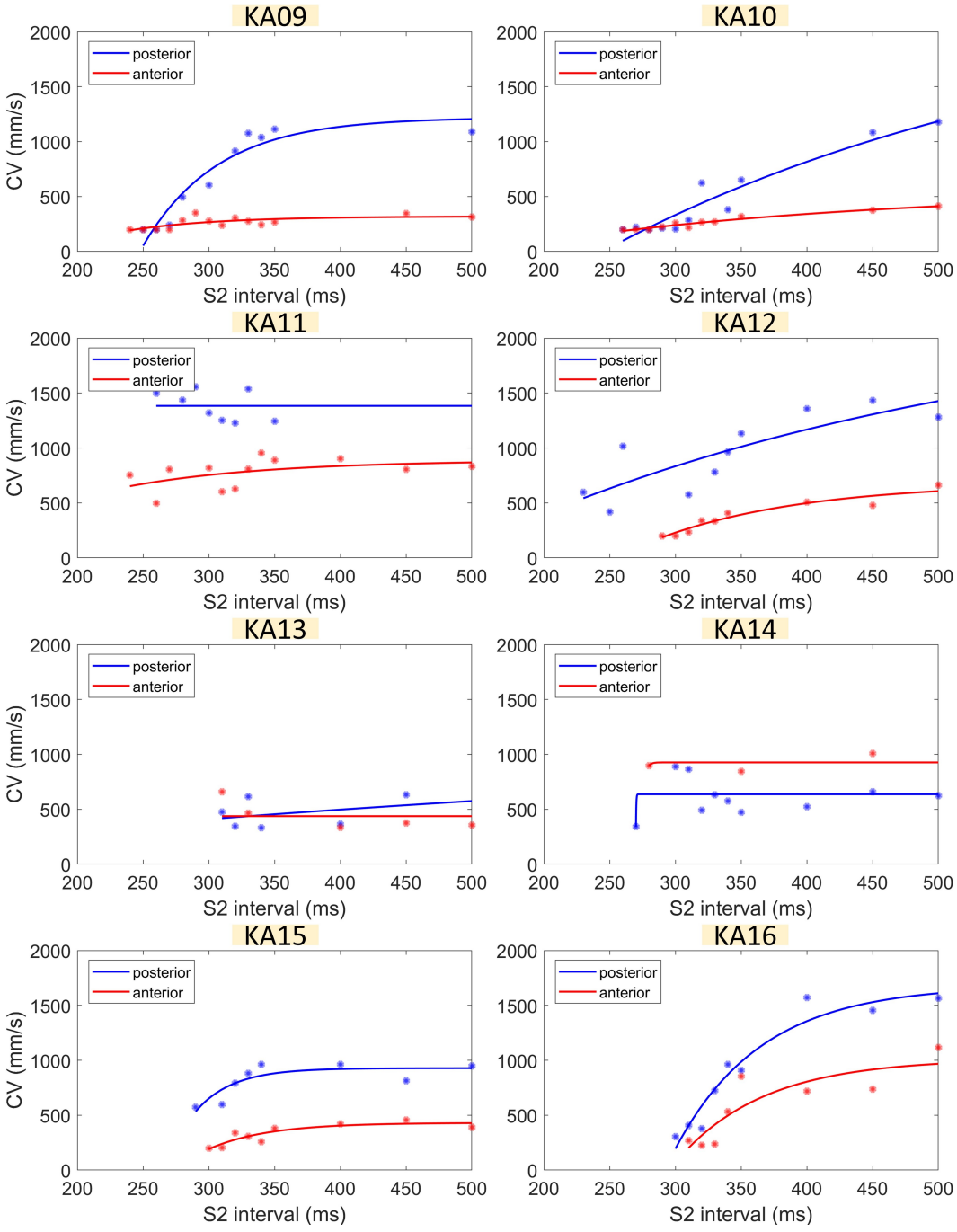

Figure E.2: Patient CV curves evaluated with the inverse double ellipse method P4.

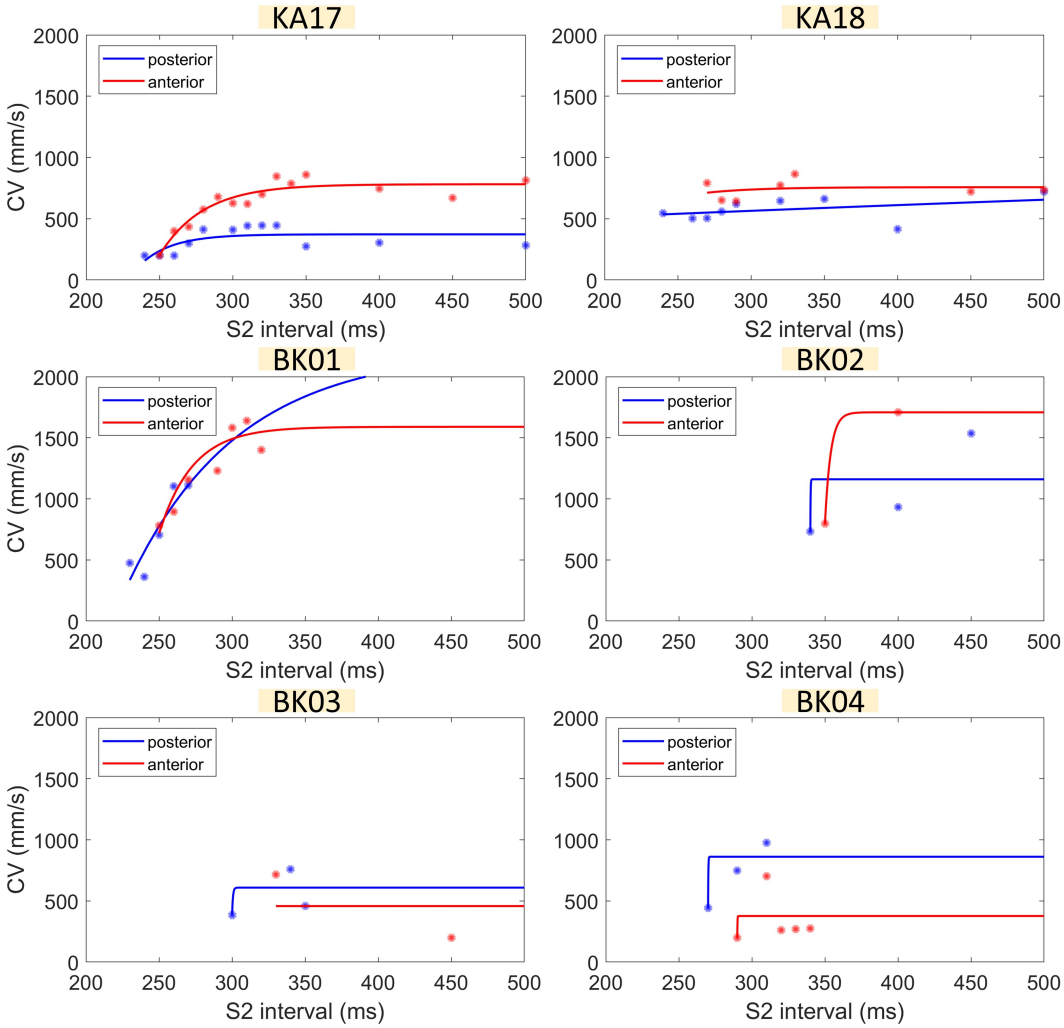

Figure E.3: Patient CV curves evaluated with the inverse double ellipse method P4.

Appendix F

Restitution Clustering

Figure F.1 shows the clustering of amplitude and conduction velocity (CV) restitution parameters before removal of Patient BK02. In the CV parameter sections BK02 always creates a single cluster suppressing further cluster development.

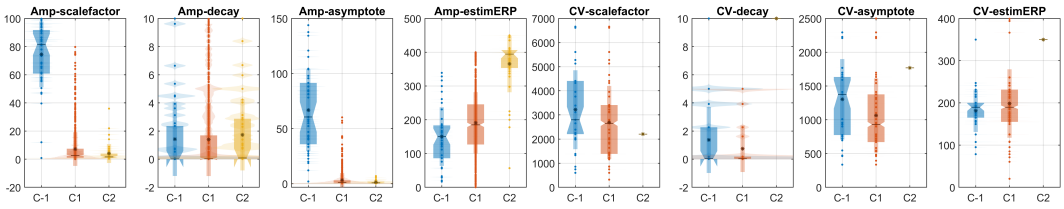

Figure F.1: Clustering result using amplitude and CV restitution parameters as input using all patient data.

References

[1] G. Hindricks, T. Potpara, N. Dagres, et al., "2020 ESC Guidelines for the diagnosis and management of atrial fibrillation developed in collaboration with the European Association for Cardio-Thoracic Surgery (EACTS)," *European Heart Journal*, vol. 42, no. 5, pp. 373–498, aug 2021.

[2] L. Staerk, B. Wang, S. R. Preis, et al., "Lifetime risk of atrial fibrillation according to optimal, borderline, or elevated levels of risk factors: Cohort study based on longitudinal data from the Framingham Heart Study," *BMJ (Online)*, vol. 361, no. 3, p. k1453, apr 2018.

[3] A. S. Go, E. M. Hylek, K. A. Phillips, et al., "Prevalence of diagnosed atrial fibrillation in adults: National implications for rhythm management and stroke prevention: The anticoagulation and risk factors in atrial fibrillation (ATRIA) study," *Journal of the American Medical Association*, vol. 285, no. 18, pp. 2370–2375, 2001.

[4] M. H. Kim, S. S. Johnston, B. C. Chu, et al., "Estimation of total incremental health care costs in patients with atrial fibrillation in the united states," *Circulation: Cardiovascular Quality and Outcomes*, vol. 4, no. 3, pp. 313–320, may 2011.

[5] L. Staerk, J. A. Sherer, D. Ko, et al., "Atrial Fibrillation: Epidemiology, Pathophysiology, Clinical Outcomes," *Circulation Research*, vol. 120, no. 9, pp. 1501–1517, apr 2017.

[6] B. A. J. Lawson, R. W. dos Santos, I. W. Turner, et al., "Homogenisation for the monodomain model in the presence of microscopic fibrotic structures," dec 2020.

[7] A. Jadidi, M. Nothstein, J. Chen, et al., "Specific Electrogram Characteristics Identify the Extra-Pulmonary Vein Arrhythmogenic Sources of Persistent Atrial Fibrillation – Characterization of the Arrhythmogenic Electrogram Patterns During Atrial Fibrillation and Sinus Rhythm," *Nature Scientific Reports*, vol. 10, no. 1, 2020.

[8] J. Heijman, D. Linz, and U. Schotten, "Dynamics of Atrial Fibrillation Mechanisms and Comorbidities," *Annual Review of Physiology*, vol. 83, no. 1, pp. 83–106, feb 2021.

[9] A. S. Jadidi, H. Cochet, A. J. Shah, et al., "Inverse relationship between fractionated electrograms and atrial fibrosis in persistent atrial fibrillation: Combined magnetic resonance imaging and high-density mapping," *Journal of the American College of Cardiology*, vol. 62, no. 9, pp. 802–812, aug 2013.

[10] M. Rodríguez-Mañero, M. Valderrábano, A. Baluja, et al., "Validating Left Atrial Low Voltage Areas During Atrial Fibrillation and Atrial Flutter Using Multielectrode Automated Electroanatomic Mapping," *JACC: Clinical Electrophysiology*, vol. 4, no. 12, pp. 1541–1552, dec 2018.

[11] G. Caixal, F. Alarcon, T. F. Althoff, et al., "Accuracy of left atrial fibrosis detection with cardiac magnetic resonance: Correlation of late gadolinium enhancement with endocardial voltage and conduction velocity," *Europace*, vol. 23, no. 3, pp. 380–388, nov 2021.

[12] J. C. Nielsen, A. Johannessen, P. Raatikainen, et al., "Radiofrequency Ablation as Initial Therapy in Paroxysmal Atrial Fibrillation," *Survey of Anesthesiology*, vol. 58, no. 1, pp. 53–54, 2014.

[13] A. G. Carrizo and C. A. Morillo, "Catheter Ablation as First-Line Therapy for Atrial Fibrillation: Ready for Prime-Time?" *Current Cardiology Reports*, vol. 18, no. 8, 2016.

[14] A. Schade, L. Costello-Boerrigter, F. Steinborn, et al., "Voltage-guided ablation in persistent atrial fibrillation—favorable 1-year outcome and predictors," *Journal of Interventional Cardiac Electrophysiology*, oct 2020.

[15] T. Kawara, R. Derksen, J. R. De Groot, et al., "Activation delay after premature stimulation in chronically diseased human myocardium relates to the architecture of interstitial fibrosis," *Circulation*, vol. 104, no. 25, pp. 3069–3075, dec 2001.

[16] S. Honarbakhsh, R. J. Schilling, M. Orini, et al., "Left atrial scarring and conduction velocity dynamics: Rate dependent conduction slowing predicts sites of localized reentrant atrial tachycardias," *International Journal of Cardiology*, vol. 278, pp. 114–119, mar 2019.

[17] A. Yagishita, Y. Takahashi, M. Kawabata, et al., "Utility of a ripple map for the interpretation of atrial propagation during atrial tachycardia," *Journal of Interventional Cardiac Electrophysiology*, vol. 56, no. 3, pp. 249–257, dec 2019.

[18] C. H. Roney, C. D. Cantwell, N. A. Qureshi, et al., "An automated algorithm for determining conduction velocity, wavefront direction and origin of focal cardiac arrhythmias using a multipolar catheter," in *2014 36th Annual International Conference of the IEEE Engineering in Medicine and Biology Society, EMBC 2014*. IEEE, aug 2014, pp. 1583–1586.

[19] C. H. Roney, J. Whitaker, I. Sim, et al., "A technique for measuring anisotropy in atrial conduction to estimate conduction velocity and atrial fibre direction," *Computers in Biology and Medicine*, vol. 104, pp. 278–290, jan 2019.

[20] S. E. Williams, J. L. Harrison, H. Chubb, et al., "Local activation time sampling density for atrial tachycardia contact mapping: How much is enough?" *Europace*, vol. 20, no. 2, pp. e11–e20, feb 2018.

[21] A. S. Jadidi, H. Lehrmann, C. Keyl, et al., "Ablation of Persistent Atrial Fibrillation Targeting Low-Voltage Areas with Selective Activation Characteristics," *Circulation: Arrhythmia and Electrophysiology*, vol. 9, no. 3, mar 2016.

[22] M. Zaniboni, "Short-term action potential memory and electrical restitution: A cellular computational study on the stability of cardiac repolarization under dynamic pacing," *PLoS ONE*, vol. 13, no. 3, p. e0193416, mar 2018.

[23] J. N. Weiss, P. S. Chen, Z. Qu, et al., "Electrical restitution and cardiac fibrillation," *Journal of Cardiovascular Electrophysiology*, vol. 13, no. 3, pp. 292–295, 2002.

[24] B. S. Kim, Y. H. Kim, G. S. Hwang, et al., "Action potential duration restitution kinetics in human atrial fibrillation," *Journal of the American College of Cardiology*, vol. 39, no. 8, pp. 1329–1336, apr 2002.

[25] M. R. Franz, "The Electrical Restitution Curve Revisited: Steep or Flat Slope - Which is Better?" *Journal of Cardiovascular Electrophysiology*, vol. 14, no. 10 SUPPL., pp. S140–S147, oct 2003.

[26] F. M. Weber, A. Luik, C. Schilling, et al., "Conduction velocity restitution of the human atriuman-An efficient measurement protocol for clinical electrophysiological studies," *IEEE Transactions on Biomedical Engineering*, vol. 58, no. 9, pp. 2648–2655, sep 2011.

[27] Wikimedia Commons, "File:Diagram of the human heart (cropped) de.svg — Wikimedia Commons{,} the free media repository," 2021.

[28] Staff, "Medical gallery of Blausen Medical 2014," *WikiJournal of Medicine*, vol. 1, no. 2, 2014.

[29] R. J. Hunter, Y. Liu, Y. Lu, et al., "Left atrial wall stress distribution and its relationship to electrophysiologic remodeling in persistent atrial fibrillation," *Circulation: Arrhythmia and Electrophysiology*, vol. 5, no. 2, pp. 351–360, apr 2012.

[30] D. Sánchez-Quintana, J. R. López-Mínguez, Y. Macías, et al., "Left atrial anatomy relevant to catheter ablation," *Cardiology Research and Practice*, vol. 2014, pp. 1–17, jun 2014.

[31] J. Rettinger, S. Schwarz, and W. Schwarz, *Electrophysiology: Basics, modern approaches and applications*. Cham: Springer International Publishing, 2016.

[32] J. Eckstein, B. Maesen, D. Linz, et al., "Time course and mechanisms of endo-epicardial electrical dissociation during atrial fibrillation in the goat," *Cardiovascular Research*, vol. 89, no. 4, pp. 816–824, mar 2011.

[33] S. Verheule, J. Eckstein, D. Linz, et al., "Role of endo-epicardial dissociation of electrical activity and transmural conduction in the development of persistent atrial fibrillation," *Progress in Biophysics and Molecular Biology*, vol. 115, no. 2-3, pp. 173–185, aug 2014.

[34] A. J. Pope, G. B. Sands, B. H. Smaill, et al., "Three-dimensional transmural organization of perimysial collagen in the heart," *American Journal of Physiology - Heart and Circulatory Physiology*, vol. 295, no. 3, pp. H1243–H1252, sep 2008.

[35] R. H. Hoyt, M. L. Cohen, and J. E. Saffitz, "Distribution and three-dimensional structure of intercellular junctions in canine myocardium," *Circulation Research*, vol. 64, no. 3, pp. 563–574, 1989.

[36] T. A. Van Veen, H. V. Van Rijen, and T. Opthof, "Cardiac gap junction channels: Modulation of expression and channel properties," *Cardiovascular Research*, vol. 51, no. 2, pp. 217–229, aug 2001.

[37] C. D. Cantwell, C. H. Roney, F. S. Ng, et al., "Techniques for automated local activation time annotation and conduction velocity estimation in cardiac mapping," *Computers in Biology and Medicine*, vol. 65, pp. 229–242, oct 2015.

[38] J. A. Jansen, T. A. van Veen, J. M. de Bakker, et al., "Cardiac connexins and impulse propagation," *Journal of Molecular and Cellular Cardiology*, vol. 48, no. 1, pp. 76–82, jan 2010.

[39] P. Kanagaratnam, S. Rothery, P. Patel, et al., "Relative expression of immunolocalized connexins 40 and 43 correlates with human atrial conduction properties," *Journal of the American College of Cardiology*, vol. 39, no. 1, pp. 116–123, 2002.

[40] Y. Zheng, Y. Xia, J. Carlson, et al., "Atrial average conduction velocity in patients with and without paroxysmal atrial fibrillation," *Clinical Physiology and Functional Imaging*, vol. 37, no. 6, pp. 596–601, nov 2017.

[41] S. Prabhu, A. Voskoboinik, A. J. McLellan, et al., "A comparison of the electrophysiologic and electroanatomic characteristics between the right and left atrium in persistent atrial fibrillation: Is the right atrium a window into the left?" *Journal of Cardiovascular Electrophysiology*, vol. 28, no. 10, pp. 1109–1116, oct 2017.

[42] V. Jacquemet and C. S. Henriquez, "Genesis of complex fractionated atrial electrograms in zones of slow conduction: A computer model of microfibrosis," *Heart Rhythm*, vol. 6, no. 6, pp. 803–810, jun 2009.

[43] M. S. Spach, J. F. Heidlage, P. C. Dolber, et al., "Electrophysiological effects of remodeling cardiac gap junctions and cell size. Experimental and model studies of normal cardiac growth," *Circulation Research*, vol. 86, no. 3, pp. 302–311, 2000.

[44] G. R. Wong, C. J. Nalliah, G. Lee, et al., "Dynamic Atrial Substrate During High-Density Mapping of Paroxysmal and Persistent AF: Implications for Substrate Ablation," *JACC: Clinical Electrophysiology*, vol. 5, no. 11, pp. 1265–1277, nov 2019.

[45] K. Fukumoto, M. Habibi, E. G. Ipek, et al., "Association of Left Atrial Local Conduction Velocity with Late Gadolinium Enhancement on Cardiac Magnetic Resonance in Patients with Atrial Fibrillation," *Circulation: Arrhythmia and Electrophysiology*, vol. 9, no. 3, mar 2016.

[46] S. Honarbakhsh, R. J. Schilling, M. Orini, et al., "Structural remodeling and conduction velocity dynamics in the human left atrium: Relationship with reentrant mechanisms sustaining atrial fibrillation," *Heart Rhythm*, vol. 16, no. 1, pp. 18–25, jan 2019.

[47] J. G. Travers, F. A. Kamal, J. Robbins, et al., "Cardiac fibrosis: The fibroblast awakens," *Circulation Research*, vol. 118, no. 6, pp. 1021–1040, mar 2016.

[48] N. G. Frangogiannis, "Cardiac fibrosis," *Cardiovascular Research*, vol. 117, no. 6, pp. 1450–1488, may 2021.

[49] A. G. Kléber and Y. Rudy, "Basic Mechanisms of Cardiac Impulse Propagation and Associated Arrhythmias," *Physiological Reviews*, vol. 84, no. 2, pp. 431–488, 2004.

[50] P. Kong, P. Christia, and N. G. Frangogiannis, "The pathogenesis of cardiac fibrosis," *Cellular and Molecular Life Sciences*, vol. 71, no. 4, pp. 549–574, feb 2014.

[51] D. H. Lau, D. Linz, U. Schotten, et al., "Pathophysiology of Paroxysmal and Persistent Atrial Fibrillation: Rotors, Foci and Fibrosis," *Heart Lung and Circulation*, vol. 26, no. 9, pp. 887–893, 2017.

[52] J. Andrade, P. Khairy, D. Dobrev, et al., "The clinical profile and pathophysiology of atrial fibrillation: Relationships among clinical features, epidemiology, and mechanisms," *Circulation Research*, vol. 114, no. 9, pp. 1453–1468, 2014.

[53] M. Haïssaguerre, P. Jaïs, D. C. Shah, et al., "Spontaneous Initiation of Atrial Fibrillation by Ectopic Beats Originating in the Pulmonary Veins," *New England Journal of Medicine*, vol. 339, no. 10, pp. 659–666, sep 1998.

[54] S. M. Narayan, D. Kazi, D. E. Krummen, et al., "Repolarization and Activation Restitution Near Human Pulmonary Veins and Atrial Fibrillation Initiation. A Mechanism for the Initiation of Atrial Fibrillation by Premature Beats," *Journal of the American College of Cardiology*, vol. 52, no. 15, pp. 1222–1230, oct 2008.

[55] A. W. Teh, P. M. Kistler, G. Lee, et al., "Electroanatomic properties of the pulmonary veins: Slowed conduction, low voltage and altered refractoriness in AF patients," *Journal of Cardiovascular Electrophysiology*, vol. 22, no. 10, pp. 1083–1091, 2011.

[56] F. S. Ng, B. S. Handa, X. Li, et al., "Toward Mechanism-Directed Electrophenotype-Based Treatments for Atrial Fibrillation," *Frontiers in Physiology*, vol. 11, aug 2020.

[57] G. Y. Lip and P. B. Nielsen, "Should Patients with Atrial Fibrillation and 1 Stroke Risk Factor (CHA2DS2-VASc Score 1 in Men, 2 in Women) Be Anticoagulated?: Yes: even 1 Stroke Risk Factor Confers a Real Risk of Stroke," *Circulation*, vol. 133, no. 15, pp. 1498–1503, apr 2016.

[58] S. Kimber, E. Downar, S. Masse, et al., "A comparison of unipolar and bipolar electrodes during cardiac mapping studies," *PACE - Pacing and Clinical Electrophysiology*, vol. 19, no. 8, pp. 1196–1204, aug 1996.

[59] F. M. Weber, C. Schilling, G. Seemann, et al., "Wave-direction and conduction-velocity analysis from intracardiac electrograms-a single-shot technique," *IEEE Transactions on Biomedical Engineering*, vol. 57, no. 10 PART 1, pp. 2394–2401, oct 2010.

[60] S. Bhatia, A. Sugrue, and S. Asirvatham, "Atrial Fibrillation: Beyond Rate Control," *Mayo Clinic Proceedings*, vol. 93, no. 3, pp. 373–380, mar 2018.

[61] G. M. Marcus, Y. Yang, P. D. Varosy, et al., "Regional left atrial voltage in patients with atrial fibrillation," *Heart Rhythm*, vol. 4, no. 2, pp. 138–144, feb 2007.

[62] K. Miyamoto, T. Tsuchiya, S. Narita, et al., "Bipolar electrogram amplitudes in the left atrium are related to local conduction velocity in patients with atrial fibrillation," *Europace*, vol. 11, no. 12, pp. 1597–1605, dec 2009.

[63] P. Jaïs, D. C. Shah, M. Haïssaguerre, et al., "Mapping and ablation of left atrial flutters," *Circulation*, vol. 101, no. 25, pp. 2928–2934, jun 2000.

[64] P. Jaïs, S. Matsuo, S. Knecht, et al., "A deductive mapping strategy for atrial tachycardia following atrial fibrillation ablation: Importance of localized reentry," *Journal of Cardiovascular Electrophysiology*, vol. 20, no. 5, pp. 480–491, may 2009.

[65] L. Saghy, C. Tutuianu, and J. Szilagyi, "Atrial Tachycardias Following Atrial Fibrillation Ablation," *Current Cardiology Reviews*, vol. 11, no. 2, pp. 149–156, 2014.

[66] S. Nath, J. P. Dimarco, and D. E. Haines, "Basic Aspects of Radiofrequency Catheter Ablation," *Journal of Cardiovascular Electrophysiology*, vol. 5, no. 10, pp. 863–876, oct 1994.

[67] B. G. Bass, "Restitution of the action potential in cat papillary muscle," *American Journal of Physiology*, vol. 228, no. 6, pp. 1717–1724, 1975.

[68] M. R. Boyet and B. R. Jewell, "Analysis of the effects of changes in rate and rhythm upon electrical activity in the heart," *Progress in Biophysics and Molecular Biology*, vol. 36, no. C, pp. 1–52, 1981.

[69] B. Echebarria and A. Karma, "Instability and Spatiotemporal Dynamics of Alternans in Paced Cardiac Tissue," *Physical Review Letters*, vol. 88, no. 20, p. 4, 2002.

[70] A. Karma, "Electrical alternans and spiral wave breakup in cardiac tissue," *Chaos*, vol. 4, no. 3, pp. 461–472, sep 1994.

[71] A. L. Hodgkin and A. F. Huxley, "A quantitative description of membrane current and its application to conduction and excitation in nerve," *The Journal of Physiology*, vol. 117, no. 4, pp. 500–544, aug 1952.

[72] M. Courtemanche, R. J. Ramirez, and S. Nattel, "Ionic mechanisms underlying human atrial action potential properties: Insights from a mathematical model," *American Journal of Physiology - Heart and Circulatory Physiology*, vol. 275, no. 1 44-1, pp. H301–H321, jul 1998.

[73] R. E. Jewett, "Characteristics of physician's assistant programs," PhD thesis, Massachusetts Institute of Technology, 1975.

[74] G. Seemann, F. B. Sachse, M. Karl, et al., "Framework for Modular, Flexible and Efficient Solving the Cardiac Bidomain Equations Using PETSc," in *Progress in Industrial Mathematics at ECMI 2008*. Springer Berlin Heidelberg, 2010, pp. 363–369.

[75] G. Plank, A. Loewe, A. Neic, et al., "The openCARP simulation environment for cardiac electrophysiology," *Computer Methods and Programs in Biomedicine*, vol. 208, p. 106223, jun 2021.

[76] S. J. Ahn, W. Rauh, and H. J. Warnecke, "Least-squares orthogonal distances fitting of circle, sphere, elipse, hyperbola, and parabola," *Pattern Recognition*, vol. 34, no. 12, pp. 2283–2303, dec 2001.

[77] N. Greggio, A. Bernardino, C. Laschi, et al., "An algorithm for the least square-fitting of ellipses," *Proceedings - International Conference on Tools with Artificial Intelligence, ICTAI*, vol. 2, pp. 351–353, 2010.

[78] J. Hadamard, "Sur les problems aux derivees patielles et leur signification physique," *Princeton University Bulletin*, vol. 13, pp. 49–52, 1902.

[79] M. Ester, H.-P. Kriegel, J. Sander, et al., "A Density-Based Algorithm for Discovering Clusters in Large Spatial Databases with Noise," *Proceedings of the 2nd International Conference on Knowledge Discovery and Data Mining*, pp. 226–231, 1996.

[80] H. Calkins, K. H. Kuck, R. Cappato, et al., "2012 HRS/EHRA/ECAS Expert Consensus Statement on Catheter and Surgical Ablation of Atrial Fibrillation: Recommendations for Patient Selection, Procedural Techniques, Patient Management and Follow-up, Definitions, Endpoints, and Research Trial Design," *Heart Rhythm*, vol. 9, no. 4, pp. 632–696.e21, 2012.

[81] G. Ciconte, G. Baltogiannis, C. De Asmundis, et al., "Circumferential pulmonary vein isolation as index procedure for persistent atrial fibrillation: A comparison between radiofrequency catheter ablation and second-generation cryoballoon ablation," *Europace*, vol. 17, no. 4, pp. 559–565, apr 2015.

[82] D. Scherr, P. Khairy, S. Miyazaki, et al., "Five-year outcome of catheter ablation of persistent atrial fibrillation using termination of atrial fibrillation as a procedural endpoint," *Circulation: Arrhythmia and Electrophysiology*, vol. 8, no. 1, pp. 18–24, feb 2015.

[83] J. A. Clarnette, A. G. Brooks, R. Mahajan, et al., "Outcomes of persistent and long-standing persistent atrial fibrillation ablation: a systematic review and meta-analysis," *Europace : European pacing, arrhythmias, and cardiac electrophysiology : journal of the working groups on cardiac pacing, arrhythmias, and cardiac cellular electrophysiology of the European Society of Cardiology*, vol. 20, no. FI3, pp. f366–f376, nov 2018.

[84] J. Seitz, C. Bars, G. Théodore, et al., "AF Ablation Guided by Spatiotemporal Electrogram Dispersion Without Pulmonary Vein Isolation: A Wholly Patient-Tailored Approach," *Journal of the American College of Cardiology*, vol. 69, no. 3, pp. 303–321, 2017.

[85] C. McGann, N. Akoum, A. Patel, et al., "Atrial fibrillation ablation outcome is predicted by left atrial remodeling on MRI," *Circulation: Arrhythmia and Electrophysiology*, vol. 7, no. 1, pp. 23–30, feb 2014.

[86] N. Akoum, A. Morris, D. Perry, et al., "Substrate modification is a better predictor of catheter ablation success in atrial fibrillation than pulmonary vein isolation: An LGE-MRI study," *Clinical Medicine Insights: Cardiology*, vol. 9, pp. 25–31, jan 2015.

[87] M. S. Spach, J. F. Heidlage, P. C. Dolber, et al., "Mechanism of origin of conduction disturbances in aging human atrial bundles: Experimental and model study," *Heart Rhythm*, vol. 4, no. 2, pp. 175–185, 2007.

[88] S. Pollnow, "Characterizing Cardiac Electrophysiology during Radiofrequency Ablation : An Integrative Ex vivo, In silico, and In vivo Approach," PhD Thesis, Karlsruhe, 2019.

[89] M. Haissaguerre, A. J. Shah, H. Cochet, et al., "Intermittent drivers anchoring to structural heterogeneities as a major pathophysiological mechanism of human persistent atrial fibrillation," *Journal of Physiology*, vol. 594, no. 9, pp. 2387–2398, 2016.

[90] L. A. Unger, L. Azzolin, M. Nothstein, et al., "Cycle length statistics during human atrial fibrillation reveal refractory properties of the underlying substrate: A combined in silico and clinical test of concept study," *Europace*, vol. 23, no. Supplement_1, pp. I133–I142, mar 2021.

[91] S. De Jong, T. A. Van Veen, H. V. Van Rijen, et al., "Fibrosis and cardiac arrhythmias," *Journal of Cardiovascular Pharmacology*, vol. 57, no. 6, pp. 630–638, 2011.

[92] K. Nademanee, J. McKenzie, E. Kosar, et al., "A new approach for catheter ablation of atrial fibrillation: Mapping of the electrophysiologic substrate," *Journal of the American College of Cardiology*, vol. 43, no. 11, pp. 2044–2053, 2004.

[93] M. Haïssaguerre, M. Hocini, P. Sanders, et al., "Localized sources maintaining atrial fibrillation organized by prior ablation," *Circulation*, vol. 113, no. 5, pp. 616–625, 2006.

[94] M. Rottmann, "Multiple Interacting Rotational , Focal , and Wavelet Activities at Heterogeneous Tissue in Atrial Fibrillation," PhD Thesis, Karlsruhe, 2017.

[95] S. Rolf, S. Kircher, A. Arya, et al., "Tailored atrial substrate modification based on low-voltage areas in catheter ablation of atrial fibrillation," *Circulation: Arrhythmia and Electrophysiology*, vol. 7, no. 5, pp. 825–833, oct 2014.

[96] A. Yagishita, J. R. Gimbel, S. De Oliveira, et al., "Long-Term Outcome of Left Atrial Voltage-Guided Substrate Ablation During Atrial Fibrillation: A Novel Adjunctive Ablation Strategy," *Journal of Cardiovascular Electrophysiology*, vol. 28, no. 2, pp. 147–155, 2017.

[97] S. Zahid, H. Cochet, P. M. Boyle, et al., "Patient-derived models link re-entrant driver localization in atrial fibrillation to fibrosis spatial pattern," *Cardiovascular Research*, vol. 110, no. 3, pp. 443–454, 2016.

[98] T. Oesterlein, D. Frisch, A. Loewe, et al., "Basket-type catheters: Diagnostic pitfalls caused by deformation and limited coverage," *BioMed Research International*, vol. 2016, 2016.

[99] P. Sanders, O. Berenfeld, and M. Hocini, "Spectral Analysis Identifies Sites of High-Frequency Activity Maintaining Atrial Fibrillation in Humans," *ACC Current Journal Review*, vol. 14, no. 12, p. 40, 2005.

[100] M. Nothstein, A. Luik, A. Jadidi, et al., "CVAR-Seg: An Automated Signal Segmentation Pipeline for Conduction Velocity and Amplitude Restitution," *Frontiers in Physiology*, vol. 12, may 2021.

[101] R. B. Schnabel, X. Yin, P. Gona, et al., "50 year trends in atrial fibrillation prevalence, incidence, risk factors, and mortality in the Framingham Heart Study: A cohort study," *The Lancet*, vol. 386, no. 9989, pp. 154–162, jul 2015.

[102] J. Ramírez and A. Tinker, "Ventricular Restitution Predicts Paroxysmal Atrial Fibrillation in Horses," *Function*, vol. 2, no. 1, nov 2020.

[103] A. Verma, O. M. Wazni, N. F. Marrouche, et al., "Pre-existent left atrial scarring in patients undergoing pulmonary vein antrum isolation: An independent predictor of procedural failure," *Journal of the American College of Cardiology*, vol. 45, no. 2, pp. 285–292, jan 2005.

[104] F. H. Fenton, E. M. Cherry, H. M. Hastings, et al., "Multiple mechanisms of spiral wave breakup in a model of cardiac electrical activity," *Chaos*, vol. 12, no. 3, pp. 852–892, sep 2002.

[105] Y. Xie, A. Garfinkel, J. N. Weiss, et al., "Cardiac alternans induced by fibroblast-myocyte coupling: Mechanistic insights from computational models," *American Journal of Physiology - Heart and Circulatory Physiology*, vol. 297, no. 2, pp. H775–H784, aug 2009.

[106] M. R. Franz, P. L. Karasik, C. Li, et al., "Electrical remodeling of the human atrium: Similar effects in patients with chronic atrial fibrillation and atrial flutter," *Journal of the American College of Cardiology*, vol. 30, no. 7, pp. 1785–1792, 1997.

[107] S. S. Kalb, H. M. Dobrovolny, E. G. Tolkacheva, et al., "The restitution portrait: A new method for investigating rate-dependent restitution," *Journal of Cardiovascular Electrophysiology*, vol. 15, no. 6, pp. 698–709, jun 2004.

[108] C. Schilling, M. Keller, D. Scherr, et al., "Fuzzy decision tree to classify complex fractionated atrial electrograms," *Biomedizinische Technik*, vol. 60, no. 3, pp. 245–255, jan 2015.

[109] G. Lenis, A. Kramlich, T. Oesterlein, et al., "Development and benchmarking of activity detection algorithms for intracardiac electrograms measured during atrial flutter," in *Workshop Biosignal*, 2016, pp. 5–8.

[110] C. Corrado, J. Whitaker, H. Chubb, et al., "Personalized models of human atrial electrophysiology derived from endocardial electrograms," *IEEE Transactions on Biomedical Engineering*, vol. 64, no. 4, pp. 735–742, apr 2017.

[111] N. Pilia, C. Nagel, G. Lenis, et al., "ECGdeli - An open source ECG delineation toolbox for MATLAB," *SoftwareX*, vol. 13, p. 100639, jan 2021.

[112] J. Malmivuo and R. Plonsey, *Bioelectromagnetism: Principles and Applications of Bioelectric and Biomagnetic Fields*. Oxford University Press, oct 2012.

[113] C. Schilling, M. P. Nguyen, A. Luik, et al., "Non-linear energy operator for the analysis of intracardial electrograms," in *IFMBE Proceedings*, 2009, vol. 25, no. 4, pp. 872–875.

[114] A. Naber, D. Berwanger, and W. Nahm, "Geodesic length measurement in medical images: Effect of the discretization by the camera chip and quantitative assessment of error reduction methods," *Photonics*, vol. 7, no. 3, p. 70, sep 2020.

[115] J. J. Blauer, F. Han, R. Ranjan, et al., "Controlled activation for interrogation of the electrophysiological substrate," in *Computing in Cardiology*, vol. 41, no. January, 2014, pp. 189–192.

[116] E. J. Vigmond, M. Hughes, G. Plank, et al., "Computational Tools for Modeling Electrical Activity in Cardiac Tissue," *Journal of Electrocardiology*, vol. 36, no. SUPPL., pp. 69–74, 2003.

[117] V. D. Corino, M. W. Rivolta, R. Sassi, et al., "Ventricular activity cancellation in electrograms during atrial fibrillation with constraints on residuals' power," *Medical Engineering and Physics*, vol. 35, no. 12, pp. 1770–1777, dec 2013.

[118] G. Lenis, N. Pilia, A. Loewe, et al., "Comparison of Baseline Wander Removal Techniques considering the Preservation of ST Changes in the Ischemic ECG: A Simulation Study," *Computational and Mathematical Methods in Medicine*, vol. 2017, pp. 1–13, 2017.

[119] M. El Haddad, R. Houben, R. Stroobandt, et al., "Algorithmic detection of the beginning and end of bipolar electrograms: Implications for novel methods to assess local activation time during atrial tachycardia," *Biomedical Signal Processing and Control*, vol. 8, no. 6, pp. 981–991, nov 2013.

[120] V. Kremen and L. Lhotska, "Novel approach to search for individual signal complexes in complex fractionated atrial electrograms using wavelet transform," in *Proceedings of the IEEE/EMBS Region 8 International Conference on Information Technology Applications in Biomedicine, ITAB*. IEEE, nov 2007, pp. 83–86.

[121] M. Marino, E. Luján, E. Mocskos, et al., "OpenEP: an open-source simulator for electroporation-based tumor treatments," *Nature Scientific Reports*, vol. 11, no. 1, p. 1423, dec 2021.

[122] C. Corrado, S. Williams, R. Karim, et al., "A work flow to build and validate patient specific left atrium electrophysiology models from catheter measurements," *Medical Image Analysis*, vol. 47, pp. 153–163, jul 2018.

[123] B. Abdi, R. C. Hendriks, A. J. van der Veen, et al., "Improved local activation time annotation of fractionated atrial electrograms for atrial mapping," *Computers in Biology and Medicine*, vol. 117, p. 103590, feb 2020.

[124] B. Verma, T. Oesterlein, A. Loewe, et al., "Regional conduction velocity calculation from clinical multichannel electrograms in human atria," *Computers in Biology and Medicine*, vol. 92, pp. 188–196, jan 2018.

[125] L. Anna Unger, T. Georg Oesterlein, A. Loewe, et al., "Noise Quantification and Noise Reduction for Unipolar and Bipolar Electrograms," in *2019 Computing in Cardiology Conference (CinC)*, vol. 45, dec 2019, pp. 1–4.

[126] M. S. Spach, P. C. Dolber, and J. F. Heidlage, "Influence of the passive anisotropic properties on directional differences in propagation following modification of the sodium conductance in human atrial muscle. A model of reentry based on anisotropic discontinuous propagation," *Circulation Research*, vol. 62, no. 4, pp. 811–832, apr 1988.

[127] D. Harrild and C. Henriquez, "A computer model of normal conduction in the human atria." *Circulation research*, vol. 87, no. 7, sep 2000.

[128] S. Coveney, C. Corrado, C. H. Roney, et al., "Gaussian process manifold interpolation for probabilistic atrial activation maps and uncertain conduction velocity: Gaussian Process Manifold Interpolation," *Philosophical Transactions of the Royal Society A: Mathematical, Physical and Engineering Sciences*, vol. 378, no. 2173, p. 20190345, jun 2020.

[129] S. Coveney, R. H. Clayton, C. Corrado, et al., "Probabilistic Interpolation of Uncertain Local Activation Times on Human Atrial Manifolds," *IEEE Transactions on Biomedical Engineering*, vol. 67, no. 1, pp. 99–109, jan 2020.

[130] C. H. Roney, R. Bendikas, F. Pashakhanloo, et al., "Constructing a Human Atrial Fibre Atlas," *Annals of Biomedical Engineering*, vol. 49, no. 1, pp. 233–250, jan 2021.

[131] D. Nairn, H. Lehrmann, B. Müller-Edenborn, et al., "Comparison of Unipolar and Bipolar Voltage Mapping for Localization of Left Atrial Arrhythmogenic Substrate in Patients With Atrial Fibrillation," *Frontiers in Physiology*, vol. 11, nov 2020.

[132] R. Killick, P. Fearnhead, and I. A. Eckley, "Optimal detection of changepoints with a linear computational cost," *Journal of the American Statistical Association*, vol. 107, no. 500, pp. 1590–1598, dec 2012.

[133] M. Masè and F. Ravelli, "Automatic reconstruction of activation and velocity maps from electro-anatomic data by radial basis functions," in *2010 Annual International Conference of the IEEE Engineering in Medicine and Biology Society, EMBC'10*. IEEE, aug 2010, pp. 2608–2611.

[134] A. R. Barnette, P. V. Bayly, S. Zhang, et al., "Estimation of 3-D conduction velocity vector fields from cardiac mapping data," *IEEE Transactions on Biomedical Engineering*, vol. 47, no. 8, pp. 1027–1035, 2000.

[135] B. Lütkenhöner, "Dipole separability in a neuromagnetic source analysis," *IEEE Transactions on Biomedical Engineering*, vol. 45, no. 5, pp. 563–571, may 1998.

[136] J. P. Wikswo, S. F. Lin, and R. A. Abbas, "Virtual electrodes in cardiac tissue: a common mechanism for anodal and cathodal stimulation," *Biophysical Journal*, vol. 69, no. 6, pp. 2195–2210, dec 1995.

[137] U. Schotten, S. Verheule, P. Kirchhof, et al., "Pathophysiological mechanisms of atrial fibrillation: A translational appraisal," *Physiological Reviews*, vol. 91, no. 1, pp. 265–325, jan 2011.

[138] MATLAB, *version 9.9.0 (R2020b)*. Natick, Massachusetts: The MathWorks Inc., 2020.

[139] M. S. van Schie, A. Heida, Y. J. H. J. Taverne, et al., "Identification of local atrial conduction heterogeneities using high-density conduction velocity estimation," *EP Europace*, may 2021.

[140] B. Flach and P. Hlavac, “Expectation Maximization Algorithm,” *Computer Vision*, pp. 265–268, 2014.

[141] R. Ahmadzadeh, “Expectation Maximization Algorithm,” MATLAB Central File Exchange, 2021.

[142] N. Kurata, M. Masuda, T. Kanda, et al., “Slow whole left atrial conduction velocity after pulmonary vein isolation predicts atrial fibrillation recurrence,” *Journal of Cardiovascular Electrophysiology*, vol. 31, no. 8, pp. 1942–1949, aug 2020.

[143] P. Attuel, R. Childers, B. Cauchemez, et al., “Failure in the rate adaptation of the atrial refractory period: its relationship to vulnerability,” *International Journal of Cardiology*, vol. 2, no. 2, pp. 179–197, 1982.

[144] G. D. Byrd, S. M. Prasad, C. M. Ripplinger, et al., “Importance of geometry and refractory period in sustaining atrial fibrillation: Testing the critical mass hypothesis,” *Circulation*, vol. 112, no. 9 SUPPL., aug 2005.

[145] M. L. Koller, M. L. Riccio, and R. F. Gilmour, “Dynamic restitution of action potential duration during electrical alternans and ventricular fibrillation,” *American Journal of Physiology - Heart and Circulatory Physiology*, vol. 275, no. 5 44-5, pp. H1635–H1642, nov 1998.

[146] C. R. Mitchell and M. K. Das, “Paroxysmal lone atrial fibrillation is associated with an abnormal atrial substrate: Characterizing the "second factor",” *Journal of Atrial Fibrillation*, vol. 1, no. 8, pp. 496–499, 2009.

[147] H. L. Greene, J. A. Werner, B. W. Gross, et al., “Prolongation of cardiac refractory times in man by clofilium phosphate, a new antiarrhythmic agent,” *American Heart Journal*, vol. 106, no. 3, pp. 492–501, 1983.

[148] P. Jaïs, M. Hocini, L. Macle, et al., “Distinctive electrophysiological properties of pulmonary veins in patients with atrial fibrillation,” *Circulation*, vol. 106, no. 19, pp. 2479–2485, nov 2002.

[149] S. Nattel, J. Heijman, L. Zhou, et al., “Molecular Basis of Atrial Fibrillation Pathophysiology and Therapy: A Translational Perspective,” *Circulation Research*, pp. 51–72, 2020.

[150] E. Anter, C. M. Tschabrunn, and M. E. Josephson, “High-Resolution Mapping of Scar-Related Atrial Arrhythmias Using Smaller Electrodes with Closer Interelectrode Spacing,” *Circulation: Arrhythmia and Electrophysiology*, vol. 8, no. 3, pp. 537–545, 2015.

[151] S. Schuler, M. W. Keller, T. Oesterlein, et al., “Influence of Catheter Orientation, Tissue Thickness and Conduction Velocity on the Intracardiac Electrogram,” *Biomedical Engineering / Biomedizinische Technik*, 2013.

[152] D. Li, S. Fareh, T. K. Leung, et al., “Promotion of atrial fibrillation by heart failure in dogs: Atrial remodeling of a different sort,” *Circulation*, vol. 100, no. 1, pp. 87–95, jul 1999.

List of Publications and Supervised Theses

Journal Articles

- **Amir Jadidi** & **Mark Nothstein** (joint authorship), Juan Chen, Heiko Lehrmann, Olaf Dössel, Jürgen Allgeier, Dietmar Trenk, Franz Josef Neumann, Axel Loewe, Björn Müller-Edenborn, Thomas Arentz, *Specific Electrogram Characteristics Identify the Extra-Pulmonary Vein Arrhythmogenic Sources of Persistent Atrial Fibrillation – Characterization of the Arrhythmogenic Electrogram Patterns During Atrial Fibrillation and Sinus Rhythm*, Nature Scientific Reports 10, 2020, doi:10.1038/s41598-020-65564-2
- **Mark Nothstein**, Armin Luik, Amir Jadidi, Jorge Sánchez, Laura Unger, Eike Wülfers, Olaf Dössel, Gunnar Seemann, Claus Schmitt, Axel Loewe, *CVAR-Seg: An Automated Signal Segmentation Pipeline for Conduction Velocity and Amplitude Restitution*, Frontiers Physiology 12 2021, doi:10.3389/fphys.2021.673047
- Jorge Sánchez, Giorgio Luongo, **Mark Nothstein**, Laura Unger, Javier Saiz, Beatriz Trenor, Armin Luik, Olaf Dössel, Axel Loewe, *Using Machine Learning to Characterize Atrial Fibrotic Substrate from Intracardiac Signals using a Hybrid in silico and in vivo Dataset*, Frontiers Physiology 12, 2021, doi:10.3389/fphys.2021.699291
- Laura Unger, Luca Azzolin, **Mark Nothstein**, Jorge Sánchez, Armin Luik, Gunnar Seemann, Srinath Yeshwant, Tobias Oesterlein, Olaf Dössel, Claus Schmitt, Peter Spector, Axel Loewe, *Cycle length statistics during human atrial fibrillation reveal refractory properties of the underlying substrate: A combined in silico and clinical test of concept study*, Europace 23, 2021, I133–I142. doi:10.1093/europace/euaa404
- Gernot Plank, Axel Loewe, Aurel Neic, Christoph Augustin, Yung-Lin Huang, Matthias Gsel, Elias Karabelas, **Mark Nothstein**, Anton J.Prassl, Jorge Sánchez, Gunnar Seemann, Edward Vigmond, *The openCARP Simulation Environment for Cardiac Electrophysiology*, Computer Methods and Programs in Biomedicine, 2021, doi:10.1016/j.cmpb.2021.106223

Refereed Conference Articles

- Jorge Sánchez, **Mark Nothstein**, Laura Unger, Javier Saiz, Beatriz Trénor, Olaf Dössel, Axel Loewe,*Influence of Fibrotic Tissue Arrangement on Intracardiac Electrograms During Persistent Atrial Fibrillation*, Computing in Cardiology (CinC) 2019
- Jorge Sánchez, **Mark Nothstein**, Aurel Neic, Yung-Lin Huang, Anton J. Prassl, Jochen Klar, Robert Ulrich, Felix Bach, Philipp Zschumme, Michael Selzer, Gernot Plank, Edward Vigmond, Gunnar Seemann, Axel Loewe, *openCARP: An Open Sustainable Framework for in-silico Cardiac Electrophysiology Research*, Computing in Cardiology (CinC) 2020

Refereed Conference Abstracts

- **Mark Nothstein**, Björn Müller-Edenborn, Thomas Arentz, Olaf Dössel, Amir Jadidi, Axel Loewe, *Mechanistic insights into arrhythmogenesis in atrial fibrillation - Exploring the underlying electrical activity in AF and effects of targeted focal ablation of the critical substrate in-silico*, Deutsche Gesellschaft für Biomedizinische Technik (DGBMT) 2020
- **Mark Nothstein**, Armin Luik, Amir Jadidi, Eike Wülfers, Olaf Dössel, Gunnar Seemann, Claus Schmitt, Axel Loewe, *Investigating the correlation of local rate dependency of atrial conduction velocity and voltage*, Deutsche Gesellschaft für Kardiologie (DGK), 2020
- **Mark Nothstein**, Armin Luik, Amir Jadidi, Eike M. Wülfers, Olaf Dössel, Gunnar Seemann, Claus Schmitt, Axel Loewe, *Rate Dependency of Global and Local Atrial Conduction Velocity based on Intracardiac Signals*, Deutsche Gesellschaft für Kardiologie (DGK), 2019
- **Mark Nothstein**, Armin Luik, Eike Wülfers, Amir Jadidi, Olaf Dössel, Claus Schmitt, Gunnar Seemann, Axel Loewe, *Automated Stimulus Artefact Removal for the Clinical S1-S2 Pacing Protocol*, Engineering in Medicine and Biology Society (EMBC), 2019
- **Mark Nothstein**, Olaf Dössel, Axel Loewe, *Rotational Activity Around Fibrotic Tissue During Atrial Fibrillation*, Deutsche Gesellschaft für Biomedizinische Technik (DGBMT), 2018

Conference Presentations

- **Tiago Almeida** & **Mark Nothstein**, Xin Li, Michela Masè, Flavia Ravelli, Diogo C Soriano, Arthur S Bezerra, Fernando Schlindwein, Takashi Yoneyama, Olaf Dössel, G André Ng, Axel Loewe, *Phase singularities in a cardiac patch model with a non-conductive fibrotic area during AF*, Computing in Cardiology CinC, 2020

Invited Talks

- **Mark Nothstein**, *Rate Dependency of Global and Local Atrial Conduction Velocity based on Intracardiac Signals*, Esanum: Das Portal für Ärzte , 2019

Supervised Student Theses

- Christoph Luz, *Determination and Transformation of Conduction Velocities during a Catheter Study using a Computational Model*, Bachelor Thesis, Institute of Biomedical Engineering, Karlsruhe Institute of Technology (KIT), 2019
- Hana Dzindo, *Behavior and Transformation of Restitution Curves of Different Stimulation Protocols under Atrial Fibrillation Conditions*, Bachelor Thesis, Institute of Biomedical Engineering, Karlsruhe Institute of Technology (KIT), 2020
- Johannes Tischer, *Implementation and assessment of a statistical fitting approach for detection of conduction velocity, anisotropy ratio and fiber orientation of cardiac tissue*, Bachelor Thesis, Institute of Biomedical Engineering, Karlsruhe Institute of Technology (KIT), 2021